



UNIVERSITAT^{DE}
BARCELONA

Carboxymethyl cellulose-based cryogels as scaffolds for pancreatic and skeletal muscle tissue engineering

Ferran Velasco Mallorquí



Aquesta tesi doctoral està subjecta a la llicència **Reconeixement 4.0. Espanya de Creative Commons.**

Esta tesis doctoral está sujeta a la licencia **Reconocimiento 4.0. España de Creative Commons.**

This doctoral thesis is licensed under the **Creative Commons Attribution 4.0. Spain License.**



UNIVERSITAT DE
BARCELONA



Programa de doctorat de Biomedicina

Facultat de Medicina

Universitat de Barcelona

TESI DOCTORAL

Carboxymethyl cellulose-based cryogels as scaffolds for pancreatic and skeletal muscle tissue engineering

Memòria de tesi doctoral presentada per Ferran
Velasco Mallorquí per optar al grau de doctor per la
Universitat de Barcelona

Tesi realitzada al group Biosensors for Bioengineering
de l'Institut de Bioenginyeria de Catalunya (IBEC)

Prof. Javier Ramón Azcón

Thesis director

Prof. Ramón Farré Ventura

Thesis tutor

Barcelona, 2021

“Ever tried. Ever failed. No matter.

Try again. Fail again. Fail better”

Samuel Beckett

ACKNOWLEDGMENTS

Estimat lector o lectora, ja sé que el primer que faràs, serà venir a llegir els agraïments, però et proposo una cosa: Fes primer una ullada a la tesi, que tanta feina porta, i després ja tornaràs aquí per el teu gaudi.

Gràcies.

Sabeu que això no se'm dona bé ni tinc ganes de fer-ho. Lo important ja està dit. Però ai... els formalismes. Així doncs, som-hi:

Primer de tot agrair a en Javi, per haver-me donat la oportunitat de fer el doctorat al seu grup. I no només això, sinó per confiar en mi per ser el seu primer doctorand dels "Ramones". Hem passat de veure un laboratori buit, a veure, com el grup de persones que has anat reunint són excel·lents persones i científiques. He dit moltes vegades que per mi, el doctorat, era més un repte personal que no professional, i part de la persona en qui m'he convertit, molt del que he après, científicament i personalment, és gràcies a tu i a la confiança que sempre m'has mostrat. Lo d'aprendre química ho haurem de deixar per més endavant, això si.

Segon al meu tutor, el professor Ramon Farré, per acceptar a tutoritzar-me la tesi i confiar en les meves decisions.

A la Mariale, vam començar junts en aquesta aventura i ara, marxem junts. Poder compartir aquests anys amb tu i aprendre de tu, m'ha ensenyat no només a ser millor científic sinó millor persona. Moltes gràcies per la teva alegria, els teus consells i voler compartir els teus coneixements, amb un predoc que no sabia a on es posava.

Xio, per acompanyar-me en aquest viatge. Per compartir penes, decepcions, i alguna alegria, per tots els experiments fallits, per les converses al mechanical tester, per fer l'antisocial junts als congressos, pel viatge a Japó, pels mems, per tots els riures que hem compartit i per les mil anècdotes més que podríem explicar.

Laura, per les infinites coses que he après de tu. Per la teva manera de viure i veure la vida, per les discussions científiques i socials. Per donar-me un punt de vista diferent, fer-me reflexionar i aprendre. Per les converses disteses que em permetien desconectar i per haver estat allà sempre que ho he necessitat, tant científicament com anímicament.

A la Júlia i en Juanma per ajudar-me a tirar endavant aquesta tesi i per el bon rollo, la bona actitud i la bona predisposició que heu tingut sempre a donar-me un cop de mà. Júlia, gràcies per l'ajuda i la paciència. A saber quin desastre hauria fet amb la part del teixit pancreàtic si no haguessis vingut a guiar-me. I Juanma, gràcies per tot el coneixement i l'ajuda inestimable en la tota la part

del múscul i per ajudar-me a tirar endavant un article que si no fos per tu, a hores d'ara encara em rondaria pel cap.

I a la resta del grup de Ramones, Francesco, Ainhoa, Gerardo, Miriam, Ainoa, Miquel, Lluís, Eduard i a tots els estudiants que en formeu part, o que n'heu format part. Gràcies per tots els comentaris, protocols, discussions, xarramequeues varies i per haver seguit amb el bon rollo que hi havia al laboratori.

Als del BLOC. Si, tranquil·les. No m'oblido pas de vosaltres, però em ve de gust fer-vos un paràgraf a part. Gràcies Irene, Marc, Alba i Jose, per haver estat sempre disposades a escoltar i ajudar, per les converses disteses, per haver acceptat les meves bromes i els meus piques amb humor, i per haver fet més entretingut els meus últims mesos de doctorand. Esteu formant un grup molt xulo amb un projecte super interessant i estic segur que tot us anirà super bé.

No voldria passar per alt l'Àlex i l'Albert i a la Jordina. No sé si mai llegireu això, però el vostre bon rollo i bon saber fer, va ser el fonament del bon ambient que es respira en aquest laboratori. El fet que jo hagi pogut acabar la tesi, també és culpa vostra, així que gràcies.

A totes aquelles altres persones que s'han creuat en algun moment per la tesi d'aquest humil doctorand. Als Elenos per haver-nos acollit al principi, quan encara erem uns sense sostre i la vostre bona predisposició sempre que fos necessari. I a tots aquells científics i científiques que en algun moment ens hem creuat, ja sigui per col·laborar, per discussions científiques o simplement per xerrar una estona. No us nombro perquè segur que em deixaria algú.

Als amics de Beer Riders i del bàsquet Vilablareix. Gràcies per haver-me permès desconnectar de la tesi quan era necessari, per haver estat sempre disposats a escoltar les meves misèries i haver permès que tingués aquestes estones d'esbarjo tant necessàries.

A la meva família. A la mare i al pare, Núria i Joan, i a la meva germana Marta, sens dubte no hagués arribat fins aquí sense el vostre suport. Encara que no entenguéssiu ni fava del que us explico, gràcies per tota l'ajuda que m'heu donat per poder arribar fins aquí i haver estat sempre allà.

I a tu Ester. Per ser el meu pilar dia a dia. Per escoltar-me i recolzar-me. Per la infinita paciència que has tingut amb mi, i per sempre fer-me costat. Tot el que et digui es quedarà curt, així que, simplement, gràcies.

TABLE OF CONTENTS

I. ABSTRACT	1
II. ABBREVIATIONS.....	5
III. FIGURES	9
1. INTRODUCTION.....	13
1.1 TISSUE ENGINEERING	15
1.1.1 3D tissue engineering.....	16
1.2 CRYOGELS IN TISSUE ENGINEERING	23
1.2.1 Cryogelation principle.....	24
1.2.2 Cryogelation for tissue engineering.....	26
1.3 ORGANS-ON-A-CHIP.....	27
1.4 DIABETES	30
1.4.1 Type 1 diabetes	32
1.4.2 Type 2 diabetes	32
1.4.3 Gestational diabetes	33
1.4.4 Tissues related to diabetes.....	33
1.5 PANCREATIC TISSUE	35
1.5.1. Pancreas histology	35
1.5.2 Pancreas and beta-cell development.....	36
1.5.3 Hormone regulation.....	39
1.5.4 Pancreatic tissue engineering.....	40
1.5.5 Cryogels in pancreatic tissue engineering	41
1.6 SKELETAL MUSCLE TISSUE.....	43
1.6.1 Skeletal muscle structure.....	43
1.6.2 Skeletal muscle formation and differentiation.....	44
1.6.3 Skeletal muscle myokines.....	46
1.6.4 Skeletal muscle tissue engineering.....	47
1.6.5 Cryogels for skeletal muscle tissue engineering	50
2. HYPOTHESIS AND OBJECTIVES	51
2.1 HYPOTHESIS AND OBJECTIVES.....	53
2.2 WORK RELATED WITH THE THESIS	54
2.2.1 Journal articles directly exposed in the thesis.	54

2.2.2 Other scientific work related with the thesis.	55
3. MATERIALS AND METHODS	57
3.1 CRYOGEL FABRICATION.....	59
3.1.1 Prepolymer solution	59
3.1.2 Fabrication of the molds for cryogel fabrication.....	60
3.1.3 Random pore cryogel fabrication protocol.....	61
3.1.4 Random Bilayer cryogel fabrication protocol	62
3.1.5 Anisotropic pore cryogel fabrication protocol	63
3.1.6 Cleaning and sterilizing protocol	64
3.2 STRUCTURAL AND MECHANICAL CHARACTERIZATION	65
3.2.1 Pore distribution and morphology	65
3.2.2 Stiffness.....	66
3.2.3 Water uptake capability of the cryogel.....	67
3.2.4 Permeability assay	68
3.2.5 Electrical properties for anisotropic structure	70
3.3 PANCREATIC TISSUE ENGINEERING.....	71
3.3.1 Cell culture.....	71
3.3.2 Cell seeding.....	72
3.3.3 Cell health analysis by metabolic activity quantification	73
3.3.4 Pancreatic tissue immunostaining	75
3.3.5 Cell cluster diameter	76
3.3.6 Pseudoislets proliferation	76
3.3.7 Glucose Stimulation Insulin Secretion (GSIS)	76
3.3.8 Enzyme-linked immunosorbent assay (ELISA)	80
3.3.9 qPCR for INS1E	82
3.3.10 Diabetes modeling.....	85
3.4 SKELETAL MUSCLE TISSUE ENGINEERING.....	85
3.4.1 C2C12 cell culture	85
3.4.2 C2C12 cell seeding.	86
3.4.3 Electrical stimulation for skeletal muscle	86
3.4.4 Live/Dead assay	87
3.4.5 Skeletal immunostaining.....	88

3.4.6 Alignment in skeletal muscle	88
3.4.7 Fusion Index.....	89
3.4.8 qPCR for skeletal muscle.....	89
3.5 STATISTICAL ANALYSIS.....	91
4. RESULTS.....	93
4.1 CRYOGEL FABRICATION.....	95
4.1.1 Cryogels as a scaffold casting technique.....	95
4.1.2 Cryogel fabrication and optimization.....	99
4.1.3 Generation of PDMS molds for cryogel fabrication.....	102
4.2 CRYOGEL CHARACTERIZATION.....	104
4.2.1 Pore diameter.....	104
4.2.2 Stiffness.....	109
4.2.3 Swelling.....	112
4.2.4 Diffusion.....	113
4.2.5 Conductivity.....	115
4.3 PANCREATIC TISSUE	117
4.3.1 Pancreatic islets	117
4.3.2 INS1E cells	124
4.4 SKELETAL MUSCLE.....	139
4.4.1 Cell seeding.....	139
4.4.2 Cell viability.....	141
4.4.3 Cell alignment.....	143
4.4.4 Myogenic maturation.....	145
5. DISCUSSION.....	149
5.1 PANCREATIC TISSUE	152
5.2 SKELETAL MUSCLE.....	157
6. CONCLUSIONS	163
6.1 CONCLUSIONS	165
6.2 FUTURE WORK	166
7. BIBLIOGRAPHY.....	169
8. RESUM EN CATALÀ.....	195
9. JOURNAL ARTICLES.....	199

I. ABSTRACT

Diabetes incidence highly increased in the last years. According to IDF (International Diabetes Federation), 463 million people suffered this disease in 2019. The estimations of diabetic people highly increase in the upcoming years, rising approximately to 700 million diabetic patients in 2045 [1]. Type 2 diabetes (T2D) is the most common type of diabetes, representing 90% of diabetic patients. It occurs when the body becomes resistant to insulin.

Body insulin resistance confirms that T2D is not only a pancreatic disease, as there are many other tissues involved, like liver, adipose tissue, or skeletal muscle. This last has a significant implication in glucose-insulin homeostasis as it is one of the main glucose-consuming organs in the body.

Nowadays, to study how two tissues crosstalk between them, animal testing is the gold standard. However, the unmatching physiological behaviors compared to humans, the variability between different animals, ethical dilemmas, and the need to go for more personalized medicine activates the search for other suitable alternatives. At this point, Organs-on-a-chip appeared as a valid alternative. Organs-on-a-chip (OOC) are 3D bioengineered microfluidic cell culture platforms to simulate microphysiological environments of an organ or its specific functions.

Nowadays, to engineer the tissues for OOC applications, encapsulating cells inside hydrogels is the most common technique. Its beneficial properties include high water content, mechanical adjustability, and moldability to generate the desired architectures [2]. However, its small porosity limits nutrient and oxygen diffusion through it [3].

This problem is a significant limitation when pancreatic islets are encapsulated inside hydrogels due to their size ($\sim 100\ \mu\text{m}$ of diameter). Pancreatic islets are cell aggregations composed of many different cells as insulin-secreting cells (Beta-cells) or glucagon-secreting cells (alpha-cells). Similarly, skeletal muscle tissue is generally encapsulated in small bundles. Skeletal muscle is a highly aligned and multinucleated tissue formed from the fusion of single cells, called myoblasts, into multinucleated cells, called myotubes.

Cryogels have been proposed as a valid alternative to overcome these limitations. Cryogels are fabricated by crosslinking a prepolymer solution at sub-zero temperatures, so while the material crosslinks, water freezes, generating the desired micropore architecture. After thawing, cryogels are sponge-like scaffolds with microporous structure, high interconnected porosity, high diffusivity, fine-tuned properties, and desired internal pore architecture.

This thesis developed two cryogel scaffolds made of gelatin and carboxymethylcellulose with different pore architectures to engineer pancreatic and skeletal muscle tissues. Here, we proved that the achieved pore architecture fits with the prerequisites to engineer each tissue. Moreover, the mechanical and physical properties of each scaffold highly resemble the 3D microenvironment of each tissue. In pancreatic tissue, we generate a random pore cryogel to aggregate beta-cells to form pseudoislets. We proved that these engineered pseudoislets are viable, functional responding correctly to the glucose and improving insulin response compared to monolayer results. In the skeletal muscle approach, we could develop a highly aligned pore architecture to prompt cell alignment and cell fusion. Moreover, we incorporate carbon nanotubes to enhance the electrical conductivity of the scaffold, so by applying electrical pulse stimulation, we could improve the early steps of the myogenic maturation.

II. ABBREVIATIONS

AAD	Adipic acid dihydrazide
ATP	Adenosine triphosphate
BSA	Bovine serum albumin
cdNA	Complementary DNA
CMC	Carboxymethyl cellulose
CNT	Carbon nanotube
DMEM	Dulbecco's Modified Eagle Medium
ECM	Extracellular matrix
EDC	1-Ethyl-3-(3-dimethyl aminopropyl)-carbodiimide
EDTA	Ethylenediaminetetraacetic acid
ELISA	Enzyme-linked immunosorbent assay
EPS	Electrical pulse stimulation
EthD-1	ethidium homodimer-1
FBS	Fetal bovine serum
GelMA	Gelatin methacryoyl
GLUT4	Glucose transporter type 4
GSIS	Glucose stimulation insulin secretion
IDF	International Diabetes Federation
IL	Interleukin
KRBH	Krebs-Ringer Bicarbonate Buffer
MafA	V-maf musculoaponeurotic fibrosarcoma oncogene homolog A
mAb	Monoclonal antibody
MES	2-(N-Morpholino)ethanesulfonic acid hydrate
MHC	Myosin Heavy Chain
Min6	Mouse insulinoma
MRE	Magnetic resonance elastography
MRF4	Myogenic regulatory factor 4
MYF5	Myogenic factor 5
MYOD	Myogenic differentiation 1
MYOG	Myogenin
NeuroD1	Neurogenic differentiation 1
NHS	N-Hydroxysuccinimide
OOC	Organs-on-a-chip
PAX3	Paired box protein 3
PAX7	Paired box protein 7
PBS	Phosphate-buffered saline
PDMS	Polydimethylsiloxane
PDX1	Pancreas/duodenum homeobox protein 1
PEG	Poly(ethylene glycol)
PEGDA	Poly(ethylene glycol) diacrylate
PGA	Poly-glycolic acid
PLA	Poly(lactic acid)
PLC	Polycaprolactone
qPCR	Quantitative PCR
RGD	polypeptide Arginine-Glycine-Aspartic acid

Abbreviations

RNA	Ribonucleic acid
RPMI	Roswell Park Memorial Institute medium
SEM	Scanning electron microscope
T1D	Type 1 diabetes
T2D	Type 2 diabetes
TF	Transcription factor
Tnnt1	Troponin 1
TBS	Tris Buffered Saline
WHO	World Health Organization

III. FIGURES

Figure 1: Overview of tissue engineering process and some of its applications.	17
Figure 2: Overview of different crosslinking techniques.	20
Figure 3: Hydrogel encapsulation casting techniques.	23
Figure 4: Cryogel principle.	25
Figure 5: Overview of different Organs-on-a-Chip (OOC) fabricated for different tissues.	28
Figure 6: Infographic of diabetes incidence.	30
Figure 7: Body alterations due to diabetes.	31
Figure 8: Glucose-insulin homeostasis in different diabetes-related tissues.	34
Figure 9: Schematic representation of the pancreas and its functional unit, pancreatic islets.	36
Figure 10: Beta-cell differentiation pathway.	37
Figure 11: Small overview of pancreatic tissue engineering.	42
Figure 12: Skeletal muscle structure.	44
Figure 13: Transcription factors expressed during the myogenic development.	45
Figure 14: Overview of skeletal muscle tissue engineering.	48
Figure 15: Cryogel formation scheme.	59
Figure 16: Images of the PDMS molds.	61
Figure 17: Scheme of the fabrication of the random pore architecture cryogel.	62
Figure 18: Scheme of the fabrication of the bilayer random pore architecture cryogel.	63
Figure 19: Scheme of the fabrication of the anisotropic pore architecture scaffold.	64
Figure 20: ImageJ pore size quantification protocol.	66
Figure 21: Mechanical testing assay to determine stiffness by compression.	67
Figure 22: Permeability and diffusion experimental design.	69
Figure 23: Metabolic activity assay.	73
Figure 24: Scheme of the set-up for the real time GSIS measurements.	79
Figure 25: Sandwich ELISA scheme.	82
Figure 26: Schematic of the electrical stimulation process.	87
Figure 27: Scheme of cryogelation process.	95
Figure 28: Biomaterials used for cryogel fabrication.	96
Figure 29: Crosslinking process of the gelatin-CMC fibers.	97
Figure 30: Different properties of the cryogels.	100
Figure 31: Scheme of the different pore architectures depending the freezing directionality applied.	101
Figure 32: Incorporation of carbon nanotubes (CNT) with the cryogel scaffold.	102
Figure 33: Random pore architecture cryogel fabrication process.	103
Figure 34: Anisotropic pore architecture cryogel fabrication process.	104
Figure 35: Pore quantification for the random pore architecture crygel.	106
Figure 36: Pore distribution for the anisotropic approach.	107
Figure 37: Scanning electron microscope images from both pore architecture approaches.	109
Figure 38: Stiffness change when different materials were used, despite percentage remains constant.	110
Figure 39: Stiffness results for anisotropic pore architecture scaffolds with and without carbon nanotube incorporation.	111
Figure 40: Swelling property of the random pore scaffolds.	112
Figure 41: Swelling ratio of the anisotropic pore structure approach.	113
Figure 42: Permeability assay profile.	114
Figure 43: Conductivity measurements.	116
Figure 44: Pancreatic islets in interaction with the cryogels scaffold.	118
Figure 45: Bilayer cryogel approximation.	119
Figure 46: Confocal reconstruction of the bilayer cryogels.	120
Figure 47: Gene expression of the pancreatic islets when seeded inside the cryogel vs in suspension.	122
Figure 48: Insulin quantification from a GSIS assay using different sensing platforms.	123
Figure 49: Different cell distributions achieved in gelatin or CMC cryogels.	126
Figure 50: Proliferation ability of the cells cultured in different substrates.	127

<i>Figure 51: Diameter of the pseudoislets increases during culture days and highly correlates with the pore size distribution.</i>	<i>128</i>
<i>Figure 52: Live/Dead images of cells cultures in both cryogels (CMC and gelatin) and traditional well plate.....</i>	<i>129</i>
<i>Figure 53: Cell viability percentages of cells seeded in different substrates.....</i>	<i>130</i>
<i>Figure 54: Metabolic activity of cells seeded over different substrates.</i>	<i>131</i>
<i>Figure 55: Gene expression of the pseudoislets comparing with dispersed cell distribution of gelatin cryogels.....</i>	<i>132</i>
<i>Figure 56: Glucose Stimulation Insulin Secretion assay.....</i>	<i>134</i>
<i>Figure 58: Stimulation index of the GSIS assay.....</i>	<i>136</i>
<i>Figure 57: Insulin released under different glucose concentrations.</i>	<i>136</i>
<i>Figure 59: Beta-cell health and functionality markers.....</i>	<i>138</i>
<i>Figure 60: Stress and pre-apoptotic markers of pseudoislets after palmitic treatment.</i>	<i>138</i>
<i>Figure 61: Cell infiltration inside the scaffold.</i>	<i>140</i>
<i>Figure 62: Viability of the cells when seeded inside the scaffold.....</i>	<i>142</i>
<i>Figure 63: Anisotropic cryogels improve cell alignment.</i>	<i>144</i>
<i>Figure 64: Electrical Pulse Stimulation (EPS) enhances myogenic maturation.....</i>	<i>146</i>

1. INTRODUCTION

1.1 TISSUE ENGINEERING

In the 80s, scientists realized that generating tissues *in vitro* would solve many problems, such as reducing the waiting list for organ transplantation and cure many diseases [4]. Following this purpose, since the late 80s, this field gained much importance due to the high possibilities it offers.

Citing Vacanti and Langer in 1993, they defined tissue engineering as “an interdisciplinary field that applies the principles of engineering and the life sciences toward the development of biological substitutes that restore, maintain, or improve tissue function.” Nowadays, we could say that tissue engineering is the combination of different scientific disciplines as cell culturing, biomaterials, and bioengineering. This field’s high multidisciplinary and its high potential in tissue generation converted tissue engineering into a potent science branch. And not only to reach Vacanti’s original purpose of organ generation for transplantation. The vast pool of knowledge tissue engineering can offer converts this field into a precious ally in many other science branches as personalized medicine, regenerative therapies, disease modeling, drug screening platforms, or metabolomic studies.

Nevertheless, not all tissues are equal. The complexity of generating tissue *in vitro* varies depending on the tissue that we want to engineer. Dr. Anthony Atala classified it into four main classes, depending on the degree of complexity [5]: 1) Flat tissues and simple organs like skin, 2) Tubular organ structures as trachea or blood vessels, 3) Hollow nontubular organ structures as the bladder, and 4) Solid organs as heart, liver or kidney. Depending on the tissue that we wanted to engineer, unique characteristics are needed. For this, different approaches were used to escalate levels up to the more complex tissues: free-scaffold approximation (2D tissue engineering) and scaffold-based tissue engineering (3D tissue engineering).

2D tissue engineering consists of generating the desired tissue over a substrate. This approximation is a handy tool to study cell-cell interactions [6], preliminary modeling of more complex tissues [7], or study the cell behavior in different substrates [8], [9]. For this, many different substrates with variable mechanical and biochemical cues had been studied. Besides plastic from the culture flasks or Petri dishes, some biomaterials are used. Each biomaterial has its unique mechanical and biochemical properties that fit the needs of every tissue. From synthetic biomaterial sheets [10] to natural

biomaterial interfaces [6] or the combination of both [11], are used in 2D tissue engineering for the mentioned purposes.

Besides biomaterials, the techniques used to generate the surfaces has a fundamental implication in tissue formation. Cells can not only sense the stiffness or the biochemical cues that the substrate promotes, but cells also can feel the topography of it. For this, different topographical 2D substrates can be generated. Going from flat surfaces [12] to 2D patterned surfaces fabricated by stamping [13] or electrospinning [10]. These patterned substrates aim to promote cell functionality by helping the cells to order in a specific manner.

Some of the most studied tissues in 2D are skin [14] or skeletal muscle [15], [16], but many other tissues were simplified and studied in 2D. For example, pancreatic tissue [17] or liver [18].

However, tissues in our body have a specific architecture. By engineering 2D tissues, the importance of each tissue's volumetric structure, the cues that the extracellular matrix (ECM) can provide (both mechanical or biochemical), the 3D cell interconnectivity, and other essential features are obviated. This lack of a 3D environment leads to many unmatching functionalities, not precisely mimicking each organ *in vivo* environment. 3D matrices made of different biomaterials, called scaffolds, with unique properties, are used to overcome these limitations.

1.1.1 3D tissue engineering

3D tissue engineering consists of combining different science fields with the final aim to engineer functional tissues in the laboratory. This approach of tissue engineering incorporates the fabrication of 3D biomaterial structures to the cell culturing processes. The unification of these two fields opens a wide range of new possibilities to engineer fully functional tissues (Figure 1). Moreover, it allows the opportunity to study complex tissues and extrapolate the previously gained knowledge in 2D surfaces to 3D constructs. This extrapolation is significant in cell behavior and tissue engineering as the cells, when surrounded by a 3D matrix, behave differently [19], [20].

Scaffolds are needed to engineer 3D tissues. Scaffolds are polymer matrices made of different and specific biomaterials to mimic the 3D environment of each tissue. By mimicking the ECM's physical and biochemical properties, cell

orientation and functionality are promoted. This scaling has the final goal to generate more resemblant tissues *in vitro* than the previously fabricated in 2D.

However, this objective to generate an extracellular-like environment makes the scalability from 2D to 3D an intricate point. The morphology, the pore diameter, the stiffness, or the biochemical cues are only a few examples of the variables that must be considered depending on the tissue we wanted to generate. To modulate all these essential scaffold properties, the biomaterials used to cast the scaffold, or the crosslinking methods are important variables to consider when designing the proper scaffold for each specific tissue.

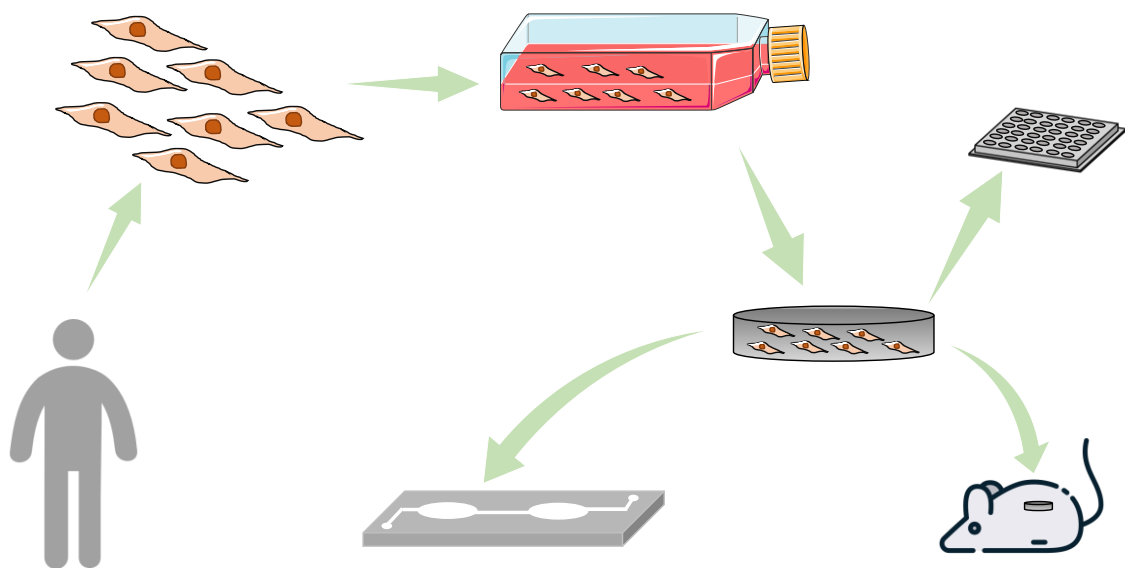


Figure 1: Overview of tissue engineering process and some of its applications. To engineer tissues in the laboratory, patient cells can be obtained by a biopsy. These cells are then cultured and expanded. Once enough cells, these are seeded inside a scaffold, a 3d microenvironment resemble to the ECM of the body. In here is were the cells traditionally differentiate into more mature constructs. Finally, when tissue is fully generated, the engineered tissue is ready to be used in multiple applications as *in vitro* test, transplantation or incorporated into microfluidic chips.

1.1.1.1 Biomaterials

Each scaffold must be made of a specific or a combination of biomaterials. Scaffolds are bioengineered biomaterial matrices that are mainly

biocompatible and can give particular architecture to the cell environment. Moreover, these biomaterials can have biochemical and physical cues that enhance cell formation and functionality. Among all the materials that can be used for scaffolding, we can split them into three main classes: natural, synthetic, and composites.

Natural biomaterials are the biomaterials that are mainly found in nature or are derivatives of it. Most of them have interesting biological features, as good biocompatibility, and good bioactivity.

One of the most common biomaterials is collagen, the most abundant protein in the human body and found in the ECM [21]. This biomaterial is perfect for some applications due to its high biocompatibility and cell activity promoters, as the polypeptide Arginine-Glycine-Aspartic acid (RGD), a cell-binding motif. On the other hand, it has low mechanical properties, low viscosity, and is degradable by mammalian cells [22]. As this material is also found in the ECM, it is very used in tissue engineering [23]. Another very used biomaterial is gelatin, a derivative of collagen obtained from its hydrolysis. It has similar biological features to collagen in terms of biocompatibility and bioactivity. Also, it is cheap, easy to obtain, and temperature-dependent [24]. However, gelatin has similar collagen drawbacks, as it is enzymatically degradable and has low mechanical properties. To overcome these limitations, collagen, gelatin, and many other biomaterials can be chemically modified to generate a mechanically enhanced fibrous-network scaffold.

One example of these chemical modifications is to replace the amino groups of the lysines with methacryloyl groups [2]. With this addition, the material can be crosslinked so that some of the detrimental properties can be reversed. For example, this chemical reaction allows the enhancement of the mechanical properties of the scaffold. This allows encapsulating cells inside in a more long-lasting scaffold, a handy tool for tissue engineering.

Another attractive biomaterial is alginate, obtained from brown algae, with good biocompatibility, low toxicity, and affordability. However, alginate needs some cationic crosslinkers as Ca^{2+} to generate the fiber mesh for cell encapsulation [22]. One interesting point of alginate is it has no bioactivity with mammalian cells. Like alginate, cellulose is also a natural polymer with a lack of cellular interactions because it is not an ECM-derived protein. Cellulose has good biocompatibility and better mechanical properties than the biomaterials mentioned above. Also, it is cheap, and it is non-temperature-dependent. As explained with gelatin and collagen, these biomaterials can also be chemically modified to improve some of their

properties. This offers the possibility to mix different natural biomaterials and so enhancing scaffold properties, generating new biomaterials with many potentials for tissue engineering [25].

On the other hand, synthetic biomaterials are biomaterials that do not come from natural sources. Although these biomaterials are also biocompatible, most of them are non-bioactive [26]. One of the most common synthetic biomaterials for tissue engineering is Poly(lactic acid) (PLA). PLA has very interesting properties as tunable mechanical stiffness, biocompatibility, and non-toxic degradability [27]. It is widely used in many different tissues as the nervous [10] or skeletal muscle [27]. Other attractive synthetic biomaterials are Poly(ethylene glycol) (PEG) and its derivatives as Poly(ethylene glycol) diacrylate (PEGDA). PEG-based scaffolds have tunable mechanical properties, facility to control scaffold architecture, easy polymerization, and bioinertness [28]. Polycaprolactone (PCL) [29] or poly-glycolic acid (PGA) [30] are other widely used synthetic biomaterials for multiple tissue engineering applications.

The high disparity in the natural and synthetic biomaterials' properties opens a third way to generate different scaffolds. By combining different biomaterials, new and unique properties can be achieved. Biocomposites aim to generate more tunable scaffolds with the desired properties of each component for precise tissue engineering. These biocomposites can be fabricated by mixing natural polymers with other natural polymers [25], [31], natural polymers with synthetic polymers [25], [32], or two synthetic biomaterials [30].

One step further, previously explained biomaterials might not accomplish all the features for engineering various specific tissues or not entirely enhance tissue maturation or functionality. To fulfill each specific tissue's particular properties, different elements can be incorporated to modify some properties, as their mechanical or biochemical properties, but without significantly affecting other primordial properties. For example, cell-binding peptides enhance cell-adhesion properties [33], or conductive elements as gold particles or carbon nanotubes [34] to prompt scaffold conductivity, help to reach the final goal to generate a fully functional tissue for different applications.

By using different materials, various properties of the scaffold can be controlled. However, other variables may influence the final properties of it. One of the most relevant parameters is the crosslinking of the biomaterial fibers to form the net-like structure.

1.1.1.2. Crosslinking techniques

Biopolymers have many advantages as good biocompatibility, cytocompatibility, and ability to degrade. However, natural materials lack many important properties as mechanical properties, as they are not stable in an aqueous solution. On the other hand, synthetic materials have good biocompatibility, but most are non-bioactive and enzymatically undegradable. To overcome these limitations and generate more stable scaffolds and better mechanical properties, crosslinking the fibers appeared to be a need to solve.

Crosslinking consists of introducing chemical or physical bonds to the biomaterial fibers and prompting their mechanical properties, stability, and tissue formation by endowing geometrical cues. Moreover, by varying various crosslinking parameters, scaffold properties as the stiffness or the water content can change. Crosslinking parameters are another variable to consider when fabricating scaffolds. Moreover, these enhanced properties obtained by the crosslinking process allow to encapsulate or seed cells inside the scaffolds and favor the tissue formation.

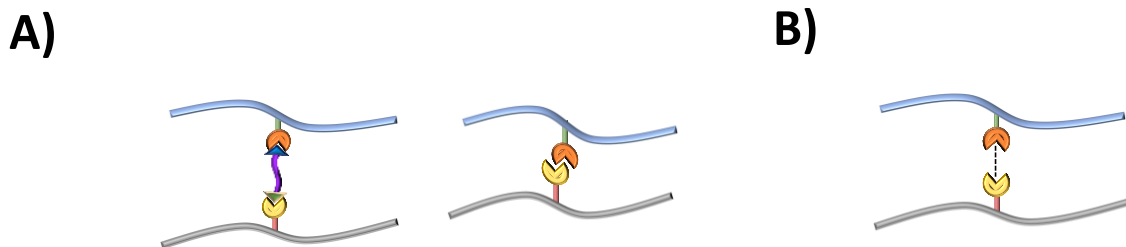


Figure 2: Overview of different crosslinking techniques. A) Chemical crosslinking. B) Physical crosslinking

However, biomaterial crosslinking for tissue engineering also have their drawbacks. Decreased degradability in biopolymers or increased cytotoxicity due to crosslinker agents are potential disadvantages that may lead to decreased cell viability [35]. Another problem is the decreasing availability of functional groups. Some materials like gelatin must be chemically modified to enable crosslinking. Also, the crosslinking bonds may have an essential effect in decreased functional group availability.

Two types of crosslink are mainly used to generate biomaterial scaffolds: chemical crosslinking and physical crosslinking. The use of each

approximation depends mostly on the polymers used and the desired properties that the final scaffold may have.

Chemical crosslinking (Figure 2A) consists of the covalent bonding of the material fibers using a linker or linking activated functional groups (Figure 2A). This linker will be the molecule in charge of bounding both functional groups of the biomaterial fibers and unite them. By linking polymer fibers with chemical reagents, highly enhanced biomechanical properties are achieved, as these fibers linking is irreversible. However, the toxicity of the unreacted chemical reagents is highly harmful to the cells [36]. Among all the chemical crosslinking approximations, UV irradiation is widely used in tissue engineering. Here, polymer chains are bounded due to the functional group activation prompted by light exposure and a photoinitiator [37]. The hydrogel's final mechanical properties can vary depending on the photoinitiator used and its activation wavelength, photoinitiator concentration, light power, or exposure time. However, most of these parameters are also toxic for the cells, so adjusting them is crucial for tissue engineering. Again, this approximation usually requires the chemical modification of the pristine material, for example, by methacrylating it. This process aims to provide the raw material the functional groups needed for the effectivity of the UV-crosslinking.

Another chemical approach is using carbodiimide crosslinking. In here, 1-Ethyl-3-(3-dimethyl aminopropyl)-carbodiimide (EDC)-based crosslinks are the most used approximations. This carbodiimide can react with various functional groups as carboxyl or hydroxyl groups [38]. The unreacted EDC, the optimal acidic conditions for the crosslinking, and other chemical reagents as N-Hydroxysuccinimide (NHS) activate carboxyl groups make the reaction more effective are parameters that need to be controlled in this approximation.

The other approximation is the physical crosslinking (Figure 2B), which consists of the non-covalent binding of two functional groups of different biomaterial fibers. However, as it is non-covalent, this crosslinking is reversible. Moreover, the unnecessary use of chemical reagents to crosslink the fibers makes this approach less toxic than chemical crosslinking. As an example, one of the most used biomaterials for this approach is alginate. Alginate can be physically crosslinked with divalent cations as Calcium (Ca^{2+}) [39]. Other physical crosslinking approximations are hydrophobic interactions, hydrogen bonding, metal coordination, or crystallization [36].

By combining the biomaterials with the crosslinking techniques explained in this section, scaffolds can be generated with many different properties. This high variability allows for generating many tissues in vitro for tissue engineering. However, the casting technique used to crosslink the prepolymers is another essential property to generate the desired scaffold geometrical architecture needed for better cell functionality.

1.1.1.3. Casting Techniques

The casting technique is another essential feature of tissue engineering. By changing the material or the crosslinking parameters, we can mainly modulate its physical and biochemical properties. Moreover, we can promote cell functionality by endowing geometrical cues to the scaffold, and here, casting techniques have an important role. The most common casting technique to engineer tissue in vitro is hydrogel encapsulation. This technique consists of entrapping cells inside a biomaterial hydrogel scaffold.

Hydrogel encapsulation has many variants to generate different architectures for specific tissues. Among all, 3D bioprinting is the gold-standard due to its high reproducibility and precise control (Figure 3A). Many different bioprinted-based approaches have been developed. However, the most used is bioprinting by extrusion. The bioinks, the polymer solution made of biomaterials, mixed with the cells are extruded in a specific pre-designed shape. The shape of the scaffold is essential to prompt cell functionality. Most of the tissues engineered with bioprinting are highly structured tissues, taking benefit of the geometrical cues that the bioprinting can highly enhance. Bioprinting highly aligned structures enhance cell directionality and cell fusion in skeletal muscle tissue [40]. Moreover, the high reproducibility of the bioprinting leads to generate many different scaffolds for a wide variety of tissues, as skin or neuronal tissue [41].

Nevertheless, bioprinting is not the only casting approach to encapsulate cells inside. Micromolding and micropatterning (Figure 3B,C) are also very used approximations. As the pre-crosslinked polymers are in a liquid state, the ability to confine this solution in a mold or a pattern and then crosslinking it permits generating multiple designs. Cylindric shape [25], trenches [42], drops [43], or pillars [44] are only a few examples of the many different scaffold architectures that this technique allows.

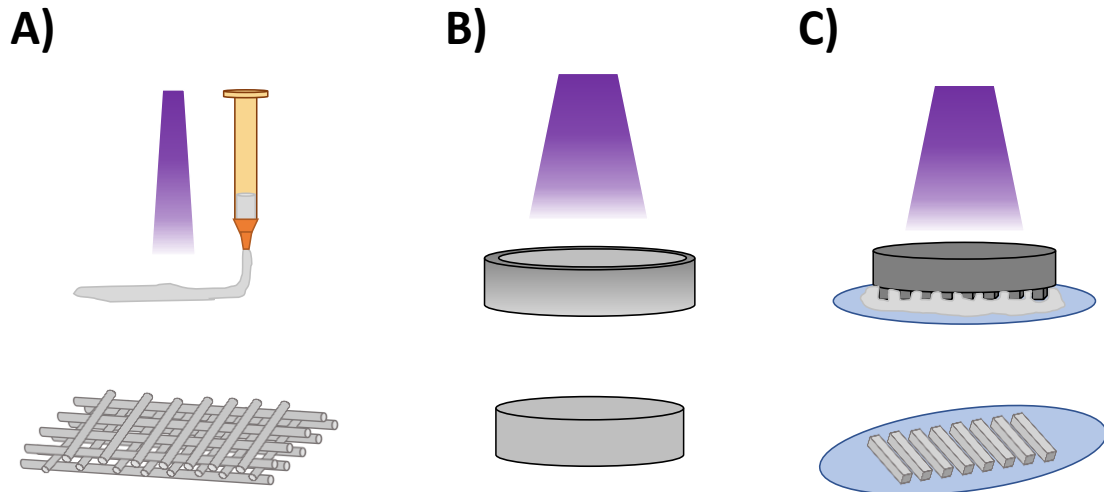


Figure 3: Hydrogel encapsulation casting techniques. A) 3D Bioprinting. B) Micromolding. C) Micropatterning.

There are other techniques to study and engineer tissues separately from hydrogel encapsulation. Electrospinning is another interesting technique to generate the desired scaffold morphologies due to its high area-volume ratio, low-cost assembling, reproducibility, and versatility [45]. This technique's principle consists of generating an electrostatic force to the polymer that electrostatic interactions will charge. After this, the polymers can be electrospun, forming a fibrous scaffold and varying the parameters, different polymer fibers diameter, fiber distribution, and bigger porosities than hydrogel encapsulation can be achieved.

Finally, cryogelation and freeze-drying techniques have gained some relevance lately due to their attractive properties. This technique consists of casting and crosslinking the prepolymer solutions at sub-zero temperatures. With this, injectable, highly porous, and highly interconnected scaffolds can be generated. Also, pore morphology, stiffness, and bulk architecture can be modeled [46].

1.2 CRYOGELS IN TISSUE ENGINEERING

The utilization of hydrogel encapsulation to generate scaffolds for tissue engineering is, nowadays, the gold-standard technique. This technique's capacity to generate 3D structures with good mechanical and structural stability makes this approach a handy tool for scaffold generation. Additionally, the high-water content and the ability to promote cell

attachment, cell survival, or cell differentiation allowed the engineering of many different tissues in vitro.

Although these beneficial properties, hydrogel encapsulation still lacks many essential points to generate fully functional tissues. Despite its good interconnectivity, its pore size limits oxygen diffusion, waste products removal, and nutrients [3], [47]. Small porosity also limits vessel formation, a key factor to engineer fully functional tissues [48], [49]. Another significant drawback of hydrogel encapsulation is crosslinkers' use, such as UV light or glutaraldehyde, highly toxic for cells.

Recently, to overcome these drawbacks, cryogelation appeared as a valid alternative. Cryogelation is a well-defined technique that generates microporous sponge-like scaffolds with highly interconnected pore structures and high-water content. Moreover, the net-like pore structure allows high solvent diffusion, overcoming the hydrogel limitations [50]. Furthermore, this technique leads to a high-water content scaffold with good mechanical properties, injectability, and good potential for angiogenesis. Combined with the option to seed the cells after scaffold fabrication, cell viability is highly increased compared to traditional hydrogels.

Another great feature of cryogels is that the internal pore morphology can be modified by changing different variables, as temperature, cooling rate, or material concentration. This permits the proper scaffolding and modification of its biochemical and physical cues for every specific tissue. These primary characteristics of the cryogelation technique make this approach a suitable scaffold fabrication method to engineer different tissues [51].

1.2.1 Cryogelation principle

Cryogels are generated by the crosslinking of the biomaterials at sub-zero temperatures (Figure 4). Once the prepolymer is prepared, it is placed at sub-zero temperatures, so while the materials start to crosslink, water-ice crystals are formed. These water ice crystals displace the fibers of the biomaterial into unfrozen areas, where they crosslink. When thawed, these ice crystals lead to an "empty" space called pores. These pores can range from few micrometers to hundreds of micrometers in diameter, showing a high interconnected microporosity scaffold. Apart from this pore structure, these scaffolds are outstanding due to their high-water content, good mechanical

properties, injectability, and the ability to load the cells after scaffold formation, leading to good cell viability.

Moreover, its pore structure can be modified to scaffold the needed properties for every specific tissue. The biomaterials used, the temperature, the cooling rate, or the crosslinking reagents may vary the scaffold's final internal structure and so its properties. By combining all these different parameters, unique scaffolds with specific properties can be generated, each for a determined tissue [51].

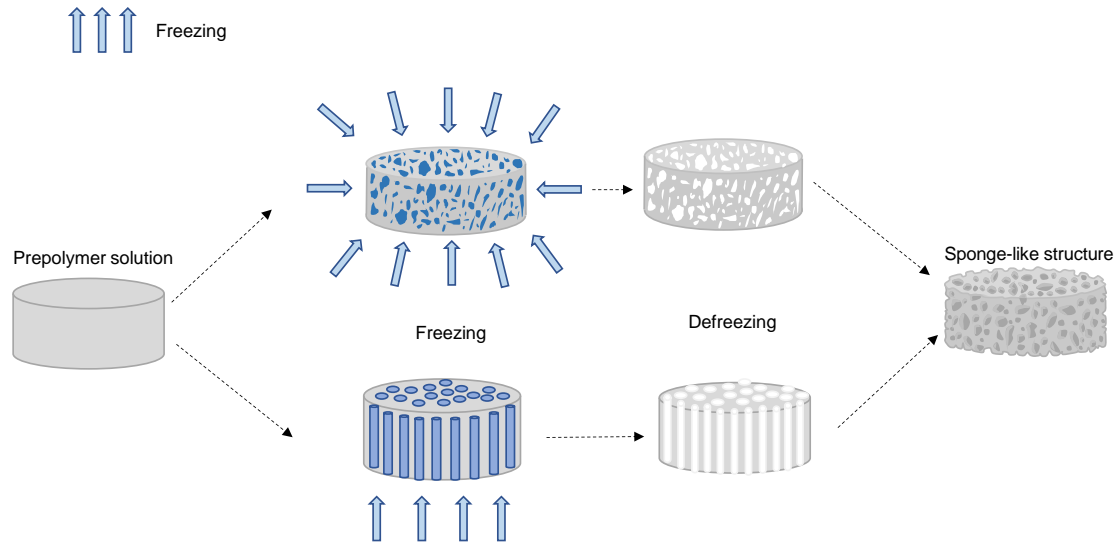


Figure 4: Cryogel principle. When prepolymer solution with crosslinking reagents are frozen. While ice-water crystal nucleation starts, the fibers are displaced, prompting the crosslinking of it. When thawed, ice crystals lead to empty spaces, that turns into porous. Finally, a sponge-like scaffold is generated. Moreover, freezing directionality changes pore architecture.

Among all the previous variables, the temperature-related parameters have high importance in cryogelation. The sub-zero temperature prompts the ice-crystal nucleation. This ice nucleation can vary depending on the temperature, the cooling rate, or even the directionality of where it comes. Briefly, at higher sub-zero temperatures (from 0°C to -10°C), ice crystals are small in a wide variety of shapes, from needles to dendrites or plates. By decreasing the temperature (from -10°C to -25°C), bigger dendrite or plates are formed. Around -20°C is where the size of these ice crystals is the biggest. By decreasing the temperature, ice crystals lead to smaller plates or cylindrical columns [52], [53]. However, this crystal morphology may vary by changing the pressure or the cooling rate and modulating the pore diameter of the cryogels [54]. Last, even the directionality of the temperature applied

can influence pore architecture. For example, placing the prepolymer solution over liquid nitrogen or carbonic ice forces the nucleation to grow in one direction, forming highly aligned and tubular pores [55].

In the freeze-drying and cryogelation technique, the most usual crosslinking is the chemical crosslinking (Section 1.1.1.2). The utilization of this kind of crosslinkers allows the formation of the pore architecture while the ice-crystals are formed. Carbodiimide, free radical, and glutaraldehyde crosslinking are the most used approximations to engineer the scaffolds. In cryogelation, due to the high porosity achieved in the scaffolds, the unreacted chemicals represent a lower risk after an easy removal of it by consecutive washings.

1.2.2 Cryogelation for tissue engineering

One of the essential variables for tissue engineering is the biomaterials used to generate the scaffold. From naturally derived to synthetic or a combination of biomaterials can be used to form cryogels. Equally, in hydrogels, each biomaterial can dote the scaffold of unique mechanical and biochemical properties to help the tissue formation. Blends of different biomaterials crosslinked by cryogelation allow obtaining different scaffolds suitable for many different tissues, as cartilage [55], bone [56], liver [57], or neural tissue [46].

Natural-ECM-derived biomaterials are the most common choice to generate cryogel scaffolds, mainly due to their biocompatibility and bioactivity. These biomaterials have many ECM-like cues, which convert these biomaterials into an excellent choice. Gelatin is the most used biomaterial due to its biochemical cues, biodegradability, and low-cost effectiveness [55]–[58]. Also, gelatin has a strong potential to be modulated in different approaches. For example, to generate bone-like tissue, a highly anisotropic structure by temperature directionality was achieved [55]. Other applications for bone tissue engineering may be using a gelatin methacrylate cryogel [56]. The scaffold's properties can be enhanced without changing its structural properties by adding microparticles or nanotubes. Here, bioglass particles were incorporated to improve osteoconductivity. Other ECM-derived biomaterials have been used besides gelatin, as collagen [59], [60] or laminin [61].

Other common biomaterials are the natural but non-ECM derived biomaterials like alginate [46], [62], chitosan [63], or cellulose [46], [64]. This

kind of biomaterials are a useful tool for scaffold generation mainly for their biocompatibility, good mechanical stability, no enzymatic degradation, and low cost.

Other approaches use synthetic biomaterials to fabricate inactive scaffolds with good mechanical properties. In synthetic materials, the biochemical cues can be provided by multiple approximations, as peptide functionalization or surface coating of different proteins [65]. Among all the synthetic biomaterials used in cryogelation, the most common is Polyethylene glycol (PEG) [66]–[68]. However, there are many different synthetic materials with plenty of different properties. Some less-used biomaterials are poly-ε-caprolactone (PCL) [69], poly(lactide-co-glycolide) (PLG)[70], Polyhydroxyethyl methacrylate (PHEMA) [71] or poly (vinylpyrrolidone) [72].

However, single biomaterial cryogels lack some properties to have the desired scaffold for tissue engineering. The combination of different biomaterials is an up-and-coming solution [73]. With this, a more ECM-resembling scaffold can be achieved. For example, polyethylene glycol (PEG) was combined with gelatin to form an improved mechanical stable cryogel for soft tissue engineering [58]. Another example could be the combination of PEG with Heparin [74] to generate a co-culture of pancreatic islets and mesenchymal stromal cells or the combination of PEG with gelatin and alginate to generate liver tissue [75].

1.3 ORGANS-ON-A-CHIP

In the last years, personalized medicine gained much relevance due to tissue engineering advances. The ability to generate tissues in the laboratory became a useful tool for drug development, drug screening, or disease modeling. Moreover, the ability to generate patient-derived tissues opens a wide range of possibilities in personalized treatment. Despite the low resemblance between engineered tissues and human tissues, tissue engineering became a useful tool to complement tests in traditional cell culture methods [76]. However, tissue engineering did not yet provide enough robustness to extrapolate results directly from the *in vitro* to the *in vivo*.

For this, animal testing is still needed and the closest approximation to human physiology. According to the UE, in 2017, around 10 million vertebrate animals are used for many studies as drug screening, metabolic assays, or

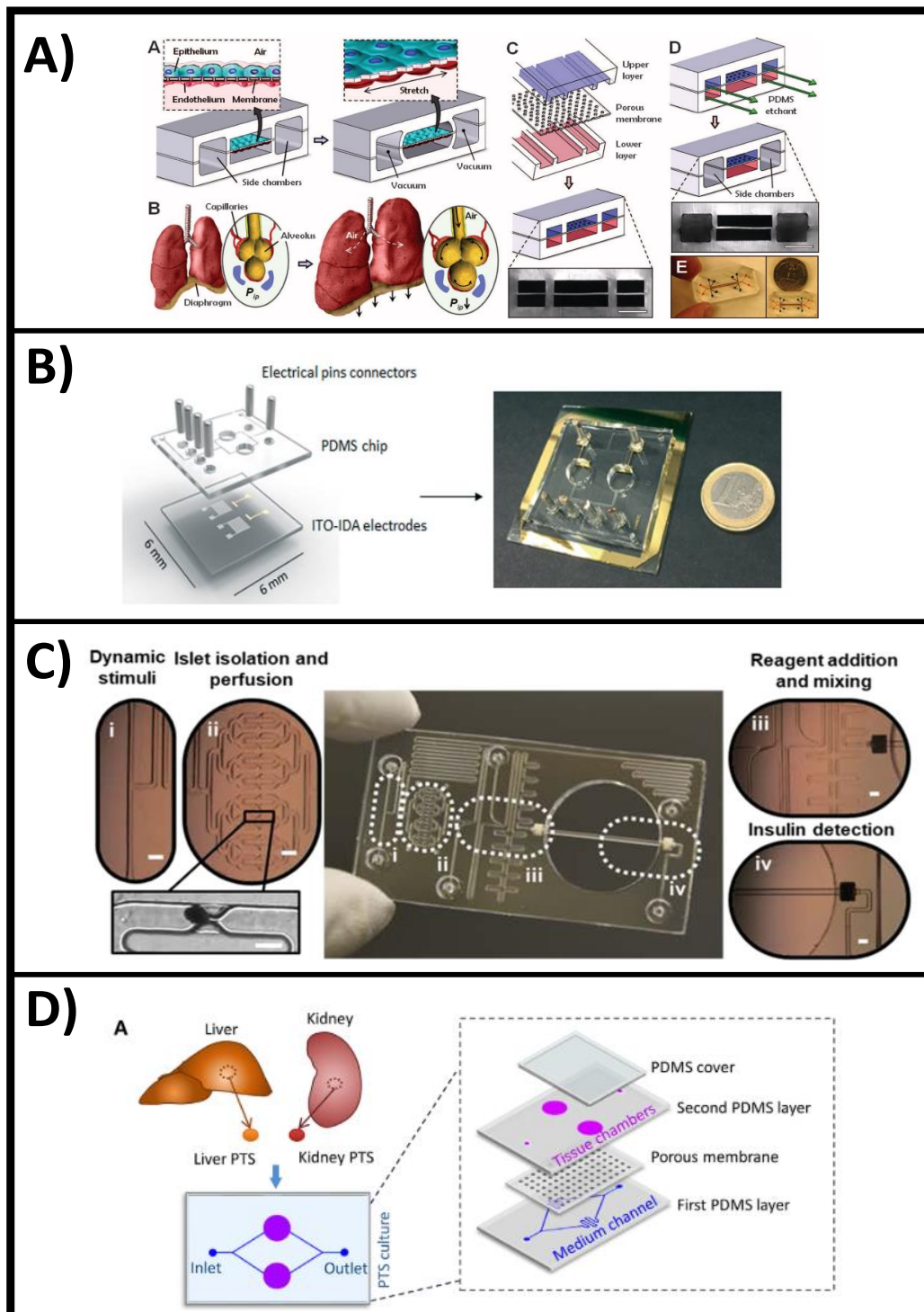


Figure 5: Overview of different Organs-on-a-Chip (OOC) fabricated for different tissues.

A) First developed OOC. It simulates the alveolar function of the lungs (Huh et al. [79]). B) A skeletal muscle-on-a-chip device. ITO electrodes are printed in the glass to generate electric pulse stimulation. (Ortega et al. [42]) C) A pancreas-on-a-chip. That allows to trap pancreatic islets and sense its insulin secretion (Gliermann et al. [258]). D) One example of next generation of Organs-on-a-chip. In here, liver tissue and kidney tissue are both studied. (Tian et al. [86])

disease modeling [77]. However, the unmatched physiological behaviors compared to humans, the variability between different animals, ethical dilemmas, and the need to go for more personalized medicine prompted other suitable alternatives.

As a potential alternative to animal testing and a trustable platform for preclinical studies or disease modeling, organs-on-a-chip appeared as a valid technology. Organs-on-a-chip (OOC) are 3D bioengineered microfluidic cell culture platforms to simulate an organ or its specific functions. For this, OOC recreates tissue-tissue interactions or its microphysiological environments by generating external physical and biochemical inputs to simulate the activity of the desired organ [78]. The highly modifiable capacity of microfabrication and microfluidic techniques makes this approach a proper tool for a wide field of applications. Moreover, OOC can be combined with biosensing platforms for constant monitoring of cell behavior. Furthermore, by engineering patient-derived tissue inside every chip, many requirements of personalized medicine could be accomplished, and so, in the future, partially substitute animal testing.

Until now, many various tissues were engineered in these microfluidic platforms. The first organ on a chip was the Lung-on-a-chip, generated by Dr. Ingber group [79]. This OOC simulates the alveolar-capillary interface on the lung. Interestingly, it has two vacuum channels, so the pulmonary respiration can be simulated. Since the first appearance of an OOC, many other organs-on-a-chip appeared and with many different applications, as drug screening or disease modeling. Intestine [80], liver [81], heart [82], skeletal muscle [42], pancreas [83] or kidney [84] are only a few examples of new OOC that appeared recently. All this OOC has the common property of being a single-tissue OOC. Nowadays, the next generation of OOC starts to appear. This new generation consists of multi-tissued OOC for more precise disease modeling or drug screening. For example, pancreas-liver OOC [85] or liver-kidney OOC [86] are examples of these multi-tissued Organs-on-a-chip.

Another example of an Organ-on-a-chip is the one being developed in our group that has the objective to study how different tissues crosstalk under diabetic conditions. Specifically, this thesis aims to generate specific scaffolds using cryogelation technique to engineer pancreatic and skeletal muscle tissues for further incorporation inside an OOC.

1.4 DIABETES

Diabetes is a group of metabolic diseases characterized by high blood glucose levels over a prolonged period. According to WHO (World Health Organization), in 2014, 422 million people suffer this disease worldwide. The number of diabetic patients highly increased in the last years. To note, according to IDF (International Diabetes Federation), 463 million people suffered this disease in 2019, and 79% of adults with diabetes live in low- or middle- income countries, 2 in 3 lives in urban areas, and 50% of diabetic patients are undiagnosed. Precisely, it is estimated that 9,3% of adults worldwide have diabetes, representing 1 in 11 adults ranging from 18 to 79 years old. Diabetes is also one of the diseases with more economic impact. In 2019, IDF estimates that the total diabetes-related health expenditure reached USD 760 billion, representing 10% of the 10% of the global health expenditure. Compared to the 2017 USD 727 billion, it represents an increase of 4,5% in only two years [1].

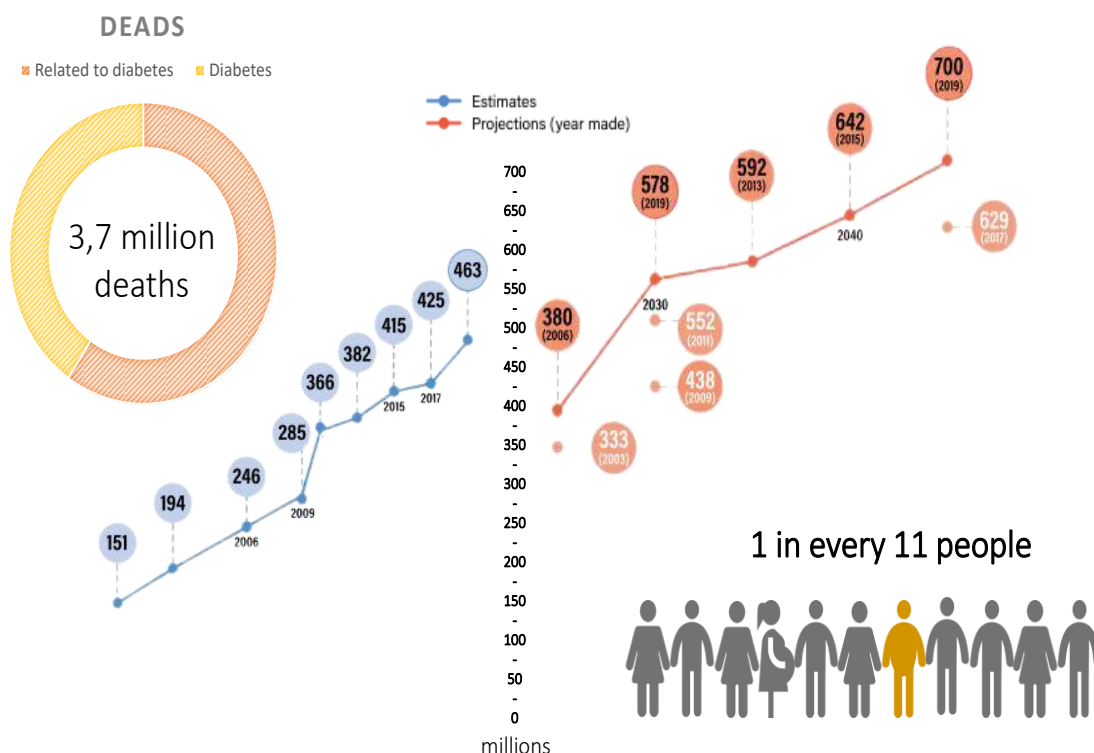


Figure 6: Infographic of diabetes incidence. (Adapted from 9th IDF atlas [1])

However, diabetes is not only about blood glucose levels. This disease and its associated high glucose levels may lead to many other complications as heart attacks, vascularization difficulties, renal insufficiency, blindness, or limb amputation. Moreover, diabetes and high blood sugar levels were the 7th leading cause of death in 2016, estimating 3.8 million deaths.

Diabetes has its origin in many different factors. Starting from genetics or population aging to unhealthy lifestyle, sedentary behaviors, and unhealthy diets, which leads to overweight and obesity [87]. Together, all these factors make that the estimations of diabetic people highly increase in the upcoming years, rising approximately to 700 million diabetic patients in 2045 [1].

Nowadays, the initial treatment for diabetes consists of a healthy diet and physical exercise. If this results unsuccessful, oral drugs or, in some cases, insulin injections may also be needed to control hyperglycemia.

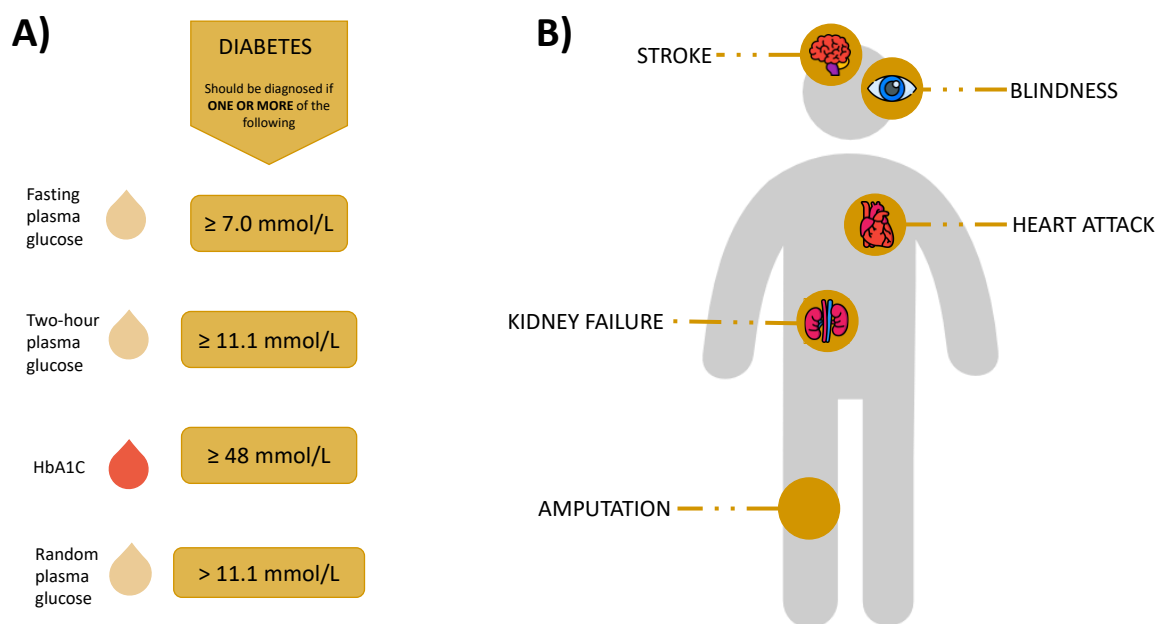


Figure 7: Body alterations due to diabetes. A) Diagnosis events for diabetes. B) Diabetes related complications

Mainly, there are three types of diabetes, type 1, type 2, and gestational diabetes:

1.4.1 Type 1 diabetes

Type 1 diabetes occurs when the pancreas does not produce enough insulin, mainly due to autoimmune defects and highly affecting insulin production. The body's autoimmune response destroys approximately 75% of the beta-cell mass, leading to a progressive insulin deficiency [88]. The chronic lack of insulin production lately affects other organs like kidneys or leads to acute cardiovascular diseases, the leading causes of mortality associated with this disease [89].

Nowadays, type 1 diabetes represents 10% of the whole diabetic patients. This disease highly increased its prevalence in the last years, passing from 2% to 5% worldwide [90]. Although type 1 diabetes can affect people of all ages, it is developed predominantly in children or young adults.

Despite the high mortality associated with this disease (3-4 times higher than a healthy patient), this disease is still not fully understood [89]. The lack of knowledge about this autoimmune disease is one of the limitations to find a cure. For this, there is not a definitive treatment. In some cases, the only preventive treatment for diabetes is the lifetime and periodic injection of insulin. This insulin injection may be done more than once per day under continuously glucose-monitoring or via automatic insulin pumping, resulting in a very dependent disease. Combining insulin injections with a healthy lifestyle (healthy nutrition and physical exercise) increases the patients' quality of life to almost average life expectancy.

1.4.2 Type 2 diabetes

Type 2 diabetes (T2D) represents 90% of the total adult patient with diabetes. This disease was traditionally associated with adult humans, although, every year, more diabetic children are diagnosed. This type of diabetes has a wide variety of risk factors. Genetics, a sedentary lifestyle, or an unhealthy diet, leading to obesity are the major causes of diabetes [87]. Nowadays, 85% of diabetic patients have obesity. Patients suffering from T2D and obesity may also suffer cardiovascular and kidney complications, the leading diabetes-related causes of mortality in T2D patients [91].

This type of diabetes occurs when the body becomes resistant to the pancreas' insulin, and finally, there is insufficient insulin production and, consequently, hyperglycemia. Diabetes starts when the organs in the body

can not properly use insulin. Due to this effectiveness, the blood glucose remains high. This situation prompts the pancreas to produce insulin continuously [1]. Over time, this pancreatic dysfunction drives beta-cell failure, losing approximately 50% of beta-cell mass [91], leading to a lack of insulin production and hyperglycemia. Moreover, this unbalanced glucose homeostasis affects many organs in the body as skeletal muscle, liver, kidney, brain, small intestine, or adipose tissue. Other complications as endothelial dysfunction, hypercoagulability, or increased platelet reactivity may also be caused by unbalanced glucose-insulin pairing [91].

Nowadays, there is no cure for T2D, but it can be prevented and slightly controlled by lifestyle modifications [87].

1.4.3 Gestational diabetes

Gestational diabetes can occur in pregnant women. It differs from T1D and T2D in that this diabetes is reversible and finishes once the pregnancy ends. However, suffering from gestational diabetes increases the risk to suffer type 2 diabetes in the future for both the mother and the children [92].

This diabetes consists of the incapacity to generate enough insulin to counter the amount of glucose and hormone production made by the placenta in the body during the pregnancy. These hyperglycemic levels are above average but below the levels for a diabetes diagnosis. However, this gestational diabetes may lead to T2D, and it can be reverted naturally past 6-12 weeks post-partum [92].

1.4.4 Tissues related to diabetes.

Diabetes is always mainly related to the pancreas, as it is the glucagon-insulin secretory organ. However, many other tissues are involved in this disease. Although pancreas, other essential tissues, and organs are the liver, the skeletal muscle, or the adipose tissue. The liver has a significant impact on insulin-glucose homeostasis. Briefly, the liver is the organ responsible for transforming the glucagon, released by the pancreatic alpha-cells, into glucose and releasing it into the blood flow by a process called glycogenolysis. Also, in high blood glucose levels, it can store glycogen by uptaking glucose through glycogenesis (Figure 8). The unbalanced insulin-glucagon secretion

of the pancreas may lead to the continuous transformation of glucagon into glucose, leading to high blood levels.

Other tissues related to diabetes are glucose-consuming tissues like muscle tissues [93]. Due to its continuous activity, skeletal or cardiac muscle tissues are highly glucose-dependent. These tissues can uptake the glucose secrete by the liver or from the blood flow and transform it into metabolic energy by glycolysis. Adipose tissue is also a critical tissue involved in insulin-glucose homeostasis. Adipose tissue has the primary function of storing lipids in a fat form to protect the body from high glucose levels. This tissue has an endocrine function that influences glucose metabolism that may alter insulin secretion [86].

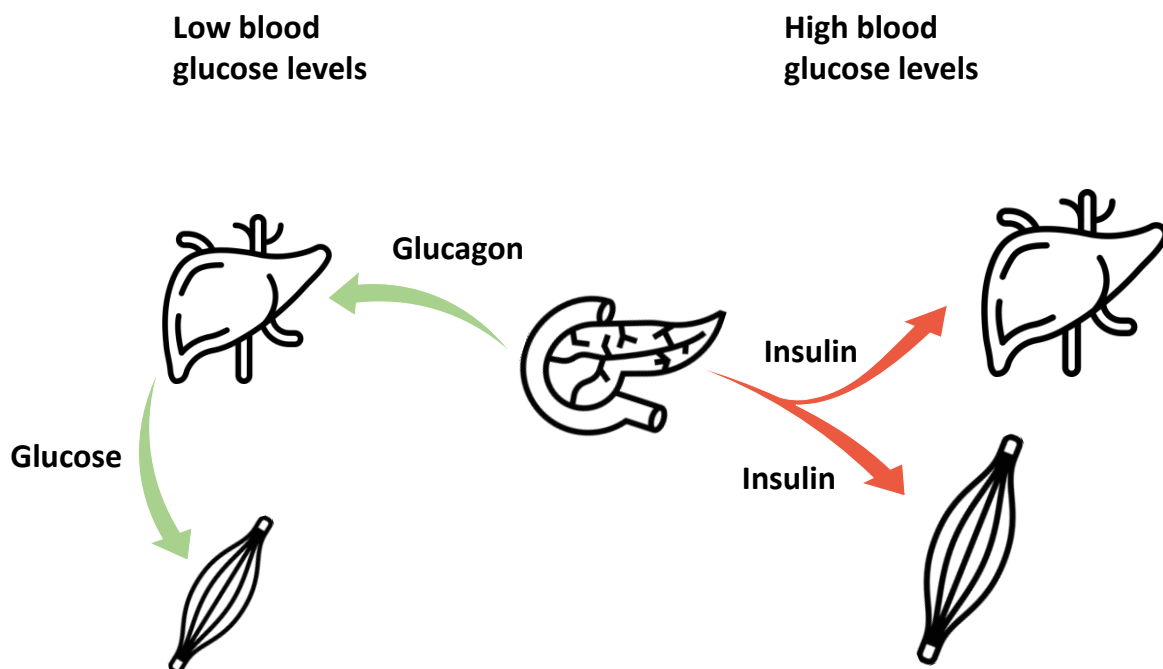


Figure 8: Glucose-insulin homeostasis in different diabetes-related tissues. When glucose levels are low, pancreatic alpha-cells secrete glucagon, and liver transform it into glucose, to be uptake by glucose-consuming organs for metabolic energy generation. When the blood glucose levels are high, pancreatic beta-cells secrete insulin, to trigger the glucose uptake by different tissues.

Among all, the relation between the pancreas and skeletal muscle in glucose-insulin homeostasis is still not clear. Although skeletal muscle is well-known tissue for its contraction and mechanical stability supporter, it also significantly impacts glucose-insulin homeostasis, as extensive glucose-

consuming tissue. Recently discoveries about the skeletal tissue's endocrine function and how skeletal muscle cytokines may affect insulin-glucose homeostasis generated some controversy. Among all the cytokines skeletal muscle releases, interleukin-6 (IL-6) seems to impact insulin secretion and glycemic regulation directly. (More information in Section 1.6.3)

Due to these skeletal muscle endocrine function findings and which cytokines and how can affect the pancreas and glucose-insulin homeostasis, it is interesting to generate both tissues in the laboratory and study its crosstalking in an Organ-on-a-chip technology.

1.5 PANCREATIC TISSUE

1.5.1. Pancreas histology

The pancreas is an essential organ of our body, located behind the stomach and half-surrounded by the duodenum. It is composed of a head, a pancreatic neck, and a tail. Although the pancreas is well known for its endocrine function of secreting hormones, it is also part of the exocrine system. Indeed, the pancreatic endocrine portion, composed of the pancreatic islets, only accounts for around 2% of this organs' total mass. In contraposition, the exocrine part is approximately 95% of the total mass [94].

The exocrine part of the pancreas is mainly composed of acinar cells. These cells produce different digestive enzymes as nucleases and lipases secreted directly to the duodenum [95]. On the other hand, the endocrine pancreas is mainly composed of Islets of Langerhans. These pancreatic islets are cell aggregations consisting of many different hormone-secreting cell types (alpha cells, beta cells, delta cells, epsilon cells, and pp cells) to regulate the glucose homeostasis in the body (Figure 9). It is known that in humans, there are around 1 million islets of Langerhans in our pancreas [96]. These cell aggregations have a wide range of sizes, ranging from a few microns to 150-200 μm in diameter [97]. However, these sizes and the pancreatic cell percentages may vary among different mammal species or their metabolic state.

Alpha and beta-cells are the most common cells within Langerhans' islets. Alpha-cells represent around 30-40% of the cells in the islets of Langerhans in humans. The primary function of these cells is to secrete glucagon into the

blood flow [98]. In contraposition, beta-cells are the most abundant cells in the pancreatic islets, representing 50-60% of the islet total cells. They are responsible for secreting insulin, the antagonist of the glucagon, and amylin. Delta, epsilon, and PP cells are responsible for secreting somatostatin, ghrelin, and pancreatic polypeptide. They are the less common cells in pancreatic islets, representing together less than 10% of the total amount of cells. In rodents, the ratio of these cells varies significantly compared with humans. Beta-cells represent almost 60-80% of the number of cells in the pancreas, whereas alpha-cells only represent 10-20%. Delta, epsilon, and PP cells represent less than 10% [99]. Additionally, in rodents, the islet architecture highly varies from humans. In rodents, beta-cells are focused on the core of the pancreatic islet, while alpha-cells are found peripherally.

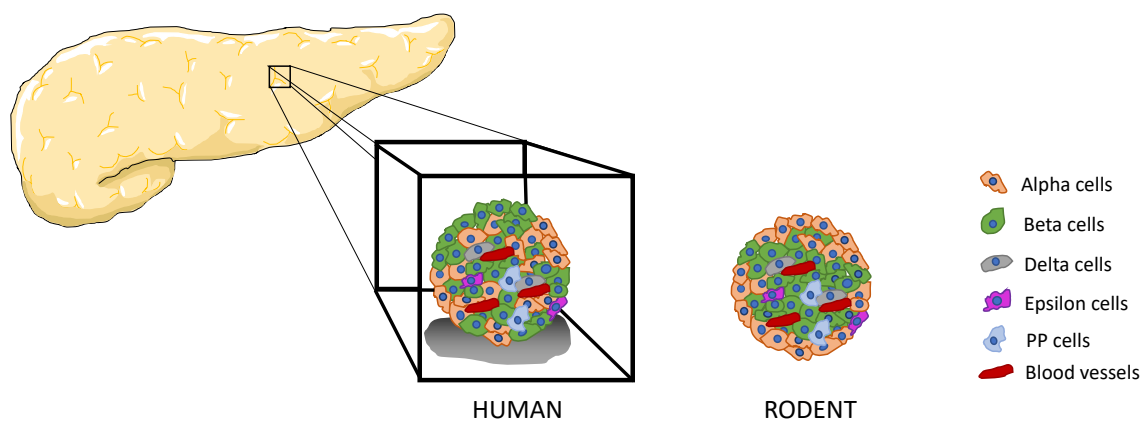


Figure 9: Schematic representation of the pancreas and its functional unit, pancreatic islets. Pancreatic islets are composed of many different cells; however, percentages and distribution are not equal in humans than in rodents.

1.5.2 Pancreas and beta-cell development

Pancreatic development begins at embryo day 8.5 in mice and gestational day 26 in humans [100]. Pancreas/duodenum homeobox protein 1 (PDX1), a homeodomain transcription factor found in mature beta-cell, plays a crucial role in pancreatic development, beta-cell differentiation, and beta-cell function [101]. It is already expressed at gestational week 4 in humans or embryonic day 8.5 in mice, where pancreas development begins. This protein is essential for early embryonic development. Also, PDX1 is needed for later differentiation of pancreatic lineages. At E11.5, PDX1 expression decreases as

pancreatic epithelium is already formed. However, in the mature pancreas and mature beta-cells, this protein is again expressed, as it is crucial in beta-cell function [102]. Interestingly, when PDX1 expression is down expressed, Neurogenic differentiation 1 (NeuroD1) starts to express at E10.5 in rodents and week 15 in humans. Since here, the expression of NeuroD1 is continuously expressed, having an essential role in beta-cell fate and insulin regulation [103]. At E13.5, V-maf musculoaponeurotic fibrosarcoma oncogene homolog A (MafA) is firstly expressed in rodents, as PDX1 regulates it. Equally in humans, MafA is firstly detected at embryo week 21. Since this first expression of MafA, this protein expression gradually increases, as this transcription factor is crucial for beta-cell maturation (Figure 10).

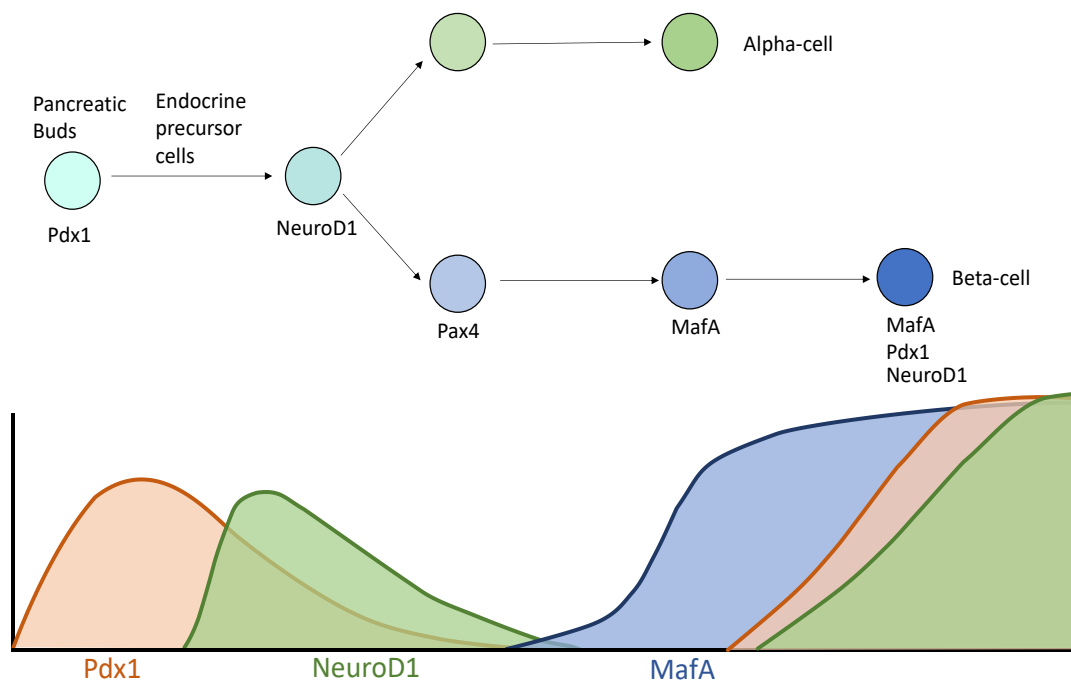


Figure 10: Beta-cell differentiation pathway. Different transcription factors expressed in early stages are also expressed in late stages, being important beta-cell health and functionality markers.

Besides, there are many transcription factors involved in maintaining beta-cell identity. These three exposed transcription factors play a crucial role in insulin-secreting cell functionality [102]. MafA, NeuroD1, and PDX1 are all in charge of activating the insulin secretion gene in response to increasing glucose levels.

Aside from the continuously increasing knowledge of the pancreas formation, the pancreatic regeneration, or the beta-cell formation and regeneration, still

has a significant lack of knowledge [95]. Different theories of how beta-cells differentiate are exposed, but none of them show some definitive light in the field.

Due to these unknown events and the difficulty of obtaining or generating fully functional human pancreatic islets *in vitro*, different strategies appeared to study the pancreatic tissue and its functionality in many pancreatic-related diseases. Studying pancreatic islets from rodents or mammals is the gold-standard technique. However, human pancreatic islets are very difficult to obtain due to the donor's cadaveric conditions. Its obtention is more straightforward in rodents than human islets; however, it implies the animal's sacrifice to obtain the islets. Moreover, the variability among donors and experiment batches complicates the comparison between them [104]. In front of these difficulties, cell lines are a valid alternative to engineer and study pancreatic tissue. Mouse insulinoma (MIN6) and rat insulinoma (INS1) are the most resembling cell lines to examine beta-cell functionality. INS1 cell line was developed in 1992 for Asfari et al. [105] and became the gold standard cell line for beta-cell studies due to its similar morphological characteristics and glucose-depending insulin responsivity. These cells have the 20% insulin content comparing to native beta-cells, and despite their low proliferation ratio compared to other immortalized cell lines, they can be passed and remain functional up to passage 80 [105]. Finally, other approximations to study diabetic diseases and alpha- and beta-cell functions are to reprogram non-insulin producing cells into beta-cell like cells [106], [107] or differentiate pluripotent stem cells into insulin-secreting cells [108], [109].

One common point of all these approximations is the enhanced functionality of the insulin-secreting cells aggregated in clusters. It has been proved that the cell-cell interactions in these pseudoislets, resembling the *in vivo* architecture of the pancreatic islets, improves beta-cell maturation and functionality in both cell lines [6], [110], [111] and stem cells [70], [112].

However, many of these approaches use non-adherent surfaces or flat strategies to generate or study beta-cell differentiation and functionality. These approximations obviate the role of the pancreatic extracellular matrix (ECM) that is found *in vivo*. ECM has an essential role in cell behavior. The mechanical cues, as the substrate stiffness [8] or the biochemical cues, can favorably modulate cell behavior and functionality [113], [114]. The use of biomaterials to generate structures similar to the pancreatic ECM is an exciting and promising point to generate a more *in vivo*-like environment for better pancreatic-tissue approximation.

1.5.3 Hormone regulation

Sugar blood regulation is one of the major homeostatic processes in the whole body, and it is carried out by glucagon and insulin, counter-regulatory hormones. These hormones are both secreted in the pancreatic islets by the alpha-cells and the beta-cells, correspondingly.

Insulin is a 51 aminoacid polypeptidic hormone. Its principal function is regulating the body's metabolism by pairing to the glucose and making it accessible for various tissues. On the other hand, glucagon is a 29 amino acid hormone. Its principal function is to increase glucose secretion by the liver during glycogenolysis, converting glucagon into glucose.

After eating, glucose levels are highly increased. When this occurs, alpha and beta-cells are capable of sensing this event. Beta-cells start to secrete insulin under these high blood sugar level conditions, and alpha-cells stop secreting glucagon. Insulin is responsible for pairing with blood glucose, so the insulin-dependent tissues as the skeletal muscle can use it to generate metabolic energy or be stored in a glycogen form in the liver through glycogenesis.

When blood glucose levels are low, the opposite process occurs. Beta-cells stop secreting insulin, and alpha-cells start to secrete glucagon. Glucagon secretion is regulated by beta-cell function, by secreting γ -amino-butyric acid (GABA), Zinc ions, and glutamate [115]. However, this is not the only path for the alpha-cells to secrete glucagon. Other factors like the autonomic and the central nervous system, some neurotransmitters, and other hormones can induce this glucagon secretion. When secreted, glucagon is uptaken by the liver, where glycogenolysis starts. This process consists of converting the glycogen stored in the liver into glucose and release it into the blood flow. This glucose can then be uptaken by the skeletal muscle and transform into metabolic energy through glycolysis.

This homeostasis is essential as the unbalanced pairing of insulin-glucose may lead to critical blood sugar levels. When these levels are low, it is named hypoglycemia. However, when blood glucose levels are elevated, hyperglycemia and persistent high blood glucose levels may lead to severe diseases such as diabetes.

1.5.4 Pancreatic tissue engineering

Pancreatic tissue engineering presents many limitations. The difficulties of obtaining pancreatic islets from donors due to cadaveric conditions elevate this tissue to a more intricate approximation. The pancreatic tissue studies mainly focus on two approaches: studying rodent or mammal pancreatic islets or studying beta-cell function as a pancreatic tissue model.

Studying pancreatic islets as functional pancreatic tissue has strong potential due to their *in vivo* properties. Its architecture, cell proportionality, and glucose secretion are strong points of using pancreatic islets. Most of the pancreatic studies with islets of Langerhans are made in suspension or non-adherent cell cultures. With this, islet size heterogeneity, spherical architecture, cell percentages, and glucose sensitivity are maintained, mimicking the in-body situation. However, as previously mentioned, this approximation has substantial limitations. Besides the variability and the difficulty to obtain pancreatic islets, study pancreatic islets in suspension, without a scaffold, did not mimic the body situation, as they are not surrounded by any matrix [114]. To improve this, some studies encapsulate islets of Langerhans inside hydrogel [31], [116]–[119]. This approximation allows a better *in vivo* resemblance by adding a soft matrix around it. Most of these studies are made for transplantation, so this matrix also protects the islets from the immune system and avoids biocompatibility defects.

The difficulty in obtaining pancreatic islets from mammals or rodents impulses new approaches to study pancreatic tissue. Differentiate stem cells to insulin-secreting cells is a valid alternative [70], [120]. However, the most used approximation to engineer pancreatic tissue is utilizing immortalized beta-cell lines, as INS1 or MIN6. These are producing insulin-cell lines that have reasonable proliferation rates for expansion and cell culturing, good glucose sensitivity, and reflect similar physiological conditions [104]. Despite insulin-secreting cell lines can be cultured and expanded in monolayer, different studies proved the better functionality of clustered cells [121]–[123]. For this, in pancreatic tissue engineering, cell aggregations are encapsulated inside hydrogels in the form of spherical aggregations [116], [124].

In pancreatic scaffolding, many different casting techniques have been used. Due to its reproducibility, 3D bioprinting is the gold-standard technique to encapsulate pancreatic islets inside hydrogel scaffolds [31], [116], [118].

However, other casting techniques as micromolding are widely used for their moldability and ability to create small and thin constructs [117], [124].

In all these approximations, many different materials have been used for islets or cell aggregates encapsulation. Natural-derived materials are the most common due to their biocompatibility and bioactivity. ECM-derived biomaterials, as collagen [125], gelatin [118], [126], or fibrin [120], are mainly used for their biochemical activity. Combining these biomaterials with non-mammalian cell degradable biomaterials as non-ECM derived biomaterials or synthetic polymers enhances its mechanical stability. Alginate [116], [118], cellulose [31], or polylactic acid (PLA) [120] are only a few examples of stable and mechanically enhanced biocomposites.

However, small porosity and low diffusion of hydrogels taunt decreased viability and glucose sensitivity [3], [47]. This problem increases as more prominent are the cell aggregations, leading to early cell core hypoxia. Moreover, pancreatic islets are highly sensitive tissue. In vivo, it needs to sense and secrete insulin or glucagon fast to respond to the sugar blood levels. If the diffusion of the scaffold is not high, this retarded sensing from the islets can lead to insulin-secreting defects or a not accurate model of pancreatic tissue. To overcome these limitations, the use of microporous cryogels gained much relevance recently.

1.5.5 Cryogels in pancreatic tissue engineering

Despite the recent advances in cryogelation and tissue engineering, cryogels with for pancreatic tissue engineering are still not much explored.

In pancreatic tissue, we can find Borg et al. [74] where they fabricated a Poly(ethylene)glycol – heparin cryogel for co-culturing of pancreatic islets and mesenchymal stromal cells. In here, cryogel was transplanted in mice for type 1 diabetes studies. Similarly, we can find other studies with pancreatic islets seeded inside silk fibroin - Heparin cryogel [127], in collagen-calcium peroxide cryogel [59], or gelatin and poly (vinylpyrrolidone) cryogel [72].

The limitations in pancreatic islet obtention and the non-resembling functionality of monolayer immortalized cell lines open another exciting approximation. Taking profit from the microporous structure of the cryogel, aggregating insulin-secreting cells inside the cryogels opens an interesting approximation for pancreatic tissue engineering. For example, dextran-gelatin cryogel was used to differentiate adipose stem cells into insulin-like cell clusters [125]. Similar to this, human pluripotent stem cells were differentiated into insulin-secreting cells and clustered inside poly(lactide-co-glycolide) (PLG) and polyethylene glycol (PEG) cryogels [70].

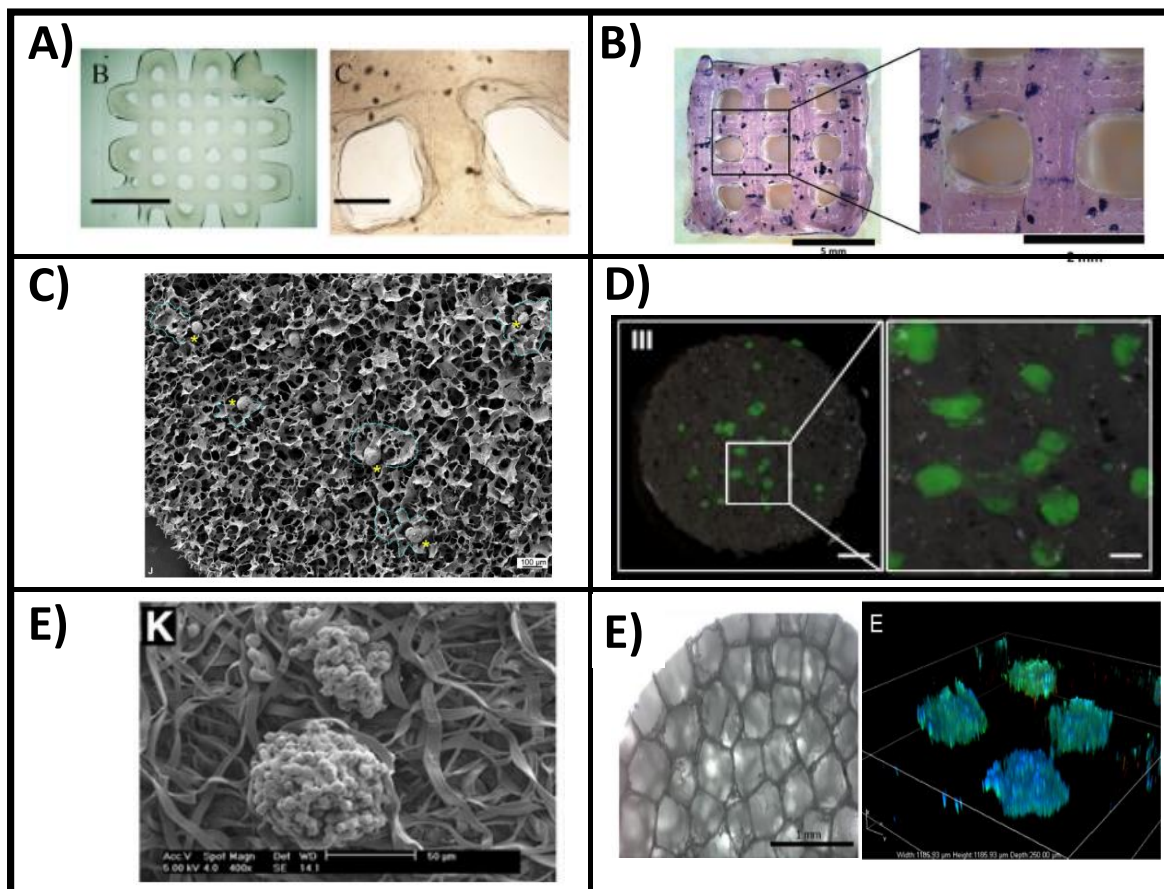


Figure 11: Small overview of pancreatic tissue engineering. A) Bioprinted scaffold for islet encapsulation in alginate-based hydrogel (Marchioli et al. [116]). B) Alginate bioploted scaffold of pancreatic islets (Duin et al. [31]). C) PEG-heparin cryogel for co-housing pancreatic islets and mesenchymal stromal cells. (Borg et al. [74]). D) Heparin-silk microporous scaffold for seeding pancreatic islets inside. (Mao et al. [127]). E) Beta-cell aggregations in gelatin electrospun scaffolds (Blackstone et al. [126]). F) Beta-cell progenitor aggregations inside microporous scaffolds fabricated by porogen leaching (Youngblood et al. [70]).

To date, cryogelation is still a not very advanced technique to generate scaffolds for tissue engineering. Pancreatic tissue engineering is still mainly focused on hydrogel encapsulation for transplantation in diabetes type 1 studies. Previously exposed limitations as oxygen and nutrient diffusivity complicates the functionality of the encapsulated pancreatic islets.

Moreover, this tissue is highly sensitive and needs fast sensing of the blood glucose levels. If the diffusion of it is slow, the delayed release of insulin makes this approach nonrealistic. To overcome this, the microporosity of the cryogels and their high diffusion rate should allow fast glucose sensing and a more realistic *in vivo* 3D environment. The possibility to seed cells after the material crosslinking and the potential to aggregate the cells in clusters is a potential option to engineer functional *in vivo* like pancreatic tissue *in vitro*. Moreover, its easy manipulation should permit to cryogelation be an exciting tool to study diabetes type 2 *in vitro*.

1.6 SKELETAL MUSCLE TISSUE

1.6.1 Skeletal muscle structure

Skeletal muscle tissue represents 40% of the mass of an adult body. Its principal function is to give mobility and support to the body [128].

The skeletal muscle structure goes from the whole tissue to single proteins capable of contracting this muscle and allowing the body's movement. The muscle is a well multi-layered tissue, highly structured, and highly aligned. Each muscle is composed of multiple sub-units called muscle fascicles surrounded by an extracellular matrix. This extracellular matrix is called perimysium, and it is mainly formed of Collagen Type I and V. At the same time, this conjunct of fascicles and ECM is surrounded by a layer of connective tissue, called epimysium, which is the most external layer of the muscle and is mainly composed of collagen type I and type III.

Each muscle fascicle is composed of many muscle fibers (myofibers). Muscle fibers are also surrounded by the last extracellular matrix layer, called endomysium [129]. Endomysium is mainly composed of Collagens type I, type III, and type V. Muscle fibers are mature multinucleated and highly aligned cells fused from single myoblasts to form myotubes. Each muscle fiber has approximately 1 cm in length [128].

Muscle fibers are composed of many muscle fibrils (myofibrils). These fibrils are composed of repetitive contractile units called sarcomeres. Finally, a sarcomere is mainly composed of two proteins: actin and myosin [130]. These two proteins are the main ones responsible for regulating the contraction of the skeletal muscle. Briefly, actin is the thin filament with a myosin-binding site. Myosin is a thick filament with two actin-binding sites. The muscle contraction occurs because of the movement of the myosin heads on actin filaments (Figure 12).

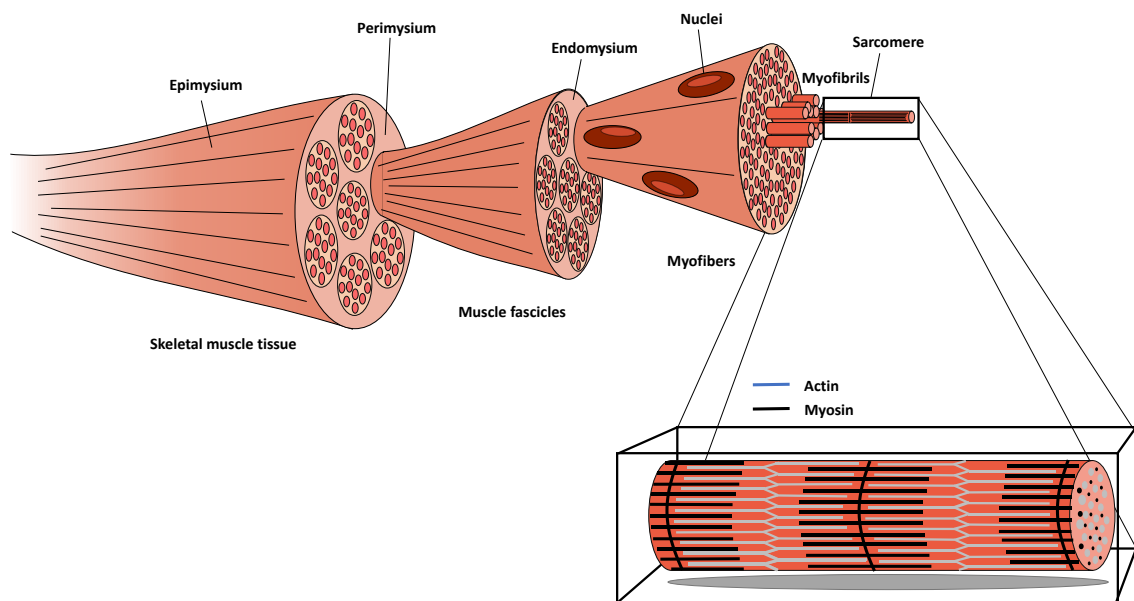


Figure 12: Skeletal muscle structure. Skeletal muscle is a highly aligned and structured tissue. Skeletal muscle is formed by a conjunct of muscle fascicles. Each muscle fascicle is, at its time, to a conjunct of myofibers. Finally, these are composed of many myofibrils, composed of sarcomeres. In these sarcomeres is where actin and myosin, the proteins responsible of contraction, are found.

1.6.2 Skeletal muscle formation and differentiation

Differently from pancreatic islets and beta cells, skeletal muscle tissue is well-known for its regeneration capability.

This regeneration ability is performed by cells located close to the muscle fibers. Progenitor muscle cells or satellite stem cells are a heterogeneous population of stem cells. These cells can enter the cell cycle by differentiating into myoblasts. Once they became myoblasts, these cells can divide, proliferate, or differentiate into myotubes by fusing with other myoblasts

[131]. Many transcription factors regulate all this cell cycle. While satellite stem cells are in a quiescent state, they express Paired box Proteins 3 and 7 (PAX3 and PAX 7). However, when they differentiate into myoblasts, this expression is downregulated, and Myogenic Factor 5 (MYF5) first and myogenic differentiation 1 (MYOD) later are expressed. These transcription factors are crucial for myogenic cell determination. In this step, myoblasts exponentially divide and proliferate before differentiating into myotubes by fusing between them [131].

When this occurs, MYOD expression starts to down express, and neither PAX7 and MYF5 are expressed. In contraposition, Myogenin (MYOG) and Myogenic regulatory factor 4 (MRF4) are expressed. However, these myotubes need to undergo maturation to be fully contractile and functional. Depending on the myogenic differentiation stage, different markers are expressed, but constantly decreasing the expression of MYOG as more mature are the myotubes. Some of the most relevant proteins expressed during myotube maturation are actin, myosin (Myosin Heavy Chain (MHC) and its isoforms), or Troponin (Figure 13).

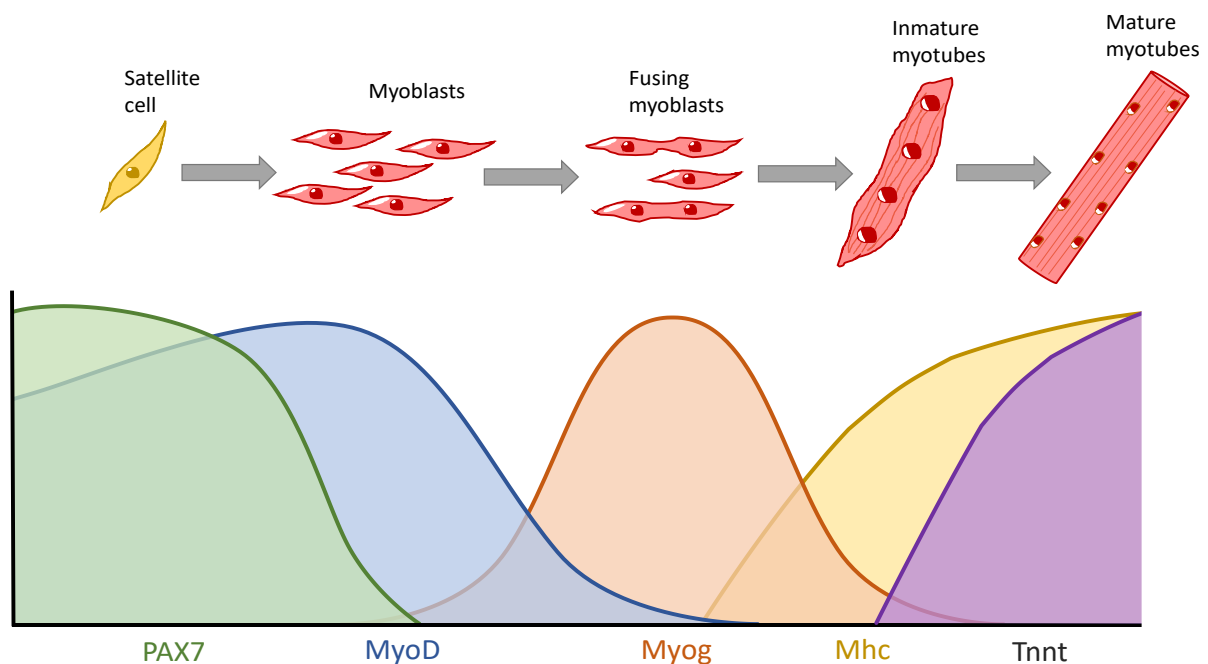


Figure 13: Transcription factors expressed during the myogenic development. During myogenic maturation different markers are expressed, sign of its grade of maturation.

1.6.3 Skeletal muscle myokines

Until now, it is well known how muscles can uptake glucose. During exercise, glucose levels decrease due to the conversion of it into Adenosine triphosphate (ATP). Because of this decrease, the skeletal muscle needs to uptake more glucose to keep converting it into ATP. This transportation of glucose inside the muscle is carried by Glucose transporter type 4 (GLUT4) [132]. However, recent discoveries proved that skeletal muscle is not only a glucose-consuming tissue. Nowadays, we also know that skeletal muscle has an endocrine function [133].

Myokines are the cytokines released by the active muscle. The essential myokines that seem to have some effect on the pancreas are interleukins. Among all the interleukins, Interleukin-6 (IL-6), a proinflammatory cytokine, is the most common skeletal muscle secreted cytokine and has a pivotal role in type 2 diabetes and obesity, as high concentration of it are found in plasma [134].

However, the correlation of high IL-6 levels in diabetic and obesity conditions is proved, there is some controversy on how it acts in glucose-insulin metabolism [135]–[137]. Firstly, the pathological influence of IL-6 in metabolism was observed. Many articles claimed that elevated interleukin-6 levels highly correlate with insulin resistance in liver and adipose tissue [138], [139]. However, other studies observed an increase in insulin sensitivity when this interleukin was secreted, helping glucose homeostasis [134]. Here, they claim that IL-6 secreted from skeletal muscle during exercise stimulates glucagon-like peptide-1 (GLP-1), so induces insulin secretion.

Also, other interleukins as IL-1 β has a crucial role in inducing β -cell damage. Another interesting skeletal muscle cytokines that have effects on pancreatic behaviors and glycemic control are angiopoietin-like protein 4 (ANGPTL4), which is observed to prompt hyperplasia in pancreatic alpha-cells [140], [141] and, Tumor necrosis factor (TNF- α) that prompts insulin resistance [142]. Finally, other more specific myokines as angiogenin and osteoprotegerin may influence favorably to protect β -cell survival by promoting anti-inflammatory actions [143].

1.6.4 Skeletal muscle tissue engineering

Skeletal muscle tissue engineering has appeared as a useful tool to study many muscular diseases, such as muscular dystrophy [144] or the crosstalking between this tissue and others, simulating multiorgan diseases as diabetes [17]. The well-understood path of muscle regeneration and the easy obtention of patient cells makes skeletal muscle tissue engineering a promising field in personalized medicine.

However, before working with patient cells, different variables as the structure of the scaffold, the biomaterials, or the casting technique needs to be optimized. To study the mentioned variables for the engineer a functional muscle bundle, immortalized cell lines are a valid alternative. In the case of skeletal muscle, the C2C12 murine myoblasts cell line is the most used. These cell lines behave similarly to the *in vivo*. As the myoblasts highly proliferate, they can fuse in myotubes, and when they are fully mature, they can go upon contraction.

To date, many different approximations have been generated to engineer skeletal muscle *in vitro*. Among all, the most used technique is the encapsulation of cells inside hydrogels [145]. Combining this principle with all the potential combinations of biomaterials and casting techniques permits fabricating high variability of different scaffolds with unique properties. For this wide tuneability, hydrogel encapsulation is a very valuable approximation for miniaturized skeletal muscle generation.

Some prerequisites are needed to engineer skeletal muscle *in vitro*, as the tissue's highly aligned structure. Scaffolds must favor the cells' alignment, directional proliferation, and cells' fusion to form mature and contractile myotubes. Nowadays, 3D bioprinting appeared as the gold-standard casting technique due to its ability to fabricate anisotropic scaffolds, highly precise extruding methods, and high reproducibility [40]. Regardless of 3D bioprinting, 3D micromolding in very structured shapes, as grooves or trenches, is widely used [42]. This technique is very used because of its easy assemble method and low-cost fabrication when compared to bioprinting. These scaffold casting techniques prompt the 3D cell orientation, favoring aligned proliferation, and favor myogenic maturation.

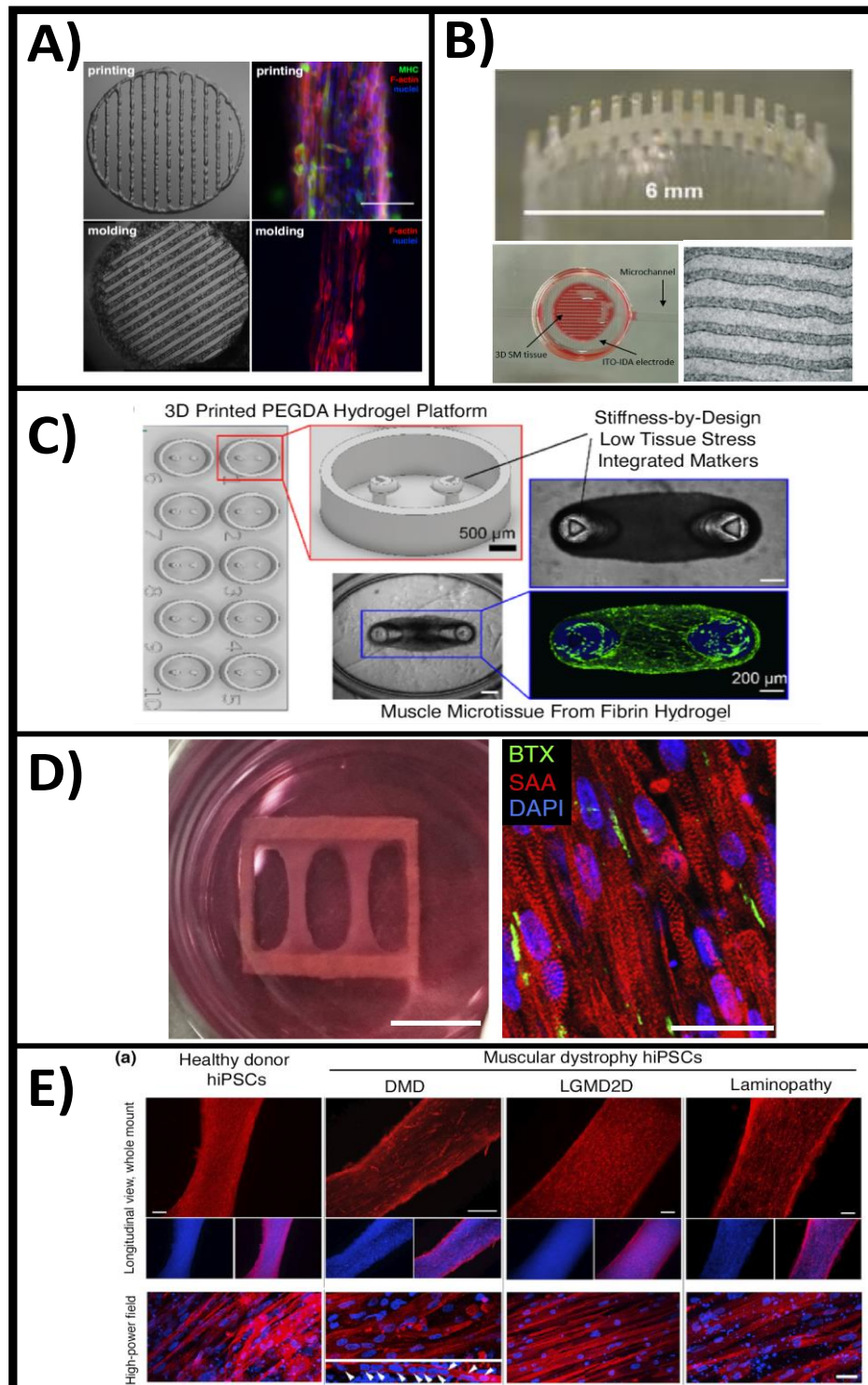


Figure 14: Overview of skeletal muscle tissue engineering. A) Different biomaterial composites engineered by 3D bioprinting or molding enhances myogenic maturation (Garcia-Lizarribar et al. [25]). B) 3D hydrogel scaffold made by micromolding improves cell alignment (Ortega et al. [42]). C) Muscle bundles generated inside fibrin hydrogels (Christensen et al. [259]). D) Skeletal muscle tissue formed from human pluripotent stem cells encapsulated in fibrin hydrogels (Rao et al. [152]). E) 3D model of a muscular dystrophy (Maffioletti et al. [260]).

Natural biomaterials are widely used in tissue engineering to cast these scaffolds. Natural polymers are common due to their biocompatibility, bioactivity prompted by biochemical cues, and the capacity to tune different physical properties like stiffness or swelling. Among all the natural polymers, ECM-derived biomaterials have a strong potential to generate skeletal muscle scaffolds, especially for their resemblance with the natural ECM. Some of the most used are collagen [21], [146], fibrinogen [147], [148], gelatin [148]–[150] or fibrin [151], [152].

However, these ECM-derived biomaterials are enzymatically and cell-mammalian degradable, temperature-dependent, and non-stable in a liquid solution. To overcome these limitations, chemical modifications and prior crosslinking are valid alternatives to enhance these properties. One of the most common chemical modifications is the methacrylation. The methacrylation allows, with the help of specific photoinitiators, as Irgacure 2959 or lithium phenyl(2,4,6-trimethylbenzoyl) phosphinate (LAP), the chemical crosslinking of the biomaterial fibers by irradiating the prepolymer solution with UV-light. From all the possible modified biomaterials, gelatin methacryloyl (GelMA) is the most used biomaterial [153]–[155]. The high versatility of this material permits us to use it in many different approximations. For example, because of its bioactivity, the presence of RGD cell adhesion peptides, temperature-dependent properties, low viscosity, and photocrosslinkable ability, GelMA-based hydrogels are a common biomaterial to engineer skeletal muscle. Combining it with previously mentioned casting techniques allows generating highly reproducible aligned bundles that help the myoblasts align and fuse. Besides gelatin, collagen methacrylate is also used in 3D bioprinting or micromolding [154].

Same as gelatin or collagen, other natural biomaterials are also used in skeletal muscle tissue engineering. Cellulose-based biomaterials, as carboxymethylcellulose methacrylated or Alginate-based biomaterials, as alginate methacrylated, are also used in hydrogel encapsulation [25], [156]. The low biochemical cues related to mammalian-cells make these natural biomaterials low bioactive for tissue engineering when used alone. These materials are mostly combined with previously mentioned ECM-derived biomaterial to fabricate a material with unique properties [25], [153]. With this combination, the final biomaterial composite can have both biomaterials' beneficial properties, overcoming some limitations of GelMA, as the low mechanical properties or the cell degradability.

However, not only the combination of natural biomaterials can improve the formation of skeletal muscle tissue. Some combinations of natural and synthetic materials can enhance specific properties, as degradation rate or conductivity. Combining fibrinogen and PEG [147] or combining PEGDA with GelMA [25] are only a few examples of it.

Besides all the possible combinations found in the literature, hydrogels still lack some properties to engineer skeletal muscle tissue. When fully mature, skeletal muscle tissue contracts for the mobility of the human body. *In vitro*, this is possible when the tissue is stimulated electrically. However, most of the biomaterials presented lacks electrical conductivity. To solve this problem, the combination of specific biomaterials with a conductive polymer or the incorporation of conductive elements as nanoparticles [157], nanotubes [150], or nanowires [146] can enhance this property without affecting other essential features of the scaffold.

However, many of these hydrogel-based approximations still have some limitations. One of the main concerns is the small porosity of these scaffolds. This may lead to diffusion problems of oxygen and nutrient supply [3]. Also, the cleaning out of some toxic reagents can lead to cell death. Another issue related to the small porosity is the blood vessel generation inside the scaffold to oxygen supply the already formed skeletal muscle tissue. This lack of angiogenesis aggravates cells' viability deep inside the scaffold or when they are highly surrounded by other oxygen and nutrient consuming cells. This insufficient diffusion through the scaffold lead by small porosity drives to decreased cell viability [3].

1.6.5 Cryogels for skeletal muscle tissue engineering

Despite the promising potential of cryogelation as a scaffold for volumetric tissues, only a few studies combine both approaches. One of them is from Singh et al. [71]. Here, Singh et al. use Poly-hydroxyethyl methacrylate (PHEMA) – gelatin cryogel to engineer skeletal muscle. In here, random pore morphology cryogels were used. In the study, the authors achieved to generate multinucleated and aligned myotubes. Another interesting approximation for skeletal muscle tissue engineering is the generation of blood and plasma cryogels [158]. These novel cryogels promote cell proliferation, alignment, and myogenic differentiation.

2. HYPOTHESIS AND OBJECTIVES

2.1 HYPOTHESIS AND OBJECTIVES

The possibility of engineering tissues in the laboratory opens a promising field for multiple applications, such as personalized medicine or disease modeling. The generation of 3D microenvironments for better mimicking the *in vivo* situation of every tissue is a real need to engineer more physiologically alikeness functional tissues. However, the perfect scaffold is not yet found. Every tissue has its requirements, so different scaffolds with unique properties can be fabricated. Among all the fabrication techniques, hydrogel encapsulation is the most used technique because of its high-water content, moldability, modurable stiffness and pore interconnectivity. However, the small porosity of the hydrogels leads to diffusion problems. This drawback is a limitation for the fabrication of volumetric tissues, as viability highly decreases when cells are deeply encapsulated. This problem is mainly found in pancreatic islets encapsulation or in the volumetric scaling up of other tissues. Recently, to overcome these limitations, cryogels appeared as an alternative as their microporous and highly interconnected structure improves the nutrient and oxygen diffusion.

This thesis is part of a DAMOC's ERC grant project that wants to study the metabolic crosstalking between different tissues as pancreas, skeletal muscle or liver in the scope of the diabetes mellitus by using organ-on-a-chip technology. Particularly this thesis aims to manufacture microporous scaffolds for the generation of skeletal muscle tissue and pancreatic tissue. To reach this final goal, more specific objectives had been proposed.

- Development and optimization of microporous scaffolds with specific pore architecture that fits with the needs of each tissue. Moreover, scaffolds need to be easy to manufacture and with good mechanical stability for incorporation in organ-on-a-chip applications.
 - In the case of pancreatic tissue, microporosity and random-sized pore distribution is needed.
 - For skeletal muscle, a highly anisotropic pore architecture is required.

- Characterization of the mechanical and physical properties of each cryogel, studying how modulating different variables affect to important properties.
- Evaluation of scaffolds bioactivity seeding cells inside and generating both pancreatic and skeletal muscle tissue. For pancreatic tissue two different approximations were studied: Seed mouse pancreatic islets inside the scaffold and generate pseudoislets by aggregating beta-cells.

2.2 WORK RELATED WITH THE THESIS

2.2.1 Journal articles related with the thesis.

- **Ferran Velasco-Mallorquí**, Juan M. Fernández-Costa, Luisa Neves, Javier Ramón-Azcón. *“New volumetric CNT-doped Gelatin-Cellulose scaffold for skeletal muscle tissue engineering”*. Nanoscale Advances (2020). DOI: 10.1039/d0na00268b

Herein, we present a combination of gelatin-carboxymethyl cellulose materials polymerised by a cryogelation process that allowed us to reach scaffold fabrication up to millimeters size and solve the main problems related with large size muscle tissue constructs. We have fabricated an anisotropic internal three-dimensional microarchitecture pore distribution with high aligned morphology to enhance cells alignment, cell fusion and myotubes formation. In conclusion, we fabricate a biocompatible and customizable scaffold for 3D cell culture suitable for a wide range of application such as organ-on-a-chip, drug screening, transplantation and disease modelling.

This paper correspond to all the skeletal muscle part. From the development of the anisotropic scaffold, to its characterization and finally to the engineering of the skeletal muscle constructs inside the scaffold.

- **F. Velasco-Mallorquí**, J. Rodríguez-Comas, J. Ramón-Azcón. *“Cellulose-based scaffolds enhance pseudoislet formation and functionality”*. (submitted)

Here, we use cryogelation technology to develop a more resemblance scaffold with the mechanical and physical properties needed to engineer pancreatic tissue. This study shows that carboxymethyl cellulose (CMC) cryogels prompted cells to generate β -cell clusters. The high porosity achieved with this approach allowed us

to create specific range pseudoislets. Overall, our results demonstrate that CMC-scaffolds can be used to control the organization and function of insulin-producing β -cells, representing a suitable technique to generate β -cell clusters to study pancreatic islet function.

This paper correspond to the fabrication and characterization of the random pore scaffold. Also, the pancreatic tissue generation by pseudoislet formation is also explained in this study.

- María A. Ortega, Júlia Rodríguez-Comas, Ozlem Yavas, **Ferran Velasco-Mallorquí**, Jordina Balaguer-Trias, Victor Parra, Anna Novials, Joan M. Servitja, Romain Quidant, Javier Ramón-Azcón. *"In-situ LSPR sensing of secreted insulin in organ-on-chip"*. Biosensors (2021) DOI: 10.3390/bios11050138

Here we aim to develop an integrated technology based on coupling a Localized Surface Plasmon Resonance (LSPR) sensing module to an OOC device to monitor the insulin in-situ secretion in pancreatic islets, a key physiological event that is usually perturbed in metabolic diseases such as type 2 diabetes (T2D). As a proof-of-concept, we developed a biomimetic Islet-on-a-chip (IOC) device composed of mouse pancreatic islets hosted in a cellulose-based scaffold as a novel approach. The developed platform offers a strong tool for enabling the in-situ response study of microtissues to external stimuli, for applications such as drug screening platform for human models surpassing animal testing.

This article correspond to the seeding of pancreatic islets inside the scaffold, and its viability and functionality studies. Moreover, the characterization and fabrication of the random pore scaffold is also explained in this paper.

2.2.2 Other scientific work related with the thesis.

2.2.2.1 Journal articles

- Andrea García-Lizarribar, Xiomara Fernández-Garibay, **Ferran Velasco-Mallorquí**, Albert G.Castaño, Josep Samitier, Javier Ramón-Azcón. *"Composite biomaterials as long-lasting scaffold for 3D bioprinting of highly aligned muscle tissue"*. Macromolecular Bioscience (2018). DOI: 10.1002/mabi.201800167

New biocompatible materials have enabled the direct 3D printing of complex functional living tissues, such as skeletal and cardiac muscle. Gelatinmethacryloyl (GelMA) is a photopolymerizable hydrogel composed of natural gelatin

functionalized with methacrylic anhydride. However, it is difficult to obtain a single hydrogel that meets all the desirable properties for tissue engineering. In this work, a library of composite biomaterials to obtain versatile, lasting, and mechanically tunable scaffolds are presented.

- Juan M. Fernández-Costa, Xiomara Fernández-Garibay, **Ferran Velasco-Mallorquí**, Javier Ramón-Azcón. “*Bioengineered in vitro skeletal muscles as new tools for muscular dystrophies preclinical studies*”. Journal of Tissue Engineering (2021). DOI: 10.1177/2041731420981339

Muscular dystrophies are a group of highly disabling disorders that share degenerative muscle weakness and wasting as common symptoms. To date, there is not an effective cure for these diseases. In the last years, bioengineered tissues have emerged as powerful tools for preclinical studies. In this review, we summarize the recent technological advances in skeletal muscle tissue engineering. Here, we reviewed and identify several ground-breaking techniques to fabricate *in vitro* bioartificial muscles.

2.2.2.2 Patents

PCT/EP2020/075278. Multi-layered cell capsules and uses thereof. Spain. 16/11/2020. FUNDACIO PRIVADA INSTITUT DE BIOENGINYERIA DE CATALUNYA (Submitted).

452021106. A system and a method of analysing a physiological condition in an analyte. Spain. 26/4/2021. FUNDACIO PRIVADA INSTITUT DE BIOENGINYERIA DE CATALUNYA.

3. MATERIALS AND METHODS

3.1 CRYOGEL FABRICATION

3.1.1 Prepolymer solution

Gelatin and carboxymethylcellulose (CMC) cryogel scaffolds were fabricated using the cryogelation technique with a carbodiimide crosslinking. As a linker, Adipic acid dihydrazide (AAD, Sigma Aldrich) was selected because of the presence of amine groups on both sides of the molecule. N-(3-Dimethylaminopropyl)-N'-ethyl carbodiimide hydrochloride (EDC, Sigma Aldrich) was the activating agent. With these biomaterials, casting techniques, and crosslinking, sponge-like microporous scaffolds can be fabricated (Figure 15A).

A prepolymer solution must be prepared to generate the scaffolds. The prepolymer solution was composed of gelatin from porcine skin (Sigma Aldrich) and 90 kDa carboxymethylcellulose (Sigma Aldrich). Both were dissolved into MilliQ, at 45°C and under stirring conditions until homogenization of the dissolution. For the proper generation of the final cryogel different concentrations of biomaterials were tested, evaluating its viscosity, crosslinking ability, and mechanical stability after thawed. Different percentage of CMC, from 5% (w/v) to 0,25% (w/v) were tested. Similar, different percentages of gelatin, from 4% (w/v) to 1% (w/v) were evaluated.

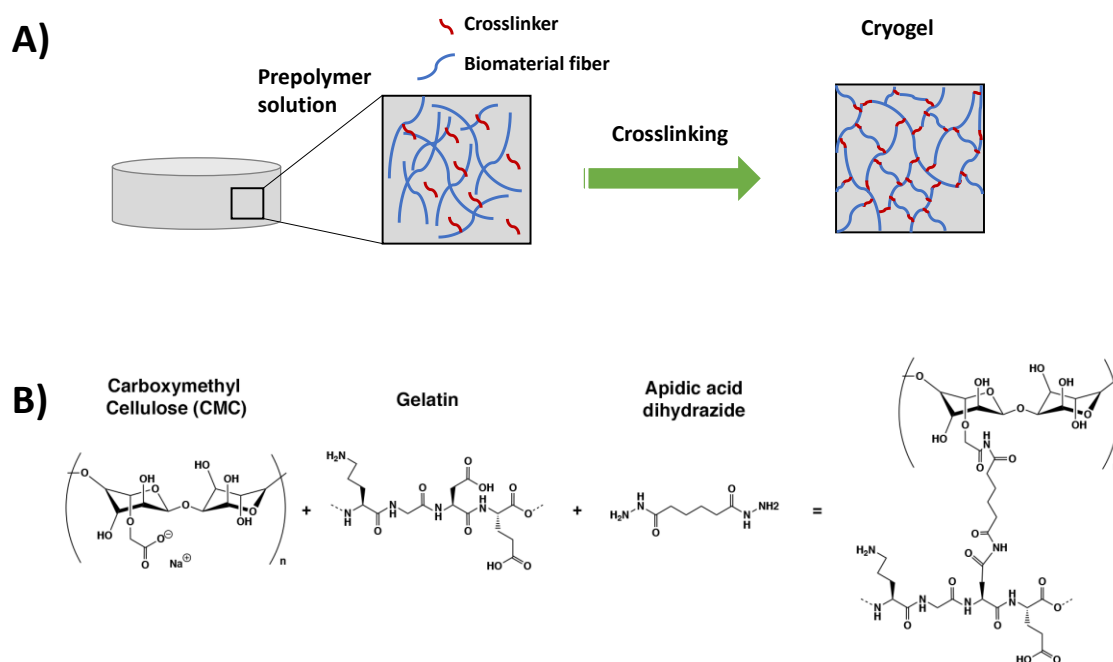


Figure 15: Cryogel formation scheme. A) Schematic representation of the cryogel matrix formation. B) Chemical structure of the biomaterials and the crosslinker used to generate the

All the reagents were mixed with the dissolved biomaterial inside 2 mL vial. Each reagent was optimized to an optimal condition, evaluating viscosity, crosslinking ability, and mechanical stability when thawed. Different concentrations of AAD, from 3% (v/v) to 0,5% (v/v), were tested to optimize the needed concentration. Equally, different EDC concentrations, from 2% (v/v) to 0,5% were tested (Figure 15B). EDC efficiency was improved using 1% (v/v) MES buffer from MES hydrate (Sigma Aldrich) to the final prepolymer solution to adjust the pH. In case needed, Aminofluorescein could be added to the prepolymer solution to stain the cryogel fibers. Finally, different carbon nanotubes (CNT, Sigma Aldrich) concentrations were also studied to achieve better distribution and conductivity inside the cryogel.

Once all the reagents were dispensed inside a 2 mL vial, vigorously pipetting was performed to achieve a proper homogenization, and PDMS molds were filled to cast the cryogels at sub-zero temperatures. Finally, different temperatures were studied, evaluating its pore size, pore architecture, and mechanical stability.

3.1.2 Fabrication of the molds for cryogel fabrication

Different set-ups were prepared depending on the pore size and pore architecture was needed. In both cases, cryogel was casted inside a cylindrical Polydimethylsiloxane (PDMS, Sylgard 184 silicone elastomer, Dow Corning, Germany) mold. PDMS molds were fabricated by mixing the silicone elastomer with the curing agent in a 1:10 ratio and vigorously mixing until homogenization. Then, the prepolymer solution was placed into a vacuum chamber to eliminate all the bubbles generated. Finally, PDMS was dispensed confined between two Poly (methyl methacrylate) (PMMA) slides with another PMMA spacer to control the height of the mold. Then, PDMS was incubated in an oven at 65°C for 48 hours. When cured, PMMA structure was removed, and PDMS were shaped into the desired mold shape and size using a bistoury and a cylindrical punch.

For the random pore morphology or the pancreatic tissue approximation, cryogels were cast inside a 10 mm diameter and 1 mm height PDMS. This PDMS mold were placed between a 24x24 cover slide and a 12-mm diameter cover slide. The mold has 2 small inlets on every side in order to fill the mold by capillarity. Finally, this set-up was placed over a plastic petri dish, and after prepolymer filling, placed at the freezer (Figure 16A).

For the skeletal muscle tissue engineering or the anisotropic scaffold, cryogels were cast inside a 6 mm height and 6 mm diameter mold. These molds were placed over a 24x24 cover slide, rounded with a polypropylene thermal isolator, and placed over a metallic sheet in carbonic ice (Figure 16B).

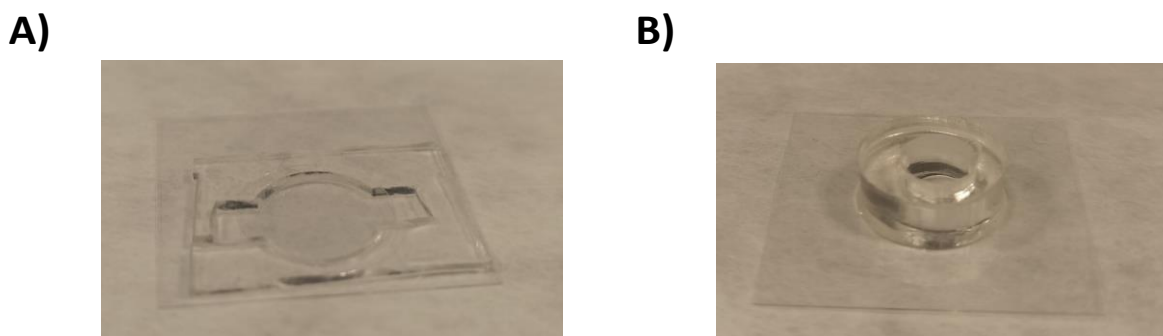


Figure 16: Images of the PDMS molds. A) PDMS mold used for the random pore architecture approximation. B) PDMS mold used for the anisotropic pore architecture approximation

3.1.3 Random pore cryogel fabrication protocol

For 1% (w/v) cryogels, CMC and gelatin from porcine skin were weighted inside a vial and diluted with MilliQ water with stirring conditions at 45°C. Once the prepolymer solution was dissolved, the crosslinking reagents were prepared; Adipic acid dihydrazide (AAD) at 50 mg/mL, MES buffer from 2-(N-Morpholino)ethanesulfonic acid hydrate (MES, Sigma Aldrich) at 0,5M and pH at 5,5 and N-(3-Dimethylaminopropyl)-N'-ethylcarbodiimide hydrochloride (EDC) at 1 mg/μl all dissolved in MilliQ water and vortexed to ensure the homogeneity in all the solution. The final prepolymer solution was fabricated adding 1 ml of the prepolymer solution, 100 μl of MES buffer, 7 μl of AAD, and 4 μl of EDC into a vial and vigorously pipetted to avoid early crosslinking before freezing (Percentages are resumed in Table 1). For stained cryogels, 12 μl of 1mM fluoresceinamine (Sigma Aldrich, Germany) was added to the final prepolymer solution. Then, the molds were filled with the prepolymer solution (Figure 17). Once filled, the mold was placed at -20°C freezer for 24 hours.

The next day, the crosslinked cryogels were removed carefully from the cover glass and the PDMS mold and were cleaned and sterilized until needed (Section 3.1.6 Cleaning and sterilizing protocol).

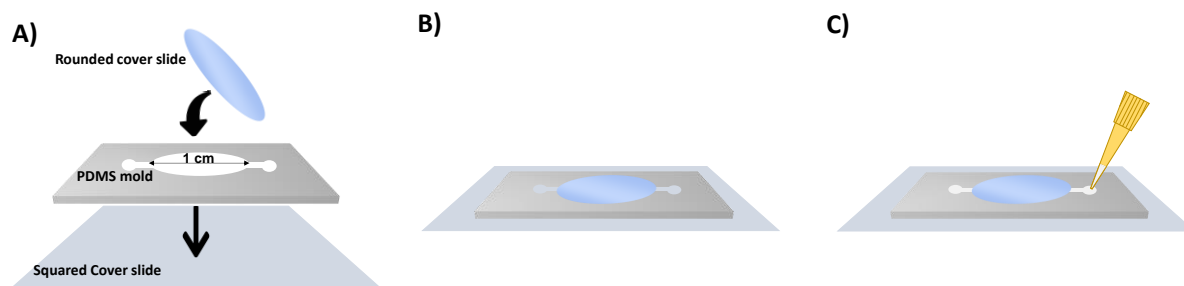


Figure 17: Scheme of the fabrication of the random pore architecture cryogel. A) Scheme of the molding. B) Picture of the mold after mounted. C) Example of the filling of the mold with the prepolymer.

3.1.4 Random Bilayer cryogel fabrication protocol

This cryogel has two different layers, the bottom layer with tiny pores and the upper with more prominent pores. This bilayer cryogel was generated using a similar protocol for random pore cryogel optimizing some steps. The first layer was fabricated using 5% (w/v) CMC cryogel in a 250 height and 10 mm diameter PDMS mold. For this, 5% (w/v) CMC solution was prepared and warmed at 45°C until fully dissolved. Once homogeneous, the prepolymer solutions were prepared as follows: 1 ml of the 5% CMC prepolymer solution, 100 μ l of MES buffer, 12 μ l of 1mM fluoresceinamine (if needed), 35 μ l of AAD, and 4 μ l of EDC were added into a vial and vigorously pipetted to avoid early crosslinking before freezing (Percentages are resumed in Table 1). Then the cryogel was cast inside the PDMS mold and frozen for 24 hours. The second layer was fabricated using 1% (w/v) cryogel over it. Briefly, instead of demolding the cryogel, the top cover slide was removed, and the 1mm height and 10 mm diameter PDMS mold for 1% CMC scaffolds was placed over it and covered with a cover slide as previously explained (Figure 18). Once the set-up was ready, 1% CMC cryogel was fabricated as previously explained in section 3.1.3 Random pore cryogel fabrication protocol).

The next day, the crosslinked cryogels were removed carefully from the cover glass and the PDMS mold and were cleaned and sterilized until needed (Section 3.1.6 Cleaning and sterilizing protocol).

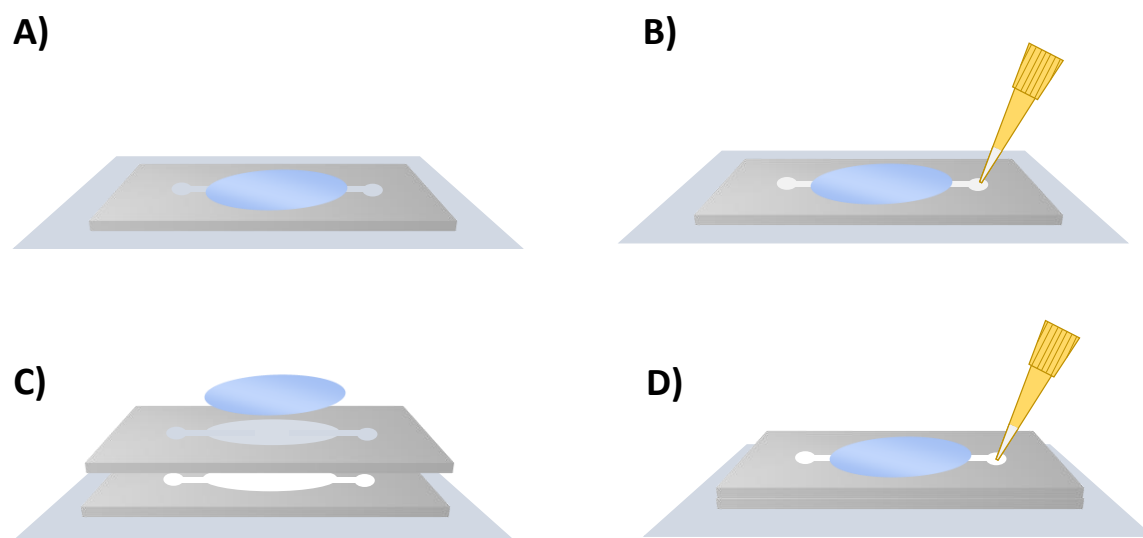


Figure 18: Scheme of the fabrication of the bilayer random pore architecture cryogel. A- B) Fabrication of the denser layer of the cryogel. It was fabricated as explained in 3.1.3. C) 24 hours later, the coverslide was removed, and another PDMS mold was placed over the first. D) Example of the filling of the mold with the prepolymer solution.

3.1.5 Anisotropic pore cryogel fabrication protocol

For the anisotropic pore architecture 3% (w/v) cryogels were fabricated. Particularly, for the fabrication of this cryogel, gelatin and CMC were both used, generating a biocomposite. Percentages of each biomaterial were determined as 1% (w/v) carboxymethylcellulose – 2% (w/v) gelatin. First, prepolymers were fabricated at the double concentration (2% and 4% respectively) and diluted into MilliQ water in stirring conditions at 45°C. Once the CMC and the gelatin were dissolved, the crosslinking reagents were prepared; Adipic acid dihydrazide at 50 mg/mL, MES buffer from MES hydrate at 0,5M and pH at 5,5, and EDC at 1 mg/μl all dissolved in MilliQ water and stirred at 45°C to ensure the homogeneity in all the solution. To fabricate the prepolymer solution 0,5 ml of 2% (w/v) CMC solution and 0,5 ml of 4% (w/v) gelatin solution, 100 μl of MES buffer, 21 μl of AAD, and 4 μl of EDC were added into a vial and vigorously pipetted to avoid early crosslinking before freezing. For stained cryogels, 12 μl of 1mM fluoresceinamine (Sigma Aldrich, Germany) was added to the prepolymer solution (Percentages are resumed in Table 1). In the case of the doped cryogels with carbon nanotubes (CNT), we added 100 μl of CNT (Sigma Aldrich) at 2 mg/ml dissolved in MilliQ water. In contraposition for non-doped cryogels, 100 μl of MilliQ water was

added to keep the material concentration equal in both conditions. Then, the molds were filled with the final prepolymer solution. Once filled, the mold was placed fast over a metallic sheet above carbonic ice and let freeze for 1 hour (Figure 19). After, the molds were placed into a -20°C freezer for 24 hours.

The next day, the crosslinked cryogels were removed carefully from the PDMS mold. For the proper pore architecture and to avoid small porosity regions, the top and bottom sites of the cryogel were sliced manually with a bistoury. Finally, cryogels were cleaned and sterilized until needed (Section 3.1.6 Cleaning and sterilizing protocol).

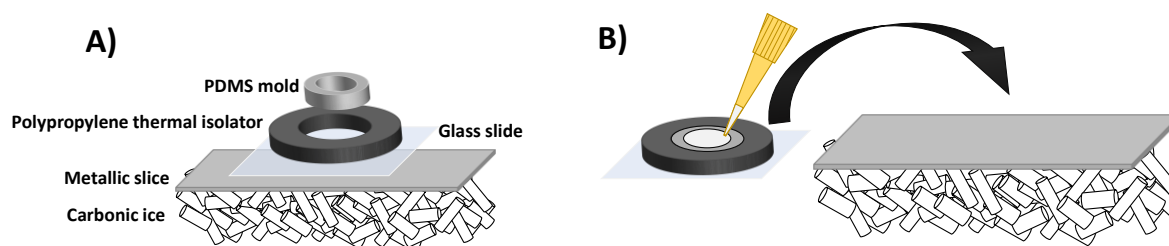


Figure 19: Scheme of the fabrication of the anisotropic pore architecture scaffold. A) Picture of the molding set-up. B) First the PDMS mold is filled with the prepolymer solution, and then placed on a metallic sheet over carbonic ice for its anisotropic ice nucleation.

Concentration (%)	MES (0,5M, 5.5 pH)	AAD (50 mg/ml)	EDC (1 $\mu\text{g}/\mu\text{l}$)	Aminofluorescein (if needed)
0,5% (w/v)	100 μl	7 μl	4 μl	12 μl
1% (w/v)	100 μl	7 μl	4 μl	12 μl
3% (w/v)	100 μl	21 μl	4 μl	12 μl
5% (w/v)	100 μl	35 μl	4 μl	12 μl

Table 1: Resume of the concentrations and volumes used for cryogel fabrication.

3.1.6 Cleaning and sterilizing protocol

To remove unreacted reagents and in order to sterilize the cryogels for cell seeding experiments, cryogels were submerged into consecutive 5 minutes cleaning steps; 1x MilliQ water, 1x 100 mM NaOH (Panreac), 1x 10 mM Ethylenediaminetetraacetic acid (EDTA, Sigma Aldrich,), 1x MilliQ and 3x

Phosphate Buffered Saline (PBS, Sigma Aldrich) (Table 2). Finally, cryogels were placed inside a laboratory bottle filled with PBS and autoclaved until needed for further experiments.

Cleaning and sterilizing steps
<ul style="list-style-type: none"> • MilliQ • 100 mM NaOH • 10 mM EDTA • MilliQ • 3x PBS • Autoclave

Table 2: Cryogel cleaning steps needed to remove unreacted reagents.

3.2 STRUCTURAL AND MECHANICAL CHARACTERIZATION

3.2.1 Pore distribution and morphology

Cryogels were fabricated as explained in previous sections. For pore quantification, the addition of fluoresceinamine is necessary. Once fabricated, washed, and autoclaved, cryogels were analyzed in wet and dry conditions.

For wet analysis, confocal images were acquired and then analyzed using ImageJ software. Confocal microscopy will allow studying the porosity in many different axes, so obtaining a general characterization of the whole scaffold. For this, 3 different z-stack were taken per cryogel. Out of this z-stack, different images between 20 μm of z-distance were analyzed. For pore quantification, ImageJ 1.53c software was used. The image was converted into black and white using a threshold to ensure that only the fibers of the cryogel were transformed. Then diameters of the pores were obtained by minFeret's diameter approximation. This approximation shows the shortest distance between two diametrical points of the pore (Figure 20). The quantification of the minimum diameter is because it would be the limitation property of our pores when pancreatic islets seeded.

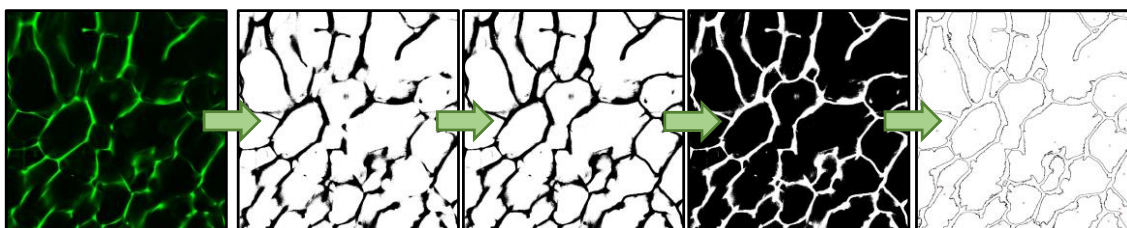


Figure 20: ImageJ pore size quantification protocol. First image was transformed to binary. Then, pores were reconstructed manually to avoid miss quantification of these pores. Finally, ImageJ quantified pore sizes using MinFerret approximation.

For a dry analysis, scanning electron microscopy (SEM) was used. This technique allows observing the surface of the scaffold to have a more precise and general image of the surface topography and morphology of the cryogel. To acquire images with a SEM, a dry scaffold is needed. Cryogel scaffolds were subjected to consecutive ethanol dehydration steps, washing the cryogels with ethanol 50%, 70%, 80%, 90%, 96% (x2), and 99,5% to maintain the structure. Once all the water was substituted for ethanol, and to replace all ethanol for CO₂, a critical point dry was performed. A final step of carbon sputtering to improve the conductive properties of the scaffold was done. With this procedure, the scaffold maintains its structure in a dry state for SEM imaging. Finally, images were acquired with a NOVA NanoSEM 230 microscope at 10 kV.

3.2.2 Stiffness

Tissue engineering aims to generate scaffolds with similar properties to the in-vivo extracellular matrix. As cells can change their behavior depending on the topography or stiffness of the scaffold, this is an exciting property to characterize. Moreover, stiffness allows us to know how different materials and topographies affect this property.

Compression assays were performed to determine the stiffness of our samples. The compression assays were performed in a Zwick Z0.5 TN instrument (Zwick-Roell, Germany) with 5N load cell (Figure 21A). The experiment was performed with samples at room temperature up to 30% final compression range at 0.1 mN of preloading force and 20%/minute of strain rate (Figure 21B). Finally, the Young modulus was calculated from 10% to 20% of the compression curve (Figure 21C).

1% gelatin, 1% CMC and 1% gelatin:CMC (ratio 1:2) were tested for the random pore cryogels. Cryogels were fabricated following the explained protocol. After autoclaving, cryogel were deep under PBS for 1 day until the sample reached equilibrium. With these cryogels, 3 compressions were applied for each cryogel. Maximum compression was set at 30% to avoid fiber breaking due to excessive compression.

For the anisotropic scaffold, the same procedure was performed. However, the compression was applied in 2 different directionalities: parallel to the fibers or perpendicular to it. The difference between the compression applied against the fibers or the compression of the empty spaces would indirectly indicate if the anisotropy was achieved.

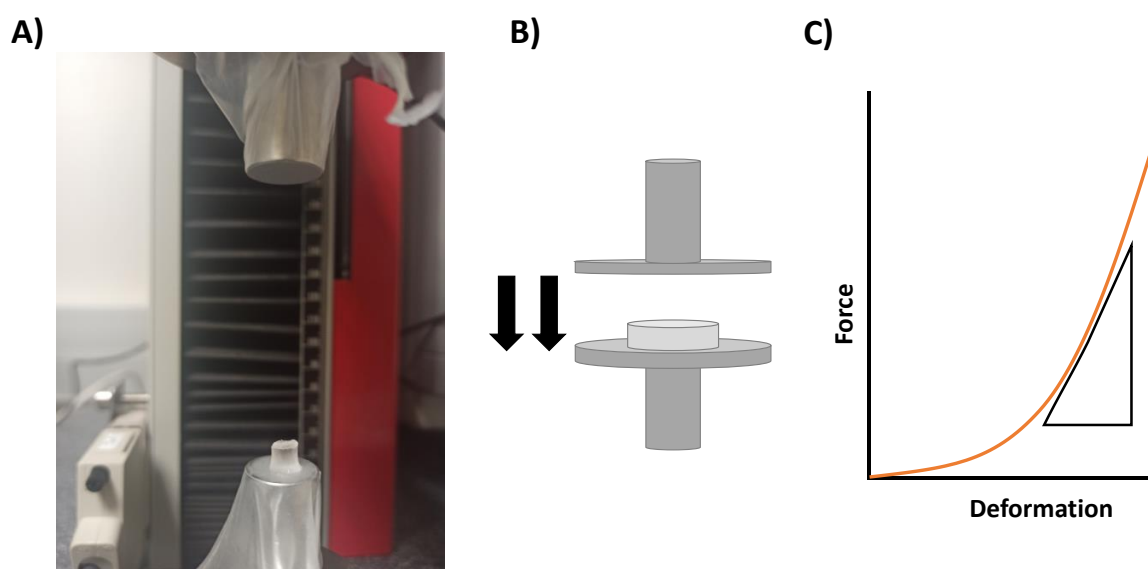


Figure 21: Mechanical testing assay to determine stiffness by compression. A) Example of the sample positioning. B) Schematic example of how compression assays were performed. C) Compression curve of the assay and determination of the Young Modulus as a tangent of the

3.2.3 Water uptake capability of the cryogel

Pore architecture, pore interconnectivity, and permeability of the scaffold are critical factors for engineering volumetric tissues inside a scaffold. These terms are highly related to cell viability as high pore sizes and high pore interconnectivity prompt nutrient and oxygen diffusion. If these parameters are high, cells will be more viable and functional when seeded inside the scaffold.

One parameter that allows an estimated reference of all these parameters is the swelling capability of a scaffold. Swelling is the water uptake capability by a cryogel. This property points how water colonizes a scaffold. By analyzing swelling behaviour, we could determine how porous and interconnected is our scaffold. High swelling ratios indicates faster water colonization of the scaffold, meaning larger pore sizes, higher pore interconnectivity, and higher permeability the scaffold could have.

Cryogels were fabricated as explained previously, and after sterilizing, cryogels were dried at room temperature. Once dried, cryogels were weighted. Next, cryogels were submerged into PBS up to 1 day, when they reached equilibrium. Finally, cryogels were weighted again. The swelling ratio was calculated as follows:

$$\text{Swelling ratio} = \frac{W_{eq} - W_d}{W_d} \times 100$$

Where W_{eq} is the weight in equilibrium and W_d is the dry weight.

3.2.4 Permeability assay

One of the most exciting properties of the cryogels is their high permeability, allowing high diffusion rates. Pancreatic islets need to rapidly sense the amount of glucose in the blood to respond appropriately to it. Thus, having a high diffusivity among all the scaffolds will ensure that cryogel does not act as a barrier to this critical need. Cryogels were placed over a transwell inside a 12 well-plate. A metallic mesh was placed over the cryogel to avoid the cryogel floating (Figure 22A, C). 0.5 ml of 1.5 mM fluorescein (Sigma Aldrich) were added at the upper compartment of the transwell to check the permeability of the scaffold, and 1.5 ml of PBS were added in the lower compartment. 100 µl of PBS from the well were taken out in consecutive times. The exact amount of fresh PBS was added to readjust the volume, again to the lower compartment. This procedure was repeated during different times up to an overnight when equilibrium was reached (Figure 22B). Finally,

the concentration of fluorescein was obtained by absorbance measurements at 494 nm with a Power wave X microplate spectrophotometer.

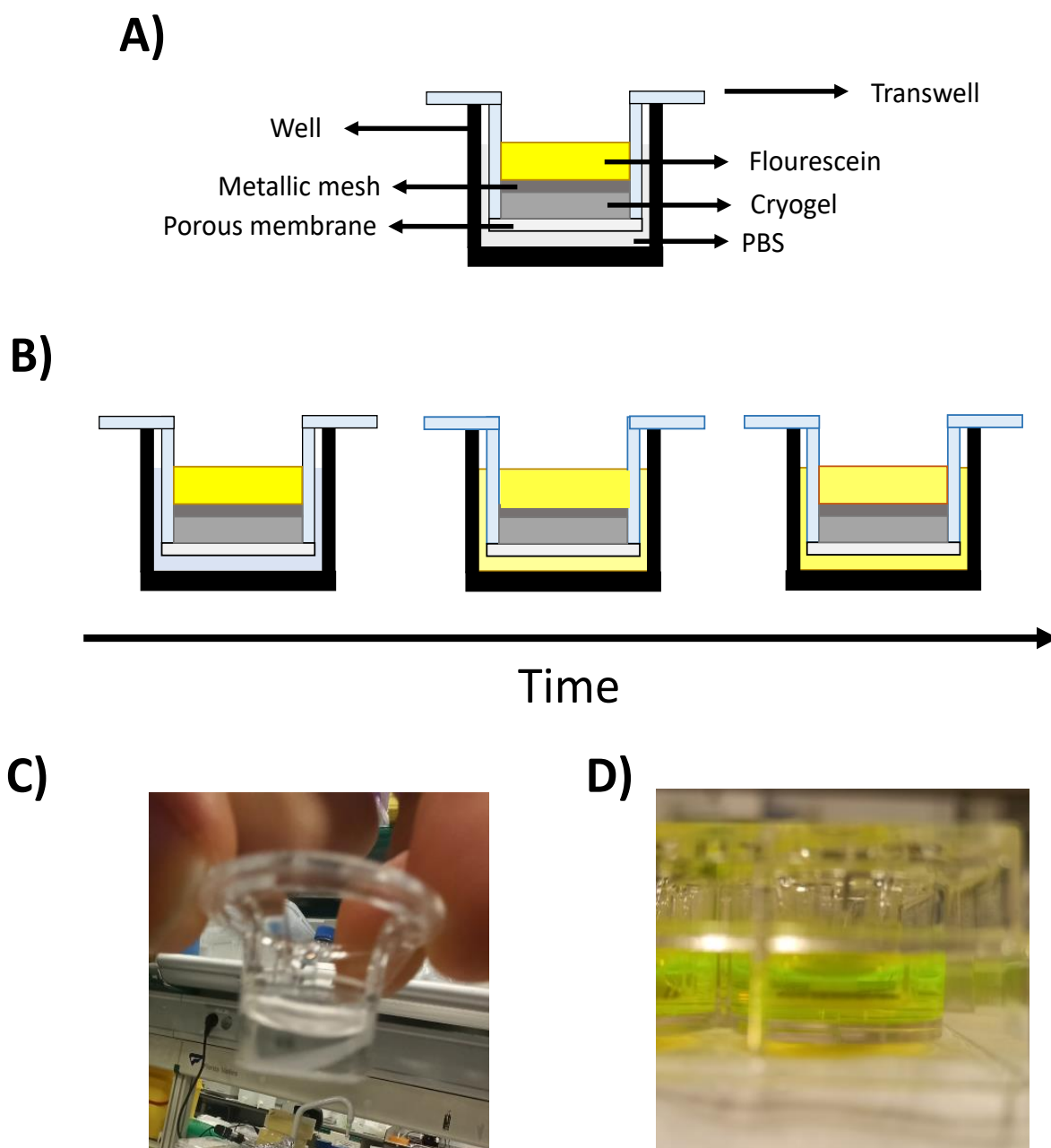


Figure 22: Permeability and diffusion experimental design. A) Experimental assembling. B) Overview of the experiment through time. Fluorescein reaches equilibrium by diffusion to the lower chamber of the transwell. C) Example of the floating of the cryogel. A metallic mesh was added over the cryogel to avoid this phenomenon. D) Equilibrium state at the final timepoint.

Permeability was calculated in the linear part of the diffusion curve by the following equation:

$$P = \frac{\Delta Q}{\Delta t} \frac{1}{AC_o}$$

Where Q is the milligrams of fluorescein that pass through the cryogel at a specific time. T is the time. A is the area of the cryogel, and Co is the initial concentration of fluorescein. Finally, the permeability of the cryogel was the difference between the total permeability and the permeability of the transwell.

$$P_{cryogel} = \frac{1}{P_{total}} - \frac{1}{P_{transwell}}$$

3.2.5 Electrical properties for anisotropic structure

A tapered transmission line method was used to measure the samples' dielectric properties; the conical feature of the cell allows the insertion of a watertight sample-holder (SH), providing a significant increase in the net sample volume. This modification permitted the evolution of the coaxial line in terms of types of materials measured [159], [160], and speed and flow of acquisition [161].

In this study, the cell was connected to a calibrated Anritsu MS46122B VNA, which allowed extracting the S-Parameters S11, S12, S21, S22, of the cell sample. Knowing the intrinsic electric distances between connectors and the sample, and considering the attenuation of the cell, it is possible to carry out a de-embedding process, where the S-Parameters of the sample are extracted through the S-Parameters of the cell and sample.

The acquisition method of the complex permittivity is based on the Nicolson-Ross [162] & Weir [163] algorithm; through the sample S-Parameters, it is possible to determine the Reflection (Γ) and Transmission (T) coefficient, as seen in (1)-(6),

$$\Gamma\Gamma = \frac{1+S_{11}^2-S_{21}^2}{2S_{11}} \pm \sqrt{\left(\frac{1+S_{11}^2-S_{21}^2}{2S_{11}}\right)^2 - 1} \quad (1)$$

$$T = \frac{S_{11} + S_{21} - \Gamma}{1 - (S_{11} + S_{21})\Gamma} \quad (2)$$

$$z_r = \left(\frac{1 + \Gamma}{1 - \Gamma} \right) \quad (3)$$

where z_r is the reduced impedance of the system, a condition that must be respected at this point is that the magnitude of $|\Gamma|$ must be equal or inferior to the unit; thus, it is possible to determine the complex permittivity ϵ^* , the complex permeability μ^* and the conductivity σ , expressed in S/m.

$$\mu_r = j \frac{c}{2\pi f L} \left(\frac{1 + \Gamma}{1 - \Gamma} \right) \ln \left(\frac{1}{T} \right) \quad (4)$$

$$\epsilon_r = j \frac{c}{2\pi f L} \left(\frac{1 - \Gamma}{1 + \Gamma} \right) \ln \left(\frac{1}{T} \right) \quad (5)$$

$$\sigma = 2\pi f \epsilon'' \epsilon_0 \quad (6)$$

Here, L represents the sample length, c the speed of light in vacuum, and ϵ_0 is the permittivity of free space, 8.85×10^{-12} F/m.

A SH of length 6 mm was used to measure the samples, from 10 MHz to 8 GHz, at room temperature conditions (26,8°C, 31% humidity).

Each sample was inserted into the SH; since the cylindrical samples have a similar diameter and length as the SH, the sample was simply introduced into the SH. Thus, the CNTs are horizontally aligned with the cell's axis.

3.3 PANCREATIC TISSUE ENGINEERING

3.3.1 Cell culture

3.3.1.1 Pancreatic cell culture

Pancreatic islets were obtained from Institut d'Investigacions Biomèdiques Agust Pi I Sunyer (IDIBAPS). Mouse pancreatic islets were isolated from 8-12 weeks-old C57BL/6 mice and were allowed to recover for 24h at 37°C and 5% CO₂ in RPMI-1640 medium with 11 mM of glucose and supplemented with

10% Fetal bovine serum (FBS, Thermofischer) (v/v), 2 mM glutamine and 1% penicillin/streptomycin.

3.3.1.2 INS1E cell culture

Rat pancreatic β -cell line INS1E cells provided by Institut d'Investigacions Biomèdiques Agust Pi I Sunyer (IDIBAPS) were cultured in RPMI-1640 with 11.1 mM glucose, supplemented with 10mM HEPES (Gibco), 2mM L-glutamine (Gibco), 1mM sodium-pyruvate (Gibco), 0.05 mM 2-mercaptoethanol (Thermofisher), 10% FBS (v/v) and 1% penicillin/streptomycin (v/v) (Thermofisher) (complete media). When cells reached confluency, cells were trypsinized. Briefly, for cell trypsinization, cells were washed with PBS, and 2 ml of 0,25% trypsin-EDTA were added to the flask. After 2 minutes, 8 ml of fresh medium was added to the flask to stop the trypsin reaction and all placed into a falcon for centrifuging. After centrifuging and resuspending cells were seeded in a new flask at 1:4 density. Cells were maintained in an incubator at 37°C and 5% CO₂.

3.3.2 Cell seeding

3.3.2.1 Pancreatic cell seeding

For islet seeding, 30 islets were selected into a drop of 20 μ l of the medium. This drop of medium with islets was placed over the cryogels and it was dried at room temperature for 20 minutes before filling the plate with additional medium. While waiting, the infiltration of the pancreatic islets was continuously monitored with a magnifying glass. If needed, reseeding the islets or low flow turbulences may be generated to help the islets to infiltrate inside the cryogel.

3.3.2.2 INS1E cell seeding.

Cryogels were dried for 30 minutes. While drying, cells were trypsinized by removing the medium from the flask and cleaning with PBS. After, 2 mL of 0,25% trypsin-EDTA were dispersed inside the flask and incubated for 2

minutes inside the incubator. After, 8 mL of complete medium was added inside the flask and vigorously pipetted to detach all the cells. Next, cells were centrifuged, the supernatant removed, and resuspended up to the desired concentration. In our case, 10^7 cells/mL was used. To seed the cells, 200.000 cells in a drop of 20 μ l of medium were seeded in each cryogel. After seeding the cells, cryogels were left at RT for 20 minutes. Besides, 1 mL of complete RPMI-1640 medium was added, and cells were left at the incubator until the experiment.

3.3.3 Cell health analysis by metabolic activity quantification

3.3.3.1 Cell health determination by alamarBlue test

Check cell health and cell viability when interacting with the scaffold is a critical point to consider. Cell viability is essential to ensure that cells can be viable and functional. AlamarBlue metabolic assay was proposed to check cell health. AlamarBlue test is a resazurin-based blue solution. When this solution interacts with the cells, cells can metabolize this resazurin by reducing it into resorufin. This reduction changes solution color from blue to red. Cell metabolic activity can be assessed by the absorbance of the solution (Figure 23).

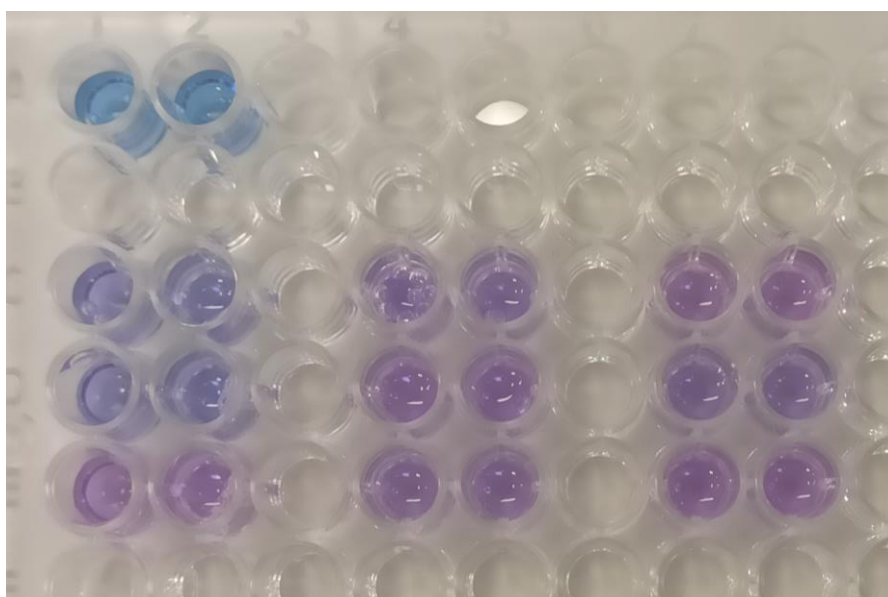


Figure 23: Metabolic activity assay. Example of alamarBlue plate, and how it changes the color depending metabolic activity of the cells.

AlamarBlue was performed according to manufacturer specifications. Briefly, the medium was removed from the well plate and substituted for a new medium with 1:10 dilution of alamarBlue. After 2-hour incubation, 100 μ l of each condition was placed in a well of 96 well plate and read in a Power wave X microplate spectrophotometer at 570 nm wavelength. Results were normalized based on INS1 cells seeded in the plate.

3.3.3.2 Cell viability determination by Live/Dead assay

Another important hallmark of the cell-biomaterial interaction is the biocompatibility of this with the cells. A viability assay is performed to study how viable the cells are inside or in contact with the scaffold. This assay was performed with the Live/dead assay kit (Thermofischer). Live/Dead kit detects cell viability based on intercellular esterase activity and cell membrane integrity. Specifically, this kit detects intercellular esterase activity, staining it with Calcein AM in green and ethidium homodimer-1 to detect the loss of the plasmatic membrane integrity, stained in red.

Viability was analyzed on days 1, 4, and 7 after cell seeding. Firstly, the cryogels were washed 5 minutes with PBS (x5). While washing steps are in the process, the working solution was prepared. For this solution, 12 μ l of 2 mM ethidium homodimer-1 (EthD-1), 3 μ l of Calcein AM, and 6 μ l of Hoechst were mixed in 6 mL of PBS (Table 3).

Live/Dead working solution
<ul style="list-style-type: none"> • 12 μl of 2 mM ethidium homodimer-1 (EthD-1) • 3 μl of Calcein AM • 6 μl of Hoechst • 6 mL of PBS

Table 3: Volumes for working solution for the Live/Dead assay

Once washed the PBS was removed and 250 μ l of working solution was added to each well and stored at the incubator. After 25 minutes, the cryogels were washed 3 times with PBS. Finally, images were taken with confocal microscopy for live/dead ratio quantification.

The quantification of live/dead ratio was calculated as follows:

$$\text{Live ratio} = \frac{\# \text{Live cells}}{\#(\text{Live cells} + \text{Dead cells})} \times 100$$

3.3.4 Pancreatic tissue immunostaining

For confocal analysis, stained cryogels were used. After culturing the cells, cryogels were washed with PBS and fixed with 10% formalin solution (Sigma – Aldrich) for 30 minutes. Then, cryogels were washed with Tris Buffered Saline (TBS, Canvax Biotech) and permeabilized with 0.1% Triton X-100 (v/v) (Sigma Aldrich) solution in TBS for 15 minutes. Cryogels were blocked with 0.5% Triton X-100 (v/v) and 3% Donkey serum (v/v) (Sigma-Aldrich) into TBS for 2 hours. Cryogels were incubated overnight with primary antibodies against Rabbit-anti Ki-67 (1:250, Invitrogen), mouse anti-insulin (1:500, Origene), or rabbit anti-Cleaved caspase 3 (1:250, Cell Signaling) in blocking solution (Table 4). The following day, cryogels were washed with permeabilization solution and were incubated with secondary antibodies for 2 hours at room temperature (Alexa-Fluor 647 conjugate anti-mouse 1:200, Alexa-Fluor 568 conjugate anti-rabbit 1:200 and Alexa-Fluor 488 conjugate anti-rabbit 1:200, Invitrogen) (Table 4). Subsequently, cryogels were incubated with 1 μ M DAPI (Thermofisher) for nuclei counterstain into blocking solution for 15 minutes. Finally, cryogels were washed with TBS for 15 minutes and stored at 4 °C until confocal microscopy acquisition. Images were taken using a LSM 800 from Zeiss.

Primary antibodies
<ul style="list-style-type: none"> • Rabbit-anti Ki-67 (1:250) • Mouse anti-insulin (1:500) • Rabbit anti-Cleaved caspase 3 (1:250)
Secondary antibodies
<ul style="list-style-type: none"> • Alexa-Fluor 488 conjugate anti-rabbit (1:200) • Alexa-Fluor 568 conjugate anti-rabbit (1:200) • Alexa-Fluor 647 conjugate anti-mouse (1:200)

Table 4: Resume of the antibodies used for the pancreatic tissue.

3.3.5 Cell cluster diameter

To calculate cell cluster diameter, the area of the stained insulin was taken. Insulin was used to acquire the diameter because it is secreted by all the cells forming the pseudoislet aggregations. Taking the diameter of the insulin area secreted, we can obtain precise diameter values. Cell cluster diameter was analyzed at days 1, 4, and 7 prior to immunostaining of the cells (Section 3.3.5). Once finished, confocal images were taken. 20 pseudoislets per cryogel were analyzed with ImageJ software. Briefly, the insulin channel was converted to binary. After, Feret diameter of the pseudoislets was quantified. Here, Feret was quantified as it is the most significant distance between two diametrical points.

3.3.6 Pseudoislets proliferation

The proliferation of cells was quantified by confocal imaging after immunostaining protocol (Section 3.3.5) at days 1, 4, and 7. After confocal imaging acquisition, images were analyzed with ImageJ software. Briefly, image channels were split and thresholded into black and white. To avoid miscounting of the nuclei and Ki-67, Watershed separation was applied in both channels. Finally, the number of areas were counted. The proliferation ratio was set as the ratio between Ki-67 positive cells against a total number of nuclei.

$$\text{Proliferation ratio} = \frac{\#(\text{Nuclei} + \text{Ki67})}{\#\text{Nuclei}} \times 100$$

3.3.7 Glucose Stimulation Insulin Secretion (GSIS)

3.3.7.1 Buffer preparation

For GSIS, Krebs-Ringer Bicarbonate Buffer (KRBH) was used. KRBH stock solutions must be prepared and mixed upon the following concentrations (Table 5).

Solution I
<ul style="list-style-type: none"> • 460 mM NaCl • Diluted in MilliQ
Solution II
<ul style="list-style-type: none"> • 96 mM NaHCO₃ • 20 mM KCl • 4 mM MgCO₂·6H₂O • Diluted in MilliQ
Solution III
<ul style="list-style-type: none"> • 10 mM CaCl₂·2H₂O • Diluted in MilliQ
Hepes 1M
<ul style="list-style-type: none"> • 1 M Hepes sodium salt • Diluted in MilliQ

Table 5: Stock buffer solutions for GSIS. These solutions can be stored for 1 month in the fridge.

For the preparation of KRBH buffer, stock solutions must be mixed in the following proportions (Table 6).

KRBH buffer
<ul style="list-style-type: none"> • Solution I.....25% • Solution II.....25% • Solution III.....25% • Hepes 1M.....2% • MilliQ.....23% • BSA.....0,5g

Table 6: Proportions for KRBH buffer used in GSIS assays.

Finally, pH must be adjusted to 7.4, and glucose has to be added up to the desired concentration of 2.8 mM and 16.7 mM of glucose.

To lysate the cells and quantify the insulin content of each, lysis buffer was prepared as follows (Table 7):

Lysis Buffer	
• Glacial acetic acid.....	5,75%
• BSA.....	0,1%
• Diluted into MilliQ water	

Table 7: Lysis buffer for insulin content extraction.

3.3.7.2 GSIS Protocol

For GSIS, cells seeded inside the cryogels or in a well plate were preincubated with KRBH buffer solution containing 2.8 mM glucose for 30 min. Then, cells were incubated at low glucose concentrations (2.8 mM, G3) for 1h followed by an incubation at high glucose concentrations (16.7 mM, G16) for another hour. Then, an additional step at 2.8 mM for an extra hour was added. After each incubation step, supernatants were collected. Finally, cellular insulin contents were recovered in lysis buffer.

For the assay with the cryogels, slight modifications were done in the protocol. After the first preincubation step, cryogels were transferred to a new well, mainly to avoid counting insulin-released from cell attached to the plate. Unlike plate cultures, instead of changing the KRBH buffer, cryogel was moved to another well, and then new KRBH buffer at the desired glucose concentration was added. All these steps were performed to avoid cell losing during the cleaning steps.

For GSIS experiment in a microfluidic chip, different KRBH buffers were pumped inside the chip and incubated for 30 minutes or 1 hour. Briefly, after mounting the chip platform, 11.1 mM glucose medium was pumped inside the chip and incubated for 30 minutes. Then, 2.8 mM KRBH buffer (G3) was connected to the pump, perfused inside, and incubated for 30 minutes. Subsequently, G3 was removed and stored, and new G3 was pumped inside the chip. This process was performed 3 times, for 30 minutes each incubation. After the last G3 incubation, G16 was pumped inside the chip and incubated for 1 hour. Then, G16 was removed and stored, and fresh G16 was pumped inside the chip. This step was repeated for up to 3 hours. Finally, cryogels were taken out from the chip for insulin content lysates.

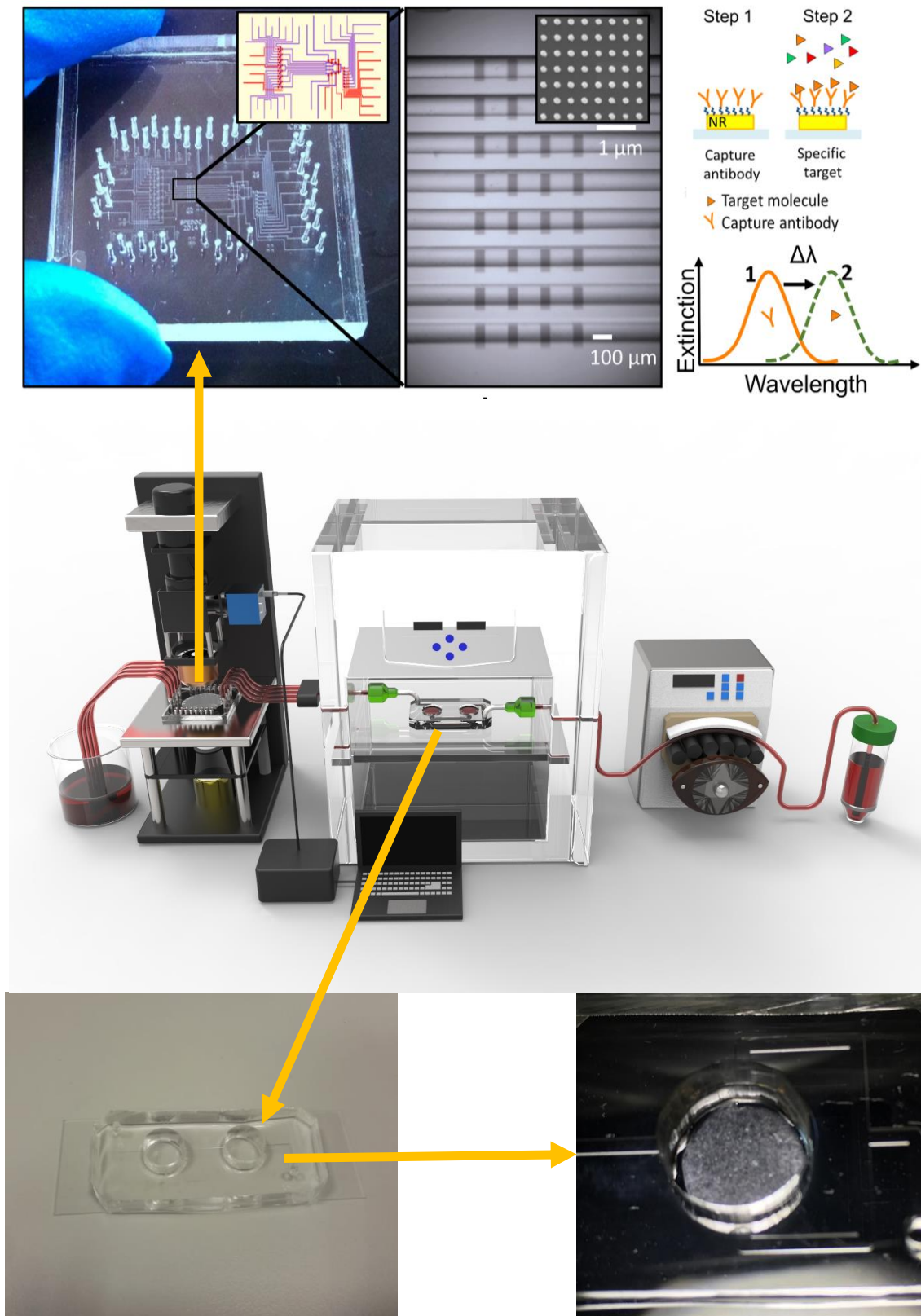


Figure 24: Scheme of the set-up for the real time GSIS measurements. Chip with the cryogel inside was connected to a pump, that continuously injects the desired buffer. Outgoing buffers flown inside the LSPR sensing platform, where light refractive index was measured. (Adapted from Ortega et al. "In-situ LSPR sensing of secreted insulin in organ-on-chip". 2021)

For the continuous insulin releasing sensing, the chip was incorporated into a Localized Surface Plasmon Resonance (LSPR) sensing platform developed at ICFO (Figure 24). Briefly, LSPR sensing platform is an optic sensor with an array of gold nanorods where antibodies were attached. To quantify the amount of insulin, the refractive index can be used, so knowing the shift of this index and its displacement, the amount of insulin can be extrapolated. For GSIS assay, KRBH buffer was continuously pumped through the chip, and then flown inside the LSPR sensing platform. LSPR sensing chip has 8 different channels, so 7 cycles were determined for the experiment. Each cycle consists of 30 minutes of continuously pumped buffer. After each cycle, LSPR sensing channel was changed. KRBH buffer was changed to G16 conditions after 120 minutes.

3.3.7.3 Insulin content

Samples were taken out from the freezer and defrosted at RT. Then, samples were boiled at 100 °C for 10 minutes and vortexed. Finally, samples were centrifugated at 4°C for 10 minutes at 12000 rpm. Finally, supernatants were collected. Insulin concentration was determined by Enzyme-Linked Immunosorbent Assay (ELISA). G3 samples were not diluted, G16 samples were dilute 1:4 into PBS, and content samples were diluted 1:200 into PBS.

3.3.8 Enzyme-linked immunosorbent assay (ELISA)

3.3.8.1 Buffer preparation

Sandwich Enzyme-Linked ImmunoSorbent Assay (ELISA) was used to quantify the amount of insulin released in the GSIS assays (Figure 25). The protocol for this assay was previously developed in the laboratory.

For ELISA assay, different buffers must be prepared (Table 8):

PBS 100 mM (for 1L)
<ul style="list-style-type: none"> • NaCl80 g • KH₂PO₄2 g • Na₂HPO₄11.4 g • KCl2 g • Dissolve in MilliQ
PBST 10 mM, pH 7.5
<ul style="list-style-type: none"> • 50 mL of PBS buffer 100 mM • 445 mL of MilliQ water • Adjust pH to 7,5 • 5 ml of Tween 20 (5%)
Coating Buffer 0.25 M (5x)
<ul style="list-style-type: none"> • Na₂CO₃ 3.975 g • NaHCO₃7.32 g • Dissolve into 500 mL of MilliQ water • pH 9.6
Citrate Buffer
<ul style="list-style-type: none"> • 0.04 M Sodium Citrate • 96 ug/mL of Tetramethylbenzidine • 0.004 % of Oxygen Peroxide • pH 5.4

Table 8: Resume of the preparation of the ELISA buffers.

3.3.8.2 Sandwich ELISA protocol

First, mouse mAB insulin 26.6 nM of capture antibody (Novus) was diluted into coating buffer (0.05M, 1x) and placed into 96-well plate at 4°C O/N.

The next day, the plate was taken out from the fridge and washed 3 times with PBST to remove all unattached antibodies. Once dried, a calibration curve was performed. The calibration curve previously optimized started at 100 nM and decreased to consecutive 1:10 dilutions into PBST. Then, each sample was placed in a well with a respective duplicate, and the plate was incubated for 1 hour at room temperature.

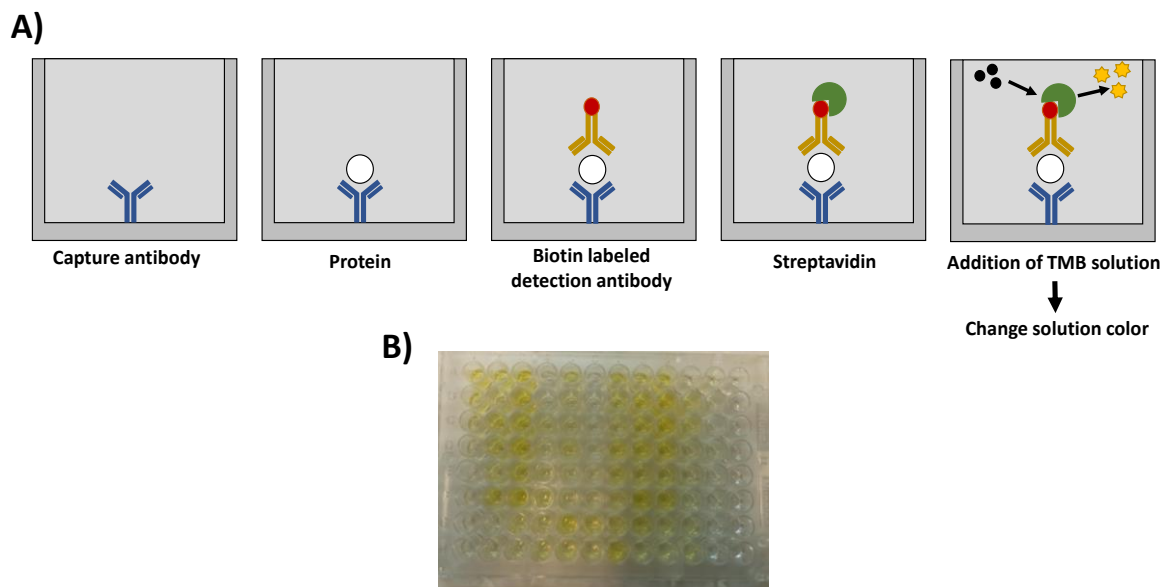


Figure 25: Sandwich ELISA scheme. A) Step-by-step process for insulin quantification. First, capture antibody was immobilized in the plate. Then, insulin was attached to it. Consecutively, detection-biotinylated antibody was attached to the protein. Later, streptavidin was added. Finally, TMB solution was mixed, prompting a color change depending on the amount of protein found. B) Example of an ELISA plate.

After protein attachment into the primary antibody, 5x PBST washings were performed to remove all unreacted proteins. Then, biotinylated secondary anti-insulin antibody was placed at 0.2 nM and incubated for 1 hour. Next, streptavidin was added at 4.73 nM (Thermo Scientific) and incubated for 30 minutes. Following, citrate buffer was added to start the reaction. After 3 minutes, 4 M Sulfuric acid were added to stop the reaction (Figure 25A). The colorimetric quantification was made with a Power wave X microplate spectrophotometer at 490 nm of wavelength (Figure 25B).

Data analysis was done using GraphPad software. Calibration curves were transformed into logarithmic and non-linear regression fitting. Samples were interpolated within the linear part of this curve.

3.3.9 qPCR for *INS1E*

3.3.9.1 RNA extraction

After cell culture or respective assay, cryogels were deep into an Eppendorf with 500 μ l of TriReagent (Thermo Scientific) and vortexed for 15 seconds.

For plate cultures, 500 μ l of TriReagent was dispensed in each well and vigorously pipetted to ensure all cells were lysate. After lysing, trizol was transferred into a tube and vortexed for 15 seconds. After, samples were placed inside a -80°C freezer until RNA extraction.

For RNA extraction, first, samples were thawed within the ice. When trizol was defrosted, the cryogels were smashed with a PCR stick, and 500 μ l more of TriReagent were added. Then, 200 μ l of Chloroform was added for phase separation, vortexed for 15 seconds, and incubated for 5 minutes at RT. Samples were centrifuged at 12000 rcf for 15 minutes at 4°C, and the colorless phase was split to a new tube. Following, 1 mL of isopropanol and 10 μ l of GlycoBlue (15 mg/mL, Thermo Fischer) were added, vortexed, and incubated at RT for 5 minutes. Centrifugation was performed at 12000 rcf for 10 minutes at 4°C, and the pellet was washed with EtOH 80%, and centrifuged again at 7500 rcf for 5 minutes at 4°C. Next, the EtOH has been air-dried with the vacuum/heater centrifuge. Finally, RNA was resuspended in RNase free water at 65°C, and the RNA was read into the Nanodrop ND-1000 spectrophotometer. Samples were stored into the -80°C until RNA digestion and cDNA synthesis.

3.3.9.2 RNA digestion and cDNA synthesis

Of total RNA, 300 ng were used for RNA digestion. For this, 300 ng of RNA sample, 1 μ l 10X DNase I reaction buffer, 1 μ l DNase I, and complete the volume until 10 μ l with free RNase water were mixed inside a vial (Table 9). This mix was incubated for 15 minutes at RT. After, 1 μ l of 25 mM EDTA was added and incubated for 10 minutes at 65°C.

RNA digestion
<ul style="list-style-type: none"> • 300 ng of RNA sample • 1 μl 10X DNase I reaction buffer • 1 μl DNase I • complete the volume until 10 μl with Nuclease-free water

Table 9: RNA digestion proportions

cDNA synthesis was done using a high-capacity cDNA reverse transcription kit (Applied Biosystems). Reagents and volumes used for cDNA transcription are listed in the following table (Table 10). For cDNA synthesis, 10 µl of the kit mixture was added to the previous digested mix. Samples were cycled with a thermocycler as follows: 10 minutes at 25°C, 2 hours at 37°C 5 minutes at 85°C, and 4°C until sample collecting.

cDNA synthesis volumes (For one sample)	
•	2 µl 10X RT buffer
•	0.8 µl 25X dNTP mix (100mM)
•	2 µl 10X Random primers
•	1 µl MultiScript Reverse Transcriptase
•	4.2 µl Nuclease-free water

Table 10: cDNA synthesis proportions

3.3.9.3 qPCR

Quantitative PCR reactions were run using SyberGreen gene expression assays according to the manufacturer's directions (Solis Biodine) in a 7900HT fast real-time PCR system (Applied Biosystems). Primer sequences used for gene expression analysis are listed in Table 11. Tbp1 was used to normalize the expression of genes of interest.

Gene	Forward	Reverse
Tbp1	ACCCTTCACCAATGACTCCTATG	ATGATGACTGCAGCAAATCGC
MafA	AAGGAGGAGGTCATCCGAC	TCTCCAGAATGTGCCGCTG
PDX-1	CCCCAGTTTACAAGCTCGCT	CTCGGTTCCATTCTGGGAAAGG
NeuroD1	GATCAATCTTCTCTTCCGGTG	TGCGAATGGCTATCGAAAGAC
Ki67	CAGCTCCTGCCTGTTTGGAA	TTGCCTCTTGCTCTTTGACTTCA
Pbk	GAAGCTTGGCTTTGGGACTG	GGAGAATGAGACAACCCTCTTGG
Ddit3/Chop	TCATCCCCAGGAAACGAAGAG	GCTTTGGGATGTGCGTGTG
Trib3	CGTGGCACACTGCCACAAG	TCCAGGTTCTCCAGCACCAG
Atf3	GTCCGGGCTCAGAATGGAC	CGTGCCACCTCTGCTTAGCT

Table 11: Primers used for gene expression in pancreatic tissue.

3.3.10 Diabetes modeling

After proving we could generate reseblant pseudoislets inside the scaffold we wanted to prove if our platform can simulate a diabetes-like situation. For this, we decided to add free fatty acids and different glucose concentrations to the cell cultures.

After seeding cells over the cryogel, cells were cultured until day 4 with complete RPMI-medium at 11 mM of glucose. On day 4, we add the free fatty acids inducing the diabetic conditions. In some samples, the medium was replaced for 25 mM glucose medium. Further, in the desired samples, 400 μ M of Palmitic acid (Sigma Aldrich) were added at day 4 after seeding. Briefly, palmitic was obtained from diluting 1g of palmitic acid into 100% isopropanol. Then palmitic was diluted into PBS/1% BSA to ensure proper dissolution. Finally, an extra 1:10 dilution in respective mediums was performed, and the culture medium was replaced for each respective treatment up to day 7 of culture.

In summary, we tested two different glucose concentrations with and without palmitic acid. All these conditions were studied in plate monolayered distributions and in cryogels where pseudoislets were formed. To understand cell viability and functionality, GSIS analyzed by insulin ELISA and gene expression analyzed by qPCR were performed.

3.4 SKELETAL MUSCLE TISSUE ENGINEERING

3.4.1 C2C12 cell culture

Frozen vials of C2C12 myoblasts (American Type Culture Collection (ATCC), USA) with $1 \cdot 10^6$ cell/mL were thawed in a bath at 37°C for 1 minute. Before the complete defrosting of the vial, cells were placed inside a 75 cm² flask and filled with 15 ml of growth medium (Dulbecco's Modified Eagle Medium (DMEM) high glucose with L-glutamine (Gibco, Thermofisher) supplemented with 10% FBS (Thermofisher) and 1% Pen/Strep (Thermofisher)). Finally, the flask was placed inside an incubator at 37°C, and 5% CO₂ and the medium was changed every 2-3 days. When cells reached ~75% of confluency, they are trypsinized for cell passaging or cell seeding inside scaffolds. For cell trypsinization, 2 ml of 0,25% trypsin-EDTA

were added to the flask and placed inside the incubator for 2 minutes. After, 8 ml of medium were added to stop the reaction. In the case of cell passaging, 2,5 ml (1:4 cell passaging) of the cell mix were added to another 75 cm² cell culture flask and filled with 15 mL of growth medium.

3.4.2 C2C12 cell seeding.

First, the cryogel was dried a bit at RT to empty the pores of water. For cell seeding, the medium was removed from the culture flask, and before trypsinization, the flask was washed using 10 mL of PBS. After PBS removing, cells were trypsinized with 2 mL of 0,25% trypsin-EDTA and placed 2 minutes inside the incubator at 37°C and 5% of CO₂. Next, minor hits were applied to the flask to ensure the total detachment of all the cells, and the flask was filled with 8 ml of fresh medium, and 10 ml in total were placed inside a 15 ml falcon. Here, 10 µl of cells were used for cell counting with a Neubauer chamber or a cell counter, while the falcon was centrifuged at 1.2 rpm for 5 minutes. When centrifuge finished, the supernatant was discarded, and cells were resuspended to 9x10⁶ cells/ml. Upon this concentration, a drop of 20 µl was seeded in the upper part of the cryogel. After 10 minutes, we collect the medium from the bottom that passed through the cryogel, and we reseed it on the top of the cryogel again. After seeding, cells were in growth medium (DMEM, 10% FBS 1% Pen/strep) for 10 days, and the medium was changed to differentiation medium (DMEM, 2% horse serum, 1% pen/strep) up to 22 days of culture. The medium was changed every 2-3 days.

3.4.3 Electrical stimulation for skeletal muscle

Electrical Pulse Stimulation (EPS) was applied on day 11 after differentiation medium. The stimulation was performed by placing the cryogels inside a 6 well-plate with a C-dish from IonOptix connected to a multifunction generator (WF 1948; NF Co.) with a specified regime (1 Hz of frequency, 1V p-p, and 10 ms of width) for 12 consecutive hours. Cryogel was placed in the middle of a 6 well and centered between the two electrodes of the C-dish. Notably, the pores of the cryogel must be oriented parallel to the electric field (Figure 26).

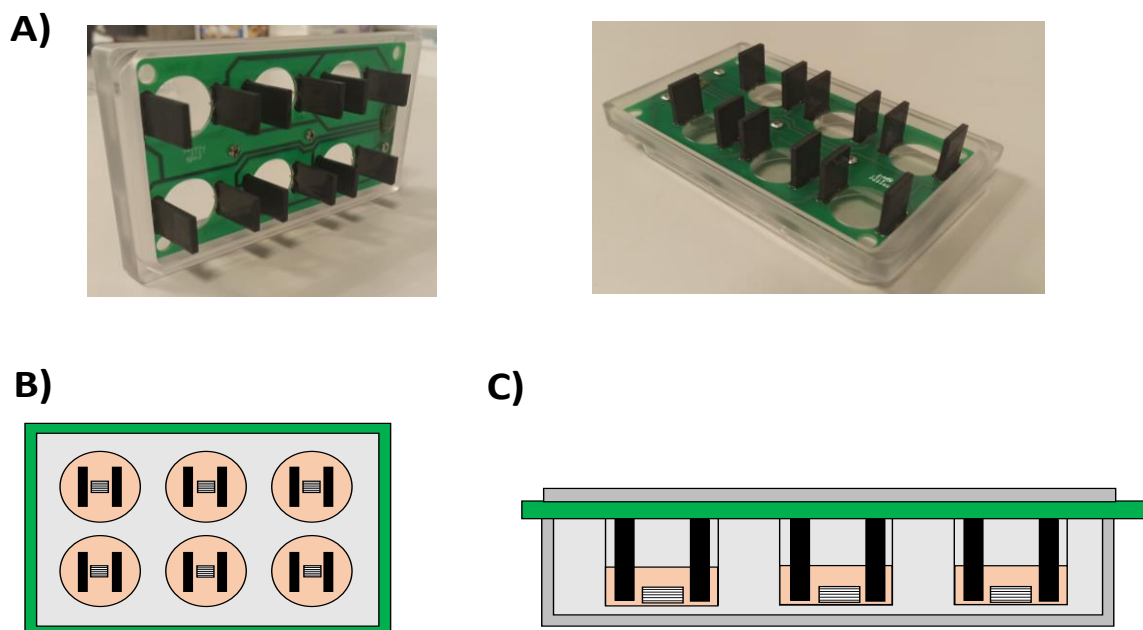


Figure 26: Schematic of the electrical stimulation process. A) Pictures of the IonOptix C-dish plate. B) Schematic image of the lower view. Cryogels were placed in the middle of the 6 well-plate. C) Side view of the stimulation set-up. Cryogels were placed centered between the electrodes of the C-dish.

3.4.4 Live/Dead assay

An important hallmark of the cell-biomaterial interaction is the biocompatibility of this with the cells. A viability assay was performed to study how viable the cells are inside or in contact with the scaffold. This assay was performed with the Live/dead assay kit (Thermofischer) at days 1, 5 and 7 after cell seeding. Firstly, the cryogels were washed 5 minutes with PBS (x5). While washing steps were performed the working solution was prepared. For this solution, 12 μL of 2 mM EthD-1, 3 μL of Calcein AM, and 6 μL of Hoechst were mixed in 6 mL of PBS. Once washed, the PBS was removed, and 250 μL of the working solution was added. Then, cryogels were stored at the incubator. After 25 minutes, the cryogels were washed 3 times with PBS. Finally, images were taken with confocal microscopy for live/dead ratio quantification.

The quantification of viability ratio was calculated as follows:

$$\text{Viability ratio} = \frac{\# \text{Live cells}}{\#(\text{Live cells} + \text{Dead cells})} \times 100$$

3.4.5 Skeletal immunostaining

For confocal analysis, stained cryogels were used. The staining was done with DAPI for nuclei, Rhodamine-Phalloidin for F-actin, and MF20 Alexa Fluor 488 for Myosin Heavy Chain. After culturing the cells for 22 days, the cryogels were washed with PBS and fixed with 10% formalin solution (Sigma - Aldrich) for 30 minutes. Then, the cryogels were washed with TBS (Canvax Biotech) and permeabilized with 0,1% v/v Triton X-100 (Sigma Aldrich) solution in TBS for 15 minutes. Besides, the blocking of the cryogels was done with a solution of 0,3% v/v Triton X-100 and 3% v/v Donkey serum (Sigma-Aldrich) into TBS for 2 hours. Then, the cryogels were incubated with 100 nM Rhodamine-Phalloidin 480 (Cytoskeleton Inc) and 5 µg/mL MF20 Alexa Fluor 488 blocking solution overnight. The following day, the cryogels were washed with permeabilization solution (3x, 10 minutes each). Subsequently, cryogels were incubated with 1 µM DAPI (Thermofisher) into blocking solution for 15 minutes. Finally, cryogels were washed with TBS for 15 minutes and stored at 4 °C until confocal microscopy acquisition.

3.4.6 Alignment in skeletal muscle

Stained cryogels were used, to calculate the alignment of the fibers. Also, nuclei and F-Actin for cells were stained following immunostaining protocol. The PlugIn "OrientationJ" from ImageJ were used to see the distribution of the fibers and the alignment of the cells in a random fiber distribution cryogel against the aligned fiber cryogels. OrientationJ calculates the orientation of an image evaluating the gradient structure tensor in a local neighborhood. Distribution from OrientationJ PlugIn was used with a cubic spline and a local window of 2 pixels.

3.4.7 Fusion Index

C2C12 myoblast cells were seeded as previously explained in the cryogel for 22 days with or without Electrical Pulse Stimulation (EPS) to differentiate them into myotubes. Cryogels were fixed for prior staining of DAPI, F-actin, and Myosin heavy chain. Cryogels were sliced vertically to improve image acquisition. Then, confocal images were taken in 5 random areas over the cryogel, and 3 cryogels per condition were used. From these images, the fusion index has been calculated. Briefly, image channels were split. Then, the blue channel (Nuclei) and green channel (Myosin Heavy Chain) were transformed into binary. Next, each channel area from different myotubes were counted. The index fusion consists of the number of cells that are differentiated and fused. To calculate the fusion index, the following equation was used:

$$Index\ fusion = \frac{\#Green \ \& \ blue \ areas}{Total \ \#nuclei} \times 100$$

For the index fusion analysis, 5 images for sample and 3 samples per condition were taken and analyzed.

3.4.8 qPCR for skeletal muscle

3.4.8.1 RNA extraction

After cell culture and stimulation, cryogels were placed into a 1.5 mL vial and were frozen in liquid nitrogen until PCR assay. Firstly, the cryogels were homogenized with 500 µl of TriReagent at room temperature, smashed with a PCR stick, and 500 µl more of TriReagent were added. Then, 200 µl of chloroform was added, vortexed for 15 seconds, and incubated for 5 minutes at RT. Samples were centrifuged at 12000 rcf for 15 minutes at 4°C, and the aqueous phase was split into a new eppendorf tube. Then, 1 mL of isopropanol and 10 µl of GlycoBlue (at 15 mg/mL) were added, vortexed, and incubated at RT for 5 minutes. Following, centrifugation was performed at 12000 rcf for 10 minutes at 4°C, and the pellet was washed with EtOH 80%, and centrifugated again at 7500 rcf for 5 minutes at 4°C. Next, the EtOH has been

air-dried with the vacuum/heater centrifuge. Finally, RNA was resuspended in RNase free water at 65°C, and the RNA was read into the Nanodrop ND-100 spectrophotometer. Samples were stored into the -80°C until RNA digestion and cDNA synthesis.

3.4.8.2 RNA digestion and cDNA synthesis

For the RNA digestion, a mixed reaction of 1 µg of RNA sample, 1 µl 10X DNase I reaction buffer, 1 µl DNase I was prepared. The volume was complete until 10 µl with free RNase water. This mix was incubated for 15 minutes at RT (Table 12). After, 1 µl of 25 mM EDTA was added and incubated for 10 minutes at 65°C.

RNA digestion
<ul style="list-style-type: none"> • 1 µg of RNA sample • 1 µl 10X DNase I reaction buffer • 1 µl DNase I • complete the volume until 10 µl with Nuclease-free water

Table 12: RNA digestion concentrations.

Later, 1 µl of random hexamer primer (10 mM) and 1 µl of dNTPs (10mM) was added and incubated at 65°C for 5 minutes and placed on ice to cDNA synthesis. The content was collected into another Eppendorf, and 4 µl of First Strand Buffer, 2 µl 0.1 M DTT, 1 µl of RNaseOUT, and 1 µl of SuperScript were added (Table 13). Then the mix was incubated into the thermocycler for 10 minutes at 25°C, 50 minutes at 42°C, and 15 minutes at 70°C. Finally, samples were kept at -20°C for further analysis.

cDNA synthesis volumes (For one sample)
<ul style="list-style-type: none"> • 1 µl random hexamer primer (10 mM) • 1 µl of dNTPs (10mM) • 4 µl of First Strand Buffer • 2 µl 0.1 M DTT • 1 µl of RNaseOUT • 1 µl of SuperScript

Table 13: cDNA synthesis protocol proportions

3.4.8.3 qPCR

Finally, quantitative PCR reactions were run using SyberGreen gene expression assays according to the manufacturer's directions (Solis Biodine). Briefly, a reaction mix was performed, as shown in Table 14.

Reaction mix (per sample)
<ul style="list-style-type: none"> • 1 µl of 5X HOT FIREPol EvaGreen qPCR Mix Plus • 0.5 µl of primer Forward • 0.5 µl of primer Reverse • 2 µl of cDNA (previously diluted 1:10) • 13 µl of H₂O RNase free

Table 14: Reaction mix proportions for qPCR standard curve

Expression levels were measured using an Applied Biosystems StepOnePlus Real-Time PCR System. Cycles were as follows: 40°C for 12 min., 90°C for 15 min., 60°C for 20 min., and 72°C for 20 min. Expression relative to ActB endogenous genes and control group was calculated using the $2^{-\Delta\Delta C_t}$ method. At least three cryogels per condition were evaluated. The primers studied were listed in Table 15. For the qPCR 3 cryogels per condition were evaluated.

Gene	Forward	Reverse
Actb	CATTGCTGACAGGATGCAGAAGG	TGCTGGAAGGTGGACAGTGAGG
Myog	GCTGGAAGATGAGTGCTCAGAG	TCCAAACCAGCCATCTCCTCTG
Myh2	GCGACTTGAAGTTAGCCCAGGA	CTCGTCCTCAATCTTGCTCTGC
Tnnt1	GAGCAGAGGATGACGCCAAGAA	TTCATCTCCCGACCAGTCTGTC

Table 15: Primers used for gene expression analysis in the skeletal muscle tissue.

3.5 STATISTICAL ANALYSIS

Data are expressed as the mean \pm SD of at least 2 independent experiments with 3 replicates each. Statistical significance for two conditions comparison was determined for parametric tests by two-tailed Student t-test with Welch's

correction when necessary and for non-parametric tests, by Mann-Whitney U test. For multiple condition comparison, one-way or two-way ANOVA when required were used. Results were considered statistically significant at $p < 0.05$.

4. RESULTS

4.1 CRYOGEL FABRICATION

4.1.1 Cryogels as a scaffold casting technique

Scaffold selection has a big relevancy in tissue engineering, as it has the objective to mimic the extracellular matrix of each tissue. By selecting the appropriate biomaterials, casting technique, crosslinking method or different surface functionalization, we could provide the scaffold with unique and specific properties for the proper tissue generation. Among others, properties as stiffness, permeability or bioactivity can be modulated by combining all these parameters.

Nowadays, hydrogel encapsulation is the scaffolding gold-standard technique. However, limitations in pore size and nutrient diffusion, turn into a non-suitable scaffold for the generation of volumetric tissues as pancreatic tissue engineering.

To solve this drawbacks cryogelation technique was the chosen fabrication process to generate scaffolds for pancreatic and skeletal muscle tissue engineering. This technique allows the generation of sponge-like scaffolds with high water content and with a microporous structure that allow high nutrient and oxygen diffusion (Figure 27). Also, by changing cooling rate, temperature, or freezing directionality, different pore architecture, and pore sizes can be achieved. Moreover, the unnecessary use of UV-light and the possibility to crosslink the biomaterial prior cell seeding, allow to generate more mechanically stable and easy to manufacture scaffolds.

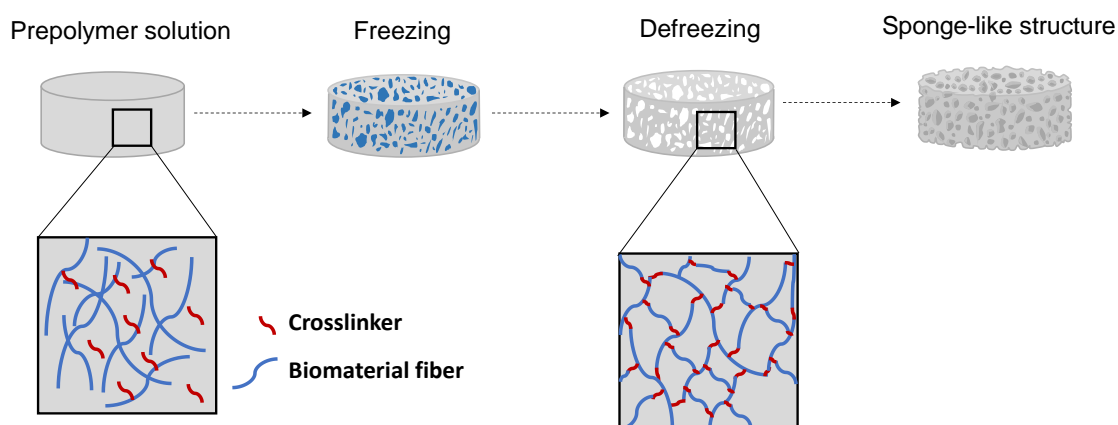


Figure 27: Scheme of cryogelation process. Prepolymer is placed at sub-zero temperatures, where while it freezes its acuose part, the fibers of the polymer crosslinks. After thawed, sponge-like microporous scaffold is fabricated.

4.1.1.1 Biomaterials used

One of the most relevant scaffolding parameters is the biomaterial selection. Biomaterials will be the main responsible for interacting with the cells, being cell-adhesive, bioactive or biocompatible. Moreover, physicomaterial properties of each biomaterial, as stiffness or swelling may favour the tissue formation.

Among all the possible biomaterials, cellulose and gelatin has been selected. Gelatin is a derivate of collagen. With high biocompatibility and cell activity promoters, as the polypeptide Arginine-Glycine-Aspartic acid (RGD), a cell-binding motif (Figure 28A). Also, it is cheap, easy to obtain, and temperature-dependent [24]. On the other hand, it has low mechanical properties, low viscosity, and is degradable by mammalian cells [22]. Gelatin is a well-established and widely used biomaterial in tissue engineering [55], [164], [165].

Cellulose is one of the most common polymers in the nature. It has good biocompatibility and better mechanical properties than the ECM-derived biomaterials. Also, it is cheap, and it is non-temperature-dependent. It lacks cellular interactions and it is not degradable by mammalian cells. However, cellulose is not water soluble, so Carboxymethyl cellulose (Figure 28B) was used, as it have same properties as pristine cellulose but it is water-soluble. Furthermore, the presence of carboxyl groups allows the carbodiimide crosslinking, making CMC a suitable biomaterial for tissue engineering and scaffold generation [166], [167]. Moreover, the generation of a biocomposite

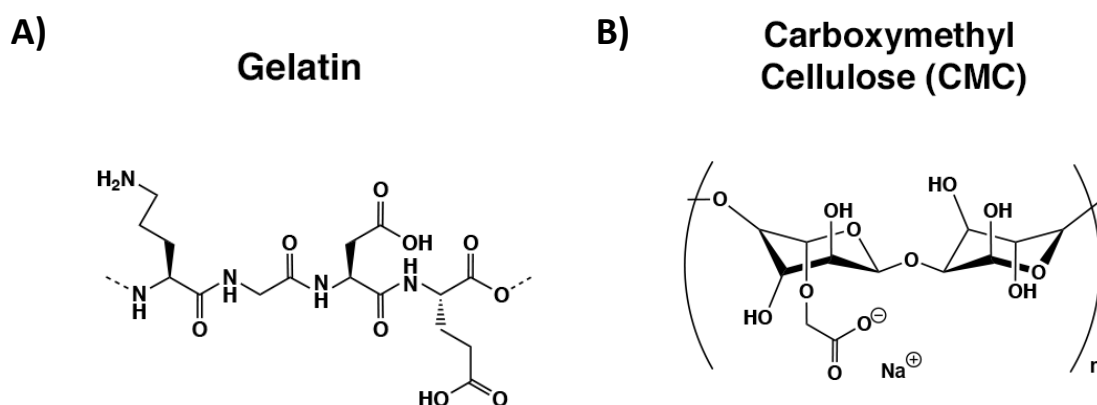


Figure 28: Biomaterials used for cryogel fabrication, A) Chemical structure of the gelatin. B) Chemical structure of the Carboxy methyl cellulose.

combining both biomaterials will be a promising scaffold for tissue engineering. Combining gelatin and cellulose we could achieve a good bioactive and mechanically stable cryogel with tunable stiffness, modulable pore structure and with high water content.

4.1.1.2 Crosslinking principle

For Carboxymethyl cellulose and gelatin cryogels a carbodiimide chemical crosslinking was used (Figure 29). Adipic acid dihydrazide was selected as a

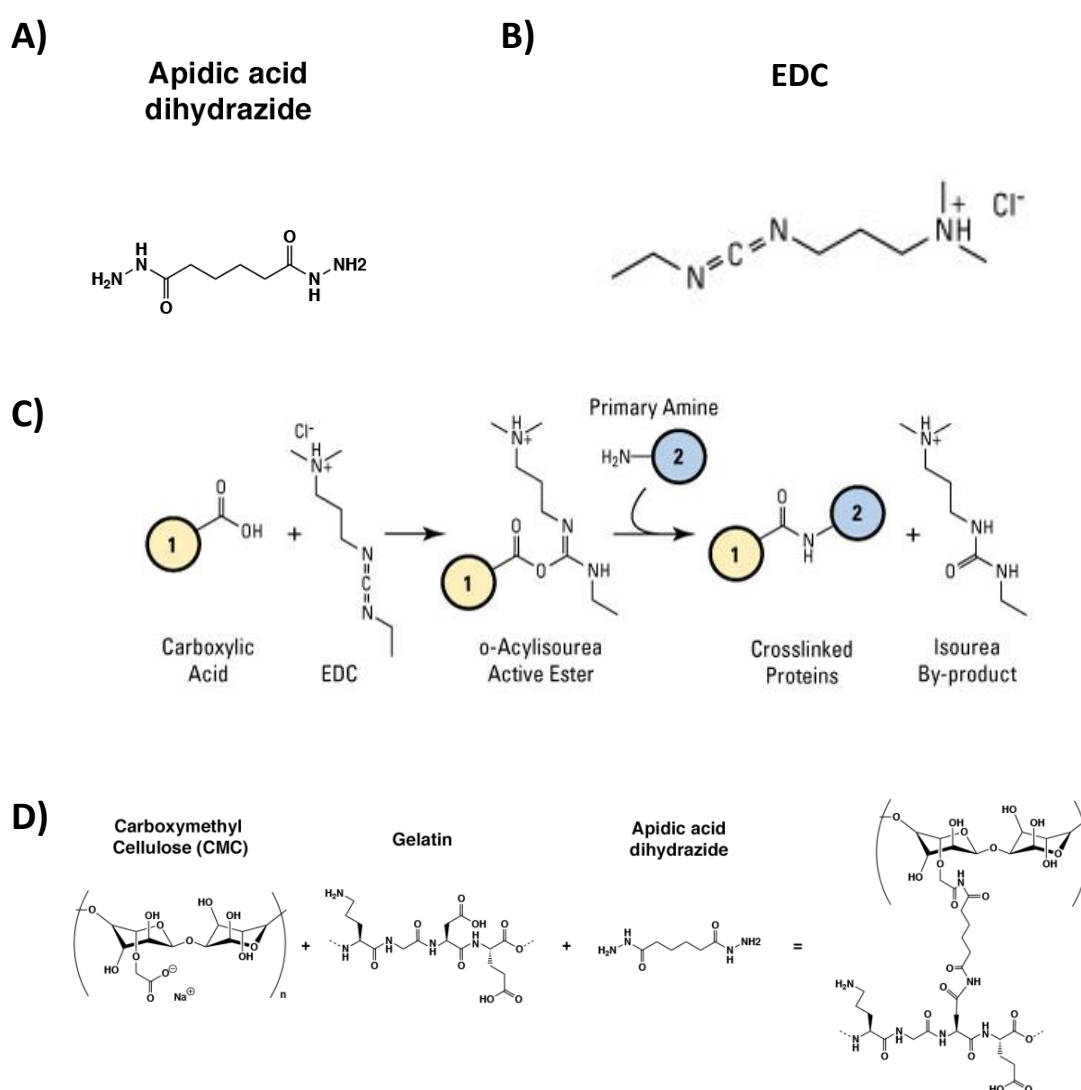


Figure 29: Crosslinking process of the gelatin-CMC fibers. A) Adipic Acid Dihydrazide. B) EDC. C) Scheme of the carbodiimide crosslinking chemistry. (1) would represent polymer fibers, (2) would represent AAD molecule. Adapted from Thermofischer's Crosslinking Technical book [261]. D) Schematic of the crosslinking network of the gelatin-CMC cryogels.

linker because the presence of amine groups in both sides of the molecule (Figure 29A), and ECD as an activating agent (Figure 29B). The main reason for this crosslinking is the EDC-activation of the carboxyl groups from both polymers. With this activation and with the help of the linker molecule, we were able to generate a polymeric network (Figure 29C). This amine groups will react with the carboxyl EDC-activated groups from the polymer, achieving a good fiber crosslinking (Figure 29D). Moreover, this reaction can succeed while prepolymer solution freezes, being a successful method to generate fiber meshes and, for instance, cryogels for tissue engineering.

4.1.1.3 Scaffold prerequisites for tissue formation

For generating different tissues, scaffolds must have similar properties as the EMC of each specific tissue. Hence, depending on the tissue we wanted to generate, a specific scaffold with unique properties has to be generated. Each scaffold was designed in based the prerequisites of each tissue:

Pancreatic tissue was generated by seeding pancreatic islets inside the cryogel or generating pseudoislets by aggregating β -cells inside the scaffold. Both pancreatic approaches needed a pore architecture with a wide range of porosities, similar to the pancreatic islets [97]. This parameter is essential to ensure pancreatic islets infiltration or resemblant pseudoislet formation. Another important feature is that pancreas is a relatively soft tissue, so the scaffold should have similar stiffness to the physiological. All this has to be made taking into account that pore interconnectivity and permeability of the scaffold should be high to avoid lack of nutrient and oxygen supply.

For the skeletal muscle similar features of pore interconnectivity, permeability and swelling must be achieved. However, pore architecture highly differs from pancreatic tissue requirements. Skeletal muscle is a highly aligned tissue, formed from the fusion of myoblast into multinucleated cells called myotubes. This cell fusion is enhanced when cells are aligned. Taking the profit that the cells can sense the topography of a substrate, an anisotropic pore architecture was generated. With this, cells will be all guided in the same direction, prompting its fusion and maturation. Another important property is the skeletal muscle stiffness, so the scaffold should be stiffer than the pancreatic approach. Finally, skeletal muscle improves its myogenic maturation when electrical pulse stimulation was applied. However, none of the biomaterials proposed has good electrical properties. Different particles

can be added to the structure of the scaffold to enhance this property and generating a more conductive scaffold. Carbon nanotubes were added to the scaffold structure to enhance electrical conductivity based on literature and for its easy acquisition and proved conductivity.

4.1.2 Cryogel fabrication and optimization

Different parameters were studied to fabricate cryogels. Firstly, different molecular weight cellulose were tested: 700 kDa Carboxymethyl cellulose (CMC) and 90 kDa CMC. Due to its solubility and viscosity, 90 kDa CMC was chosen. Moreover, 700 kDa crosslink before freezing difficulting the obtention of mechanically stable cryogel.

Once chosen the pristine biomaterial, other variables were modulated to optimize the protocol. Different biomaterial percentages, AAD and EDC concentrations were tested to check the mechanical stability of the cryogels. First, different CMC percentage cryogels were tested. We could observe that crosslinking reagents needed to be directly scaled up when more concentrated CMC cryogels were fabricated. However, when CMC percentage was decreased AAD and EDC were in excess and there was no need to downscale it. Second, Maintaining CMC and EDC percentage constant, different concentrations of AAD were modulated. Here, we could observe that AAD concentrations has no apparent effect in cryogel mechanical stability. Finally, studying EDC concentrations we could observe that when EDC was increased, early polymerization occurs, not generating mechanically stable cryogels. On the other hand, when EDC was highly decreased, crosslinking underperform and no mechanically stable cryogels were fabricated either.

After determining the appropriate crosslinking concentrations for each cryogel, different CMC percentage cryogels were fabricated. Starting at 5% (w/v) and by decreasing the amount of material, we could observe that the crosslinking effectivity of the cryogels strongly decrease when the material concentration goes under 1%, as they break when demolding, probably due to the unefective crosslinking and low material concentrations. Despite this, when crosslinking process succeed, cryogels present a good mechanical stability and a good handling (Figure 30). Moreover, cryogels present an interesting capability to pass through tinny constructs, for example a syringe. A resume of the final reagent concentrations for different cryogel fabrication can be found in Materials and methods, Section 3.1. Table 1.

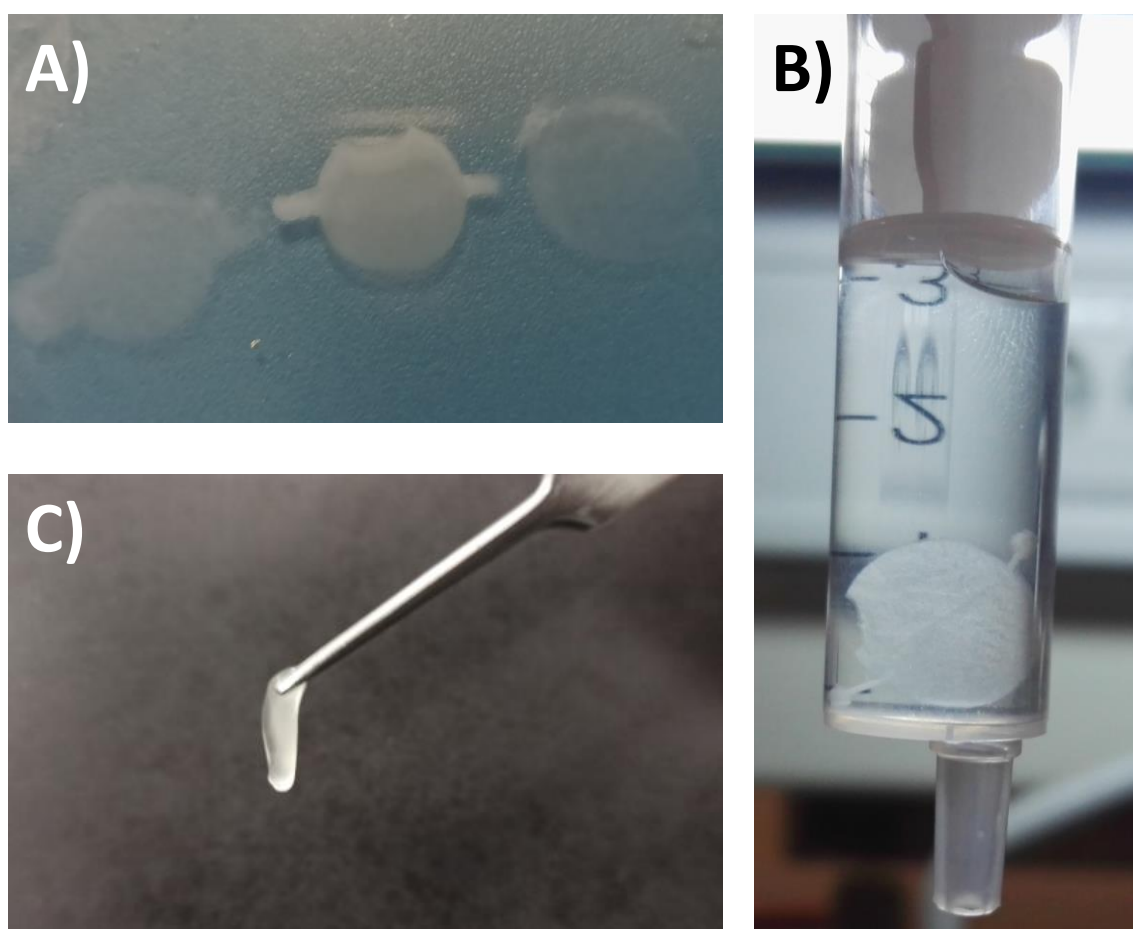


Figure 30: Different properties of the cryogels. A) Different cryogels with variable material concentrations. 1% at left, 5% at center and 0,5% in the right side. B) Cryogels can be absorbed by a syringe, while maintaining its structure. C) Cryogels are easy to handle, and they can recover easily its shape.

Cryogel porosity is mainly dependant on ice nucleation and so, highly related to temperature. Different temperatures were studied and checking its polymerization and mechanical stability to understand this parameter and generate the desired pore architecture. In here, -20°C freezer, over carbonic ice, -80°C freezer, and over liquid nitrogen were tested. In the beginning, -20°C were the only cryogels that crosslinked. However, if cryogels placed at -80°C or over carbonic ice were then placed at -20°C for an overnight, the cryogel crosslinked properly and had good mechanical stability. Although both approaches crosslinked, smaller pores were formed at lower temperatures.

For the skeletal muscle approximation, temperature optimization was also a key factor. Freezing directionality was needed to generate pore alignment. This happens because ice nucleation and growing are forced to succeed only in one axis (Figure 31). Here, two temperature set-ups were tried: crosslinking the prepolymer solution with liquid nitrogen or over carbonic ice. After placing at -20°C , the liquid nitrogen approach did not crosslink. However, carbonic ice set-up cryogels crosslinked, forming a good tubular pore architecture.

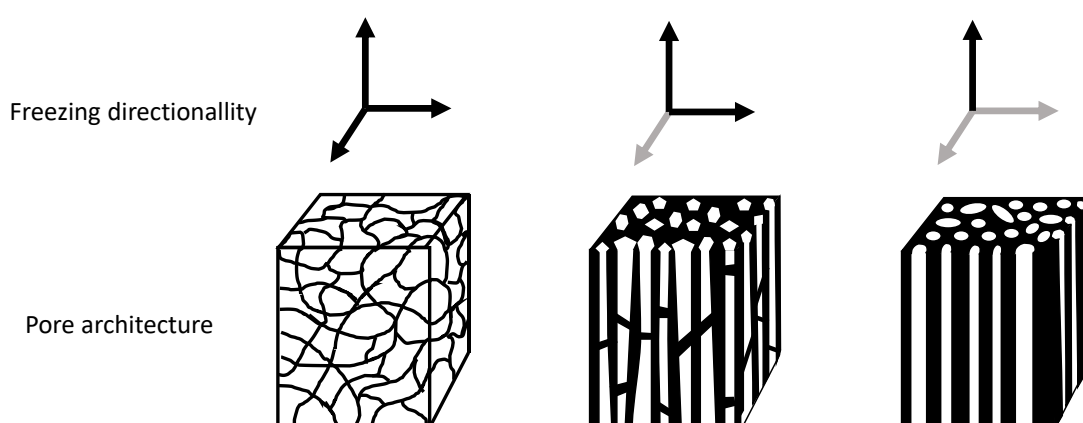


Figure 31: Scheme of the different pore architectures depending the freezing directionality applied. If temperature freezes the water without no directionality, random pores were formed. However, if water is frozen in one specific directionality, highly aligned pores can be formed.

The last step of anisotropic scaffolds was incorporating carbon nanotubes (CNT) into the fiber structure to generate an electrically conductive biomaterial. The finality of this is to stimulate the scaffold electrically to improve myogenic maturation [168]. We could observe that CNT could be incorporated in the scaffold matrix by mixing it inside the prepolymer solution (Figure 32A). After demolding, the mechanical stability of the scaffolds did not change when CNT were added. During the fabrication process, CNT tend to form small aggregates not distributing uniformly through the whole scaffold (Figure 32B). We could observe by optical microscopy that CNT clusters were aligned following the pore structure despite these aggregations. Moreover, by taking images with a Scanning Electron Microscope (SEM), we could observe that not all CNT formed clusters, but other CNTs can be found dispersedly in the scaffold (Figure 32C).

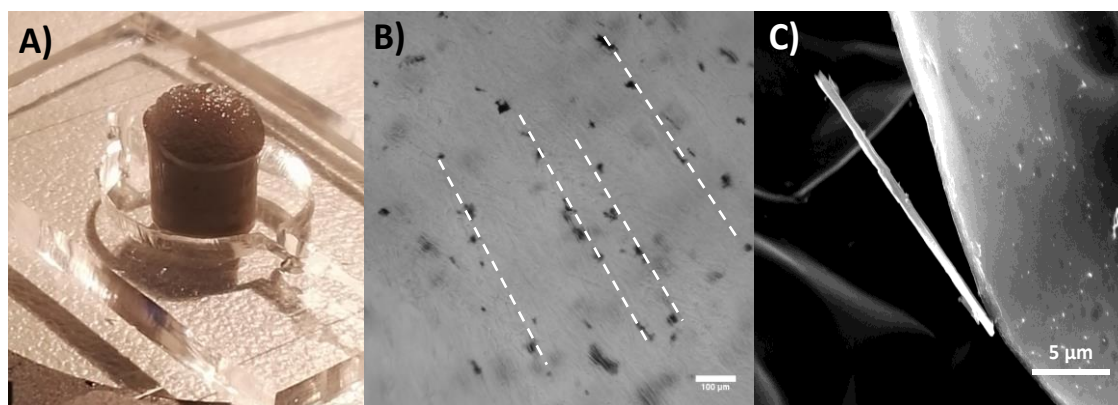


Figure 32: Incorporation of carbon nanotubes (CNT) with the cryogel scaffold. A) Example of highly CNT-concentrated anisotropic scaffold. B) Example of the alignment of the CNT clusters White dot line shows the pore directionality, Scale bar = 100 µm C) Scanning electron microscopy of a CNT.

4.1.3 Generation of PDMS molds for cryogel fabrication

Two different set-ups were optimized to fabricate cryogels depending on the tissue we wanted to engineer. Every tissue has its specific requirements, so the fabricating set-up, the biomaterials used, the material concentration, and many other variables changed to acquire the needed scaffold properties. Both cryogels were cast inside a polydimethylsiloxane (PDMS) molds with specific conditions for the generating of the desired cryogel structure.

4.1.3.1 Random pore architecture set-up

For pancreatic scaffolds or random pore scaffolds, the mold was cylindrical, with a diameter of 10 mm and a height of 1 mm. Different heights were studied, but more than 1 mm height was too much as it has an excessive volume/area ratio for the desired amount of pancreatic islets/pseudoislets seeded inside. For fewer heights, the demolding and manipulation of the cryogels were complicated. Finally, the set-up was optimized by placing the PDMS mold in the middle of two cover slides, a squared 24x24 mm at the bottom and a 12 mm diameter. For filling the prepolymer solution, small entries were made in the cylinder sides, so filling the mold by capillarity with the prepolymer solution was the easiest way (Figure 33). With this molding

set-up we could achieve a easy to fabricate method with high reproducibility and cryogels with desired pore architecture, dimensions and mechanical stability.

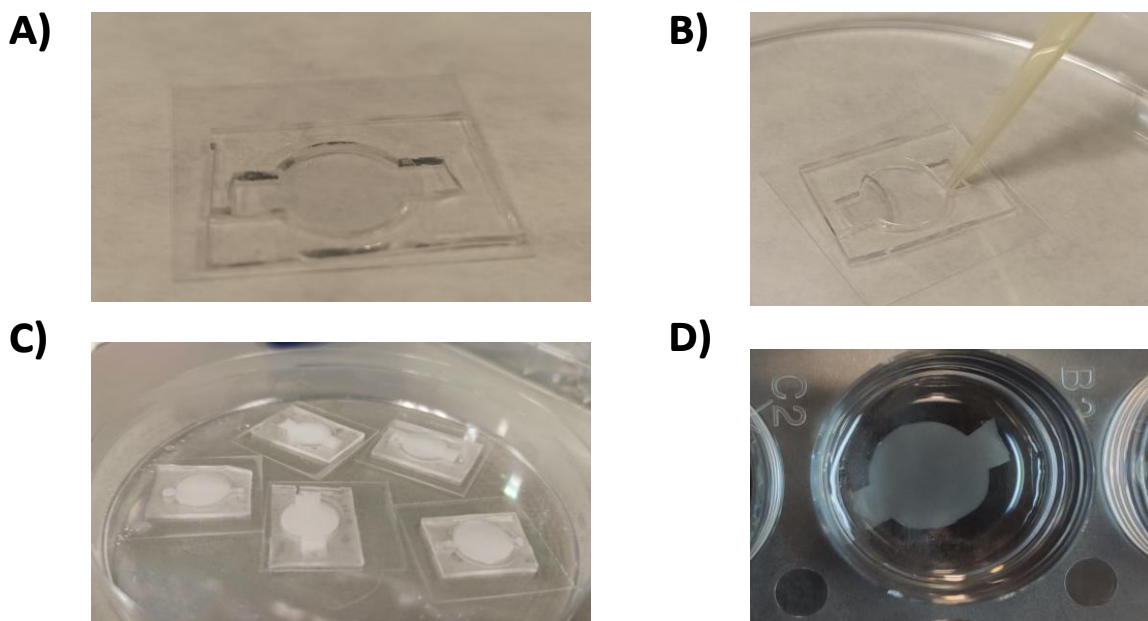


Figure 33: Random pore architecture cryogel fabrication process. A) PDMS mold, B) Filling the mold with the prepolymer solution. C) The mold was placed at -20°C freezer for an overnight. D) Final image of the cryogel after demolding.

4.1.3.2 Anisotropic pore architecture set-up

For the skeletal muscle scaffold or anisotropic pore scaffold, a different set-up was prepared. Differently, in this approach, we needed to generate a temperature directionality. After determining casting temperature placing the cryogels over carbonic ice, different molds and approximations were studied. The use of 1 mm high molds were not enough to generate a proper anisotropic distribution, so first step was to generate higher molds. Here, the mold was cylindrical with 6 mm in diameter and 6 mm in height (Figure 34). This taller scaffold is necessary to generate the ice nucleation and the tubular ice growing for generating the anisotropic structure. This height was enough to generate the anisotropy. However, not a straight-forward architecture was achieved. To improve the freezing directionality, a polypropylene thermal isolator was placed around the PDMS mold, and a metallic sheet was placed over the carbonic ice to homogenize temperature and get more replicable scaffolds.

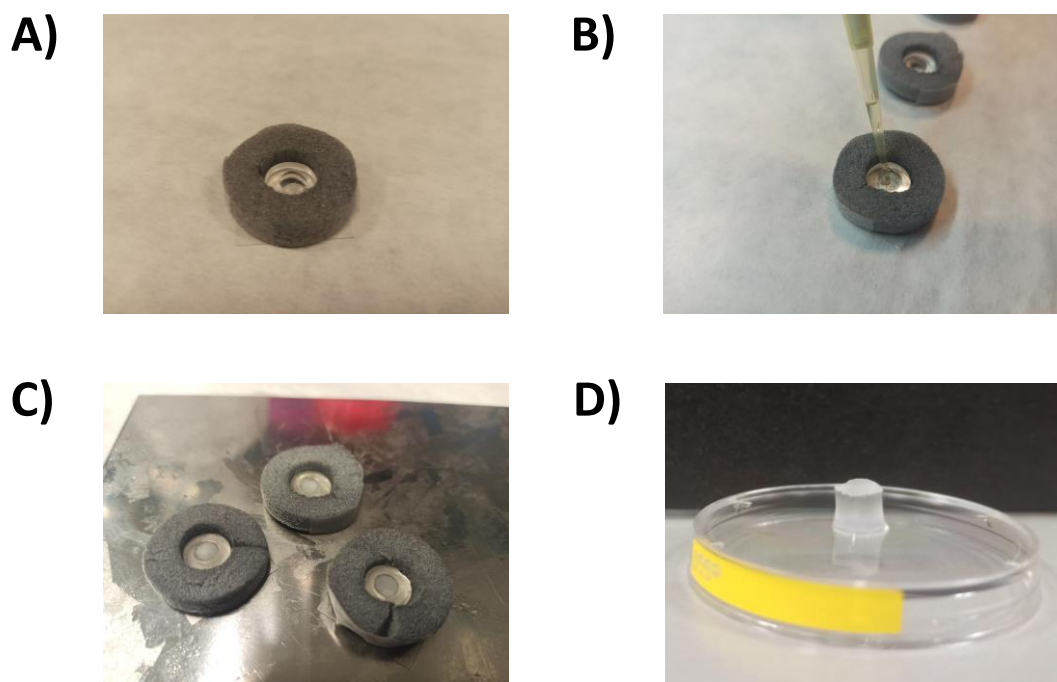


Figure 34: Anisotropic pore architecture cryogel fabrication process. A) PDMS mold, covered with a thermo isolator. B) Filling the mold with the prepolymer solution. C) The mold was placed on a metallic sheet over carbonic ice. D) After 1 hour in carbonic ice, and overnight at -20°C freezer, cryogel can be demolded and sliced.

4.2 CRYOGEL CHARACTERIZATION

Once we optimized the cryogel fabrication process, the proper pristine biomaterial concentrations, the temperatures we needed, and optimized the fabrication set-ups, we could characterize scaffold properties, such as pore sizes, stiffness, swelling, or diffusion rate. These scaffold properties has high relevance as are key factors for the proper tissue generation.

4.2.1 Pore diameter

We analyzed the pore diameter and architecture to understand how all the parameters mentioned above affect the cryogels. This variable may be a limitation in the pancreatic approach as we need a specific pore size distribution to seed or generate pancreatic tissue. Moreover, the pores should have similar sizes as physiological pancreatic islets to generate pseudoislets in an approximate range of sizes compared to in vivo pancreatic islets,

ranging from few micrometers up to 200 μm approximately [169], [170]. The biggest pores possible for the skeletal muscle tissue are needed to ensure the maximum cell infiltration while maintaining the anisotropy and the scaffold's mechanical stability.

4.2.1.1 Random pore quantification

The first variable we checked is the variability of the pore size when material concentration fluctuates. By fabricating cryogels with the fibers stained, we could quantify the minimum diameter of each pore. Confocal images were taken with a confocal microscope to quantify the pore diameter. Different images of pores in different depths of different cryogels were acquired and quantified. ImageJ software was used to analyze the images. Firstly, images were thresholded into black and white. After, all the pores were reconstructed manually to avoid miscounting of the diameters. Finally, MinFeret's ImageJ was quantified. MinFeret is the closest distance between two diametrical points of a pore. The main reason for analyzing MinFeret instead and typical diameter is because this distance is the limitation threshold to seed pancreatic cells.

First different CMC cryogels were analyzed (Figure 35A). Here, we observed that pore disparity is big, ranging from few micrometers to 100-200 μm depending on the material concentration. In 5% CMC cryogel, the pores range between few microns up to 100 μm . By decreasing the material concentration, this pore distribution enlarges. In 1% CMC cryogel maximum pore sizes reaches 150 μm , in 0,5% up to 200 micrometers and in 0,25% the porosity reaches almost 250 μm . Even some pores bigger than 300 μm were found (Figure 35B). Despite the enlarging of the pore distribution, its mechanical stability decreases when material concentration decreases. Indeed, 0,25% and 0,5% CMC cryogels had good porosity distribution, but the fabrication success ratio was low due to its low material percentage as many of the scaffolds break when demolding, not accomplishing the easy-manufacturing requisite. Knowing the sizes of the pancreatic islets, we determined that 1% CMC cryogel has the pore distribution that fits better with our needs.

After setting the amount of material at 1% for random porosity, the gelatin integration was studied. Here, we fabricated different 1% cryogel with different gelatin:CMC ratios (Figure 35C). We could appreciate that the porosity range did not vary significantly if the material concentration remains

constant. We can also appreciate that all the pore distribution ranges from few microns to 150 microns approximately, as expected (Figure 35D). We can conclude that gelatin incorporation did not affect the pore range distribution while the material concentration remains constant.

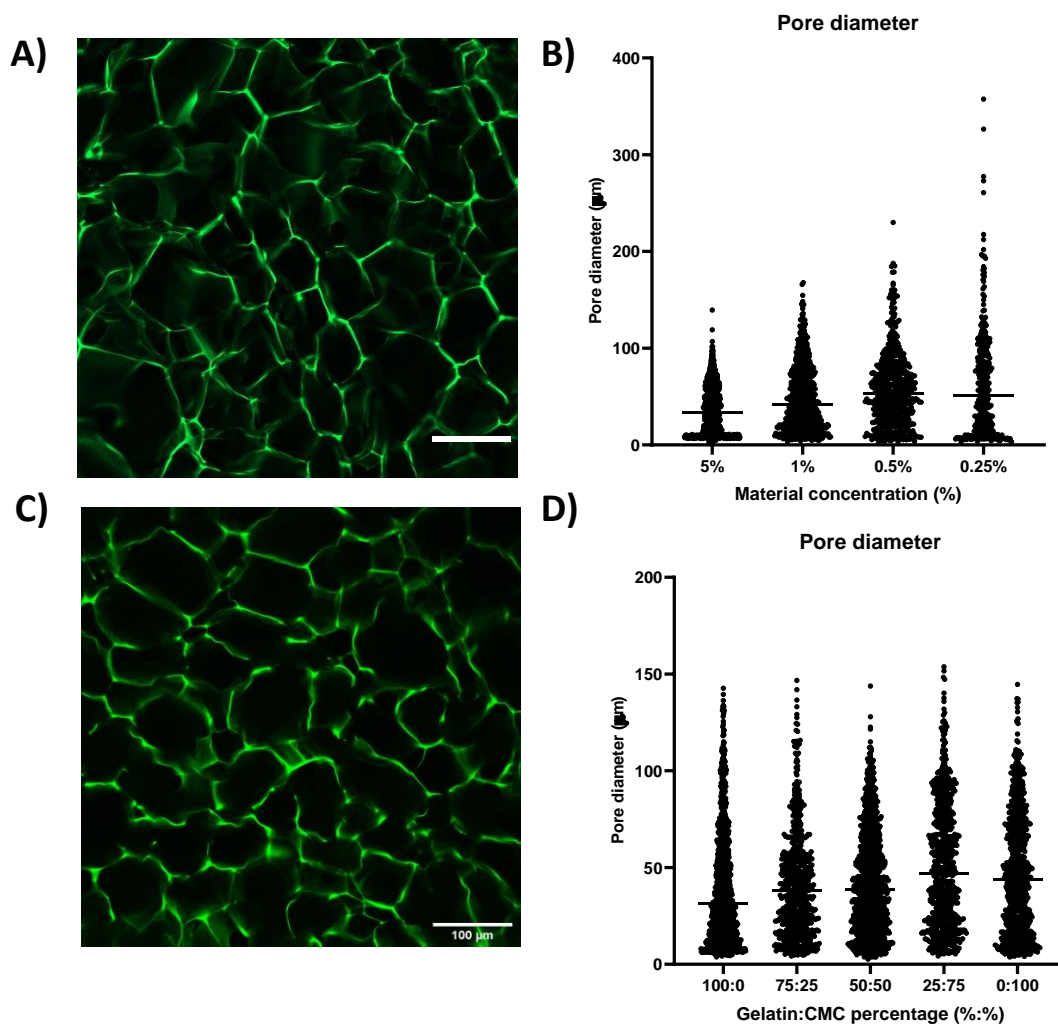


Figure 35: Pore quantification for the random pore architecture crygel. A) Confocal image of the 1% CMC crygel stained with aminofluorescien. Scale bar = 100 μm . B) Pore distribution of different material concentrations. C) Confocal image of the 1% gelatin crygel, with the fibers stained in green. Scale bar =100 μm . D) Pore distribution of different 1% crygels with different percentages of gelatin and CMC.

4.2.1.2 Anisotropic scaffold pore quantification

We take the previously acquired knowledge for the skeletal muscle approach and directly fabricated different gelatin:CMC cryogels, from 1% to 5% total material concentration. In here, we wanted the pores as big as possible, implying the less amount of material possible. Nevertheless, lower percentage cryogels were not stable enough to manipulate it, as cryogel collapses as fibers were not stiff enough to support the structure. Thus, 3% material concentration (2% gelatin:1% CMC) was the chosen material proportions, as the lower material concentration but mechanically stable

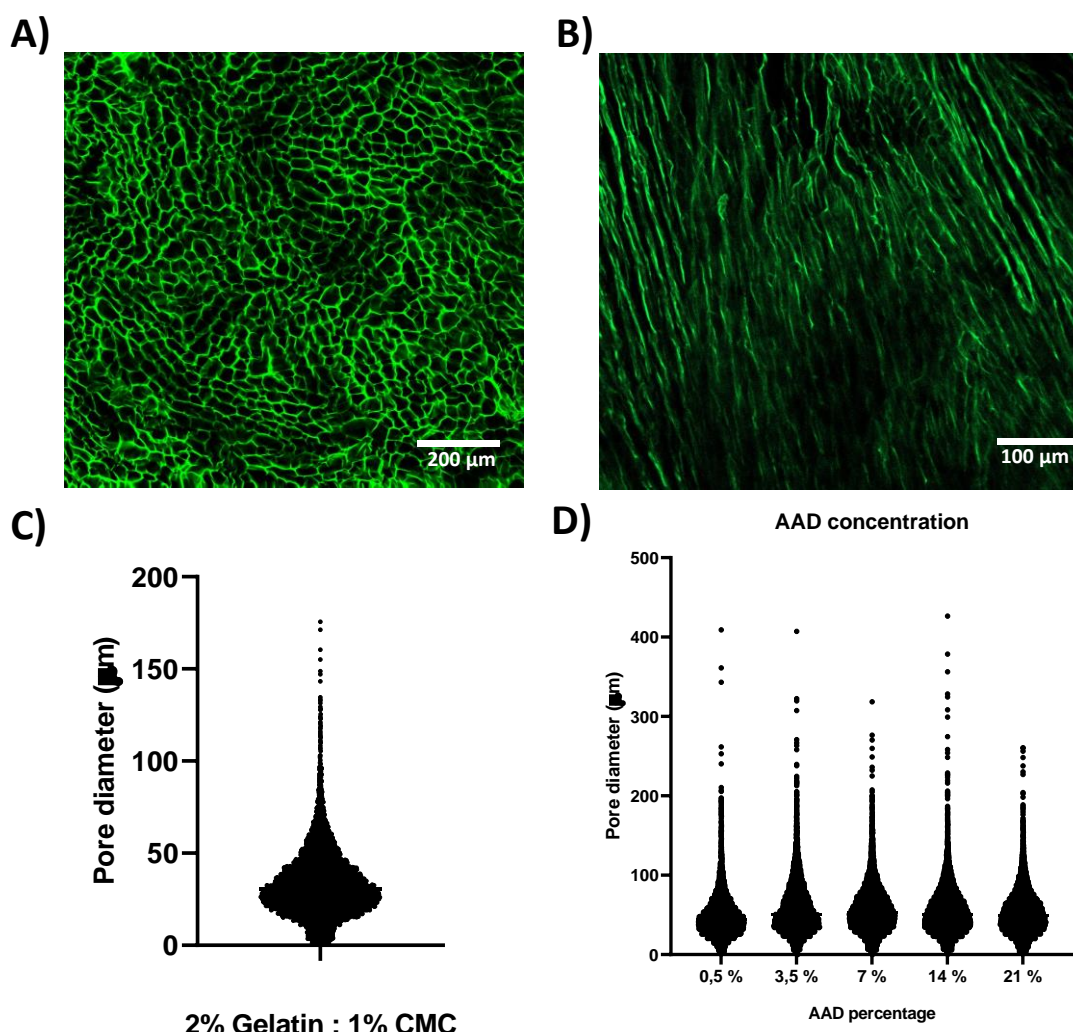


Figure 36: Pore distribution for the anisotropic approach. A) Confocal image of the anisotropic pores. Top view where the tubular structure can be appreciated. B) Confocal image of the anisotropic structure of the cryogel. Side view. For this, cryogel was sliced vertically. C) Pore distribution for 3% cryogel (2% gelatin:1% CMC). Most of the pores are found between 30 and 75 μm. D) Different concentrations of AAD were tested. Pore distribution did not change.

cryogel (Figure 36A-B). The percentage of gelatin was determined because we wanted to be sure to promote cell adhesion in the cryogel. By analyzing the pore distribution, we can observe that small pores are always present. Interestingly, most of the pores are in a specific range between 30 and 75 μm in diameter (Figure 36C). This pore range is appropriated to seed the cells over the cryogel as it allows cell infiltration, cell growth, and migration of the cells. Moreover, we could prove that cells were found through the whole cryogel. To note, this pore size should allow the myotube formation as myotubes are not bigger than 30 μm in width [165], [171], [172].

Despite 3% Gelatin:CMC cryogel has promising pore distribution, we wanted to know if this could be enlarged for better cell infiltration. Here, we changed AAD concentrations to assess the AAD's effect during the crosslinking process. For this, different 3% stained cryogels with different AAD concentrations were fabricated. As we could quickly appreciate, mechanical stability did not change, remaining stable even when AAD was decreased. After analyzing pores of all the AAD concentrations, we could appreciate that no significant porosity changes were achieved (Figure 36D). Finally, knowing that the myotubes are in a similar range to our tubular pores, the final concentration of material was chosen as 3%, without changing the initial concentration of AAD for the skeletal muscle pore approximation.

4.2.1.3 Scanning electron microscope (SEM)

Scanning Electron Microscope (SEM) images were taken to support previously confocal imaging and pore acquisition and to have a general overview of how is the internal structure of the cryogels. SEM images were acquired after dehydration and critical point dry. In the random pore approximation, can be observed that pore distribution is heterogeneous, and pores from many different sizes were formed (Figure 37), supporting the previous data shown (Figure 35-Figure 36). This wide variance of pore size, similar to the size of pancreatic islets, should help the islets infiltration and the generation of physiologically resemblance pseudoislets.

On the other hand, in anisotropic cryogel, scanning electron microscope images showed this same distribution, with less variability among all the pores. Also, we can appreciate the tubular shape of these pores. This feature is an essential to engineer skeletal muscle tissue, as skeletal muscle tissue needs high alignment and super organization to differentiate from myoblast

to myotubes. With this technique, we achieved a good pore distribution and pore sizes that allows a good infiltration of the cells. Moreover, the pores of the cryogel have a high alignment that enhances the fusion and differentiation of the skeletal muscle myotubes.

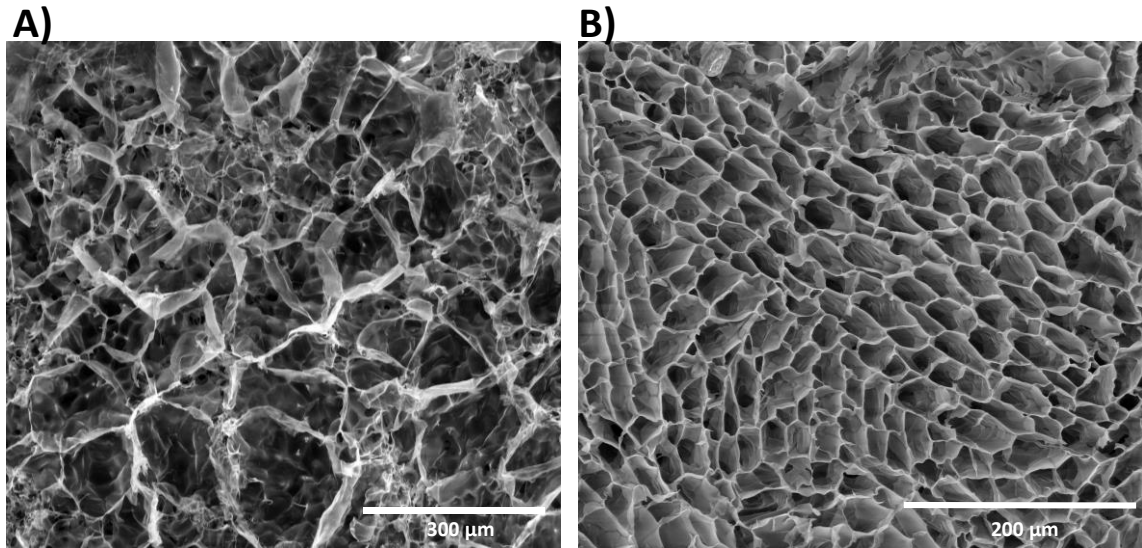


Figure 37: Scanning electron microscope images from both pore architecture approaches.
 A) Random pore approach. Scale bar = 300 μm . B) Anisotropic pore architecture approach. Scale bar = 200 μm .

4.2.2 Stiffness

Mimicking tissue's physiological environment is another essential property to consider when designing scaffolds for tissue engineering. Every tissue has its specific and characteristic environments. Thus, the resemblance with the *in vivo* ECM is an essential feature for proper tissue formation. ECM has the objective to support cells and plays a vital role in cell viability and functionality by doting the cells of specific biochemical and physical signals [173]. As cells behave differently when scaffold stiffness changes [174], [175] obtaining scaffold stiffness resembling the *in vivo* is fundamental for tissue engineering. A compression assay was performed to analyze the bulk stiffness of the cryogels. Young's modulus was the curve's slope between 20% and 30% of strain compression.

4.2.2.1 Random pore scaffold

For the random approach, 1% CMC cryogel has a stiffness of $0,66 \pm 0,08$ kPa. Besides we knew that gelatin did not change significantly the pore distribution of the cryogels, we wanted to know if the incorporation of it, can change other important properties as the stiffness. For this full gelatin cryogel and 50:50 gelatin:CMC cryogels were studied. In here, we could observe that gelatin random cryogel is much softer than CMC cryogel ($0,27 \pm 0,13$ kPa). For gelatin:CMC cryogel, as expected, the stiffness is in-between its raw material cryogels ($0,5 \pm 0,09$ kPa) (Figure 38). To note, CMC stiffness achieved correlates well with the proper stiffness defined for pancreatic tissue. As the pancreas is a soft tissue, its stiffness ranges from 0.1 kPa to 10 kPa [176].

Moreover, pancreatic cells seem to respond properly to this low stiffness interval, as cells can increase insulin mRNA expression and glucose sensitivity [124]. In other approaches, the stiffness of native healthy pancreas was set as approximately 1 kPa when measured by magnetic resonance elastography (MRE) [177], [178], a similar value with the scaffold stiffness achieved. Also,

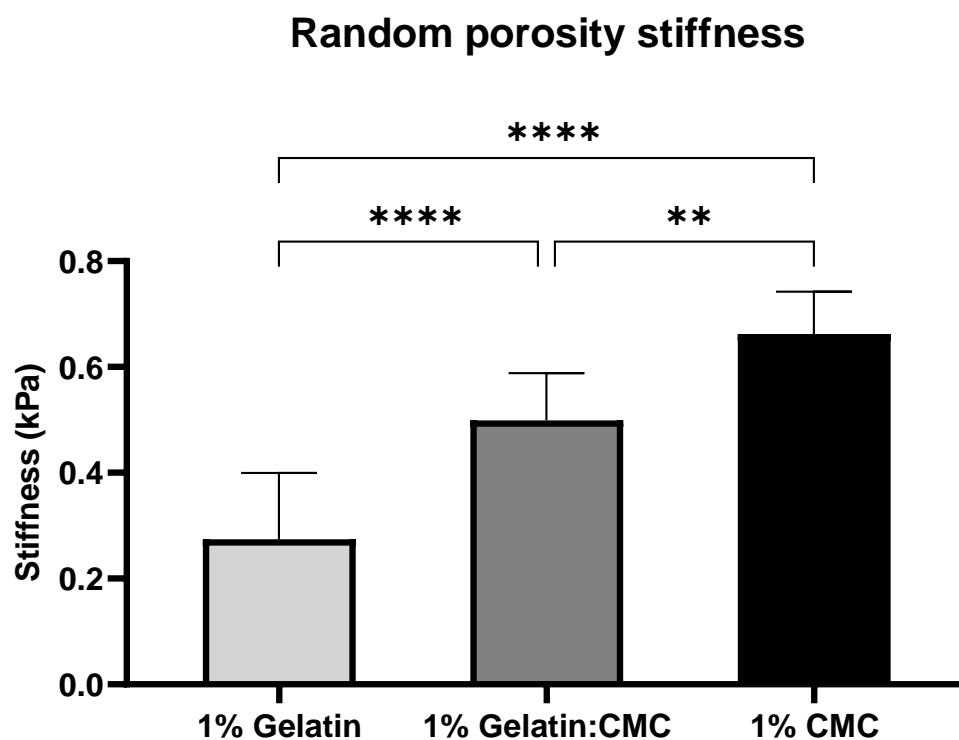


Figure 38: Stiffness change when different materials were used, despite percentage remains constant. CMC appears to be more stiffer than the gelatin, being closer to physiological results. Results are mean \pm SD. * p -value = 0.05

soft scaffolds favor cell coalescence and preserve the cluster-like organization, while in stiff substrates, the extracellular-cell interactions cause cell scattering and loss of islet-like structure [179].

4.2.2.2 Anisotropic pore scaffold

The anisotropic cryogel has stiffer properties than the random cryogel because the increasing of material concentration and fiber architecture. Moreover, because of its anisotropic structure, stiffness can vary depending on the axis directionality that the compression is applied (Figure 39A). If the compression is applied in the same axis that the pores are aligned, the Young modulus is $11,21 \pm 6,22$ kPa. If the compression is applied perpendicularly to these pores, the stiffness decreases to $6,52 \pm 3,74$ kPa (Figure 39B). This happens because, in parallel compression, fibers oppose resistance to this compression. However, in perpendicular compression, some empty spaces from the pores that allow the cryogel to compress. Same tendency can be observed in the CNT-doped cryogels ($9,23 \pm 4,45$ kPa vs $3,90 \pm 2,70$ kPa). Comparing the compression directionality of CNT-doped against non-doped cryogel, we can observe that the values remain similar (Perpendicular: $11,21 \pm 6,22$ kPa and Parallel: $6,52 \pm 3,74$ kPa), meaning that the addition of CNT did not significantly affect the stiffness of our cryogel. Remarkably, the

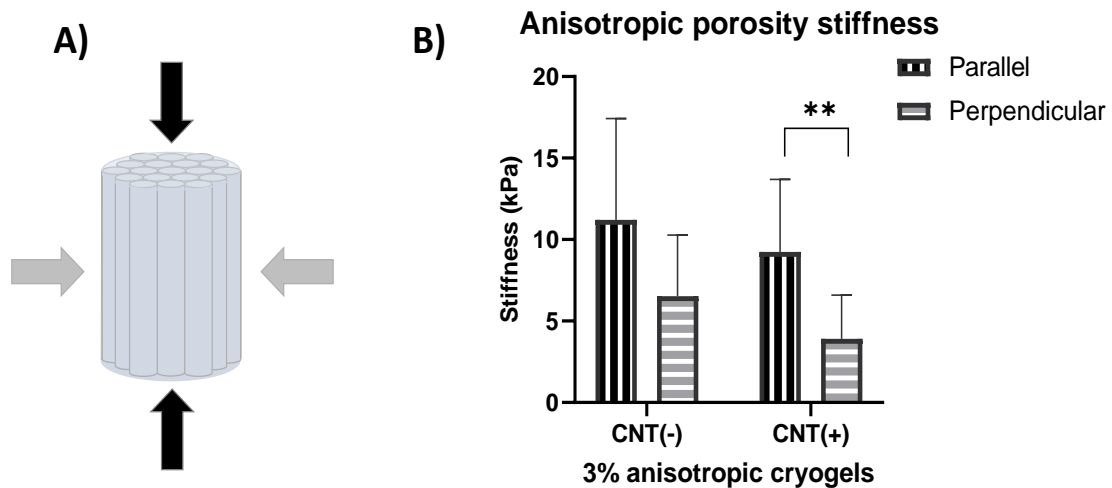


Figure 39: Stiffness results for anisotropic pore architecture scaffolds with and without carbon nanotube incorporation. A) Compression directionality scheme. B) Stiffness results. Carbon nanotubes did not change the stiffness. Moreover, stiffness changes depending the compression directionality, indirect measurement of anisotropy. Results are mean \pm SD. * p -value = 0.05

stiffness of the cryogel shows *in vivo* similarity mechanical properties [174], [180] to the skeletal muscle ECM, which is around 12 kPa.

4.2.3 Swelling

4.2.3.1 Random pore scaffold

Another feature that we wanted to improve is the diffusion of nutrients through the scaffold. Swelling is the water uptake capability of a hydrogel, an indirect measurement of pore interconnectivity [181]. The pore diameter distribution and the high pore interconnectivity, typical of cryogels, enhances this swelling property [51]. After only 24 hours, our cryogel reached equilibrium because its high interconnected porosity structure (Figure 40A). Swelling ratio of CMC cryogels was $98.14 \% \pm 0,32$ and $96.30 \pm 0.38 \%$ for gelatin cryogel. As happens with the stiffness, the 50:50 gelatin:CMC scaffold has an intermediate swelling ratio of $97,17 \pm 0,34 \%$ (Figure 40B). Although this property is higher in CMC cryogels than in gelatin, both ratios are higher than 95%. This high percentage indicates that the scaffold's structure is highly interconnected, as PBS could colonize all the scaffold structure minutes after to submerge the scaffolds in.

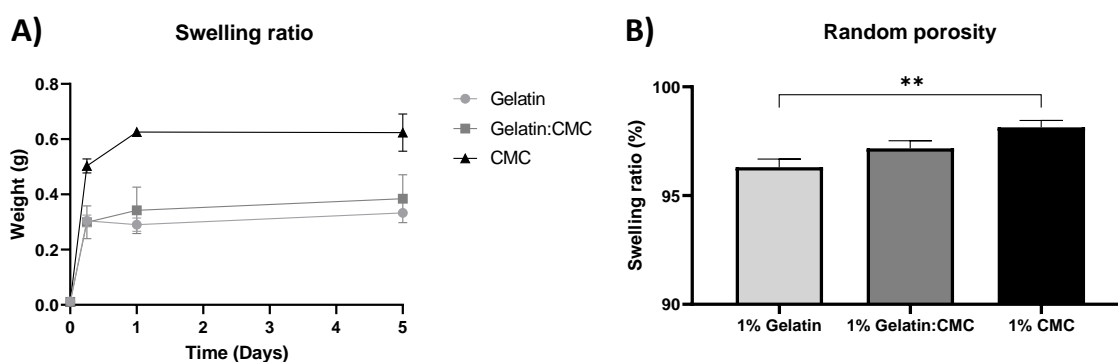


Figure 40: Swelling property of the random pore scaffolds. A) Change in weight of the cryogels during 5 days. Equilibrium is reached after 1 day. B) Values of the swelling ratio of different cryogels. Results are mean \pm SD. * p -valor = 0.05

4.2.3.2 Anisotropic pore scaffold

In the anisotropic scaffold, this swelling ratio is inferior compared to the random scaffold, probably due to less pore interconnectivity. However, the water uptake capability remains higher than 80% ($84,81 \pm 3,52$ %), indicating that the anisotropic cryogel also has good porosity and good interconnectivity. On note, the addition of CNTs into the cryogels did not affect the swelling characteristic ($81,58 \pm 2,78$ %) (Figure 41)

This water uptake capability found in both cryogel approaches indicates high pore interconnectivity, which leads to high nutrient diffusion rates. However, to understand better how solvents diffuse among the random scaffold, diffusion and permeability test were performed.

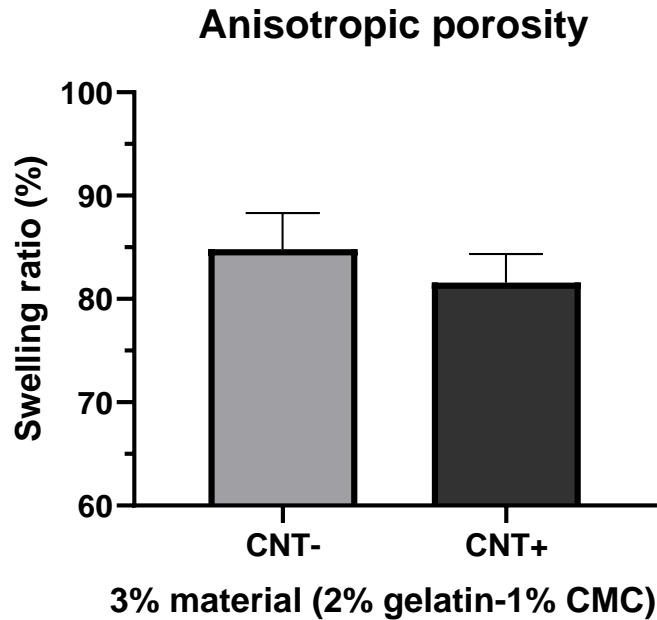


Figure 41: Swelling ratio of the anisotropic pore structure approach. Carbon nanotubes did not change water uptake capability of the anisotropic cryogels. Results are mean \pm SD. * p -value = 0.05

4.2.4 Diffusion

Nutrient diffusion is an essential feature for scaffolds in tissue engineering and even more in volumetric scaffolds or tissues. Pancreatic islets have to continuously sense the amount of glucose in the blood [182]. This triggering

or the stop of secreting insulin should be done faster to avoid hypoglycemia or hyperglycemia. For this, checking how the scaffold allows diffusion is a critical point to consider. Although swelling can approximate how a liquid diffuses through the scaffold, we perform a small assay to support these results. Here, 3 different conditions were prepared: CMC cryogel, gelatin cryogel, and a single transwell as a control. Using aminofluorescein by its easy colorimetric read-out, we observe how it passes through the cryogels among time.

In this experiment, we could appreciate that the fluorescein diffuses faster in the transwell alone as it reaches equilibrium earlier (Figure 42). In comparison, cryogels permeates lower, but gelatin and CMC cryogels reached equilibrium equally after 240 minutes. Moreover, since the first acquisition at 3 minutes, aminofluorescein is already found at the bottom compartment, meaning a fast permeation.

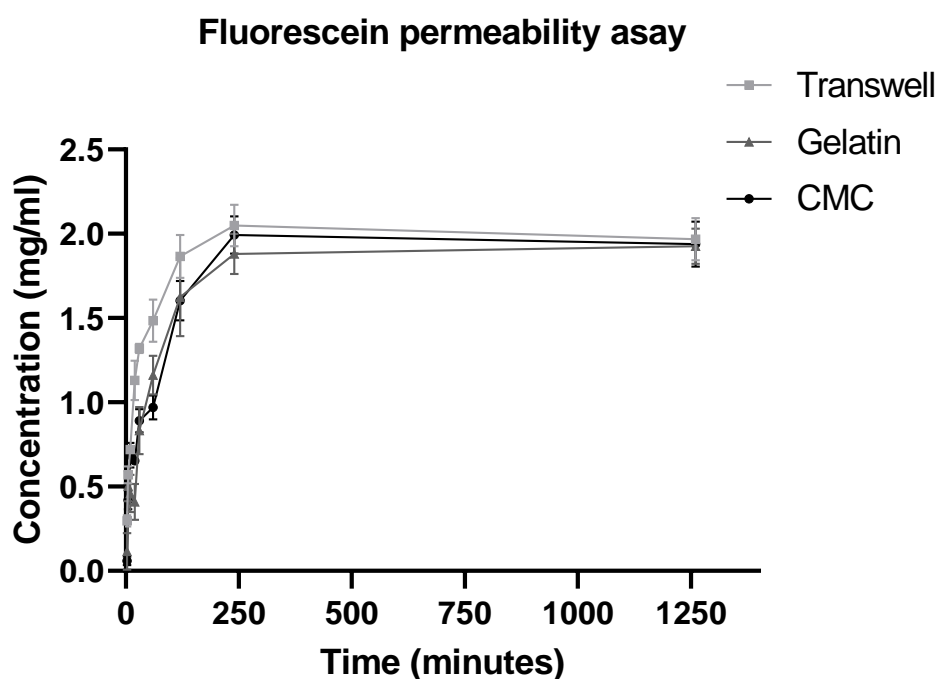


Figure 42: Permeability assay profile. Concentration of fluorescein that passed through the cryogel scaffold at consecutive times. Results are mean \pm SD.

Also, in this experiment, the permeability of the scaffold may be set. Following the permeability equation and taking the linear part of the curve (from 0 to 30 minutes), we could set the scaffold permeability as 0,42 mm/s in CMC cryogels and 0,34 mm/s in gelatin cryogels. This difference in diffusion indicates that CMC cryogels are more permeable than gelatin cryogels [51]. This rapid equilibrium reached shows that the cryogel has barely any

interaction as a diffusion barrier. This high permeability ensures that we generate a microporous cryogel able to sustain cells in all the scaffold's depths with no hypoxia or nutrient problems. Moreover, it shows that generating pancreatic tissue inside the cryogel should not limit insulin secretion's fast triggering.

4.2.5 Conductivity

Skeletal muscle tissue can be stimulated by electrical pulse so it can mature faster [183] or contract when fully mature bundles are formed [184], [185]. Unfortunately, most of the scaffolds used for tissue engineering have low conductivity, and therefore this electrical stimulation to enhance myogenic maturation is poorly effective. To increase the conductivity of our scaffolds, we incorporate carbon nanotubes (CNTs). We expected to generate a more conductive interface with this incorporation,, so improving Electrical Pulse Stimulation (EPS) for better myogenic maturation.

Dra. Luisa Neves performed measurements at Multiwave facilities. In there, they have an equipment that allows measuring the conductivity and the dielectric properties of the samples by tapered transmission line method from a cylindrical scaffold (Figure 43A-B). However, the range of frequencies they could measure goes from MegaHertz to GigaHertz. After analyzing the results, we could observe that from 1×10^7 to 2.5×10^8 Hz, the conductivity ranges are around 1 S/m for both cryogels, without and with CNTs. However, by increasing the frequency, the conductivity of CNT cryogels increases more than the ones without CNT incorporated. The CNT-doped scaffolds have higher conductivity in higher frequencies, where it reaches 5,71 S/m. On the other hand, cryogels without CNTs has a conductivity of 4,08 S/m (Figure 43C). The conductivity achieved with our scaffolds is similar or higher to other scaffolds used for the maturation of myotubes [186], [187].

With this technique, we could observe an improvement in the electrical properties of the CNT-doped scaffold compared to the non-doped CNT scaffold, meaning that the addition of CNT has a positive effect on electrical conductivity. In previous electrically stimulated scaffolds for skeletal muscle maturation studies, conductivities from 10 mS/m to 6,4 S/m were achieved, and maturation of the tissue was enhanced [186], [187]. In our case, we can not only enhance the electrical properties of the scaffold, but we are also able to modulate the frequency and so modulate the conductivity of these

scaffolds. In this way, we can get different conductive values, but always in the range of previous studies. To note, the conductivity could also be modulated by changing the concentration of CNT [188]. However, there is a significant disparity in the literature about the ideal conductivity of a scaffold to engineer and enhance myogenic differentiation. This disparity gives a real advantage to our scaffold as we can modulate the conductive properties of it. The conductivity achieved in our cryogels may make them suitable for many EPS needed assays as maturation or even contraction of skeletal muscle tissue.

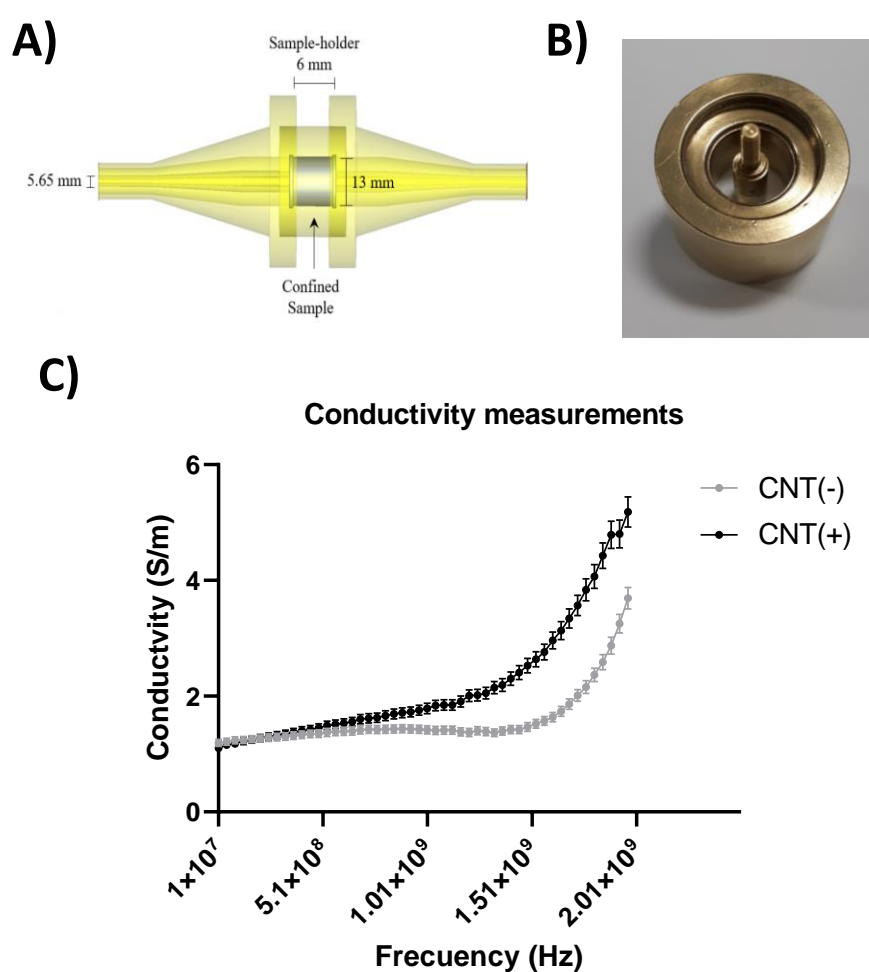


Figure 43: Conductivity measurements. A) Scheme of the sample holder used to perform the measurements. B) Picture of the sample holder. C) Conductivity measurements. When increasing the frequency, scaffold conductivity improves. The addition of CNT elevates the conductivity of the scaffold. Results are mean \pm SD.

4.3 PANCREATIC TISSUE

For pancreatic tissue, two different approximations were studied. First, a CMC scaffold was designed to support mouse primary pancreatic islets. To this aim, pancreatic islets were manually seeded inside the cryogel. However, due to some scaffold limitations, (e.g. very similar size distribution of the cryogel pores and the pancreatic islets) this approximation was ineffective.

To generate pancreatic tissue, we take profit from the aggregation ability of beta-cells. We generated a scaffold that allow the formation of controlled cell aggregations. These pseudoislets are morphologically resemblant to the in vivo pancreatic islets. Moreover, after forming, these pseudoislets will be anchored inside the scaffold.

4.3.1 Pancreatic islets

Pancreatic islets were obtained from Institut d'Investigacions Biomèdiques Agust Pi I Sunyer (IDIBAPS). Mouse pancreatic islets were isolated from 8-12 weeks-old C57BL/6 mice and were allowed to recover for 24h at 37°C and 5% CO₂ in RPMI-1640 medium with 11 mM of glucose and supplemented with 10% FBS (v/v), 2 mM glutamine and 1% penicillin/streptomycin.

4.3.1.1 Islet seeding

Before seeding, cryogels were dried at room temperature for 20 minutes. For islets seeding, 30 islets from different ranges were picked up within 20 µl of 11mM glucose RPMI-1640 medium. After seeding, we waited 20 minutes so the islets can infiltrate inside the scaffold. While waiting, constant monitoring of the infiltration of the pancreatic islets was done with a magnifying glass (Figure 44A). In case that the pancreatic islets did not infiltrate properly, reseeded of the islets or weak medium flow turbulences were performed to help the islets infiltrate inside the scaffold. These steps were necessary because not all the islets find a pore with bigger diameter to infiltrate inside the scaffold.

As pancreatic islets present a similar range in size to the 1% CMC cryogel porous, we performed the initial experiments with this material concentration. Although some islets were found inside the cryogel (Figure

44B-D), having the same pore size-islet diameter distribution entailed some difficulties. The main problem was the low infiltration ratio for bigger islets due to probabilistic, as bigger islets can only infiltrate through bigger pores. Besides, some of the smaller islets pass through the cryogel without

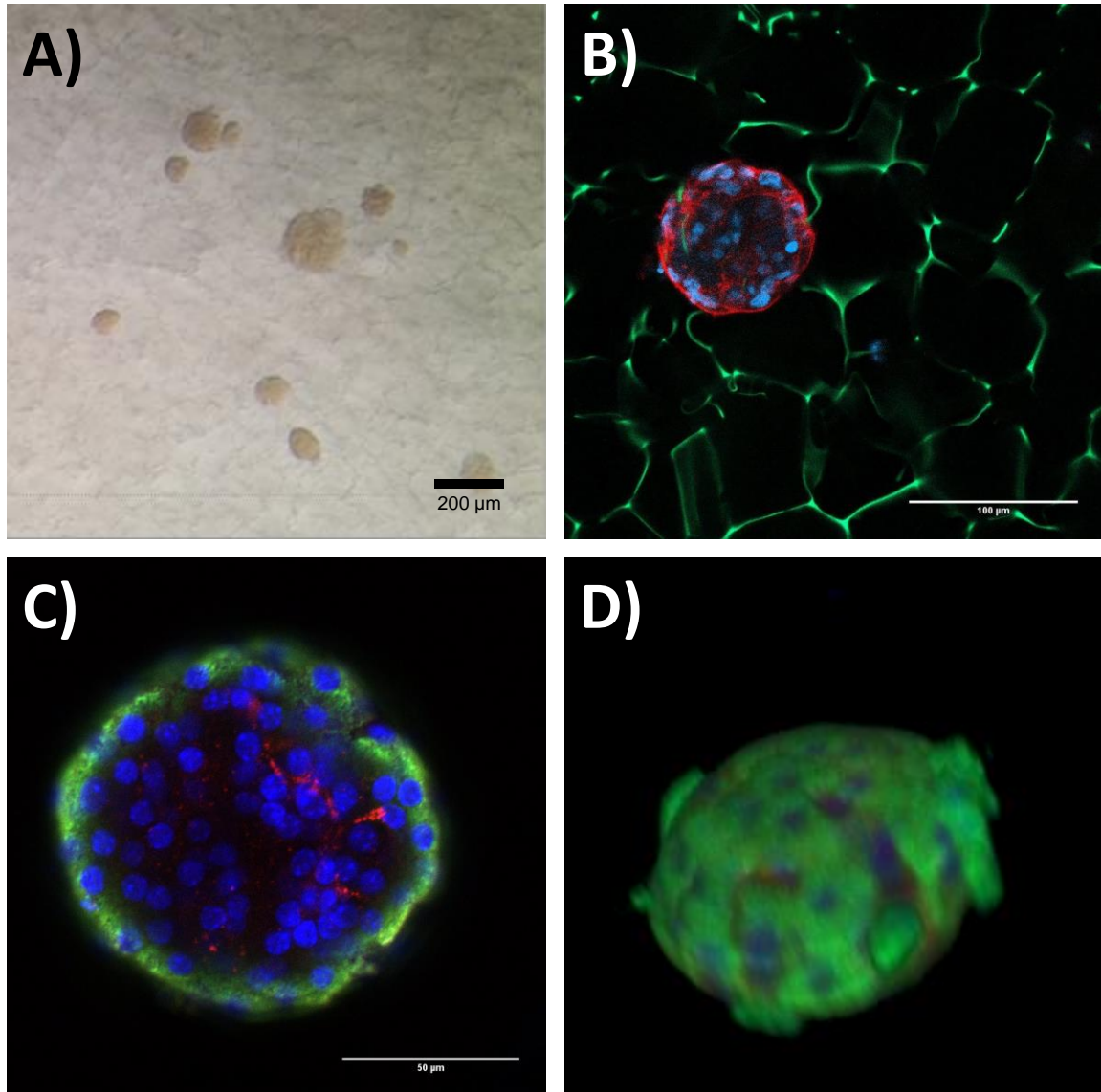


Figure 44: Pancreatic islets in interaction with the cryogels scaffold. A) Images of the magnifying glass where the pancreatic islets are just seeded over the cryogel. Scale bar = 200 μm . B) Pancreatic islet inside the cryogel fiber matrix stained in green. Nuclei are stained in blue and actin in red. Scale bar = 100 μm . C) Image of the center of a pancreatic islet immunostained for insulin (green) and caspase-3 (red), a preapoptotic marker. Nuclei are stained in blue. Scale bar = 100 μm . D) 3D volumetric reconstruction of a pancreatic islet, where can be observed that the spherical architecture of the pancreatic islet is maintained. Stainings are nuclei (blue), actin (red) and insulin (green).

anchoring in it. These two problems act as a limitation to have pancreatic islets anchored inside.

4.3.1.2 Bilayer cryogel

A bilayer cryogel was purposed to solve the small pancreatic islet retention. This bilayer cryogel is formed by a denser layer at the bottom, with 5% CMC cryogel, and over it, generate 1% CMC cryogel with the appropriate pore morphology. With this approach, we could not achieve a good infiltration of bigger pancreatic islets, but we could avoid losing the smaller ones. The point of this approximation is that small pancreatic islets ($<75\ \mu\text{m}$) are necessary for good insulin regulation, as they have higher beta-cell percentage and higher insulin secretion per volume than the biggest ones ($>150\ \mu\text{m}$) [189]. Moreover, large islets can easier suffer from hypoxia, therefore small islets may stay alive inside the cryogel for a longer time.

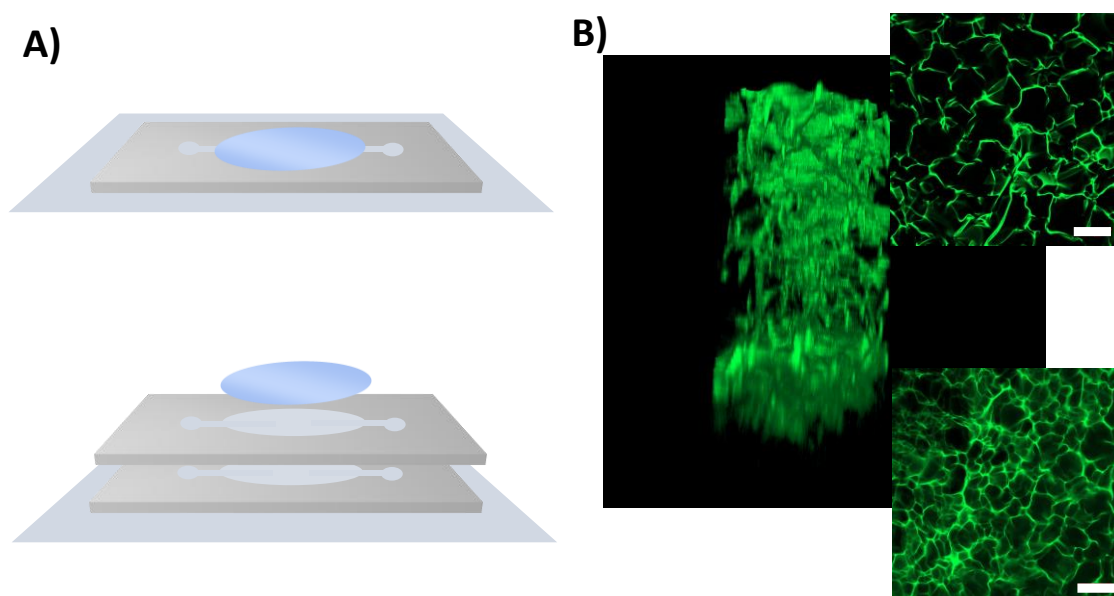


Figure 45: Bilayer cryogel approximation. A) Scheme of the fabrication of the bilayer cryogel. Following the normal protocol to fabricate cryogels, once the first dense cryogel was fabricated, another cryogel was fabricated above it. B) Confocal images of the fibers of the cryogel stained in green. A 3D reconstruction of the bilayer cryogel (left), where the different layers can be observed. In the right, two images of the denser cryogel (Bottom) and the normal cryogel (top). Scale bar = $100\ \mu\text{m}$.

The above-mentioned explained protocol for cryogel fabrication was followed to fabricate these bilayer cryogels. Briefly, 250 μm high 5% CMC cryogel was generated. In this case, before demolding, 500 μm high 1% CMC cryogel was fabricated over this first 5% cryogel (Figure 45A). Notably, 1% CMC cryogel fibers also mixed with previously fabricated 5% cryogel fibers, generating a very dense layer. After, the same protocol of washing and sterilizing was applied. 0,5% cryogel were also fabricated as a top layer to increase the big islet infiltration.

Different experiments were performed to prove that this approach was well fabricated and could retain small pancreatic islets. Firstly, images from both sides of the cryogel were taken. In these images, it can be appreciated that the bottom face of the cryogel is much denser than the upper face (Figure 45B).

Confocal images with pancreatic islets seeded inside were also obtained. In this case, we stained pancreatic islets with Dapi for nuclei and Rhodamine-Phalloidin for F-actin. Images were acquired at the "density" layer. Here, it can be appreciated that all the pancreatic islets are in the 0,5% cryogel (Figure 46), meaning that this layer retained the islets.

Despite the promising retention of smallest islets, the infiltration of large pancreatic islets is still a challenge to overcome. However, the technical difficulties in the fabrication of this bilayer cryogel did not compensate for the low improvement in small islet retention. Finally, for further

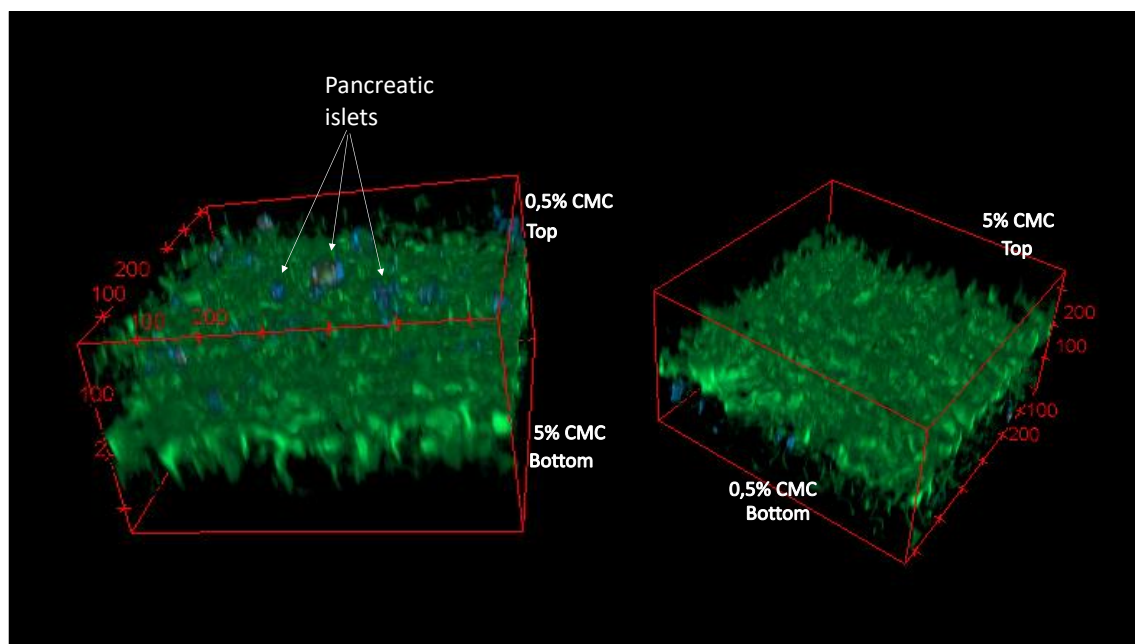


Figure 46: Confocal reconstruction of the bilayer cryogels. Here, we could appreciate that the pancreatic islets were retained in the bigger pore cryogel.

experiments, normal 0,5% cryogels were used. This decision was taken because we wanted to maximize cell infiltration inside the cryogel. The slight improvement in cell infiltration, prompted by the increased pore diameter distribution, compensate the technical fabrication limitations of the 0,5% cryogel. Moreover, the non-anchorage of the small islets could be improved by reseeding them.

4.3.1.4 Viability and functionality of islets

These experiments were part of ORGANSSENSE project done in collaboration with Institut d'Investigacions Biomèdiques Agust Pi I Sunyer (IDIBAPS) and Institut de Ciències Fotòniques (ICFO). Therefore, the following results were performed in collaboration with Dra. Ortega from our group, Dra. Rodríguez-Comas from IDIBAPS, and Dra. Yavas from ICFO. In this project a Localized Surface Plasmon Resonance (LSPR) sensing platform was combined with a microfluidic chip to monitor insulin secretion continuously. Beside this final goal, interesting results were obtained regarding viability and β -cell health of the pancreatic islets inside the cryogel. The results from this project that has a direct relevance with this thesis are following exposed.

Once determined the cryogel material and protocol, and optimizing the seeding method, in collaboration with Dra. Júlia Rodríguez-Comas, we checked the viability of the pancreatic islets inside the cryogels by analyzing pancreatic beta-cell identity markers and stress transcription factors by qPCR. *Pdx1* (pancreatic-duodenal homeobox factor 1), *MafA* (V-maf musculoaponeurotic fibrosarcoma oncogene homologue A), and *NeuroD1* (Neurogenic differentiation 1), three transcription factors essential for β -cell function were used to determine the β -cell health. *Chop/Ddit3* (C/EBP homologous protein / DNA damage inducible transcript 3), *Trib3* (Tribbles Pseudokinase 3) and *Atf3* (Activating transcription factor 3) were studied as cell stress markers. We found no differences regarding the expression of these markers when comparing the results from the pancreatic islets seeded inside the cryogels and the pancreatic islets in suspension. These results indicate that seeding islets inside cryogels did not affect either functionality or the viability of the cells, and no stress was produced during all the seeding process or consecutive culture days. All these data indicates that our cellulose-based cryogel provides a physiologically relevant environment and

facilitates the diffusion of oxygen and nutrients, demonstrating that islets do not suffered stress when integrated inside the CMC-scaffold (Figure 47).

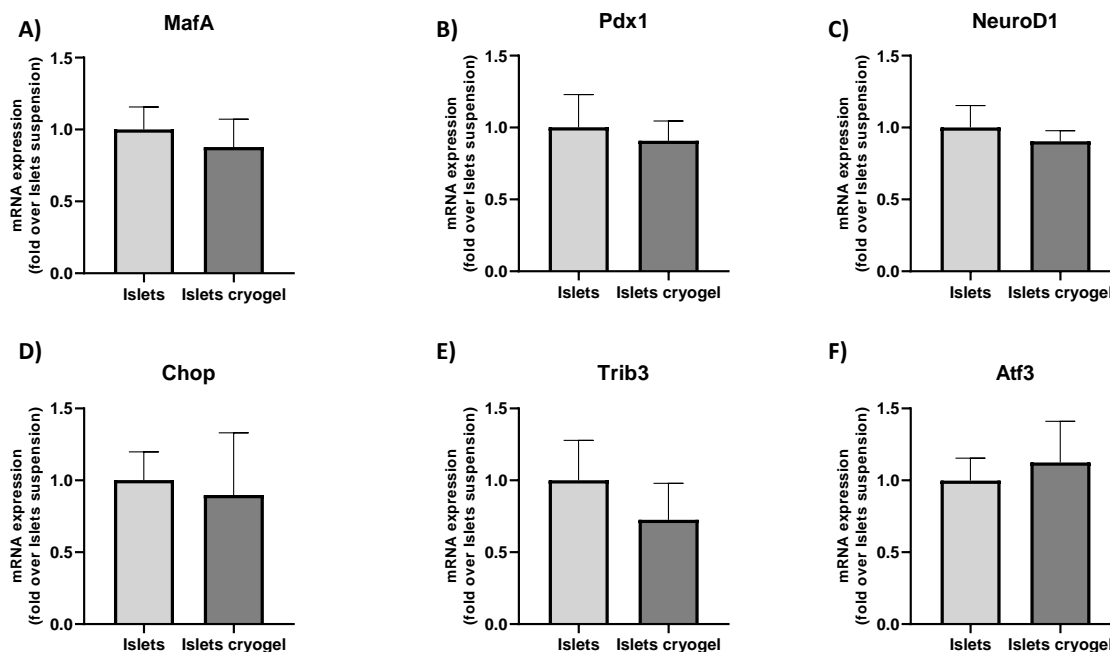


Figure 47: Gene expression of the pancreatic islets when seeded inside the cryogel vs in suspension. A-C) Beta-cell health markers. D-E) Cell stress cell markers. Results are mean \pm SD.

* p -valor = 0.05

Besides, a glucose stimulation insulin secretion (GSIS) assay in continuous flow was performed to check the cell functionality. For this experiment, a microfluidic chip developed by Dra. Maria Alejandra Ortega was used. The cryogel with pancreatic islets was placed inside the chip, and the cell culture medium was pumped continuously. Different glucose concentration mediums were recirculated with this set-up to see if pancreatic islets inside the scaffold could sense and respond accordingly to these changes of glucose (Figure 48). Initially, the islets were incubated with 2.8 mM glucose, which decrease the insulin secretory capacity of the β -cells, followed by incubation with 16.7 mM glucose that highly stimulates the insulin secretion of the islets. Here, 30 minute recirculated medium was stored and further quantified by conventional enzyme-linked immunosorbent assay (ELISA). Our results show that islets remain functional as they can sense the glucose in the medium and secrete insulin according to it. After proving that islets are functional in microfluidic conditions, real-time sensing was studied by using a Localized Surface Plasmon Resonance (LSPR) sensing platform in collaboration with ICFO and performed by Dra. Ortega and Dra. Yavas.

Briefly, LSPR sensing platform is an optic sensor with an array of gold nanorods where antibodies were attached. To quantify the amount of insulin, the refractive index is analyzed, so knowing how this shift displaces in different insulin concentrations, the amount of insulin of the experiment can be extrapolated. For GSIS assay, KRBH buffer was continuously pumped through the chip, and then flown inside the LSPR sensing platform. LSPR sensing chip has 8 different channels, so 7 cycles were determined for the experiment. Each cycle consists in 30 minutes of continuously pumped buffer. After the cycle, LSPR sensing channel was changed, so another cycle can be measured.

As expected, we could observe that islets seeded inside the cryogel responded to an increased glucose concentration in the medium, as insulin released was increased (Figure 48B). This study concludes that microfluidic technology and LSPR sensing platforms are valuable tools to sense small glucose changes in microfluidic conditions.

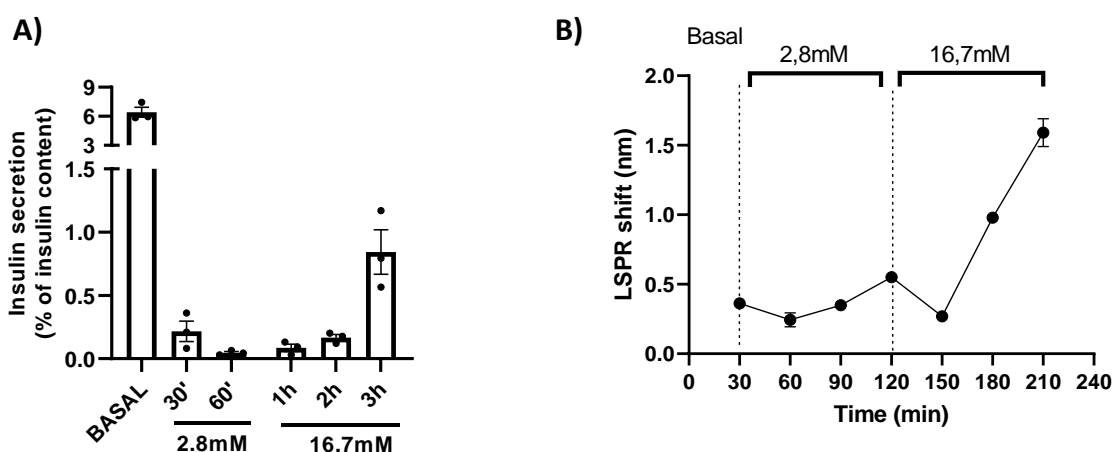


Figure 48: Insulin quantification from a GSIS assay using different sensing platforms. A) Non-continuous assay analyzed by sandwich ELISA. B) Continuous sensing using LSPR sensing platform. In both sensing platforms we could observed an increasing of insulin secretion when high glucose mediums are dispensed. Results are mean \pm SD. * p -valor = 0.05

Specifically, and focusing on cryogel development, we could seed pancreatic islets inside a cryogel and prove they are functional and viable. Moreover, we could prove that the cryogel can be easy handled and integrated inside a microfluidic chip. With this integration, we observed no apparent losing of pancreatic islets due to the flow generated inside the chip. Also, even though cryogel floats a bit, there was not obstruction of the microfluidic channels.

With this, we could say that our cryogel has a good potential scaffold for different microfluidic assays as organ-on-a-chip technology.

However, as it has been mentioned before, this approach presents significant limitations. The infiltration ratio of the pancreatic islets, prompted by the difficulties to generate higher pore distribution, fostered us to search for other alternatives to generate pancreatic tissue in vitro.

4.3.2 INS1E cells

To overcome all the previous exposed limitations we decided to generate pseudoislets using pancreatic β -cell lines. The rat insulinoma cell line INS1E is a well-established model to study pancreatic β -cell function. This cell line presents the positive factor that is responsiveness to glucose, similar to a physiological range, cells possess high insulin contents, high proliferative ability, and the capacity to form cell clusters in the appropriate environment, mimicking the primary pancreatic islets [190]. Moreover, there is no need of animal sacrifice to study and generate pancreatic tissue. With the ability of these cells to form cell aggregations is where our cryogel can have a positive impact, as its porosity may enhance and control cell clustering ability. For these reasons, INS1E pancreatic β -cell line was used to engineer pancreatic pseudoislets as an approximation for pancreatic tissue engineering to study type 2 diabetes mellitus and its crosstalking with skeletal muscle under diabetic conditions.

4.3.2.1 Cell seeding

After fabricating and autoclaving, 1% CMC cryogels were placed in a 48-well plate and dried at room temperature during cell trypsinization. In the end, cells were resuspended at a concentration of 1×10^7 cells/ml. Among this concentration, only 200.000 cells into a 20 μ l drop were seeded in each condition. This amount of cells was determined as an approximation for the generation of around 200 pseudoislets per cryogel. CMC cryogels and gelatin cryogels were studied, comparing the results with cells seeded in traditional culture well-plates. Experiments were performed on days 1, 4, and 7.

4.3.2.2 Pseudoislet formation

To generate a functional 3D structure able to support β -cells, we seeded INS1E cells onto the scaffolds. After cell seeding, INS1E morphology was evaluated in gelatin and CMC-based scaffolds at days 1, 4, and 7. Interestingly, at day 1, after seeding, instead of the typical monolayer architecture is seen in culture flasks, cells cultured in 3D CMC cryogel scaffolds formed round-shaped clusters, morphologically resembling pancreatic islets (Figure 49). In contrast, a dispersed organization was observed in gelatin-based cryogels. Similar cell architecture was found in the following days of culture. The difference in cell organization observed in CMC and gelatin scaffolds can be explained by the presence or absence of the cell adhesion motifs in these structures. Gelatin is known to contain RGD (arginine-glycine-aspartic acid) motifs, cell adhesion sites found in several ECM proteins [191]. Hence, gelatin has a profound effect on the ability of cells to adhere to this material. On the other hand, CMC cryogels do not present cell-binding motifs, so it displays shallow adhesion properties for anchorage-dependent growth of INS1E cells, promoting cells to interact between them and cluster together, forming islet-like structures.

To study better these cell aggregations, pseudoislets proliferative ability, and pseudoislets sizes were analyzed. For the proliferation ratio of the cells, we counted the cells expressing Ki-67 proliferation marker in the cell nuclei against the total amount of nuclei. In both cryogels we could observe that this ratio is high at day 1 ($51,34 \pm 17,08$ % for CMC vs $66,63 \pm 16,02$ % for gelatin) (Figure 50). Moreover, this high proliferative profile is also seen in a plate ($82,99 \pm 12,81$ %). However, as longer in time was the culture, lower the proliferation rate is. At day 4, in CMC cryogels proliferation ratio was $17,10 \pm 18,75$ % and at gelatin cryogels $46,74 \pm 16,70$ %. Similar decrease of proliferation ratio is seen in plate cultures at day 4 ($11,23 \pm 11,06$ %). Consistently with this decrease in the 4th day, there was barely nonproliferation in the cultures at one week of culture, neither CMC nor gelatin cryogels or flat cell cultures ($7,98 \pm 10,16$ % vs $10,83 \pm 8,61$ % and $14,63 \pm 7,31$ %). In rodent islets, the proliferative capacity of β -cells is confined to the early stages of life, linked to an immature functional phenotype [192], [193]. Thus, reduced proliferative capacity is one of the characteristics of mature β -cells, and maturation of β -cells defines their functional identity. In this experiment, high errors were found, mainly due to the disparity of the proliferation ratios between different pseudoislets in the same cell cultures, mainly depending on the cells' confluency. We could

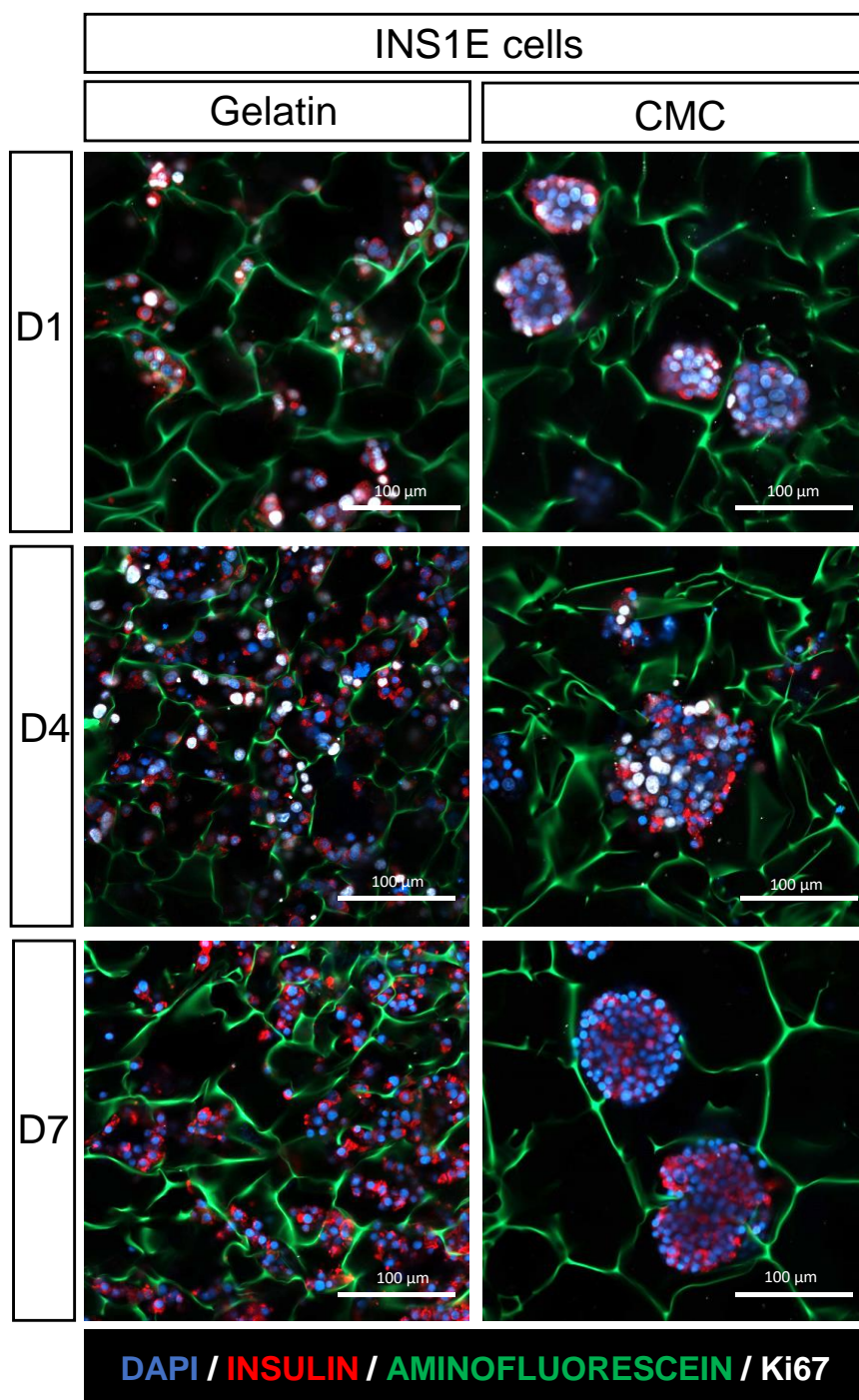


Figure 49: Different cell distributions achieved in gelatin or CMC cryogels. In CMC cryogels, cells formed spherical architecture aggregations, or from now, pseudoislets. On the other hand, in gelatin cryogels, due to RGD cell binding motifs, cells form a dispersed distribution, not forming spherical cell aggregations. This happens because cells preferred to interact with the material instead of themselves. In here, material fibers are stained in green, nuclei in blue, insulin in red and Ki-67, a proliferation marker, in white. Scale bar = 100 μm .

observe that as more cell confluency in the culture, less proliferation ratio. However, cell proliferative behavior in each biological replicate and in each pseudoislet entangles an intricate point to determine a specific proliferation ratio for each condition. Besides this, the low proliferative capacity of our pseudoislets is approximate to the *in vivo* proliferative ability of the pancreatic islets, taking this point as a positive and resemblant property of our approach.

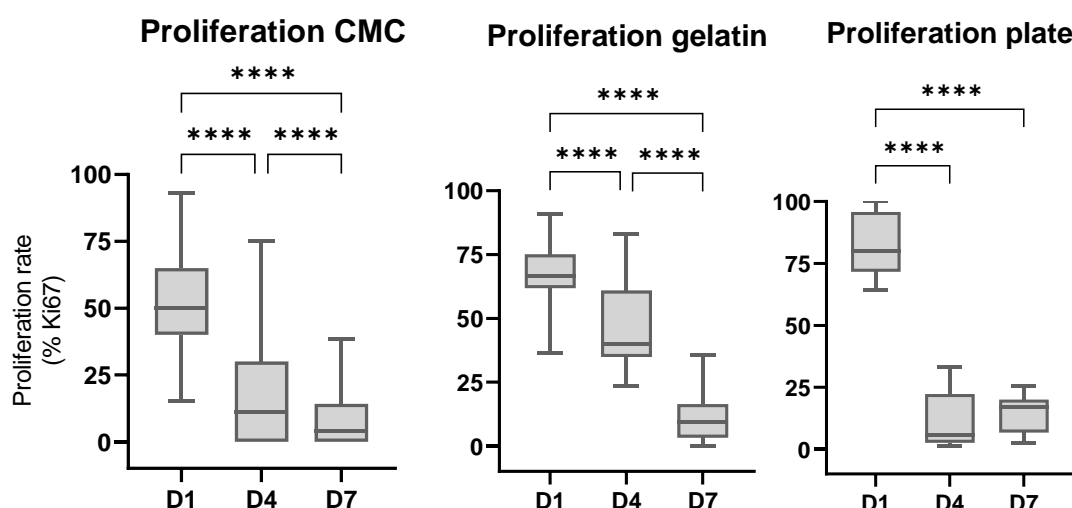


Figure 50: Proliferation ability of the cells cultured in different substrates. Cell proliferation decreases upon the days of culture. Results are mean \pm SD. * p -valor = 0.05

Interestingly, as this proliferation ratio decreases, the pseudoislets enlarges. As expected, in gelatin cryogels nor in plate no pseudoislets were formed. However, in CMC cryogels, pseudoislets were formed. Moreover, the pseudoislet size increases correlating to the proliferation ratio. On day 1, pseudoislets has a diameter of $60,64 \pm 32,87 \mu\text{m}$, and on day 4, the diameter of it increases up to $68,98 \pm 29,95 \mu\text{m}$. On day 7, pseudoislets generated in CMC cryogels are $74,56 \pm 38,23 \mu\text{m}$ in diameter (Figure 51A). Again, comparing the mean of many pseudoislets with different sizes and different proliferation ratios, as seen previously, entangles big error bars. However, this wide disparity in the sizes of the pancreatic islets is a favorable point. Primary rodent pancreatic islets present a considerable heterogeneity in size and shape, varying from small cell clusters to larger islets [194], [195]. Several studies have revealed that islet heterogeneity influences the insulin secretory response of β -cells, so heterogeneity should be an essential consideration when understanding T2D pathogenesis, both at a single-cell and islet level [196]–[198]. Our approach is capable of replicating this wide cell cluster heterogeneity seen in physiological environments.

More appreciations can be made by observing the sizes of the islets in a histogram. Here, we can observe that the small islets decrease during the culture days. On day 1, up to 12% of the clusters ranged from 0-25 μm , whereas on days 4 and 7, aggregations smaller than 25 μm represented less than 3%. On the other hand, middle and big islets percentage increases during the culture days. Islets bigger than 200 μm were found only on day 7 (Figure 51B). Finally, we can compare this pseudoislet size histogram with the pore size distribution of the CMC cryogels (Figure 51C). In here we could appreciate some similitude, where small pores and pseudoislets (0-75 μm) are more common, and as the pore frequency increases, it also decreases the pseudoislet size population. This may indicate that the pores of our cryogel can have a positive impact in controlling cell clustering.

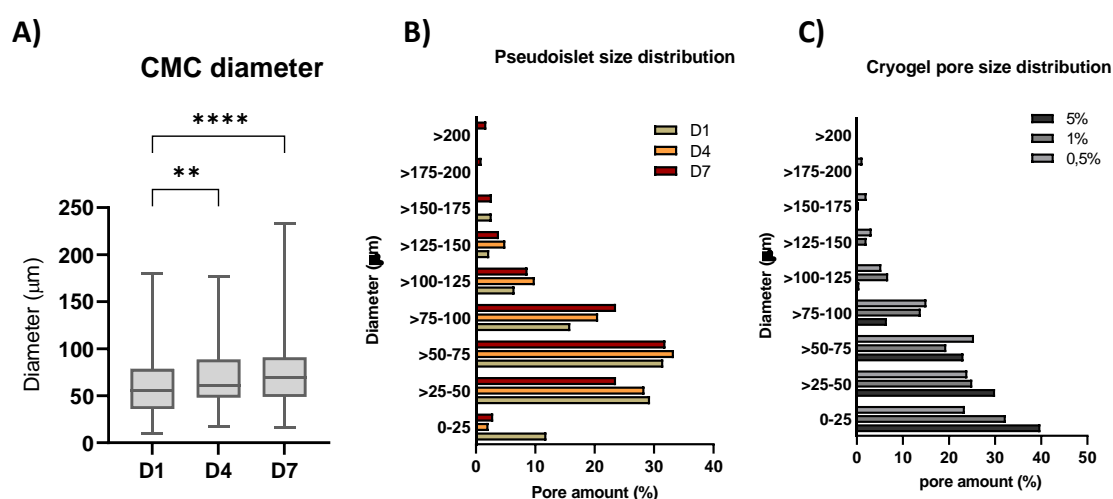


Figure 51: Diameter of the pseudoislets increases during culture days and highly correlates with the pore size distribution. Results are mean \pm SD. * p -value = 0.05

4.3.2.3 Cell viability

Since 3D pseudoislets may have less access to nutrients, it was of interest to establish cells viability along one week of culture. Cell viability was assessed at culture days 1, 4, and 7 by a live/dead assay and Alamar blue metabolic assay.

The first assay was a Live/dead assay up to day 7 of cell culture. This assay allows us to see the percentage of live cells at different days of cell culture. The viability ratio was designed as the number of live cells compared to the total amount of it. Both cryogels (CMC and gelatin) and traditional well-plate

were studied at day 1, day 4, and day 7 after seeding. Images were obtained by confocal imaging and analyzed with ImageJ software (Figure 52).

Comparing the viability of each cryogel in different days we can appreciate that this viability remains elevated during the 7 days of culture. In CMC cryogels, viability decreases during days of culture. Specifically, day 1 has $98,55 \pm 1,86 \%$, compared to $89,09 \pm 8,08 \%$ that is viable at day 4. Also, compared to day 1, at day 7 viability also decreases ($98,55 \pm 1,86 \%$ vs $92,83 \pm 7,05 \%$). Although this decreasing, by comparing day 4 against day 7, we

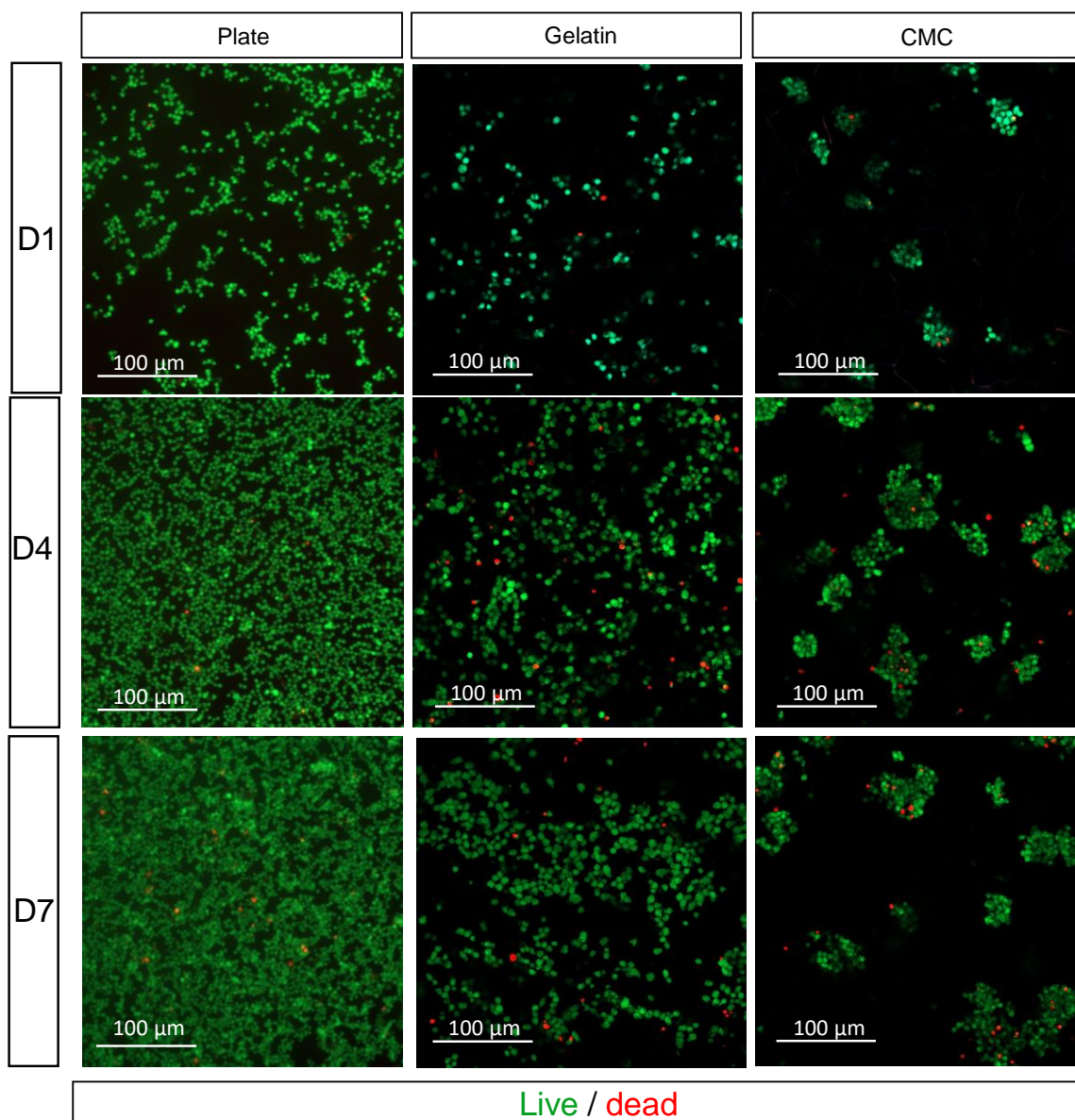


Figure 52: Live/Dead images of cells cultures in both cryogels (CMC and gelatin) and traditional well plate. In green, live cells were marked with calcein AM. in red, dead cells marked with EthD-1. Interestingly, pseudoislet configuration can be appreciated in CMC images, contrarily to dispersed architecture found in gelatin cryogels or traditional well plate. Scale bar = 100 μm .

saw a slight increase. Despite this variability in the viability ratios, the live cell ratio is high in all the days, remaining over 90% of viable cells. This high rate implies excellent cell viability during 7 days of culture. These high values of viability are also observed in gelatin cryogels, where a slightly decrease is observed, despite the +92% of viability ratio among all the cell culture period ($95,48 \pm 4,06$ % at day 1, $94,70 \pm 3,49$ % at day 4, and $92,45 \pm 2,86$ % at day 7) (Figure 53). These high viability ratios observed in CMC and gelatin cryogels confirms that cells are viable when seeded in cryogels.

To prove that these cells did not lose viability when seeded inside cryogels, we can compare the viability of it with cells seeded over a plate, where they are traditionally cultured for cell culturing and cell passaging. Plate cultures has also high viability ratios during cell culture ($96,86 \pm 1,50$ % at day 1, $97,95 \pm 0,81$ % at day 4 and $93,99 \pm 3,74$ % at day 7). Comparing different substrates, in same days, there are no big differences either. Interestingly, on day 7, last day of culture, there is no statistical significance between all the substrates. All this may indicate no change in cell viability when cells cultured inside the cryogels, meaning that cryogels did not affect cell survival (Figure 53).

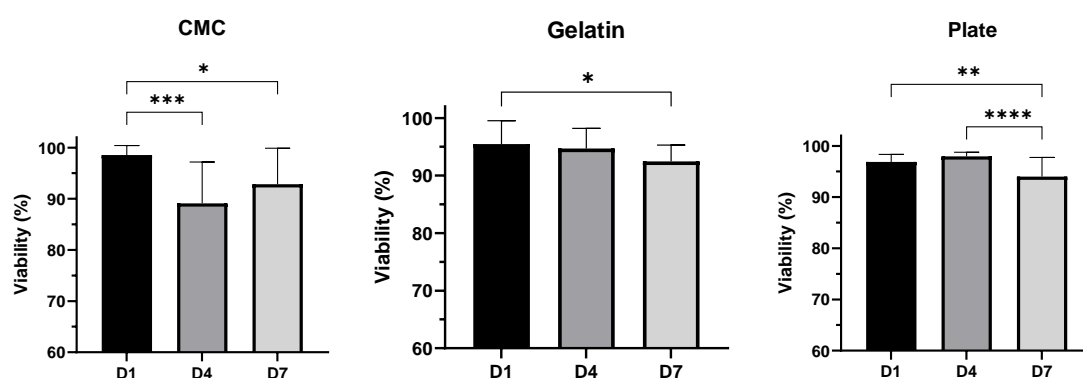


Figure 53: Cell viability percentages of cells seeded in different substrates. Independently of the cryogel or plate, cell survival remains higher than 90%, representing a very good cell viability. Results are mean \pm SD. * p -valor = 0.05

Another different assay for determining cell viability is alamarBlue assay. This assay determines the metabolic activity of the cells. Assays were also performed at days 1, 4, and 7. Its important to highlight taht alamarBlue test is highly dependent on number of cells, as more cells, more metabolic activity. For this, we normalized every result to the plate result of the same day. The normalization was performed to avoid accumulating errors. On day 1, we saw that the cells cultured in cryogels have almost the same metabolic activity that

the cells cultured in the plate ($82,07 \pm 3,61$ % in CMC vs $87,56 \pm 4,55$ % in gelatin) (Figure 54). At day 4, metabolic activity slightly decreases, however remain constant between cryogels ($83,05 \pm 27,87$ % in CMC vs $83,08 \pm 10,44$ % in gelatin). However, at day 7 there is a gap in this metabolic activity ($66,94 \pm 4,27$ for CMC vs $83,78 \pm 5,18$ % for gelatin). As the cell viability seen by Live/Dead assays show no differences in cell viability, these differences may come from the number of cells in each cryogel. Correlating with the proliferation results shown previously (Section 4.3.2.2 Pseudoislet formation), we could observe that the proliferation ratio of cells seeded in gelatin cryogels is higher than CMC cryogels at day 4. This proliferation ratio means that almost 50% of the cells in gelatin cryogels are still proliferating at day 4. Consequently, on day 7, more cells will be found in gelatin cryogels than in CMC cryogels, and so more metabolic activity was found due to this cell population increase. As seen previously, cells in plate grow faster and reach earlier confluency than cells seeded in cryogels. For this, we considered normal the decrease in metabolic activity if comparing the plate with the cryogels.

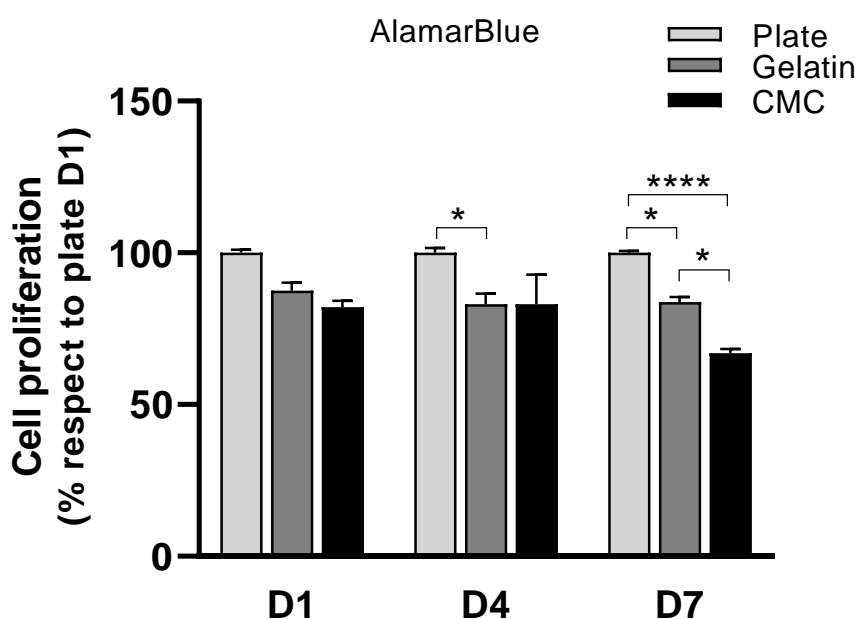


Figure 54: Metabolic activity of cells seeded over different substrates. Results were normalized to plate metabolic activity of each day. Because this normalization, the decrease of metabolic activity is expected. Results are mean \pm SD. * p -valor = 0.05

4.3.2.4 Gene expression analysis

The ability of CMC scaffolds to efficiently aggregate single cells into engineered pseudoislets, with round-shaped structures similar to native islets, prompted us to examine the gene expression profile of these pseudoislets over time compared to gelatin-based monolayer INS1E cells. We first focused on the genes encoding MafA, Pdx1, and NeuroD1, three β -cell specific transcription factors involved in β -cell functionality. Although many transcription factors (TF) have been involved in the maintenance of the β -cell identity, these specific transcriptional regulators have been demonstrated to play a crucial role in maintaining the function of the insulin-producing cells. Indeed, it has been demonstrated that this TF activates the insulin gene expression in a coordinated and synergistic manner in response to increased glucose levels. Furthermore, the fine-tune regulation of these TF ensures β -cell identity [199]–[201].

Interestingly, cells supported within the cellulose-based scaffold presented a gradually increased expression level of the β -cell specific marker *Pdx1* concerning cells cultured in a gelatin cryogel. This beta-cell identity was also checked with MafA. Here, we could not appreciate any gradually increasing, but there is no decrease of β -cell identity. Finally, studying NeuroD1, we can

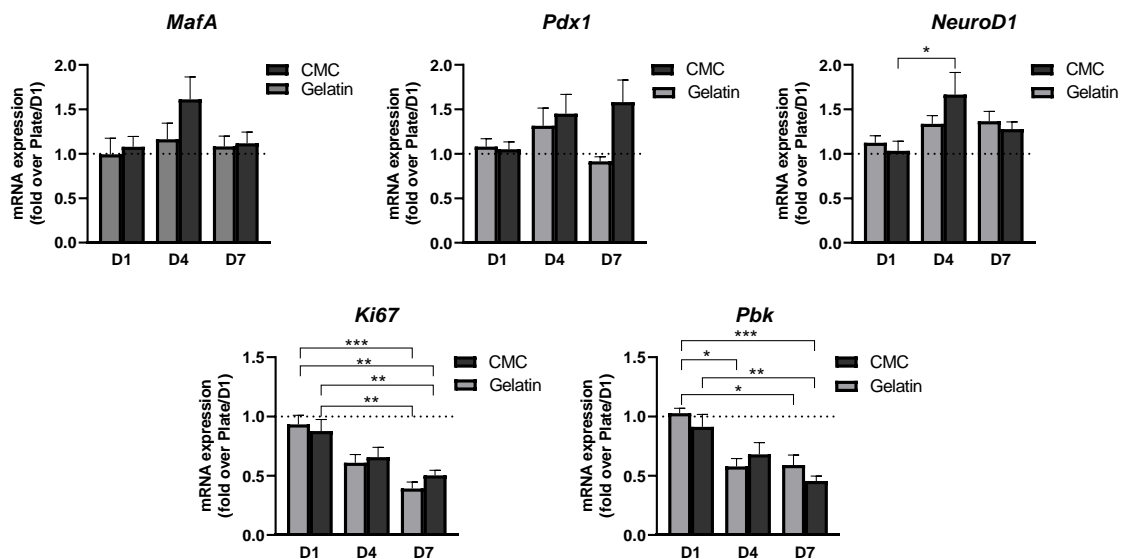


Figure 55: Gene expression of the pseudoislets comparing with dispersed cell distribution of gelatin cryogels. MafA, Pdx1 and NeuroD1 as a beta-cell health and functionality markers. Ki67 and Pbk correspond to proliferation markers. Results are mean \pm SD. * p -value = 0.05

appreciate an increase compared to day 1 in both gelatin and CMC cryogels. Interestingly, NeuroD1 expression increases at day 4 for the cells seeded in CMC cryogels compared to gelatin cryogels (Figure 55). The results obtained are consistent with previous works demonstrating how reaggregating cells to form 3D spheroids significantly enhances the gene expression profile of β -cells [123].

This better-differentiated phenotype of β -cells when cultured within a 3D extracellular matrix, is consistent with the decreased proliferation markers, *Ki67* and *Pbk* (Figure 55) corroborating the balance between an increased β -cell identity and a reduced ability to proliferate of these cells [192]. Moreover, the decreasing of *Ki67* transcription factor highly correlates with previously shown results of cell proliferation.

4.3.2.5 Glucose stimulation insulin secretion assay (GSIS)

Several findings indicate that islet architecture has a pivotal role in determining β -cell functionality as cell-cell interactions are fundamental for the correct cellular function [6], [202], [203]. Indeed, it has been described that the secretory response of structurally coupled β -cells is higher than that of insulin-producing β -cells not arranged within the islet architecture [122]. INS1E cells traditionally seeded in a monolayer do not present reproducible responses to dynamic glucose stimulations.

To determine whether pseudoislet formation within the cryogel correlates with increased β -cell function, we tested the dynamic response of pseudoislets to glucose. To check islet functionality, a glucose-stimulated insulin secretion (GSIS) assay, which defines the ability of β -cells to secrete the suitable amount of insulin in response to proportional extracellular glucose stimuli, was performed in all conditions. As shown in Figure 56, cell clustering improved the insulin secreted stimulation index under high glucose stimulation concerning the basal insulin secreted in low glucose conditions. This result demonstrates the benefit of cell aggregation in islet functionality as often monolayer β -cell lines do not reach this threshold level or display a reproducible behavior [204]. Indeed, at day 1, INS1E cells seeded in 48 well-plate presented a 2.51 ± 0.6 -fold increase of insulin secretion when cells were challenged with 16.7 mM compared to cells incubated with 2.8 mM glucose. Cells seeded in gelatin cryogels showed a 6.47 ± 1.8 -fold increase. Interestingly, we reached a fold increase of 7.52 ± 1.6 of insulin secretion when CMC-based pseudoislets were challenged with 16.7 mM glucose (Figure 56).

This trend was repeated along the week, indicating that the stimulation index for insulin response to glucose is significantly higher in pseudoislets than dispersed and non-organized cells.

Like other tissues, β -cell functionality is greatly influenced by cell-cell and cell-matrix interactions, controlling basal and stimulated insulin secretion. Remarkably, GSIS defects in monolayer INS1E cell cultures arise from an increased insulin release under basal conditions (2.8 mM glucose) in addition to a decreased insulin secretory response under stimulatory glucose conditions. These results are consistent with other studies showing that aggregating β -cells enhances the secretory responsiveness to nutrients than compared with cells configured as monolayers [111], [121]. Moreover, it also suggests that β -cells interactions might be sufficient to sustain a normal glucose response.

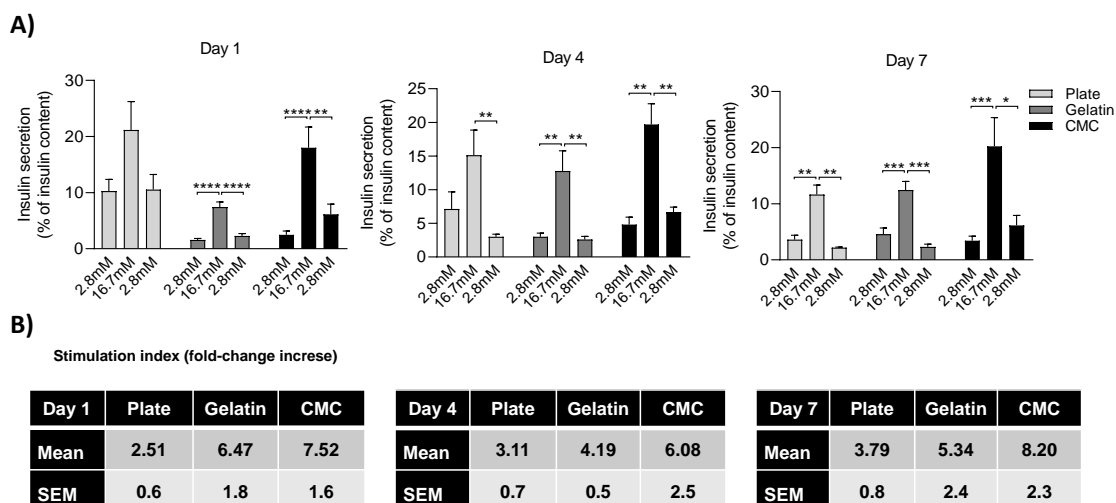


Figure 56: Glucose Stimulation Insulin Secretion assay. A) Insulin released in GSIS assay under different glucose concentrations. B) Stimulation index of each cryogel in different days. Results are mean \pm SD. * p -valor = 0.05

Therefore, our study validates that a correct structural arrangement is essential for appropriate insulin response, demonstrating a robust glucose-stimulated insulin secretion by pseudoislets formed within a cryogel. Moreover, CMC cryogel is a very viable option to generate heterogeneous population of β -cell clusters, with appropriate viability and functionality for in vitro studies.

4.3.2.6 Diabetic conditions

After optimizing the biomaterial and prove its pseudoislet aggregation capability, excellent cell viability and promising insulin secretion, we wanted to go one step further in the research. As one of the possible applications of the scaffold its is incorporation inside Organs-on-a-chip, we wanted to study its possible potential to generate a model for type 2 diabetes mellitus. Here, we wanted to simulate elevated concentrations of free fatty acids and high blood glucose levels found in diabetic or obese patients. For this, different glucose concentrations (11 mM glucose medium (G11) and 25mM glucose medium (G25)) and the addition of free fatty acids were studied by adding palmitic acid. Beta-cell functionality was analyzed by Glucose Stimulation Insulin Secretion assay (GSIS) and cell viability and beta-cell health was analyzed by qPCR.

All experiments were performed at 7 days of culture. For type 2 diabetic conditions modelling, Ins1 cells were cultured with complete RPMI-1640 medium up to day 4, where pseudoislets are already formed. On day 4, the medium was changed to simulate diabetic conditions. Here, combinations of G11 or G25 with or without 400 μ M of palmitic acid was studied.

For cell functionality, GSIS assay was performed. Briefly, this experiment consist in challenging the cells by stimulating them with higher concentrations of glucose concentrations (16.8 mM of glucose, G16) after a relaxing period under low glucose concentrations (2.8 mM of glucose, G3). Results of this experiment shows the insulin released against the insulin content in both glucose concentrations. We observed that insulin secretory response when cells were challenged with G16, decreases when cultures were treated with palmitic acid (Figure 58). Interestingly, we could observe that the plate cultures treated with palmitic acid did not present an increasing of insulin releasing (Plate/G11/+PA: 1.59 ± 0.87 for G3 vs 1.99 ± 0.44 for G16; Plate/G25/+PA: 2.43 ± 0.37 for G3 vs 2.67 ± 0.34 for G16) (Figure 58A). On the other hand, plate cultures non-treated with palmitic present a slight increase of insulin releasing (Plate/G11/-PA: 1.89 ± 0.42 For G3 vs 2.82 ± 1.12 for G16; Plate/G25/-PA: 2.20 ± 0.26 for G3 vs 3.49 ± 1.15 for G16). Contrarily, in the pseudoislet cultures we observe a increasing of insulin releasing in all the challenging G16 conditions indistinctly.

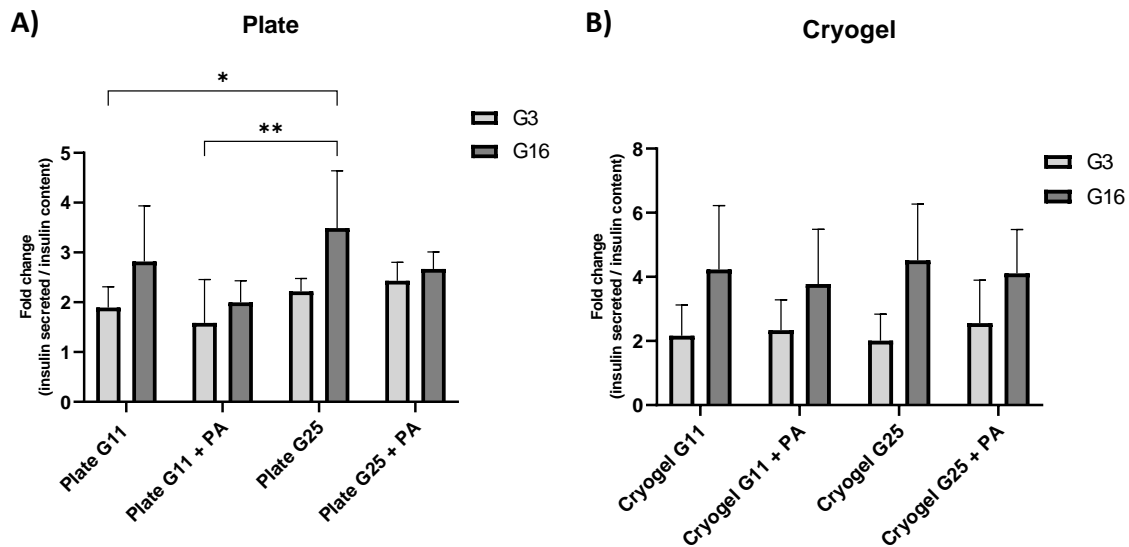


Figure 58: Insulin released under different glucose concentrations. Theoretically, cells challenged with higher glucose concentrations should secrete more insulin. A) GSIS assay of cells cultured in a plate. B) GSIS assay of cells cultures in pseudoislet architectures. Results are mean \pm SD. * p -valor = 0.05

However, clear results can be obtained by studying the stimulation of this assay. Stimulation index is the fold change between insulin secreted at G16 against the insulin secreted at G3. Here, we could observe the results mentioned above, as palmitic treatments has a negative effect, as fold slightly decreases (Figure 57) (Table 16-Table 17). Also, we could observe that insulin secretion assays in cryogel present a higher stimulation index than

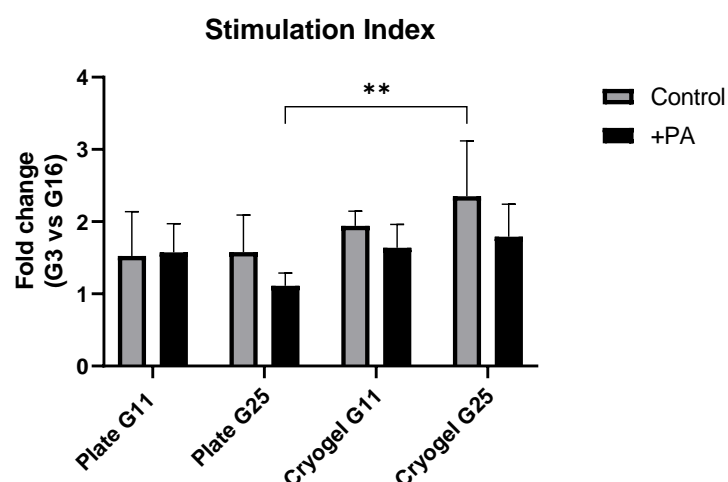


Figure 57: Stimulation index of the GSIS assay. Stimulation index is the fold change of the insulin released at G16 against the insulin released at G3, when cells are relaxed. Results are mean \pm SD. * p -valor = 0.05

monolayer cultures, indistinctly of the treatment or glucose concentration (Table 17). Furthermore, we could observe that cultures non treated with palmitic acid present similar stimulation indices in both plate conditions. Even, seems that cryogel with G25/-PA present higher fold change than the other conditions. However, the interesting data in here is the appreciation of how the treatment with palmitic acid decreases all the insulin secreting capability of the cells if compared to non-treated. Interestingly, this situation happens in both cultures, cryogel and plate, and in both glucose concentrations.

	Fold-change (Mean)	Standard desviation
Plate/G11/-PA	1.52	0.62
Plate/G25/-PA	1.58	0.51
Plate/G11/+PA	1.57	0.39
Plate/G25/+PA	1.13	0.18

Table 16: Stimulation index of plate cultures

	Fold-change (Mean)	Standard desviation
Cryogel/G11/-PA	1.94	0.20
Cryogel/G25/-PA	2.35	0.77
Cryogel/G11/+PA	1.64	0.32
Cryogel/G25/+PA	1.79	0.45

Table 17: Stimulation index of CMC cryogel cultures

However we could observe that palmitic acid has a negative impact in cell functionality, we wanted to check how viable and stressed are the cell cultures under diabetic conditions. For this, a gene expression at day 7 of cell culture was studied by qPCR. Here, previously studied beta-cell health transcription factors MafA, Pdx1 and NeuroD1 were analyzed. Moreover, markers for cell stress as Chop, Trib3 and Atf3 were also analyzed. All results were normalized against plate G11 conditions, used as a control, for its better understanding.

Supporting previous gene expression assay, we could observe that all cell health-markers present a slightly increase of expression when pseudoislets were formed inside the cryogel. Interestingly, a dowregulation of these β -health markers could be observed when cells cultured in high glucose concentrations in MafA and Pdx1. Although no clear results are found, there is a tendency in many conditions were palmitic acid treatmens slightly decrease beta-cell health markers. However, treatments with palmitic did not

show any remarkable downexpression in this markers, as expected after GSIS results (Figure 59).

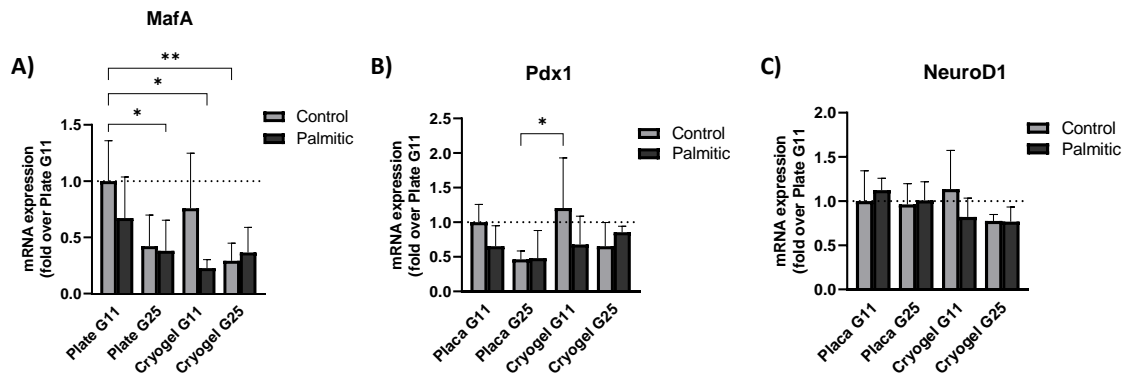


Figure 59: Beta-cell health and functionality markers. A) *MafA*. B) *Pdx1*. C) *NeuroD1*. Results are mean \pm SD. * p -valor = 0.05

However, stress and pre-apoptotic markers were also analyzed and showed some light in the previous results (Figure 60). Firstly, we could observe that cells cultured in the cryogel without palmitic treatment did not increase stress markers compared to the plate cultures, meaning that cells are viable and functional. However, when palmitic treatment was applied, these stress Transcription Factors (TF) showed an upregulation in most of the conditions. But always higher in plate than in cryogel.

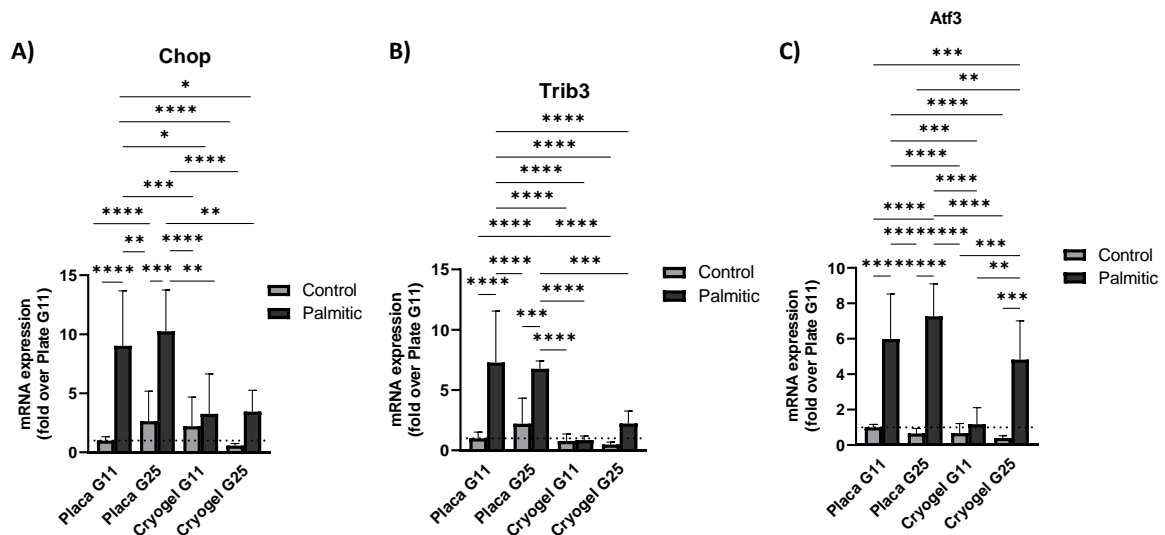


Figure 60: Stress and pre-apoptotic markers of pseudoislets after palmitic treatment. A) *Chop*. B) *Trib3*. C) *Atf3*. Results are mean \pm SD. * p -valor = 0.05

The hypothesis for these results is that palmitic reached easily the cells cultured in monolayer than the pseudoislets cultured inside cryogels. This is because the formation of micelles by the palmitic acid, due to its

hydrophobic/hydrophilic configuration. Some of this uncontrollable-sized micelles may not go inside the cryogel, and so, not being metabolized by the cells. Another hypothesis for this lower decreasing ratio is the self architecture of the pseudoislets, that as spherical-shaped aggregation, palmitic acid could not reach core cells, and so not damaging it. In contrast, in monolayer, the palmitic could reach all the cells and so stressing them all equally.

Finally another interesting point to consider is that cells presented more stress markers when high glucose and palmitic treatments are combined. These results can be appreciated in Trib3 and Atf3.

4.4 SKELETAL MUSCLE

The possibilities in pore distribution and architecture that offers the cryogelation technique, allows us to search for other exciting approaches with other tissues. One tissue that highly fits with one of the pore architectures we achieved is the skeletal muscle tissue. Anisotropic scaffold structure is an important prerequisite to engineer skeletal muscle tissue, as the alignment of the cells prompts myoblast fusion into myotubes and enhances myogenic maturation.

After developing a promising scaffold to engineer this tissue, we studied its viability to engineer skeletal muscle tissue. We evaluated cell interaction with the scaffold, by studying cell infiltration, cell alignment and cell viability. Finally, by applying an electrical pulse stimulation, we studied the fusion of the cells and the maturation of the formed myotubes.

4.4.1 Cell seeding

Before cell seeding, the first step was slicing the top and the bottom of the cryogel to avoid small porosities formed by ice nucleation. With this, the scaffold has the porosity range quantified previously, and we only seed the cells in the anisotropic part, previously characterized. After slicing, cryogels were dried at room temperature during cell trypsinization. Briefly, for cell trypsinization, cell mediums were washed with PBS, and 2 ml of 0,25% trypsin-EDTA were added to the flask. After 2 minutes, 8 ml of fresh medium

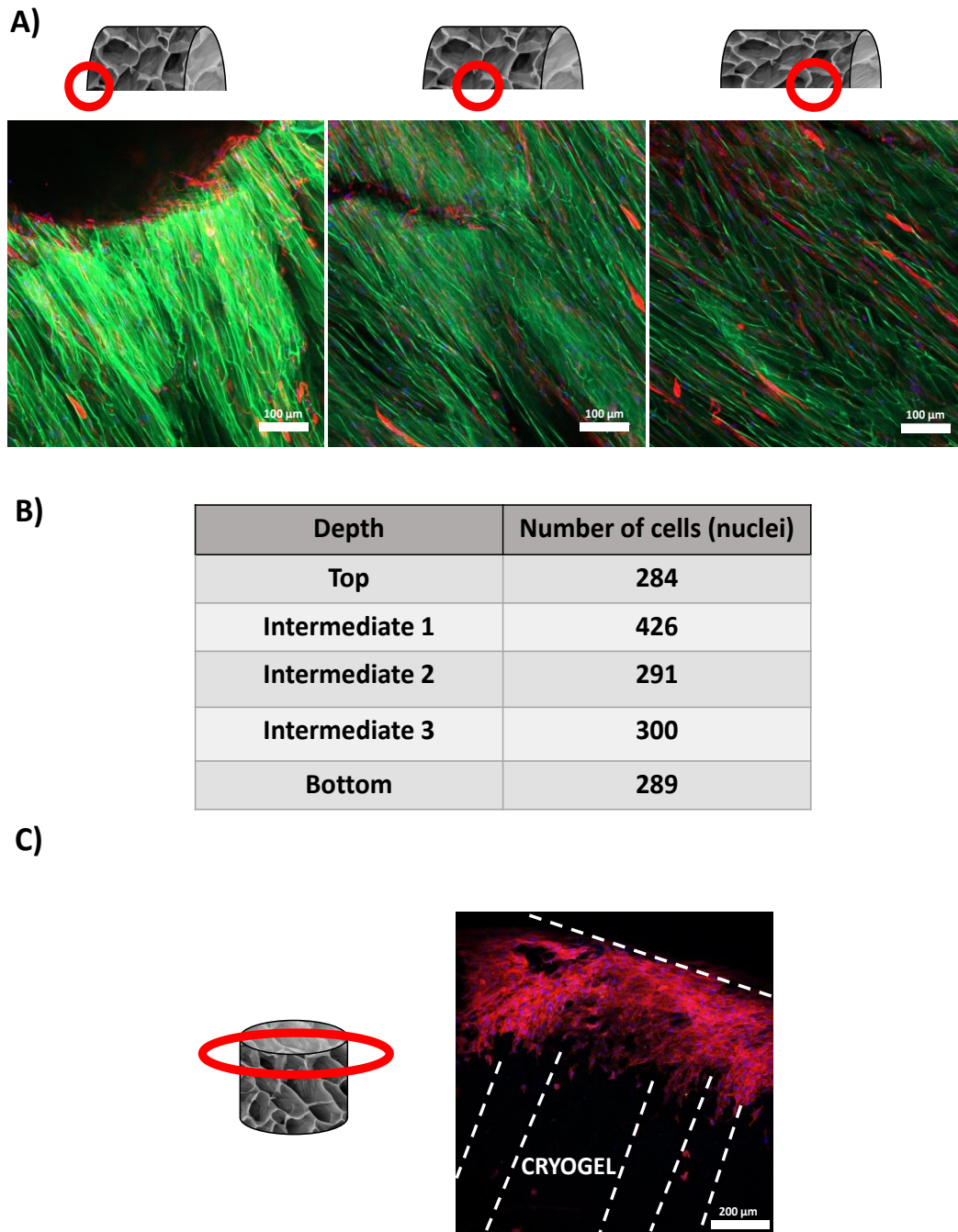


Figure 61: Cell infiltration inside the scaffold. Cells could colonize all depth of the scaffold.

A) Images of 3 different depths of a cryogel. In here it can be observed that cells are found in all the depths. Staining of cryogel fibers (green), cell nuclei (blue) and F-actin (red). Scale bars = 100 μm . B) Quantification of the amount of nuclei in 5 different images of different depths of a cryogel. Only one cryogel were analyzed. C) If cell density is highly increased, cells form a monolayer at the top of the cryogel, preventing cells infiltrate inside the cryogel. Cells were stained for F-actin (red) and nuclei (blue). Scale bar = 200 μm .

was added to the trypsin to stop the reaction and placed into a falcon for centrifuging. During centrifugation, cells were counted. C2C12 cells (mouse skeletal muscle immortalized myoblasts) were seeded inside the cryogel by gravity, placing a drop of medium and cells over it and waiting 30 minutes.

An essential point to engineer skeletal muscle is the cell density seeded inside the scaffold, as myoblasts need to be confluent to fuse into myotubes. We have optimized the cell density in 9×10^6 cells/mL to allow proliferation and colonization through all the biomaterial. Cell colonization was checked by counting nuclei in different depths of one scaffold after seeding. Here, we could appreciate that there were not many differences of cells in different depths (Figure 61A-B). Confirming these good infiltration results, cells were found in all the scaffold indistinctively in all experiments. Other models for engineering skeletal muscle tissue use similar or higher densities [42] [205]. Nevertheless, at higher concentrations, the cells do not colonize our cryogel by forming a layer on the top (Figure 61C). On the other side, lower concentration difficulties cell fusing.

After cell depositing, cryogel was left at room temperature for 30 minutes. With this, we achieved a good cell infiltration as cells infiltrate inside the scaffold by gravity. Also, the liquid inside the cryogel dries a bit, helping cell infiltration through the cryogel. After 30 minutes, the cryogel was submerged into a well-plate with the DMEM medium. Cells were cultured for 10 days in growth medium (GM) to promote cell proliferation and scaffold colonization. The medium was then replaced with differentiation media (DM) to promote myotube formation for 12 days more. Electrical pulse stimulation was applied on day 11 of DM (21 of total culture days) at 1V p-p squared pulse, at 1 Hz of frequency and 10 ms of stimulation width.

4.4.2 Cell viability

One of the most important things is to determine if the cells are alive after cell seeding process, if they can survive seeded deep in the scaffold, and to check if CNT doped cryogel allows cell survival and functionality. To solve these doubts we decide analyze cell viability using a Live/Dead assay to determine the viability of the C2C12 cells during one week of culture. We analyze cell viability at days 1, 5, and 7 by confocal imaging. Viability was determined by live cell counting using imageJ software (Figure 62A). Briefly, cell viability was determined as the amount of live cells against the total amount of cells.

Here, we could appreciate that cell viability is always higher than 88%, and there is no statistical significance between any day and condition (Figure

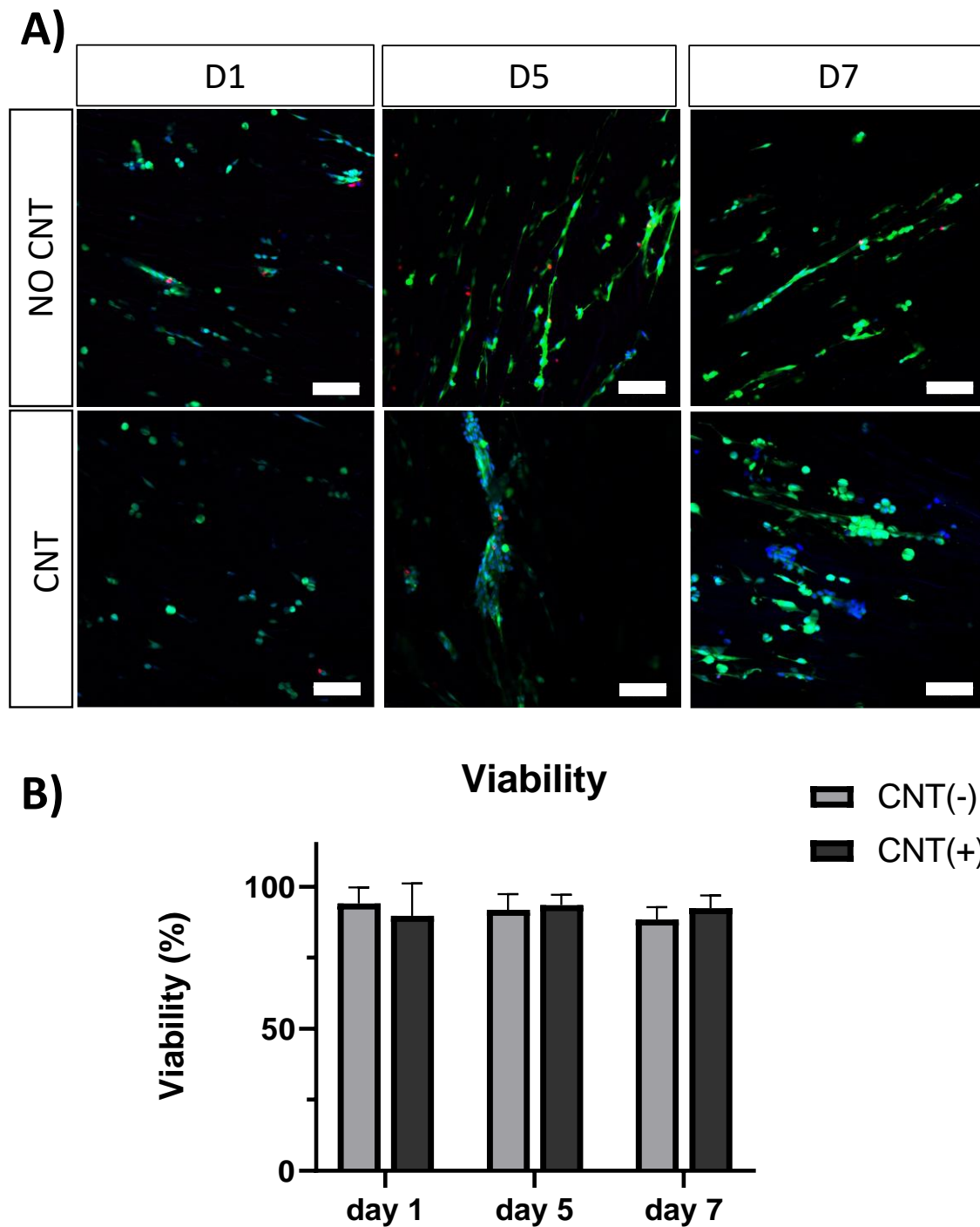


Figure 62: Viability of the cells when seeded inside the scaffold. A) Confocal images of the Live/Dead assay. Live cells stained in green (Calcein AM), dead cells stained in red (Ethd-1) and nuclei stained in blue. Scale bar = 100 μ m. B) Viability ratio of the cells determined as the amount of live cells against the total amount. Results are mean \pm SD. * p -valor = 0.05

62B). Specifically, on day 1, $94,14 \pm 5,64$ % of the cells were alive in non-dopped cryogel.

In longer cell culture days, we can appreciate that cell viability decreases slightly but being around 90% of cell viability ($91,84 \pm 5,60$ % at day 4 and $88,49 \pm 4,29$ % at day 7).

On the other hand, similar results were observed in the CNT-dopped scaffold. At day 1, $89,80 \pm 11,33$ % of the cells were alive. Consistently, at day 4, this percentage increases up to $93,49 \pm 3,75$ %, and finally, at day 7, the cell viability was $92,45 \pm 4,65$ % (Figure 62B). Comparing the cell viability among days, we could observe similar results, always around 90% of cell survival, meaning that scaffold did not affect cell viability. Moreover, we can appreciate that CNT did not affect cell survival and functionality (Table 18). An increase of dead can be appreciated during the whole experiment, but this cell viability ratio did not decrease, as the cells proliferate. These high viability results may be because of the crosslinking technique that allows to seed cells without suffering any damage due to the crosslinking process. The pore size and the high pore distribution, which leads to high nutrient diffusion, also positively affects the high cell viability. Importantly, as reported previously, the CNT has no toxic effect [150] [206]. The results compared at the same day with and without CNT are non-statistically significant, also meaning good viability in the CNT scaffolds.

Days of culture	CNT(-) (% Viability)	CNT(+) (% Viability)
1	$94,14 \pm 5,64$	$89,80 \pm 11,33$
4	$91,84 \pm 5,60$	$93,49 \pm 3,75$
7	$88,49 \pm 4,29$	$92,45 \pm 4,65$

Table 18: Resume of cell viability percentage of different scaffolds at different days of culture

4.4.3 Cell alignment

Skeletal muscle is a very aligned tissue, as it is formed from the fusion of myoblasts into myotubes. This alignment is a requisite to generate skeletal muscle tissue *in vitro*, as it improves cell fusion, alignment and subsequent the maturation of the myotubes [165]. By generating anisotropic cryogels, we induced the cells to grow in the same directionality, facilitating their fusion.

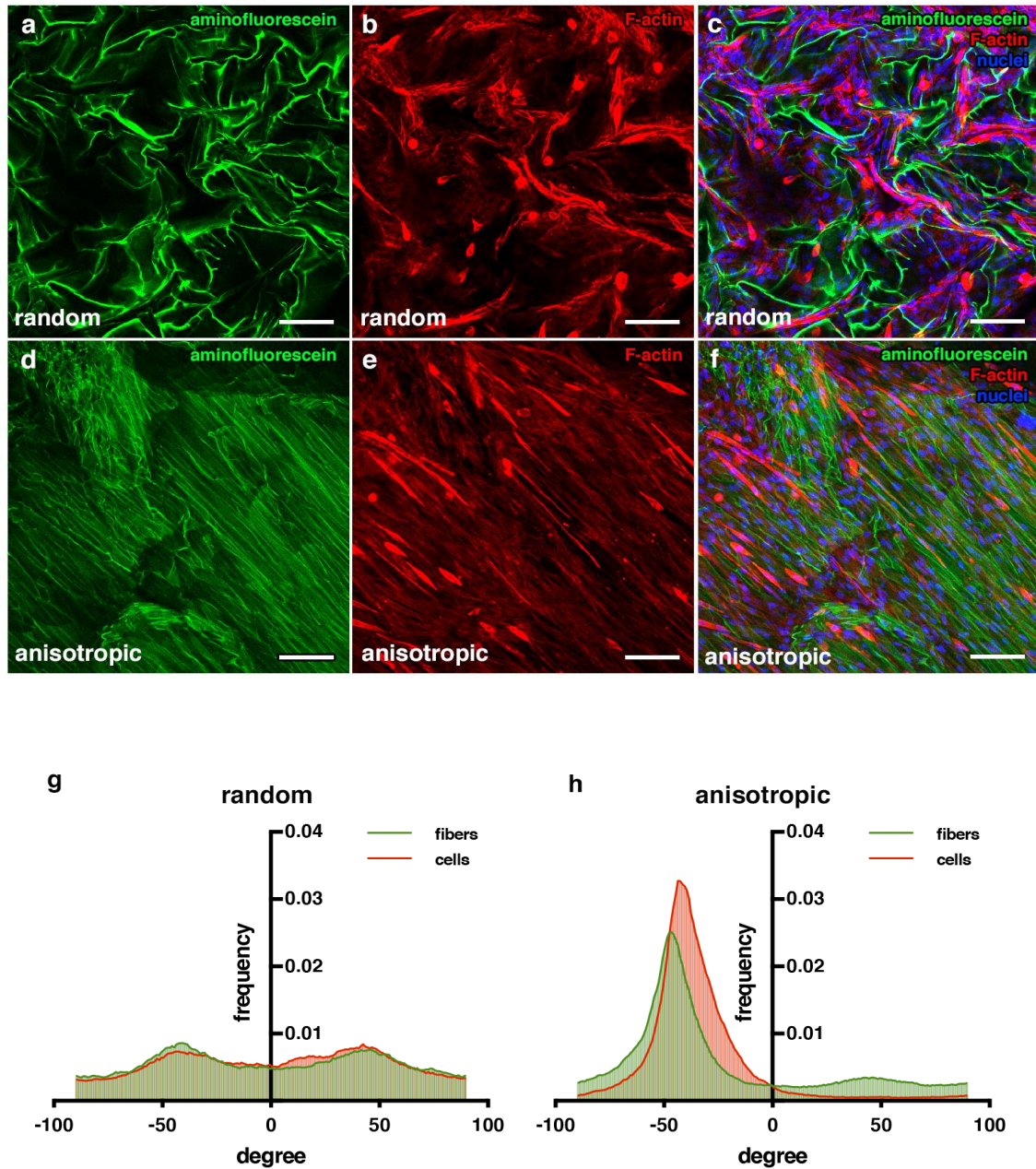


Figure 63: Anisotropic cryogels improve cell alignment. (A – F) Confocal microscopy images showing aminofluorescein marked cryogel in green (a, d), cells marked with phalloidin in red (B, E) and cell nuclei counterstained in blue with DAPI. (C, F) Images showing merged channels. Scale bars = 100 μm . (G, H) Quantification of fibers and cells orientation. Graphs show frequency of fibers in each orientation degree.

After seeding cells inside the cryogel, cell distribution and alignment were analyzed by F-actin immunostaining. As the fibers of the cryogel were stained, we could also compare pore architectures with cell alignments. The alignment of fibers and cells were analyzed with ImageJ PlugIn "OrientationJ." By comparing the cell distribution in random pore morphology against the

anisotropic pore morphology scaffolds, we can appreciate that the cells in the anisotropic architecture aligned much more clearly than the cells seeded in the random pore architecture (Figure 63A-F). Moreover, the random pore cell alignment distribution has more variability among all the angles than the anisotropic structure (Figure 63G, H). Also, it can be appreciated that in both pore morphologies, the alignment distribution for the cryogel fibers and the cell distribution are very similar. These results indicate that the cells sense the pore morphology, and they can distribute and align following the pores' directionality. The cells' alignment is proved that enhances the fusion of them [207], so these results point to our cryogels could improve the myogenic maturation.

4.4.4 Myogenic maturation

Myogenic maturation is related to the fusion of the myoblasts into myotubes and its posterior maturation. Electrical Pulse Stimulation (EPS) was applied to prove that this new electrically improved composite enhances the myogenic maturation of the C2C12 myoblasts. To check the myotube formation, we analyze the expression of the muscle maturation marker Myosin Heavy Chain (Mhc) by immunostaining at day 22 of culture (10 in GM and 12 in DM). EPS was applied on day 11 of DM culture. The fusion index was calculated from confocal images and later analyzed with ImageJ. Fusion index was determined as the ratio of nuclei co-stained with myosin heavy chain against the total nuclei (Figure 64A).

By analyzing the images, we could appreciate that cryogels with EPS has a higher fusion index (51.84 ± 5.30 %), compared with non-EPS cryogels (25.54 ± 5.06 %), indicating that the electrically stimulated cryogel enhances the fusion of the cells into myotubes [168], [208], [209] (Figure 64B). This assay also indicates that the myoblasts are already fusing into myotubes, the first step of the myogenic process. The ratio of 50% of myotubes also points out that half of the cells are still not fused.

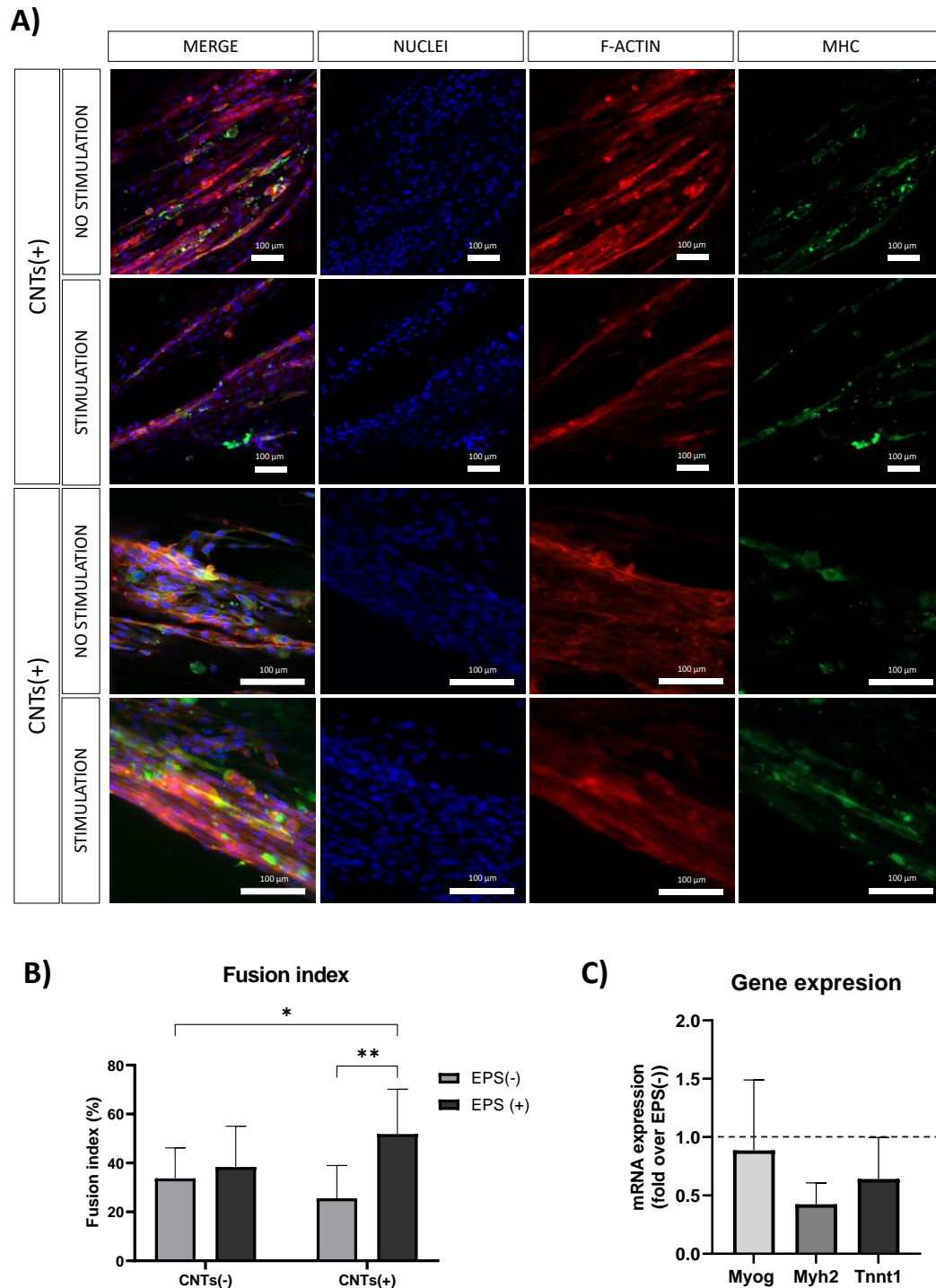


Figure 64: Electrical Pulse Stimulation (EPS) enhances myogenic maturation. A) Confocal merged images showing cells marked with phalloidin in red, cell nuclei counterstained in blue with DAPI and Mhc marked with Alexa-488 in green. Scale bars = 100 μ m. B) Graphs showing fusion index of CNTs(-) cryogels in light grey and CNTs(+) cryogels in dark grey. C) Graphs of myogenic maturation markers expression relative to the housekeeping gene ActB. Myogenin (Myog), Myosin heavy chain (Myh2), and Troponin T1 (Tnnt1). Results are mean \pm SD. * p -value = 0.05

Complementary, we study the gene expression of some myogenic markers by qPCR to further analyze the effect of EPS in myogenic maturation. We select three genes whose dynamic expression changes during the muscle maturation: Myogenin (Myog), Myosin heavy chain 2 (Myh2), and Troponin T1 (Tnnt1). Myog is a marker that is expressed in early maturation steps when myotubes are fusing. Myh2 is a middle-late maturation marker, and Tnnt1, a very late maturation marker.

By gene amplification, we could observe that Myogenin is still expressed in the EPS(+) cryogels (Figure 64C). On the other hand, Myh2 and Tnnt1, markers from late myotube maturation, are downregulated. These results may indicate that the cell constructs are in a very early stage of myogenic maturation, as Myog is still expressed, and Myh2 and Tnnt1 are less expressed.

These results can be correlated with fusion index results to confirm this hypothesis. Although we did not detect an increase of late maturation markers by qPCR, we found Mhc expression by immunostaining, a marker of myotube formation. Mhc is a cell fusion indicative, so this marker is expressed since cells started to fuse. However, it does not give any information on which step of this maturation cells are. Knowing that cells already started to fuse, we can say that cells started the myogenic differentiation, as myotubes are formed. Supporting this information, we could observe that Myog is expressed, meaning that this myogenic maturation is in a very early stage. This expression supports the point that not all the myoblasts fused into myotubes as the fusion index in EPS(+) is 51.84 ± 5.30 %. These results corroborate that cells are still in an early phase of maturation. Moreover, in late myogenic maturation steps, the expression of Myh2 and Tnnt1 is expected. In our assays we could observe a downregulation of this markers, pointing that our constructs are not fully mature.

With fusion index analysis and qPCR, we could conclude that the maturation process of the tissue already started. Taking this point as a mature step, because myogenic maturation already started, we can conclude that our scaffold enhances the cell maturation when EPS is applied.

5. DISCUSSION

Hydrogel encapsulation is the most common technique to engineer tissues. It is mainly because of its beneficial properties: high water content, mechanical adaptability, and moldability to generate desired architectures [2]. These properties allow the generation of a wide variability of matrices to generate many different tissues [44], [144], [210], [211]. However, their main limitation is their small porosity that limits nutrient and oxygen diffusion [3]. Cells encapsulated inside hydrogels in depths more than $\sim 150\text{ }\mu\text{m}$ start to suffer from hypoxia, and its viability strongly decreases [25]. It is important to note that when pancreatic islets are encapsulated inside hydrogels [47], this problem is exponentially increased due to its sizes [212]. These pancreatic islets are cell aggregations of $\sim 100\text{ }\mu\text{m}$ in diameter composed of many different cells as the insulin-secreting cells (β -cells) and the glucagon secreting cells (α -cells). Encapsulating these cell clusters limits more oxygen and nutrient diffusion, highly decreasing cell survival.

On the other hand, skeletal muscle tissue is generally encapsulated in small hydrogel bundles. Skeletal muscle is a highly aligned and multinucleated tissue that is formed from the fusion of single cells, called myoblasts, into multinucleated cells, called myotubes. One of the prerequisites to engineer skeletal muscle tissue is the alignment of the cells to prompt the myogenic maturation [40]. Generating a geometrically cued scaffold to prompt cell alignment in volumetric constructs is again highly difficult due to the scaffolds' narrow porosity that leads to low cell survival.

For generating skeletal and pancreatic tissues, cryogels have been proposed as a valid alternative to be used as scaffolds. Cryogels are microporous structures with high interconnected porosity, high diffusivity, modifiable mechanical properties, and adaptable internal pore architecture [46]. Moreover, cryogels are crosslinked at sub-zero temperatures and before cell seeding. This attractive feature allows avoiding other cell death factors related to hydrogel encapsulating, as UV light or the use of crosslinkers.

This thesis hypothesizes that cryogels will be a suitable alternative to engineering volumetric tissues, e.g., skeletal muscle and pancreatic tissue. The simple fabrication method and its interesting mechanical properties convert cryogels into a promising scaffolding option for posterior incorporation into organs-on-a-chip.

5.1 PANCREATIC TISSUE

Encapsulation of pancreatic islets is a common technique to study pancreatic tissue and β -cell function. Traditionally, pancreatic islets were encapsulated inside hydrogels, generating a scaffold with fitting properties [31], [116], [213], [214], but hindering oxygen and nutrient diffusion and having low stimulation folds. Cryogels appeared a promising alternative to overcome these limitations, due to their large pore sizes and permeation ability [74].

Despite this possible improvement, pancreatic tissue engineering entangles other essential drawbacks. Most recent studies use cadaveric or animal islets with wide variability among experiments due to the metabolic state of the animal or fluctuations in cell percentage. For this, cell lines or stem cells appeared as a valid alternative to study pancreatic tissue. Further, these studies proved that cells aggregated in spherical pseudoislets improve insulin secretion compared to monolayer cultures [111], [121], [123], [215]–[217]. To note, in this thesis, we used mouse pancreatic islets as a cryogel potential proof of concept and Ins1 β -cell line due to its proliferation ability, similar morphological characteristics, glucose-depending insulin responsivity, and well-characterized behavior [105]. Besides the promising pseudoislet formation and insulin secretion, these studies hinder the role of the pancreatic islets 3D microenvironment, not mimicking the physiological environment found in the pancreas [113], [126], [218], [219]. Here, the cryogel technique and its microporosity structure have a strong potential as a scaffolding technique to generate resemblant pseudoislets in a controlled and resembling ECM-like 3D microenvironment.

As mentioned, microporous cryogelation was the casting technique selected to engineer pancreatic tissue. Besides its large pore sizes and pore interconnectivity, cryogelation also allows controlling the pores distribution, size, and morphology. By generating a scaffold with a similar pore distribution as the pancreatic islets, we expected the pancreatic islets to infiltrate inside the scaffold and generate resemblant-sized pseudoislets.

We chose carboxymethylcellulose (CMC) as the main biomaterial For generating the scaffold to engineer pancreatic tissue,. Using CMC, the point is to avoid cell interaction with ECM cell-binding motifs that some ECM-derived biomaterials have. Avoiding this interaction, we ensure that pancreatic islets did not disaggregate due to cell attachment but anchor inside the scaffold matrix. Moreover, to generate pseudoislets is crucial to avoid cells interacting with the scaffold, enhancing cell-cell interaction and promoting cell clustering.

The first scaffold property analyzed was the pore size of the cryogels. By changing the biomaterial concentration, we could achieve different porosity size distributions. Correlating with previous results, we could observe that larger pore distributions could be achieved by decreasing the biomaterial concentration [220], [221]. So, after analyzing pore distributions of different biomaterial concentrations, 1 % CMC cryogels were chosen. In these cryogels, pore diameter ranges from few micrometers up to 150-200 μm . Besides other cryogelation materials that endorse achieving similar or even higher pore sizes [74], [222]–[224], we considered that fitting the pore size distribution with the distribution of the pancreatic islets would improve islet retention and pseudoislet size resemblance. Knowing that the pancreatic islets have an approximate diameter of 100 μm , we expected a good infiltration of both cells and islets.

Importantly, to resemble ECM pancreatic environment, the mechanical properties of the scaffold should match. Interestingly, 1% CMC cryogels has a stiffness of $0,66 \pm 0,08$ kPa. As the pancreas is a soft tissue, its stiffness ranges from 0.1 kPa to 10 kPa [176]. Pancreatic cells seem to respond properly to this low stiffness interval, as cells can increase insulin mRNA expression and glucose sensitivity [124]. Also, soft scaffolds favor cell coalescence and preserve the cluster-like organization, while in stiffer substrates, the extracellular-cell interactions cause cell scattering and loss of islet-like structure [179]. Interestingly, previous studies with magnetic resonance elastography (MRE) showed that the stiffness of the pancreas is around 1kPa [177], [178].

Another important mechanical property to study was the swelling ratio. Swelling is the scaffold's water uptake capability, an indirect measurement of pore size and pore interconnectivity. Due to its bigger and more interconnected porosity, the swelling ratio of 1% CMC cryogel is $98.14 \% \pm 0,32$. It is essential to highlight that the cryogel reaches swelling equilibrium in less than 30 minutes, implying a fast permeation. This high and fast ratio is very promising for pancreatic tissue generation. As pancreatic islets are cell aggregation of ~ 100 μm in diameter, and rapidly respond to the glucose changes, having a very interconnected structure, and high-water content will improve the protein diffusion through the scaffold. Moreover, nutrient and oxygen diffusion is a critical point in encapsulated pancreatic tissue, affecting cell survival.

Although the fast water uptake of the scaffold points to an excellent diffusion among all the scaffold, a permeability assay was performed to demonstrate it.

Using aminofluorescein for its easy read-out, we dispensed it over the cryogel on a transwell and quantified its amount that passes through in different time points. Here, we could observe that cryogel barely interacts with the fluorescein, allowing a high permeation. Combining all these parameters, we could prove that we generated a scaffold with microporous structure, highly interconnected and with good permeation properties, overcoming one of the traditional hydrogel limitations [31], [116]. Moreover, combined with the stiffness resemblance, we could prove that our scaffold highly resembles the 3D microphysiological environment of the pancreatic islets.

Once the scaffold fabrication process was optimized and characterized, the next step was to engineer pancreatic tissue and check cell behavior. Here, two different approaches were determined to study scaffold behavior and its cell interaction to engineer pancreatic tissue.

The first approach consists of seeding pancreatic islets inside the scaffold for posterior incorporation into organ-on-a-chip technology and sensing platforms. The importance of generating an organ-on-a-chip for pancreatic tissue has significant relevance in studying many insulin-released diseases. Insulin-glucose homeostasis is highly dependent on the fast triggering of insulin by the pancreatic islets. Sensing the insulin secreted continuously could give exciting information and get a bigger picture of this homeostasis between the pancreas and other tissues [12], [132]. By incorporating the scaffold with pancreatic islets inside an organ-on-a-chip, we proved that the cryogel could be easily handled to be incorporated inside microfluidic devices without suffering any damage. Moreover, we could prove that pancreatic islets maintained their beta-cell health, and cell stress markers were not overexpressed. This point was important as we could prove that cells can be anchored inside without suffering any adverse effects. Hence, a functionality experiment was performed to check if cells responded adequately to the glucose and if this insulin secretion can be sensed using different sensing platforms as traditional sandwich ELISA or an LSPR sensing platform. A glucose stimulation insulin secretion assay was performed inside a microfluidic chip to study pancreatic islets functionality. This study proved that our scaffold did not affect cell functionality, as cells responded adequately to the glucose stimulations, proving that cryogels have solid possibilities for organ-on-a-chip applications.

However, the low infiltration ratio of the islets inside the scaffold encourages us to search for other approximations to generate pancreatic tissue. To overcome the limitation in the infiltration ratio, we decided to seed single

cells inside the scaffold to generate pseudoislets by aggregating them in cell clusters. For this approximation, we used Ins1 cells due to their proliferative ability and their insulin responsivity similar to physiological [105]. The non-animal derived cells used here would be a first proof to use other cells obtained from different sources.

For this approximation, 1% CMC scaffold was also used because of the similar pore-pancreatic islets size distribution. By achieving this similarity, we expected that cells aggregate inside the pores. So, if the pores have similar sizes to the physiological pancreatic islets, a high resembling pseudoislet architecture could be achieved. In that way, we would be able to control the pseudoislet size distribution.

After seeding the cells on the cryogel, we could observe that they can infiltrate inside the scaffold and aggregate in spherical pseudoislets. To better value the decision of using CMC cryogels, we also seed cells in gelatin cryogel, where a dispersed monolayer was obtained. This point proves our hypothesis of using a non-ECM-derived biomaterial to avoid cell-binding motifs found in its structure. As gelatin presents RGD motifs, cells prefer to interact within the fiber matrix instead of themselves [225]. This behavior is not found in CMC cryogels. Moreover, we could observe that pseudoislets were found in a wide disparity of sizes, matching with the pore diameters. With this, we could accomplish the objective of obtaining similar-sized pseudoislets to the distribution of pancreatic islets found *in vivo* [97], [170]. Having this wide variability of pseudoislets is essential for glucose-insulin homeostasis as islets of different sizes behave differently [189], [226], but all are essential for the proper insulin regulation. Also, we could observe that clustered cells stop proliferating during a week of culture. Although pancreatic islets have a meager percentage of proliferation [227], [228], pseudoislets generated inside the scaffold progressively decrease this ability, generating physiologically similar cell behavior to the mature pancreatic islets found in the body.

Once we proved that we could generate pseudoislets with a proper cell architecture, we wanted to check their cell viability, identity, and functionality. A metabolic assay determined by alamarBlue test and a cell integrity study determined by Live/dead assay were used to analyze cell viability. Complementary, a gene expression performed by qPCR was studied to determine beta-cell health. Here, we could determine that our cells were highly alive inside the cryogel and maintain their beta-cell health and identity, improving previous viability results obtained with cells encapsulated inside

hydrogels [31], [116], [213]. Furthermore, a GSIS assay was performed to see if β -cell clusters can respond appropriately to glucose stimulations. As previously seen in the literature and confirming our hypothesis, we could observe that pseudoislet responses better to a glucose stimulation than monolayered distributions [122], [126], [215], [216]

Finally, we wanted to simulate diabetic conditions in our tissue by augmenting the glucose concentration of the cell culture and treating them with free fatty acids [123]. For this, mediums and palmitic treatments were applied on day 4 of culture, when pseudoislets were already formed. GSIS assay and gene expression were analyzed to analyze cell behavior.

After a GSIS assay, we could appreciate a decrease in the insulin secretory response when palmitic acid was added. This may indicate that cells metabolize palmitic acid, not responding correctly to the insulin secretions [229]. Although the folds obtained were low, we wanted to know if this lower folding when cells treated with palmitic affected the β -cell health or induced cell stress. We could appreciate an apparent loss of cell viability by analyzing the β -cell health transcription factors when cells were cultured with higher glucose levels and treated with free fatty acids. This downregulation of cell-viability expression may indicate that cells suffer some damage induced by high glucose mediums or palmitic treatment.

Cell-stress markers were analyzed by qPCR to confirm this hypothesis. Here, we could observe an evident upregulation of these stress and apoptotic markers. Interestingly, stress markers were less upregulated in cryogels than in plates. The hypothesis for these results is that palmitic easily reached the cells cultured in monolayer because of its dispersed distribution. Moreover, palmitic acid has a hydrophobic and a hydrophilic site, prompting micelles formation when dissolved in the medium. Besides palmitic is a small molecule, different sized micelles were found, and some were bigger than the pores, being a limitation for palmitic acid micelles to distribute through all the cryogel uniformly. This factor, combined with the low surface/area of the pseudoislets, leads us to think that palmitic acid did not reach equally to all the pseudoislets. Another hypothesis for this lower decreasing ratio in cryogels is the spherical architecture of the pseudoislets formed inside the cryogels. This spherical distribution protects the core cells from the palmitic acid avoiding damaging these cells. In contrast, in monolayer, the palmitic acid could reach all the cells and stress them equally. Finally, another interesting point to consider is that cells are more stressed when high glucose and palmitic are combined but being palmitic acid the primary stress

condition. These results show some correlation with previous studies [12], [123], pointing that our approach could be a promising platform to simulate diabetic conditions for further studies.

In summary, we proved that by fabricating CMC cryogels, we could generate a promising scaffold to engineer pancreatic tissue. The easy fabrication method, its tunable properties, and its mechanical stability show a promising technique to generate a scaffold for its possible incorporation into organ-on-a-chip applications. Moreover, cryogel prompts resemblant pseudoislet formation with high cell viability of the pseudoislets and enhanced cell functionality when pseudoislets were generated inside the scaffold. Finally, this whole platform has strong potential to simulate diabetic conditions.

5.2 SKELETAL MUSCLE

Unlike pancreatic islets, skeletal muscle tissue is a highly aligned tissue, formed of multinucleated and highly aligned cells called myotubes that came from the fusion of single cells, called myoblasts. A prerequisite to engineering skeletal muscle is to prompt this cell fusion. Different studies promote it by generating geometrically cued and highly aligned scaffolds [25], [146], [165]. Taking profit that the cells can sense the topography of the scaffold, we generated a highly aligned pore architecture in our scaffolds, so we enhanced the ability of the myoblasts to fuse into myotubes. For this, generating a pore anisotropy architecture in our scaffold has considerable relevance. For generating this anisotropy, a freezing directionality was applied, so the ice nucleation and growing occurs only in one axis [230]. Different set-ups were studied to achieve this directionality, but finally, cryogels were cast over carbonic ice and with a thermal polypropylene isolator around the PDMS mold.

Another interesting point to enhance cell directionality was the biomaterials used. One common approach in scaffolding is combining naturally-ECM-derived biomaterials with mechanically stable biomaterials [231]–[236]. The first ones are used to devote to the cells of critical biochemical cues. In skeletal muscle, where cell guidance has significant relevancy, the cell attachment property has a vital role in enhancing cell fusion. However, ECM-derived biomaterials have poor mechanical stability. Non-mammalian cell-degradable biomaterials were used to solve this drawback. Here, gelatin was used as an ECM-derived biomaterial, combined with CMC, to improve the

gelatin's scaffolds durability and low mechanical properties. Mainly gelatin is one of the most used biomaterials in tissue engineering and has cell-binding motifs in its structure [24]. On the other hand, cellulose is less studied, but its easy obtention turns it into a promising biomaterial to be used as a mechanical supporter. Moreover, previous studies in the laboratory [25] showed good biocompatibility and good bioactivity of these biomaterials for skeletal muscle tissue engineering. The promising features of this biocomposite for hydrogel encapsulation make us think of the potential use of this combination of biomaterials for cryogel fabrication.

Skeletal muscle is also an electrically active tissue, as it can contract for motion and support of the whole body. However, natural biomaterials lack this essential property as they are not electrically conductive. As proven in previous studies, generating an electrically conductive biomaterial and applying electrical pulse stimulations [77], [237], [238] improves cell maturation and contraction. These improved electrical properties are often achieved by incorporating some conductive particles into the scaffold matrix. Different particles have been studied, as gold nano-wires or carbon nanotubes [146], [239]. In this thesis, we decided to incorporate carbon nanotubes because its widely proved biocompatibility and non-toxicity [150].

To engineer skeletal muscle using cryogels, 3% gelatin:CMC cryogel (2% gelatin:1% CMC) was fabricated. This percentage of biomaterial was chosen as the lowest mechanically stable material concentration. Due to the freezing directionality, these cryogels have a pore diameter distribution that ranges from few micrometers up to $\sim 130\text{ }\mu\text{m}$ micrometers. However, most of the pores are between $30\text{ }\mu\text{m}$ up to $75\text{ }\mu\text{m}$ in range, and pores out of this interval are much less common. This pore range is enough for cell infiltration. Moreover, we could appreciate that tubular pores are formed uniaxially, generating a very aligned pore architecture. This feature is an essential feature to engineer skeletal muscle tissue, as skeletal muscle tissue needs high alignment and super organization to differentiate from myoblast into myotubes. Despite there are other techniques to achieve this alignment to enhance cell fusion, like bioprinting [240], stamping [174], [241], or stretching [242], our technique allows us to enhance this alignment using surface directionality, as some 2D approaches used to generate this alignment without encapsulating [242]–[245]. Combining 3D directionality plus millimeter sized-scaffold, we could obtain a good scaffold to engineer highly organized tissue, like skeletal muscle. Moreover, the pore architecture will not limit myotube formation, as myotubes are not wider than $30\text{ }\mu\text{m}$ [165], [171]. Cryogelation shows a strong and non-harmful technique to generate

scaffolds, with higher pore distribution, a synonym of higher nutrient diffusion, and low confinement of the cells that implies fewer difficulties in proliferation and migration.

Once determined and optimized the fabrication set-up and biomaterial concentrations, we could characterize the mechanical properties of the cryogels. One of the meaningful properties of a scaffold is stiffness. This property is attractive as the scaffold aims to be as more similar as possible to the extracellular matrix properties. Here, because of the pore architecture, different stiffness may be achieved depending on the directionality of the compression. When the compression is applied parallelly to the anisotropic structure, the stiffness is higher as all the fibers challenge the compression. However, if compression is applied perpendicular to the fiber architecture, the stiffness decreases, as there are empty spaces due to pore morphology that can be compressed easily. Also, the addition of carbon nanotubes (CNT) did not change this axial property. All this data shown is another indirect measurement of the well-formed pore anisotropy. Remarkably, the stiffness of the cryogel shows *in vivo* similarity mechanical properties [174].[180], around 12 kPa stiffness, while traditional hydrogels with the same amount of material have less *in vivo* resemblance [240].[246]. However, previous studies proved that stiffness from 1 kPa up to 10 kPa is suitable for engineer skeletal muscle [247].

Another essential feature of the scaffolds is their high water content. This property is highly correlated with pore interconnectivity. It informs how water can colonize all the accessible pores of our scaffold. High swelling ratios are found in anisotropic scaffolds, both with and without CNT. Besides indicating that the scaffold has high-water content, this property also indicates that it can rapidly reach all the pores, meaning good interconnectivity. These results are promising as the high interconnectivity will allow the cell culture medium to reach all the scaffold pores, enhancing cell viability.

Electric stimulation improves *in vitro* myotube maturation [183]. Unfortunately, most of the scaffolds used for tissue engineering have low conductivity, and therefore applying electrical stimulation to enhance myogenic maturation is poorly effective. We incorporated CNTs into our cryogels to enhance their electrical properties. Here, we could prove that incorporating CNT enhanced the scaffold's conductivity without affecting other essential features. However, there is a significant disparity in the literature about electrically conductive scaffolds. In previous electrically

stimulated scaffolds for skeletal muscle tissue engineering studies, conductivities from 8 mS/m up to 6 S/m were achieved, and all enhanced the maturation of the tissue [67]–[70].

Once we proved that the scaffold has the desired properties, we generated the tissue inside it. Nevertheless, first, different cell behavior experiments were performed. Despite the adequate pore sizes, the colonization of the cells through the scaffold was determined by taking confocal images in different depths. Equally, cell alignment was tracked because, as mentioned, it is one of the trivial points in skeletal muscle tissue engineering [248] [249]. In our case, by generating a highly anisotropic structure forcing ice nucleation in only one axis, the scaffold has highly aligned tubular pores, and cells can infiltrate inside it, colonize all the scaffold and align following the pore directionality.

Previous studies proved that gelatin is a well-established biomaterial [25], [250]–[253], CMC is biocompatible [254]–[256], and CNT does not show any toxicity [150]. Despite these facts, we wanted to check cell viability inside the scaffold due to the novelty of the casting and seeding techniques. It is important to highlight, the viability ratio remains over 90% of live cells in both cryogels, proving that gelatin:CMC composite allows cell culturing and that CNT did not have any cytotoxic effect [257]–[206]. These high viability results are also due to the casting technique that allows to seed cells without suffering any damage due to the crosslinking process. Usually, encapsulation of the cells inside hydrogels implies the polymerization of the matrix using external crosslinkers like UV light, chemical reagents, or temperature changes. This exposition to different crosslinkers could damage these cells. Cryogelation technique can solve this main drawback, as scaffold polymerization occurs before seeding. Moreover, the pore size and the high pore distribution, which leads to a high nutrient diffusion, also positively affects the high cell viability. Remarkably, viable cells were found in all the scaffold, meaning that the cells could infiltrate deeply inside it. These results points the possibility to engineer bigger engineered muscles taking profit from the microporous architecture of the scaffold.

Finally, Electrical Pulse Stimulation (EPS) was applied to prove that this new electrically improved composite enhances the myogenic maturation of the C2C12 myoblasts. On the last day, 12 hours of EPS were applied to improve the myogenic maturation of the cells. We could observe that the cells fused better in EPS(+), meaning that the myogenic differentiation process started and was improved when EPS was applied. However, if we check late

maturation transcription markers we do not see an increase in expression, meaning that cells are not fully mature. One hypothesis regarding this results is the possible insufficient stimulation regime applied, due to limitations of the function generator used. However, as cells fused better when EPS was applied, we can conclude that our scaffold supports an improvement of the early myogenic maturation steps.

In summary, we have generated a scaffold with highly anisotropy microporous architecture and electrically conductive that allow cell alignment and survival for skeletal muscle tissue engineering. Moreover, we could prove that applying an EPS enhances the primary steps of the myogenic differentiation process.

6. CONCLUSIONS

6.1 CONCLUSIONS

An increasing need to engineer advanced 3D scaffolds for tissue engineering has emerged to provide cellular structural support and mimic the complicated physical and biochemical properties of the native extracellular matrix. With this improvement, more resemblance tissues can be engineered for many applications as drug screening or disease modeling. Many tissues have been generated in the laboratory, but the main limitation for tissue engineering is the lack of proper nutrients and oxygen diffusion in micrometers size tissues. In this thesis, a novel scaffolding approach was established based on microporous size scaffolds to fit skeletal muscle and pancreatic cells. The research core was developed in a consistent part of this Ph.D. project that was organized in two complementary phases.

Pancreas, (i) particular attention must be paid when engineering islet-like structures as an adequate round-shaped islet architecture to maintain and improve β -cell functionality. Besides, the scaffold's diffusion and permeability are crucial features for islets secretion and survivability. Skeletal muscle, (ii) to engineer skeletal muscle in a volumetric size is crucial to control the scaffold's external morphology and the internal pore morphology and size in a highly controlled way.

The resulting conclusions and perspectives for future investigations are detailed below.

- We have developed new cryogel composites with specific pore architecture to engineer pancreatic and skeletal muscle tissue. We studied the mechanical properties of both cryogels. We could prove that changing material concentrations or freezing set-up different properties can be modulated. Moreover, we demonstrate that our cryogels have high pore interconnectivity and high permeability. We could also demonstrate that our cryogels have proper stiffness, resembling the extracellular matrix of both tissues. Finally, we could demonstrate that the incorporation of carbon nanotubes increases scaffolds conductive properties without affecting other essential properties for skeletal muscle tissue.
- For pancreatic tissue, we demonstrate that our CMC cryogel with random pores allows and enhances cell aggregation in pseudoislet forms. Moreover, our cryogel pores favor the formation of pseudoislets

in resemblant sizes as the pancreatic islets. Furthermore, cell viability is not negatively affected when cells seeded inside the scaffold, and beta-cell identity is improved compared to monolayer distributions. Finally, pseudoislets respond better to glucose stimulations proving an enhanced functionality compared to cells seeded in monolayer distributions in gelatin cryogels.

- For skeletal muscle, we developed a new set-up to generate gelatin:CMC scaffolds with highly aligned structure and with pore dimensions that allow cell infiltration. We proved that our scaffold prompts cell alignment following the pore architecture. Moreover, we could demonstrate that seeding cells inside the scaffold did not affect cell viability, and cells could colonize all the scaffold structure. Finally, we demonstrate that by applying an electrical pulse stimulation, we achieved a better fusion index and improved the early stages of myogenic maturation.
- Our results proved that cryogels are a suitable technique to generate microporous scaffolds with high potential in tissue engineering. Cryogels exciting properties, as adjustable pore architecture, elevate pore interconnectivity, stiffness, or high swelling ratio allows the generation of volumetric tissues without affecting cell viability. Moreover, its easy handleability and its simple and cost-effective fabrication method make this casting technique an attractive method to generate scaffolds for volumetric tissue engineering for multiple applications as organ-on-a-chip.

6.2 FUTURE WORK

The obtained results encourage us to exploit this model as a tool for disease modeling, such as type 2 diabetes. Moreover, the possibility to generate co-cultures opens a wide possibility of options to study how this two tissues crosstalk. These experiments could be done in static, or in organs-on-a-chip, as we proved the feasibility of this incorporation. The integration inside organs-on-a-chip, combined with possible biosensing approaches would allow to study the metabolism of these tissues in real time. Another option to continue this thesis should be to explore our system with primary human cells or tissues, for final validation.

And last but not least, another possibility would be using the cryogelation technique to generate other important tissues related with T2D as fat tissue or hepatic tissue, for posterior studies as the ones proposed above.

7. BIBLIOGRAPHY

- [1] International Diabetes Federation, *9th IDF diabetes atlas*. 2019.
- [2] K. Yue *et al.*, "Synthesis, properties, and biomedical applications of gelatin methacryloyl (GelMA) hydrogels," *Biomaterials*, vol. 73, no. 3, pp. 254–271, 2016, doi: 10.1016/j.biomaterials.2015.08.045.Synthesis.
- [3] M. K. Lee, M. H. Rich, K. Baek, J. Lee, and H. Kong, "Bioinspired tuning of hydrogel permeability-rigidity dependency for 3D cell culture," *Sci. Rep.*, vol. 5, pp. 1–7, 2015, doi: 10.1038/srep08948.
- [4] R. Langer and J. P. Vacanti, "Tissue engineering," *Science (80-.)*, vol. 260, no. 5110, pp. 920 LP – 926, May 1993, doi: 10.1126/science.8493529.
- [5] A. Shafiee and A. Atala, "Tissue Engineering: Toward a New Era of Medicine," *Annu. Rev. Med.*, vol. 68, pp. 29–40, 2017, doi: 10.1146/annurev-med-102715-092331.
- [6] A. C. Hauge-Evans, P. E. Squires, S. J. Persaud, and P. M. Jones, "Pancreatic β -cell-to- β -cell interactions are required for integrated responses to nutrient stimuli: Enhanced Ca^{2+} and insulin secretory responses of MIN6 pseudoislets," *Diabetes*, vol. 48, no. 7, pp. 1402–1408, 1999, doi: 10.2337/diabetes.48.7.1402.
- [7] K. Yoshioka, A. Ito, Y. Kawabe, and M. Kamihira, "Novel neuromuscular junction model in 2D and 3D myotubes co-cultured with induced pluripotent stem cell-derived motor neurons," *J. Biosci. Bioeng.*, vol. 129, no. 4, pp. 486–493, 2020, doi: 10.1016/j.jbiosc.2019.10.004.
- [8] D. E. Discher, "Tissue Cells Feel and Respond to the Stiffness of Their Substrate," *Science (80-.)*, vol. 310, no. 5751, pp. 1139–1143, Nov. 2005, doi: 10.1126/science.1116995.
- [9] K. Von Der Mark, V. Gauss, H. Von Der Mark, and P. Müller, "Relationship between cell shape and type of collagen synthesised as chondrocytes lose their cartilage phenotype in culture," *Nature*, vol. 267, no. 5611, pp. 531–532, Jun. 1977, doi: 10.1038/267531a0.
- [10] H. B. Wang *et al.*, "Creation of highly aligned electrospun poly-L-lactic acid fibers for nerve regeneration applications," *J. Neural Eng.*, vol. 6, no. 1, 2009, doi: 10.1088/1741-2560/6/1/016001.
- [11] S. Ostrovidov *et al.*, "Gelatin-Polyaniline Composite Nanofibers Enhanced Excitation-Contraction Coupling System Maturation in Myotubes," *ACS Appl. Mater. Interfaces*, vol. 9, no. 49, pp. 42444–42458, 2017, doi: 10.1021/acsami.7b03979.
- [12] J. Barlow and T. P. J. Solomon, "Conditioned media from contracting skeletal muscle potentiates insulin secretion and enhances mitochondrial

- energy metabolism of pancreatic beta-cells," *Metabolism.*, vol. 91, pp. 1–9, 2019, doi: 10.1016/j.metabol.2018.11.004.
- [13] A. Bettadapur *et al.*, "Prolonged Culture of Aligned Skeletal Myotubes on Micromolded Gelatin Hydrogels," *Sci. Rep.*, vol. 6, 2016, doi: 10.1038/srep28855.
- [14] A. Keirouz, M. Chung, J. Kwon, G. Fortunato, and N. Radacsi, "2D and 3D electrospinning technologies for the fabrication of nanofibrous scaffolds for skin tissue engineering: A review," *Wiley Interdiscip. Rev. Nanomedicine Nanobiotechnology*, vol. 12, no. 4, pp. 1–32, 2020, doi: 10.1002/wnan.1626.
- [15] T. Hoshiba and N. Yokoyama, "Decellularized extracellular matrices derived from cultured cells at stepwise myogenic stages for the regulation of myotube formation," *Biochim. Biophys. Acta - Mol. Cell Res.*, vol. 1867, no. 4, 2020, doi: 10.1016/j.bbamcr.2020.118658.
- [16] H. Takahashi, T. Shimizu, M. Nakayama, M. Yamato, and T. Okano, "The use of anisotropic cell sheets to control orientation during the self-organization of 3D muscle tissue," *Biomaterials*, vol. 34, no. 30, pp. 7372–7380, 2013, doi: 10.1016/j.biomaterials.2013.06.033.
- [17] J. Barlow and T. P. J. Solomon, "Conditioned media from contracting skeletal muscle potentiates insulin secretion and enhances mitochondrial energy metabolism of pancreatic beta-cells," *Metabolism.*, vol. 91, pp. 1–9, 2019, doi: 10.1016/j.metabol.2018.11.004.
- [18] D. Rajendran, A. Hussain, D. Yip, A. Parekh, A. Shrirao, and C. H. Cho, "Long-term liver-specific functions of hepatocytes in electrospun chitosan nanofiber scaffolds coated with fibronectin," *J. Biomed. Mater. Res. Part A*, vol. 105, no. 8, pp. 2119–2128, Aug. 2017, doi: 10.1002/jbm.a.36072.
- [19] M. Kapałczyńska *et al.*, "2D and 3D cell cultures – a comparison of different types of cancer cell cultures," *Arch. Med. Sci.*, vol. 14, no. 4, pp. 910–919, 2018, doi: 10.5114/aoms.2016.63743.
- [20] E. Knight and S. Przyborski, "Advances in 3D cell culture technologies enabling tissue-like structures to be created in vitro," *J. Anat.*, vol. 227, no. 6, pp. 746–756, 2015, doi: 10.1111/joa.12257.
- [21] C. F. Marques, G. S. Diogo, S. Pina, J. M. Oliveira, and T. H. Silva, "Collagen-based bioinks for hard tissue engineering applications : a comprehensive review," *J. Mater. Sci. Mater. Med.*, 2019, doi: 10.1007/s10856-019-6234-x.
- [22] K. Y. Lee and D. J. Mooney, "Hydrogels for tissue engineering," *Chem. Rev.*, vol. 101, no. 7, pp. 1869–1879, 2001, doi: 10.1021/cr000108x.

- [23] M. F. M. Busra and Y. Lokanathan, "Recent Development in the Fabrication of Collagen Scaffolds for Tissue Engineering Applications: A Review.," *Curr. Pharm. Biotechnol.*, vol. 20, no. 12, pp. 992–1003, 2019, doi: 10.2174/1389201020666190731121016.
- [24] S. Afewerki, A. Sheikhi, S. Kannan, S. Ahadian, and A. Khademhosseini, "Gelatin-polysaccharide composite scaffolds for 3D cell culture and tissue engineering: Towards natural therapeutics," *Bioeng. Transl. Med.*, vol. 4, no. 1, pp. 96–115, 2019, doi: 10.1002/btm2.10124.
- [25] A. García-Lizarribar, X. Fernández-Garibay, F. Velasco-Mallorquí, A. G. Castaño, J. Samitier, and J. Ramon-Azcon, "Composite Biomaterials as Long-Lasting Scaffolds for 3D Bioprinting of Highly Aligned Muscle Tissue," *Macromol. Biosci.*, vol. 18, no. 10, p. 1800167, Oct. 2018, doi: 10.1002/mabi.201800167.
- [26] P. M. Gilbert *et al.*, "Substrate elasticity regulates skeletal muscle stem cell self-renewal in culture," *Science (80-.)*, vol. 329, no. 5995, pp. 1078–1081, 2010, doi: 10.1126/science.1191035.
- [27] M. Santoro, S. R. Shah, J. L. Walker, and A. G. Mikos, "Poly(lactic acid) nanofibrous scaffolds for tissue engineering," *Adv. Drug Deliv. Rev.*, vol. 107, no. 3, pp. 206–212, Dec. 2016, doi: 10.1016/j.addr.2016.04.019.
- [28] J. Zhu, "Bioactive modification of poly(ethylene glycol) hydrogels for tissue engineering," *Biomaterials*, vol. 31, no. 17, pp. 4639–4656, 2010, doi: 10.1016/j.biomaterials.2010.02.044.
- [29] N. Siddiqui, S. Asawa, B. Birru, R. Baadhe, and S. Rao, "PCL-Based Composite Scaffold Matrices for Tissue Engineering Applications," *Mol. Biotechnol.*, vol. 60, no. 7, pp. 506–532, 2018, doi: 10.1007/s12033-018-0084-5.
- [30] M. Generali, D. Kehl, A. K. Capulli, K. K. Parker, S. P. Hoerstrup, and B. Weber, "Comparative analysis of poly-glycolic acid-based hybrid polymer starter matrices for in vitro tissue engineering," *Colloids Surfaces B Biointerfaces*, vol. 158, pp. 203–212, 2017, doi: 10.1016/j.colsurfb.2017.06.046.
- [31] S. Duin *et al.*, "3D Bioprinting of Functional Islets of Langerhans in an Alginate/Methylcellulose Hydrogel Blend," *Adv. Healthc. Mater.*, vol. 8, no. 7, pp. 1–14, 2019, doi: 10.1002/adhm.201801631.
- [32] A. Vila *et al.*, "Hydrogel co-networks of gelatine methacrylate and poly(ethylene glycol) diacrylate sustain 3D functional in vitro models of intestinal mucosa," *Biofabrication*, vol. 12, no. 2, 2020, doi: 10.1088/1758-5090/ab5f50.
- [33] R. H. Schmedlen, K. S. Masters, and J. L. West, "Photocrosslinkable polyvinyl alcohol hydrogels that can be modified with cell adhesion peptides for use

- in tissue engineering," *Biomaterials*, vol. 23, no. 22, pp. 4325–4332, 2002, doi: 10.1016/S0142-9612(02)00177-1.
- [34] L. Van den Broeck, S. Piluso, A. H. Soultan, M. De Volder, and J. Patterson, "Cytocompatible carbon nanotube reinforced polyethylene glycol composite hydrogels for tissue engineering," *Mater. Sci. Eng. C*, vol. 98, no. July 2018, pp. 1133–1144, 2019, doi: 10.1016/j.msec.2019.01.020.
- [35] N. Reddy, R. Reddy, and Q. Jiang, "Crosslinking biopolymers for biomedical applications," *Trends Biotechnol.*, vol. 33, no. 6, pp. 362–369, 2015, doi: 10.1016/j.tibtech.2015.03.008.
- [36] W. Hu, Z. Wang, Y. Xiao, S. Zhang, and J. Wang, "Advances in crosslinking strategies of biomedical hydrogels," *Biomater. Sci.*, vol. 7, no. 3, pp. 843–855, 2019, doi: 10.1039/c8bm01246f.
- [37] J. R. Choi, K. W. Yong, J. Y. Choi, and A. C. Cowie, "Recent advances in photo-crosslinkable hydrogels for biomedical applications," *Biotechniques*, vol. 66, no. 1, pp. 40–53, Jan. 2019, doi: 10.2144/btn-2018-0083.
- [38] A. Oryan, A. Kamali, A. Moshiri, H. Baharvand, and H. Daemi, "Chemical crosslinking of biopolymeric scaffolds: Current knowledge and future directions of crosslinked engineered bone scaffolds," *Int. J. Biol. Macromol.*, vol. 107, no. PartA, pp. 678–688, 2018, doi: 10.1016/j.ijbiomac.2017.08.184.
- [39] R. Pereira, A. Carvalho, D. C. Vaz, M. H. Gil, A. Mendes, and P. Bártolo, "Development of novel alginate based hydrogel films for wound healing applications," *Int. J. Biol. Macromol.*, vol. 52, no. 1, pp. 221–230, 2013, doi: 10.1016/j.ijbiomac.2012.09.031.
- [40] S. Ostrovidov *et al.*, "3D Bioprinting in Skeletal Muscle Tissue Engineering," *Small*, vol. 15, no. 24, pp. 1–14, 2019, doi: 10.1002/sml.201805530.
- [41] C. Mandrycky, Z. Wang, K. Kim, and D. H. Kim, "3D bioprinting for engineering complex tissues," *Biotechnol. Adv.*, vol. 34, no. 4, pp. 422–434, 2016, doi: 10.1016/j.biotechadv.2015.12.011.
- [42] M. A. Ortega *et al.*, "Muscle-on-a-chip with an on-site multiplexed biosensing system for in situ monitoring of secreted IL-6 and TNF- α ," *Lab Chip*, vol. 19, no. 15, pp. 2568–2580, 2019, doi: 10.1039/C9LC00285E.
- [43] T. Desai and L. D. Shea, "Advances in islet encapsulation technologies," *Nat. Rev. Drug Discov.*, vol. 16, no. 5, pp. 338–350, 2017, doi: 10.1038/nrd.2016.232.
- [44] A. G. Castaño, M. García-Díaz, N. Torras, G. Altay, J. Comelles, and E. Martínez, "Dynamic photopolymerization produces complex microstructures on hydrogels in a moldless approach to generate a 3D

- intestinal tissue model,” *Biofabrication*, vol. 11, no. 2, 2019, doi: 10.1088/1758-5090/ab0478.
- [45] C. Kengla, S. J. Lee, J. J. Yoo, and A. Atala, *3-D bioprinting technologies for tissue engineering applications*. 2019.
- [46] A. Bédier *et al.*, “A compressible scaffold for minimally invasive delivery of large intact neuronal networks,” *Adv. Healthc. Mater.*, vol. 4, no. 2, pp. 301–312, Jan. 2015, doi: 10.1002/adhm.201400250.
- [47] R. Cao, E. Avgoustiniatos, K. Papas, P. de Vos, and J. R. T. Lakey, “Mathematical predictions of oxygen availability in micro- and macro-encapsulated human and porcine pancreatic islets,” *J. Biomed. Mater. Res. - Part B Appl. Biomater.*, vol. 108, no. 2, pp. 343–352, 2020, doi: 10.1002/jbm.b.34393.
- [48] A. L. Farris, A. N. Rindone, and W. L. Grayson, “Oxygen delivering biomaterials for tissue engineering,” *J. Mater. Chem. B*, vol. 4, no. 20, pp. 3422–3432, 2016, doi: 10.1039/c5tb02635k.
- [49] M. Gholipourmalekabadi, S. Zhao, B. S. Harrison, M. Mozafari, and A. M. Seifalian, “Oxygen-Generating Biomaterials: A New, Viable Paradigm for Tissue Engineering?,” *Trends Biotechnol.*, vol. 34, no. 12, pp. 1010–1021, 2016, doi: 10.1016/j.tibtech.2016.05.012.
- [50] T. M. A. Henderson, K. Ladewig, D. N. Haylock, K. M. McLean, and A. J. O’Connor, “Cryogels for biomedical applications,” *Journal of Materials Chemistry B*, vol. 1, no. 21. Royal Society of Chemistry, pp. 2682–2695, Jun. 07, 2013, doi: 10.1039/c3tb20280a.
- [51] A. Memic *et al.*, “Latest Advances in Cryogel Technology for Biomedical Applications,” *Adv. Ther.*, vol. 2, no. 4, p. 1800114, 2019, doi: 10.1002/adtp.201800114.
- [52] G. Petzold and J. M. Aguilera, “Ice morphology: Fundamentals and technological applications in foods,” *Food Biophys.*, vol. 4, no. 4, pp. 378–396, 2009, doi: 10.1007/s11483-009-9136-5.
- [53] D. L., S. Mishra, and R. Paul, “Cirrus Clouds and Climate Engineering: New Findings on Ice Nucleation and Theoretical Basis,” *Planet Earth 2011 - Glob. Warm. Challenges Oppor. Policy Pract.*, no. June 2014, 2011, doi: 10.5772/24664.
- [54] H. Zhang, C. Liu, L. Chen, and B. Dai, “Control of ice crystal growth and its effect on porous structure of chitosan cryogels,” *Chem. Eng. Sci.*, vol. 201, pp. 50–57, 2019, doi: 10.1016/j.ces.2019.02.026.
- [55] X. Wu *et al.*, “Preparation of aligned porous gelatin scaffolds by unidirectional freeze-drying method,” *Acta Biomater.*, vol. 6, no. 3, pp.

- 1167–1177, 2010, doi: 10.1016/j.actbio.2009.08.041.
- [56] S. Kwon *et al.*, “Bioglass-Incorporated Methacrylated Gelatin Cryogel for Regeneration of Bone Defects,” *Polymers (Basel)*, vol. 10, no. 8, p. 914, Aug. 2018, doi: 10.3390/polym10080914.
 - [57] M. Ghaderi Gandomani, A. Sahebghadam Lotfi, D. Kordi Tamandani, S. Arjmand, and S. Alizadeh, “The enhancement of differentiating adipose derived mesenchymal stem cells toward hepatocyte like cells using gelatin cryogel scaffold,” *Biochem. Biophys. Res. Commun.*, vol. 491, no. 4, pp. 1000–1006, 2017, doi: 10.1016/j.bbrc.2017.07.167.
 - [58] A. Sharma, S. Bhat, V. Nayak, and A. Kumar, “Efficacy of supermacroporous poly(ethylene glycol)-gelatin cryogel matrix for soft tissue engineering applications,” *Mater. Sci. Eng. C*, vol. 47, pp. 298–312, 2015, doi: 10.1016/j.msec.2014.11.031.
 - [59] M. Razavi, R. Primavera, B. D. Kevadiya, J. Wang, P. Buchwald, and A. S. Thakor, “A Collagen Based Cryogel Bioscaffold that Generates Oxygen for Islet Transplantation,” *Adv. Funct. Mater.*, vol. 30, no. 15, p. 1902463, Apr. 2020, doi: 10.1002/adfm.201902463.
 - [60] S. C. Rodrigues, C. L. Salgado, A. Sahu, M. P. Garcia, M. H. Fernandes, and F. J. Monteiro, “Preparation and characterization of collagen-nanohydroxyapatite biocomposite scaffolds by cryogelation method for bone tissue engineering applications,” *J. Biomed. Mater. Res. - Part A*, vol. 101 A, no. 4, pp. 1080–1094, 2013, doi: 10.1002/jbm.a.34394.
 - [61] M. Jurga *et al.*, “The performance of laminin-containing cryogel scaffolds in neural tissue regeneration,” *Biomaterials*, vol. 32, no. 13, pp. 3423–3434, 2011, doi: 10.1016/j.biomaterials.2011.01.049.
 - [62] S. a Bencherif *et al.*, “Injectable preformed scaffolds with shape-memory properties,” *Proc. Natl. Acad. Sci. U. S. A.*, vol. 109, no. 48, pp. 19590–5, 2012, doi: 10.1073/pnas.1211516109.
 - [63] T. Gç E Kutlusoy, B. Oktay, K. Apohan, M. Süleymano˘ Glu B, and S. E. Kuruca, “Chitosan-co-Hyaluronic acid porous cryogels and their application in tissue engineering,” *Int. J. Biol. Macromol.*, vol. 103, pp. 366–378, 2017, doi: 10.1016/j.ijbiomac.2017.05.067.
 - [64] A. Béduer *et al.*, “Additive manufacturing of hierarchical injectable scaffolds for tissue engineering,” *Acta Biomater.*, vol. 76, pp. 71–79, 2018, doi: 10.1016/j.actbio.2018.05.056.
 - [65] A. Golunova *et al.*, “N-(2-Hydroxypropyl) methacrylamide based cryogels - Synthesis and biomimetic modification for stem cell applications,” *Physiol. Res.*, vol. 64, pp. S19–S27, 2015, doi: 10.33549/physiolres.933134.

- [66] Y. Hwang, C. Zhang, and S. Varghese, "Poly(ethylene glycol) cryogels as potential cell scaffolds: effect of polymerization conditions on cryogel microstructure and properties," *J. Mater. Chem.*, vol. 20, no. 2, pp. 345–351, 2010, doi: 10.1039/B917142H.
- [67] T. Dispinar, W. Van Camp, L. J. De Cock, B. G. De Geest, and F. E. Du Prez, "Redox-Responsive Degradable PEG Cryogels as Potential Cell Scaffolds in Tissue Engineering," *Macromol. Biosci.*, vol. 12, no. 3, pp. 383–394, 2012, doi: 10.1002/mabi.201100396.
- [68] Y. Hwang, N. Sangaj, and S. Varghese, "Interconnected Macroporous Poly(Ethylene Glycol) Cryogels as a Cell Scaffold for Cartilage Tissue Engineering," *Tissue Eng. Part A*, vol. 16, no. 10, pp. 3033–3041, Oct. 2010, doi: 10.1089/ten.tea.2010.0045.
- [69] J. Van Rie *et al.*, "Cryogel-PCL combination scaffolds for bone tissue repair," *J. Mater. Sci. Mater. Med.*, vol. 26, no. 3, 2015, doi: 10.1007/s10856-015-5465-8.
- [70] R. L. Youngblood, J. P. Sampson, K. R. Lebioda, and L. D. Shea, "Microporous scaffolds support assembly and differentiation of pancreatic progenitors into β -cell clusters," *Acta Biomater.*, vol. 96, pp. 111–122, 2019, doi: 10.1016/j.actbio.2019.06.032.
- [71] D. Singh, V. Nayak, and A. Kumar, "Proliferation Of Myoblast Skeletal Cells On Three-Dimensional Supermacroporous Cryogels," *Int. J. Biol. Sci.*, vol. 6, no. 4, pp. 371–381, 2010, doi: 10.7150/ijbs.6.371.
- [72] S. Muthyala, R. R. Bhonde, and P. D. Nair, "Cytocompatibility studies of mouse pancreatic islets on gelatin-PVP semi IPN scaffolds in vitro: Potential implication towards pancreatic tissue engineering," *Islets*, vol. 2, no. 6, pp. 357–366, 2010, doi: 10.4161/isl.2.6.13765.
- [73] P. Petrov, P. Mokreva, I. Kostov, V. Uzunova, and R. Tzoneva, "Novel electrically conducting 2-hydroxyethylcellulose/polyaniline nanocomposite cryogels: Synthesis and application in tissue engineering," *Carbohydr. Polym.*, vol. 140, pp. 349–355, 2016, doi: 10.1016/j.carbpol.2015.12.069.
- [74] D. J. Borg *et al.*, "Macroporous biohybrid cryogels for co-housing pancreatic islets with mesenchymal stromal cells," *Acta Biomater.*, vol. 44, pp. 178–187, 2016, doi: 10.1016/j.actbio.2016.08.007.
- [75] J. Kumari, A. K. Teotia, A. A. Karande, and A. Kumar, "A minimally-invasive cryogel based approach for the development of human ectopic liver in a mouse model," *J. Biomed. Mater. Res. - Part B Appl. Biomater.*, vol. 108, no. 3, pp. 1022–1032, 2020, doi: 10.1002/jbm.b.34454.
- [76] L. A. Low, C. Mummery, B. R. Berridge, C. P. Austin, and D. A. Tagle, "Organs-on-chips: into the next decade," *Nature Reviews Drug Discovery*. Nature

- Research, 2020, doi: 10.1038/s41573-020-0079-3.
- [77] A. Abbott, “Animal-research data show effects of EU’s tough regulations,” *Nature*, Feb. 2020, doi: 10.1038/d41586-020-00352-6.
 - [78] S. N. Bhatia and D. E. Ingber, “Microfluidic organs-on-chips,” *Nat. Biotechnol.*, vol. 32, no. 8, pp. 760–772, 2014, doi: 10.1038/nbt.2989.
 - [79] D. E. I. Dongeun Huh, Benjamin D. Matthews, Akiko Mammoto, Martín Montoya-Zavala, Hong Yuan Hsin, “Reconstituting Organ-Level Lung,” *Science (80-.)*, no. June, pp. 1662–1668, 2010.
 - [80] A. Bein *et al.*, “Microfluidic Organ-on-a-Chip Models of Human Intestine,” *Cmgh*, vol. 5, no. 4, pp. 659–668, 2018, doi: 10.1016/j.jcmgh.2017.12.010.
 - [81] K. J. Jang *et al.*, “Liver-Chip: Reproducing Human and Cross-Species Toxicities,” *bioRxiv*, 2019, doi: 10.1101/631002.
 - [82] A. Mathur *et al.*, “Human iPSC-based cardiac microphysiological system for drug screening applications,” *Sci. Rep.*, vol. 5, pp. 1–7, 2015, doi: 10.1038/srep08883.
 - [83] A. Essaouiba *et al.*, “Microwell-based pancreas-on-chip model enhances genes expression and functionality of rat islets of Langerhans,” *Mol. Cell. Endocrinol.*, vol. 514, no. January, p. 110892, 2020, doi: 10.1016/j.mce.2020.110892.
 - [84] E. J. Weber *et al.*, “Human kidney on a chip assessment of polymyxin antibiotic nephrotoxicity,” *JCI Insight*, vol. 3, no. 24, pp. 1–17, Dec. 2018, doi: 10.1172/jci.insight.123673.
 - [85] A. Essaouiba *et al.*, “Development of a pancreas-liver organ-on-chip coculture model for organ-to-organ interaction studies,” *Biochem. Eng. J.*, vol. 164, no. August, 2020, doi: 10.1016/j.bej.2020.107783.
 - [86] H. Tian *et al.*, “A Novel Tissue-Based Liver–Kidney-on-a-Chip Can Mimic Liver Tropism of Extracellular Vesicles Derived from Breast Cancer Cells,” *Biotechnol. J.*, vol. 15, no. 2, pp. 1–11, 2020, doi: 10.1002/biot.201900107.
 - [87] Y. Zheng, S. H. Ley, and F. B. Hu, “Global aetiology and epidemiology of type 2 diabetes mellitus and its complications,” *Nat. Rev. Endocrinol.*, vol. 14, no. 2, pp. 88–98, 2018, doi: 10.1038/nrendo.2017.151.
 - [88] A. Willcox and K. M. Gillespie, “Histology of Type 1 Diabetes Pancreas,” in *Type-1 Diabetes: Methods and Protocols*, K. M. Gillespie, Ed. New York, NY: Springer New York, 2016, pp. 105–117.
 - [89] A. M. Secrest, R. E. Washington, and T. J. Orchard, “Chapter 35: Mortality in Type 1 Diabetes,” *Diabetes Am.*, pp. 1–16, 2014.
 - [90] D. M. Maahs, N. A. West, J. M. Lawrence, and E. J. Mayer-Davis,

- "Epidemiology of type 1 diabetes," *Endocrinol. Metab. Clin. North Am.*, vol. 39, no. 3, pp. 481–497, 2010, doi: 10.1016/j.ecl.2010.05.011.
- [91] S. Chatterjee, K. Khunti, and M. J. Davies, "Type 2 diabetes," *Lancet*, vol. 389, no. 10085, pp. 2239–2251, 2017, doi: 10.1016/S0140-6736(17)30058-2.
- [92] E. Chiefari, B. Arcidiacono, D. Foti, and A. Brunetti, "Gestational diabetes mellitus: an updated overview," *J. Endocrinol. Invest.*, vol. 40, no. 9, pp. 899–909, 2017, doi: 10.1007/s40618-016-0607-5.
- [93] C. Castaño, M. Mirasierra, M. Vallejo, A. Novials, and M. Párrizas, "Delivery of muscle-derived exosomal miRNAs induced by HIIT improves insulin sensitivity through down-regulation of hepatic FoxO1 in mice," *Proc. Natl. Acad. Sci.*, vol. 117, no. 48, pp. 30335–30343, Dec. 2020, doi: 10.1073/pnas.2016112117.
- [94] D. Longnecker, "Anatomy and histology of the pancreas," *Pancreapedia Exocrine Pancreas Knowl. Base*, pp. 1–26, 2014, doi: 10.3998/panc.2014.3.
- [95] Q. Zhou and D. A. Melton, "Pancreas regeneration," *Nature*, vol. 557, no. 7705, pp. 351–358, 2018, doi: 10.1038/s41586-018-0088-0.Pancreas.
- [96] P. Rorsman and M. Braun, "Regulation of insulin secretion in human pancreatic islets," *Annu. Rev. Physiol.*, vol. 75, pp. 155–179, 2013, doi: 10.1146/annurev-physiol-030212-183754.
- [97] G. Kilimnik, J. Jo, V. Periwal, M. C. Zielinski, and M. Hara, "Quantification of islet size and architecture," *Islets*, vol. 4, no. 2, pp. 167–172, 2012, doi: 10.4161/isl.19256.
- [98] J. Gromada, P. Chabosseau, and G. A. Rutter, "The α -cell in diabetes mellitus," *Nat. Rev. Endocrinol.*, vol. 14, no. 12, pp. 694–704, 2018, doi: 10.1038/s41574-018-0097-y.
- [99] J. Dolenšek, M. S. Rupnik, and A. Stožer, "Structural similarities and differences between the human and the mouse pancreas," *Islets*, vol. 7, no. 1, pp. 2–9, 2015, doi: 10.1080/19382014.2015.1024405.
- [100] F. C. Pan and M. Brissova, "Pancreas development in humans," *Curr. Opin. Endocrinol. Diabetes Obes.*, vol. 21, no. 2, pp. 77–82, Apr. 2014, doi: 10.1097/MED.0000000000000047.
- [101] H. Kaneto *et al.*, "PDX-1 and MafA play a crucial role in pancreatic β -cell differentiation and maintenance of mature β -cell function," *Endocr. J.*, vol. 55, no. 2, pp. 235–252, 2008, doi: 10.1507/endocrj.K07E-041.
- [102] Y. Zhu, Q. Liu, Z. Zhou, and Y. Ikeda, "PDX1, Neurogenin-3, and MAFA: Critical transcription regulators for beta cell development and regeneration," *Stem Cell Res. Ther.*, vol. 8, no. 1, pp. 1–7, 2017, doi:

10.1186/s13287-017-0694-z.

- [103] E. Conrad, R. Stein, and C. S. Hunter, "Revealing transcription factors during human pancreatic β cell development," *Trends Endocrinol. Metab.*, vol. 25, no. 8, pp. 407–414, 2014, doi: 10.1016/j.tem.2014.03.013.
- [104] M. G. Nibbelink, G. Marchioli, L. Moroni, M. Karperien, and A. Van Apeldoorn, "A protocol to enhance INS1E and MIN6 functionality—The use of theophylline," *Int. J. Mol. Sci.*, vol. 17, no. 9, pp. 1–9, 2016, doi: 10.3390/ijms17091532.
- [105] M. Asfari, D. Janjic, P. Meda, G. Li, P. A. Halban, and C. B. Wollheim, "Establishment of 2-mercaptoethanol-dependent differentiated insulin-secreting cell lines," *Endocrinology*, vol. 130, no. 1, pp. 167–178, Jan. 1992, doi: 10.1210/endo.130.1.1370150.
- [106] Y. Heremans *et al.*, "Recapitulation of embryonic neuroendocrine differentiation in adult human pancreatic duct cells expressing neurogenin 3," *J. Cell Biol.*, vol. 159, no. 2, pp. 303–311, 2002, doi: 10.1083/jcb.200203074.
- [107] C. Aguayo-Mazzucato and S. Bonner-Weir, "Pancreatic β Cell Regeneration as a Possible Therapy for Diabetes," *Cell Metab.*, vol. 27, no. 1, pp. 57–67, 2018, doi: 10.1016/j.cmet.2017.08.007.
- [108] F. W. Pagliuca *et al.*, "Generation of functional human pancreatic β cells in vitro," *Cell*, vol. 159, no. 2, pp. 428–439, 2014, doi: 10.1016/j.cell.2014.09.040.
- [109] A. Rezania *et al.*, "Reversal of diabetes with insulin-producing cells derived in vitro from human pluripotent stem cells," *Nat. Biotechnol.*, vol. 32, no. 11, pp. 1121–1133, 2014, doi: 10.1038/nbt.3033.
- [110] M. J. Luther *et al.*, "MIN6 β -cell- β -cell interactions influence insulin secretory responses to nutrients and non-nutrients," *Biochem. Biophys. Res. Commun.*, vol. 343, no. 1, pp. 99–104, Apr. 2006, doi: 10.1016/j.bbrc.2006.02.003.
- [111] A. Chowdhury *et al.*, "Signaling in insulin-secreting MIN6 pseudoislets and monolayer cells," *J. Proteome Res.*, vol. 12, no. 12, pp. 5954–5962, 2013, doi: 10.1021/pr400864w.
- [112] G. G. Nair *et al.*, "Recapitulating endocrine cell clustering in culture promotes maturation of human stem-cell-derived β cells," *Nat. Cell Biol.*, vol. 21, no. 2, pp. 263–274, 2019, doi: 10.1038/s41556-018-0271-4.
- [113] J. Daoud, M. Petropavlovskaya, L. Rosenberg, and M. Tabrizian, "The effect of extracellular matrix components on the preservation of human islet function in vitro," *Biomaterials*, vol. 31, no. 7, pp. 1676–1682, Mar. 2010,

doi: 10.1016/j.biomaterials.2009.11.057.

- [114] J. C. Stendahl, D. B. Kaufman, and S. I. Stupp, "Extracellular matrix in pancreatic islets: Relevance to scaffold design and transplantation," *Cell Transplant.*, vol. 18, no. 1, pp. 1–12, 2009, doi: 10.3727/096368909788237195.
- [115] D. Kawamori and R. N. Kulkarni, "Insulin modulation of glucagon secretion: the role of insulin and other factors in the regulation of glucagon secretion.," *Islets*, vol. 1, no. 3, pp. 276–279, 2009, doi: 10.4161/isl.1.3.9967.
- [116] G. Marchioli *et al.*, "Fabrication of three-dimensional bioplotting hydrogel scaffolds for islets of Langerhans transplantation," *Biofabrication*, vol. 7, no. 2, 2015, doi: 10.1088/1758-5090/7/2/025009.
- [117] R. A. Pareta, A. C. Farney, and E. C. Opara, "Design of a bioartificial pancreas," *Pathobiology*, vol. 80, no. 4, pp. 194–202, 2013, doi: 10.1159/000345873.
- [118] X. Liu *et al.*, "Development of a Coaxial 3D Printing Platform for Biofabrication of Implantable Islet-Containing Constructs," *Adv. Healthc. Mater.*, vol. 8, no. 7, pp. 1–12, 2019, doi: 10.1002/adhm.201801181.
- [119] P. de Vos, M. M. Faas, B. Strand, and R. Calafiore, "Alginate-based microcapsules for immunoisolation of pancreatic islets," *Biomaterials*, vol. 27, no. 32, pp. 5603–5617, 2006, doi: 10.1016/j.biomaterials.2006.07.010.
- [120] J. Song and J. R. Millman, "Economic 3D-printing approach for transplantation of human stem cell-derived β -like cells," *Biofabrication*, vol. 9, no. 1, p. 015002, Dec. 2016, doi: 10.1088/1758-5090/9/1/015002.
- [121] H. Guo-Parke, J. T. McCluskey, C. Kelly, M. Hamid, N. H. McClenaghan, and P. R. Flatt, "Configuration of electrofusion-derived human insulin-secreting cell line as pseudoislets enhances functionality and therapeutic utility," *J. Endocrinol.*, vol. 214, no. 3, pp. 257–265, 2012, doi: 10.1530/JOE-12-0188.
- [122] A. Chowdhury, O. Dyachok, A. Tengholm, S. Sandler, and P. Bergsten, "Functional differences between aggregated and dispersed insulin-producing cells," *Diabetologia*, vol. 56, no. 7, pp. 1557–1568, Jul. 2013, doi: 10.1007/s00125-013-2903-3.
- [123] A. D. Green, S. Vasu, N. H. McClenaghan, and P. R. Flatt, "Pseudoislet formation enhances gene expression, insulin secretion and cytoprotective mechanisms of clonal human insulin-secreting 1.1B4 cells," *Eur. J. Physiol.*, vol. 467, no. 10, pp. 2219–2228, 2015, doi: 10.1007/s00424-014-1681-1.
- [124] C. E. Nyitray, M. G. Chavez, and T. A. Desai, "Compliant 3D microenvironment improves β -cell cluster insulin expression through

- mechanosensing and β -catenin signaling," *Tissue Eng. - Part A*, vol. 20, no. 13–14, pp. 1888–1895, 2014, doi: 10.1089/ten.tea.2013.0692.
- [125] N. Aloysious and P. D. Nair, "Enhanced survival and function of islet-like clusters differentiated from adipose stem cells on a three-dimensional natural polymeric scaffold: An in vitro study," *Tissue Eng. - Part A*, vol. 20, no. 9–10, pp. 1508–1522, 2014, doi: 10.1089/ten.tea.2012.0615.
- [126] B. N. Blackstone, A. F. Palmer, H. R. Rilo, and H. M. Powell, "Scaffold architecture controls insulinoma clustering, viability, and insulin production," *Tissue Eng. - Part A*, vol. 20, no. 13–14, pp. 1784–1793, 2014, doi: 10.1089/ten.tea.2013.0107.
- [127] D. Mao *et al.*, "A macroporous heparin-releasing silk fibroin scaffold improves islet transplantation outcome by promoting islet revascularisation and survival," *Acta Biomater.*, vol. 59, pp. 210–220, Sep. 2017, doi: 10.1016/j.actbio.2017.06.039.
- [128] W. R. Frontera and J. Ochala, "Skeletal muscle: a brief review of structure and function.," *Calcif. Tissue Int.*, vol. 96, no. 3, pp. 183–195, Mar. 2015, doi: 10.1007/s00223-014-9915-y.
- [129] A. R. Gillies and R. L. Lieber, "Structure and function of the skeletal muscle extracellular matrix," *Muscle and Nerve*, vol. 44, no. 3, pp. 318–331, Sep. 2011, doi: 10.1002/mus.22094.
- [130] K. Mukund and S. Subramaniam, "Skeletal muscle: A review of molecular structure and function, in health and disease.," *Wiley Interdiscip. Rev. Syst. Biol. Med.*, vol. 12, no. 1, p. e1462, Jan. 2020, doi: 10.1002/wsbm.1462.
- [131] N. A. Dumont, C. F. Bentzinger, M. C. Sincennes, and M. A. Rudnicki, "Satellite cells and skeletal muscle regeneration," *Compr. Physiol.*, vol. 5, no. 3, pp. 1027–1059, 2015, doi: 10.1002/cphy.c140068.
- [132] M. E. Kondash, A. Ananthakumar, A. Khodabukus, N. Bursac, and G. A. Truskey, "Glucose Uptake and Insulin Response in Tissue-engineered Human Skeletal Muscle," *Tissue Eng. Regen. Med.*, vol. 17, no. 6, pp. 801–813, 2020, doi: 10.1007/s13770-020-00242-y.
- [133] M. A. Febbraio and B. K. Pedersen, "Contraction-induced myokine production and release: Is skeletal muscle an endocrine organ?," *Exerc. Sport Sci. Rev.*, vol. 33, no. 3, pp. 114–119, 2005, doi: 10.1097/00003677-200507000-00003.
- [134] H. Ellingsgaard *et al.*, "Interleukin-6 enhances insulin secretion by increasing glucagon-like peptide-1 secretion from L cells and alpha cells," *Nat. Med.*, vol. 17, no. 11, pp. 1481–1489, 2011, doi: 10.1038/nm.2513.
- [135] M. A. Febbraio, "Point : Counterpoint BENEFICIAL ROLE IN INSULIN

- SENSITIVITY AND," *J. Appl. Physiol.*, no. February 2007, pp. 816–818, 2007.
- [136] E. E. Spangenburg, "Interleukin-6 does/does not have a beneficial role in insulin sensitivity and glucose homeostasis," *J. Appl. Physiol.*, vol. 102, no. 2, pp. 820–823, Feb. 2007, doi: 10.1152/japplphysiol.01353.2006.
- [137] R. A. Mooney, "Counterpoint: Interleukin-6 does not have a beneficial role in insulin sensitivity and glucose homeostasis," *J. Appl. Physiol.*, vol. 102, no. 2, pp. 816–818, 2007, doi: 10.1152/japplphysiol.01208a.2006.
- [138] J. J. Senn, P. J. Klover, I. A. Nowak, and R. A. Mooney, "Interleukin-6 induces cellular insulin resistance in hepatocytes," *Diabetes*, vol. 51, no. 12, pp. 3391–3399, 2002, doi: 10.2337/diabetes.51.12.3391.
- [139] P. J. Klover, T. A. Zimmers, L. G. Koniaris, and R. A. Mooney, "Chronic Exposure to Interleukin-6 Causes Hepatic Insulin Resistance in Mice," *Diabetes*, vol. 52, no. 11, pp. 2784–2789, 2003, doi: 10.2337/diabetes.52.11.2784.
- [140] D. Ben-Zvi, O. Barrandon, S. Hadley, B. Blum, Q. P. Peterson, and D. A. Melton, "Angptl4 links α -cell proliferation following glucagon receptor inhibition with adipose tissue triglyceride metabolism," *Proc. Natl. Acad. Sci. U. S. A.*, vol. 112, no. 50, pp. 15498–15503, 2015, doi: 10.1073/pnas.1513872112.
- [141] B. W. Van Der Kolk, G. H. Goossens, J. W. Jocken, S. Kersten, and E. E. Blaak, "Angiopoietin-like protein 4 and postprandial skeletal muscle lipid metabolism in overweight and obese prediabetics," *J. Clin. Endocrinol. Metab.*, vol. 101, no. 6, pp. 2332–2339, 2016, doi: 10.1210/jc.2015-4285.
- [142] M. C. K. Severinsen and B. K. Pedersen, "Muscle-Organ Crosstalk: The Emerging Roles of Myokines," *Endocr. Rev.*, vol. 41, no. 4, pp. 594–609, 2020, doi: 10.1210/endrev/bnaa016.
- [143] S. Rutti *et al.*, "Angiogenin and Osteoprotegerin are type II muscle specific myokines protecting pancreatic beta-cells against proinflammatory cytokines," *Sci. Rep.*, vol. 8, no. 1, pp. 2–11, 2018, doi: 10.1038/s41598-018-28117-2.
- [144] J. M. Fernández-Costa, X. Fernández-Garibay, F. Velasco-Mallorquí, and J. Ramón-Azcón, "Bioengineered in vitro skeletal muscles as new tools for muscular dystrophies preclinical studies," *J. Tissue Eng.*, vol. in press, no. in press, p. in press, 2020, doi: 10.1177/2041731420981339.
- [145] N. E. Fedorovich, J. Alblas, J. R. De Wijn, W. E. Hennink, A. B. J. Verbout, and W. J. A. Dhert, "Hydrogels as extracellular matrices for skeletal tissue engineering: State-of-the-art and novel application in organ printing," *Tissue Eng.*, vol. 13, no. 8, pp. 1905–1925, 2007, doi: 10.1089/ten.2006.0175.

- [146] W. J. Kim, C. H. Jang, and G. H. Kim, "A Myoblast-Laden Collagen Bioink with Fully Aligned Au Nanowires for Muscle-Tissue Regeneration," *Nano Lett.*, vol. 19, no. 12, pp. 8612–8620, 2019, doi: 10.1021/acs.nanolett.9b03182.
- [147] M. Costantini *et al.*, "Microfluidic-enhanced 3D bioprinting of aligned myoblast-laden hydrogels leads to functionally organized myofibers in vitro and in vivo," *Biomaterials*, vol. 131, pp. 98–110, 2017, doi: 10.1016/j.biomaterials.2017.03.026.
- [148] R. Mestre, T. Patiño, X. Barceló, S. Anand, A. Pérez-Jiménez, and S. Sánchez, "Force Modulation and Adaptability of 3D-Bioprinted Biological Actuators Based on Skeletal Muscle Tissue," *Adv. Mater. Technol.*, vol. 4, no. 2, p. 1800631, Dec. 2019, doi: 10.1002/admt.201800631.
- [149] J. M. Lee and W. Y. Yeong, "Engineering macroscale cell alignment through coordinated toolpath design using support-assisted 3D bioprinting: Engineering macroscale cell alignment through coordinated toolpath design using support-assisted 3D bioprinting," *J. R. Soc. Interface*, vol. 17, no. 168, 2020, doi: 10.1098/rsif.2020.0294rsif20200294.
- [150] J. Ramón-Azcón *et al.*, "Dielectrophoretically aligned carbon nanotubes to control electrical and mechanical properties of hydrogels to fabricate contractile muscle myofibers," *Adv. Mater.*, vol. 25, no. 29, pp. 4028–4034, 2013, doi: 10.1002/adma.201301300.
- [151] H. Vandenburgh *et al.*, "Drug-screening platform based on the contractility of tissue-engineered muscle," *Muscle Nerve*, vol. 37, no. 4, pp. 438–447, Apr. 2008, doi: 10.1002/mus.20931.
- [152] L. Rao, Y. Qian, A. Khodabukus, T. Ribar, and N. Bursac, "Engineering human pluripotent stem cells into a functional skeletal muscle tissue," *Nat. Commun.*, vol. 9, no. 1, pp. 1–12, 2018, doi: 10.1038/s41467-017-02636-4.
- [153] Seyedmahmoud *et al.*, "Three-Dimensional Bioprinting of Functional Skeletal Muscle Tissue Using GelatinMethacryloyl-Alginate Bioinks," *Micromachines*, vol. 10, no. 10, p. 679, Oct. 2019, doi: 10.3390/mi10100679.
- [154] W. J. Kim and G. H. Kim, "3D bioprinting of functional cell-laden bioinks and its application for cell-alignment and maturation," *Appl. Mater. Today*, vol. 19, p. 100588, 2020, doi: 10.1016/j.apmt.2020.100588.
- [155] M. Costantini *et al.*, "Engineering Muscle Networks in 3D Gelatin Methacryloyl Hydrogels: Influence of Mechanical Stiffness and Geometrical Confinement," *Front. Bioeng. Biotechnol.*, vol. 5, no. APR, pp. 1–8, Apr. 2017, doi: 10.3389/fbioe.2017.00022.
- [156] T. Distler, A. A. Solisito, D. Schneidereit, O. Friedrich, R. Detsch, and A. R. Boccaccini, "3D printed oxidized alginate-gelatin bioink provides guidance

- for C2C12 muscle precursor cell orientation and differentiation via shear stress during bioprinting,” *Biofabrication*, vol. 12, no. 4, p. 045005, Jul. 2020, doi: 10.1088/1758-5090/ab98e4.
- [157] R. Dong, P. X. Ma, and B. Guo, “Conductive biomaterials for muscle tissue engineering,” *Biomaterials*, vol. 229, no. October 2019, p. 119584, 2020, doi: 10.1016/j.biomaterials.2019.119584.
- [158] L. Elowsson, H. Kirsebom, V. Carmignac, B. Mattiasson, and M. Durbeej, “Evaluation of macroporous blood and plasma scaffolds for skeletal muscle tissue engineering,” *Biomater. Sci.*, vol. 1, no. 4, pp. 402–410, 2013, doi: 10.1039/c2bm00054g.
- [159] É. Georget, R. Abdeddaim, and P. Sabouroux, “A quasi-universal method to measure the electromagnetic characteristics of usual materials in the microwave range,” *Comptes Rendus Phys.*, vol. 15, no. 5, pp. 448–457, May 2014, doi: 10.1016/j.crhy.2014.02.003.
- [160] D. Ba and P. Sabouroux, “EpsiMu, A toolkit for permittivity and permeability measurement in microwave domain at real time of all materials: Applications to solid and semisolid materials,” *Microw. Opt. Technol. Lett.*, vol. 52, no. 12, pp. 2643–2648, Dec. 2010, doi: 10.1002/mop.25570.
- [161] A. L. Neves, E. Georget, N. Cochinaire, and P. Sabouroux, “Real-time microwave sensor system for detection of polluting substances in pure water,” *Rev. Sci. Instrum.*, vol. 88, no. 8, p. 084706, Aug. 2017, doi: 10.1063/1.4998982.
- [162] A. M. Nicolson and G. F. Ross, “Measurement of the Intrinsic Properties of Materials by Time-Domain Techniques,” *IEEE Trans. Instrum. Meas.*, vol. 19, no. 4, pp. 377–382, Nov. 1970, doi: 10.1109/TIM.1970.4313932.
- [163] W. B. Weir, “Automatic measurement of complex dielectric constant and permeability at microwave frequencies,” *Proc. IEEE*, vol. 62, no. 1, pp. 33–36, 1974, doi: 10.1109/PROC.1974.9382.
- [164] J. W. Nichol, S. Koshy, H. Bae, C. M. Hwang, and A. Khademhosseini, “Cell-laden microengineered gelatin methacrylate hydrogels,” *Biomaterials*, vol. 31, no. 21, pp. 5536–5544, 2011, doi: 10.1016/j.biomaterials.2010.03.064.Cell-laden.
- [165] A. Bettadapur *et al.*, “Prolonged Culture of Aligned Skeletal Myotubes on Micromolded Gelatin Hydrogels,” *Sci. Rep.*, vol. 6, pp. 1–14, 2016, doi: 10.1038/srep28855.
- [166] R. Reeves, A. Ribeiro, L. Lombardo, R. Boyer, and J. B. Leach, “Synthesis and characterization of carboxymethylcellulose-methacrylate hydrogel cell scaffolds,” *Polymers (Basel)*, vol. 2, no. 3, pp. 252–264, 2010, doi: 10.3390/polym2030252.

- [167] B. Gaihre and A. C. Jayasuriya, "Fabrication and characterization of carboxymethyl cellulose novel microparticles for bone tissue engineering," *Mater. Sci. Eng. C*, vol. 69, no. 1, pp. 733–743, Dec. 2016, doi: 10.1016/j.msec.2016.07.060.
- [168] H. Park *et al.*, "Effects of electrical stimulation in C2C12 muscle constructs," *J. Tissue Eng. Regen. Med.*, vol. 2, no. 5, pp. 279–287, 2008, doi: 10.1002/term.93.
- [169] G. Kilimnik, J. Jo, V. Periwal, M. C. Zielinski, and M. Hara, "Quantification of islet size and architecture," *Islets*, vol. 4, no. 2, pp. 167–172, Mar. 2012, doi: 10.4161/isl.19256.
- [170] J. Jo, M. Hara, U. Ahlgren, R. Sorenson, and V. Periwal, "Mathematical models of pancreatic islet size distributions," *Islets*, vol. 4, no. 1, pp. 10–19, 2012, doi: 10.4161/isl.18660.
- [171] P. Molnar, W. Wang, A. Natarajan, J. W. Rumsey, and J. J. Hickman, "Photolithographic patterning of C2C12 myotubes using vitronectin as growth substrate in serum-free medium," in *Biotechnology Progress*, 2007, vol. 23, no. 1, pp. 265–268, doi: 10.1021/bp060302q.
- [172] A. Khodabukus *et al.*, "Electrical stimulation increases hypertrophy and metabolic flux in tissue-engineered human skeletal muscle," *Biomaterials*, vol. 198, no. July 2018, pp. 259–269, Apr. 2019, doi: 10.1016/j.biomaterials.2018.08.058.
- [173] J. Liu, S. Liu, Y. Chen, X. Zhao, Y. Lu, and J. Cheng, "Functionalized self-assembling peptide improves INS-1 β -cell function and proliferation via the integrin/FAK/ERK/cyclin pathway," *Int. J. Nanomedicine*, vol. 10, pp. 3519–3531, 2015, doi: 10.2147/IJN.S80502.
- [174] A. J. Engler, M. A. Griffin, S. Sen, C. G. Bönnemann, H. L. Sweeney, and D. E. Discher, "Myotubes differentiate optimally on substrates with tissue-like stiffness: Pathological implications for soft or stiff microenvironments," *J. Cell Biol.*, vol. 166, no. 6, pp. 877–887, 2004, doi: 10.1083/jcb.200405004.
- [175] S. Romanazzo *et al.*, "Substrate stiffness affects skeletal myoblast differentiation in vitro," *Sci. Technol. Adv. Mater.*, vol. 13, no. 6, p. 064211, Dec. 2012, doi: 10.1088/1468-6996/13/6/064211.
- [176] G. Alessandra *et al.*, "Shaping Pancreatic β -Cell Differentiation and Functioning: The Influence of Mechanotransduction," *Cells*, vol. 9, no. 2, p. 413, Feb. 2020, doi: 10.3390/cells9020413.
- [177] F. Dittmann *et al.*, "Tomoelastography of the abdomen: Tissue mechanical properties of the liver, spleen, kidney, and pancreas from single MR elastography scans at different hydration states," *Magn. Reson. Med.*, vol. 78, no. 3, pp. 976–983, 2017, doi: 10.1002/mrm.26484.

- [178] Y. Shi *et al.*, "Pancreatic Stiffness Quantified with MR Elastography: Relationship to Postoperative Pancreatic Fistula after Pancreaticoenteric Anastomosis," *Radiology*, vol. 288, no. 2, pp. 476–484, Aug. 2018, doi: 10.1148/radiol.2018170450.
- [179] A. Galli *et al.*, "Cluster-assembled zirconia substrates promote long-term differentiation and functioning of human islets of Langerhans," *Sci. Rep.*, vol. 8, no. 1, pp. 1–17, 2018, doi: 10.1038/s41598-018-28019-3.
- [180] N. Sachot, E. Engel, and O. Castano, "Hybrid Organic-Inorganic Scaffolding Biomaterials for Regenerative Therapies," *Curr. Org. Chem.*, vol. 18, no. 18, pp. 2299–2314, 2014, doi: 10.2174/1385272819666140806200355.
- [181] S. A. Bencherif, R. W. Sands, D. Bhatta, P. Arany, C. S. Verbeke, and D. A. Edwards, "Injectable preformed scaffolds with shape-memory properties," *PNAS*, 2012, doi: 10.1073/pnas.1211516109/-/DCSupplemental.www.pnas.org/cgi/doi/10.1073/pnas.1211516109.
- [182] P. E. MacDonald, J. W. Joseph, and P. Rorsman, "Glucose-sensing mechanisms in pancreatic β -cells," *Philos. Trans. R. Soc. B Biol. Sci.*, vol. 360, no. 1464, pp. 2211–2225, 2005, doi: 10.1098/rstb.2005.1762.
- [183] H. Park *et al.*, "Effects of electrical stimulation in C2C12 muscle constructs," *J. Tissue Eng. Regen. Med.*, vol. 2, no. 5, pp. 279–287, Jul. 2008, doi: 10.1002/term.93.
- [184] M. A. Bakooshi *et al.*, "A 3d culture model of innervated human skeletal muscle enables studies of the adult neuromuscular junction," *Elife*, vol. 8, pp. 1–29, May 2019, doi: 10.7554/eLife.44530.
- [185] K. Shimizu, S. Ohsumi, T. Kishida, O. Mazda, and H. Honda, "Fabrication of contractile skeletal muscle tissues using directly converted myoblasts from human fibroblasts," *J. Biosci. Bioeng.*, vol. 129, no. 5, pp. 632–637, 2020, doi: 10.1016/j.jbiosc.2019.11.013.
- [186] S. Sirivisoot and B. S. Harrison, "Skeletal myotube formation enhanced by electrospun polyurethane carbon nanotube scaffolds," *Int. J. Nanomedicine*, vol. 6, pp. 2483–2497, 2011, doi: 10.2147/ijn.s24073.
- [187] M. C. Chen, Y. C. Sun, and Y. H. Chen, "Electrically conductive nanofibers with highly oriented structures and their potential application in skeletal muscle tissue engineering," *Acta Biomater.*, vol. 9, no. 3, pp. 5562–5572, 2013, doi: 10.1016/j.actbio.2012.10.024.
- [188] M. Kharaziha *et al.*, "Tough and flexible CNT-polymeric hybrid scaffolds for engineering cardiac constructs," *Biomaterials*, vol. 35, no. 26, pp. 7346–7354, 2014, doi: 10.1016/j.biomaterials.2014.05.014.
- [189] B. Farhat *et al.*, "Small human islets comprised of more β -cells with higher

- insulin content than large islets,” *Islets*, vol. 5, no. 2, pp. 87–94, 2013, doi: 10.4161/isl.24780.
- [190] M. Skelin, M. Rupnik, and A. Cencic, “Pancreatic beta cell lines and their applications in diabetes mellitus research,” *ALTEX*, vol. 27, no. 2, pp. 105–113, 2010, doi: 10.14573/altex.2010.2.105.
- [191] H. Shin, S. Jo, and A. G. Mikos, “Biomimetic materials for tissue engineering,” *Biomaterials*, vol. 24, no. 24, pp. 4353–4364, 2003, doi: 10.1016/S0142-9612(03)00339-9.
- [192] S. Puri *et al.*, “Replication confers β cell immaturity,” *Nat. Commun.*, vol. 9, no. 1, pp. 1–12, 2018, doi: 10.1038/s41467-018-02939-0.
- [193] R. N. Kulkarni, E. B. Mizrahi, A. G. Ocana, and A. F. Stewart, “Human β -cell proliferation and intracellular signaling: Driving in the dark without a road map,” *Diabetes*, vol. 61, no. 9, pp. 2205–2213, 2012, doi: 10.2337/db12-0018.
- [194] O. Cabrera, D. M. Berman, N. S. Kenyon, C. Ricordi, P. O. Berggren, and A. Caicedo, “The unique cytoarchitecture of human pancreatic islets has implications for islet cell function,” *Proc. Natl. Acad. Sci. U. S. A.*, vol. 103, no. 7, pp. 2334–2339, 2006, doi: 10.1073/pnas.0510790103.
- [195] F. Folli *et al.*, “Pancreatic islet of Langerhans’ cytoarchitecture and ultrastructure in normal glucose tolerance and in type 2 diabetes mellitus,” *Diabetes, Obes. Metab.*, vol. 20, no. 5, pp. 137–144, 2018, doi: 10.1111/dom.13380.
- [196] R. K. P. Benninger and D. J. Hodson, “New Understanding of β -Cell Heterogeneity and In Situ Islet Function,” *Diabetes*, vol. 67, no. 4, pp. 537–547, Apr. 2018, doi: 10.2337/dbi17-0040.
- [197] S. S. Roscioni, A. Migliorini, M. Gegg, and H. Lickert, “Impact of islet architecture on β -cell heterogeneity, plasticity and function,” *Nat. Rev. Endocrinol.*, vol. 12, no. 12, pp. 695–709, 2016, doi: 10.1038/nrendo.2016.147.
- [198] A. Wojtuszczyński, M. Armanet, P. Morel, T. Berney, and D. Bosco, “Insulin secretion from human beta cells is heterogeneous and dependent on cell-to-cell contacts,” *Diabetologia*, vol. 51, no. 10, pp. 1843–1852, 2008, doi: 10.1007/s00125-008-1103-z.
- [199] S. S. Andrali, M. L. Sampley, N. L. Vanderford, and S. Özcan, “Glucose regulation of insulin gene expression in pancreatic β -cells,” *Biochem. J.*, vol. 415, no. 1, pp. 1–10, 2008, doi: 10.1042/bj20081029.
- [200] K. Fujimoto and K. S. Polonsky, “Pdx1 and other factors that regulate pancreatic β -cell survival,” *Diabetes, Obes. Metab.*, vol. 11, no. SUPPL. 4,

- pp. 30–37, Nov. 2009, doi: 10.1111/j.1463-1326.2009.01121.x.
- [201] T. Matsuoka *et al.*, “MafA regulates expression of genes important to islet β -cell function,” *Mol. Endocrinol.*, vol. 21, no. 11, pp. 2764–2774, 2007, doi: 10.1210/me.2007-0028.
 - [202] D. Pipeleers, P. I. in’t Veld, E. Maes, and M. Van De Winkel, “Glucose-induced insulin release depends on functional cooperation between islet cells,” *Proc. Natl. Acad. Sci.*, vol. 79, no. 23, pp. 7322–7325, Dec. 1982, doi: 10.1073/pnas.79.23.7322.
 - [203] A. Charollais *et al.*, “Junctional communication of pancreatic β cell contributes to the control of insulin secretion and glucose tolerance,” *J. Clin. Invest.*, vol. 106, no. 2, pp. 235–243, 2000, doi: 10.1172/JCI9398.
 - [204] S. Miyazaki, F. Tashiro, T. Tsuchiya, K. Sasaki, and J. ichi Miyazaki, “Establishment of a long-term stable β -cell line and its application to analyze the effect of Gcg expression on insulin secretion,” *Sci. Rep.*, vol. 11, no. 1, pp. 1–10, 2021, doi: 10.1038/s41598-020-79992-7.
 - [205] A. S. Salimath and A. J. García, “Biofunctional hydrogels for skeletal muscle constructs,” *J. Tissue Eng. Regen. Med.*, vol. 10, no. 11, pp. 967–976, Nov. 2016, doi: 10.1002/term.1881.
 - [206] J. Ren *et al.*, “Superaligned Carbon Nanotubes Guide Oriented Cell Growth and Promote Electrophysiological Homogeneity for Synthetic Cardiac Tissues,” *Adv. Mater.*, vol. 29, no. 44, pp. 1–8, 2017, doi: 10.1002/adma.201702713.
 - [207] H. Takahashi, T. Shimizu, M. Nakayama, M. Yamato, and T. Okano, “The use of anisotropic cell sheets to control orientation during the self-organization of 3D muscle tissue,” *Biomaterials*, vol. 34, no. 30, pp. 7372–7380, 2013, doi: 10.1016/j.biomaterials.2013.06.033.
 - [208] R. Banan Sadeghian, M. Ebrahimi, and S. Salehi, “Electrical stimulation of microengineered skeletal muscle tissue: Effect of stimulus parameters on myotube contractility and maturation,” *J. Tissue Eng. Regen. Med.*, vol. 12, no. 4, pp. 912–922, 2018, doi: 10.1002/term.2502.
 - [209] A. Ito *et al.*, “Induction of functional tissue-engineered skeletal muscle constructs by defined electrical stimulation,” *Sci. Rep.*, vol. 4, 2014, doi: 10.1038/srep04781.
 - [210] Z.-K. Cui, S. Kim, J. J. Baljon, B. M. Wu, T. Aghaloo, and M. Lee, “Microporous methacrylated glycol chitosan-montmorillonite nanocomposite hydrogel for bone tissue engineering,” *Nat. Commun.*, vol. 10, no. 1, p. 3523, Dec. 2019, doi: 10.1038/s41467-019-11511-3.
 - [211] M. Ali, A. K. PR, J. J. Yoo, F. Zahran, A. Atala, and S. J. Lee, “A Photo-

- Crosslinkable Kidney ECM-Derived Bioink Accelerates Renal Tissue Formation," *Adv. Healthc. Mater.*, vol. 8, no. 7, p. 1800992, Apr. 2019, doi: 10.1002/adhm.201800992.
- [212] K. K. Papas, H. De Leon, T. M. Suszynski, and R. C. Johnson, "Oxygenation strategies for encapsulated islet and beta cell transplants," *Adv. Drug Deliv. Rev.*, vol. 139, pp. 139–156, 2019, doi: 10.1016/j.addr.2019.05.002.
- [213] B. R. Lee *et al.*, "In situ formation and collagen-alginate composite encapsulation of pancreatic islet spheroids," *Biomaterials*, vol. 33, no. 3, pp. 837–845, 2012, doi: 10.1016/j.biomaterials.2011.10.014.
- [214] G. Marchioli *et al.*, "Layered PEGDA hydrogel for islet of Langerhans encapsulation and improvement of vascularization," *J. Mater. Sci. Mater. Med.*, vol. 28, no. 12, 2017, doi: 10.1007/s10856-017-6004-6.
- [215] A. Essaouiba *et al.*, "Analysis of the behavior of 2D monolayers and 3D spheroid human pancreatic beta cells derived from induced pluripotent stem cells in a microfluidic environment," *J. Biotechnol.*, no. September 2020, Feb. 2021, doi: 10.1016/j.jbiotec.2021.02.009.
- [216] J. Hilderink *et al.*, "Controlled aggregation of primary human pancreatic islet cells leads to glucose-responsive pseudoislets comparable to native islets," *J. Cell. Mol. Med.*, vol. 19, no. 8, pp. 1836–1846, 2015, doi: 10.1111/jcmm.12555.
- [217] M.-J. Lecomte *et al.*, "Aggregation of Engineered Human β -Cells into Pseudoislets: Insulin Secretion and Gene Expression Profile in Normoxic and Hypoxic Milieu," *Cell Med.*, vol. 8, no. 3, pp. 99–112, 2016, doi: 10.3727/215517916x692843.
- [218] V. K. Ramiya, M. Maraist, K. E. Arfors, D. A. Schatz, A. B. Peck, and J. G. Cornelius, "Reversal of insulin-dependent diabetes using islets generated in vitro from pancreatic stem cells," *Nat. Med.*, vol. 6, no. 3, pp. 278–282, Mar. 2000, doi: 10.1038/73128.
- [219] L. G. Griffith and M. A. Swartz, "Capturing complex 3D tissue physiology in vitro," *Nat. Rev. Mol. Cell Biol.*, vol. 7, no. 3, pp. 211–224, Mar. 2006, doi: 10.1038/nrm1858.
- [220] C. Oelschlaeger, F. Bossler, and N. Willenbacher, "Synthesis, Structural and Micromechanical Properties of 3D Hyaluronic Acid-Based Cryogel Scaffolds," *Biomacromolecules*, vol. 17, no. 2, pp. 580–589, Feb. 2016, doi: 10.1021/acs.biomac.5b01529.
- [221] K. M. Salleh, S. Zakaria, S. Gan, K. W. Baharin, N. A. Ibrahim, and R. Zamzamin, "Interconnected macropores cryogel with nano-thin crosslinked network regenerated cellulose," *Int. J. Biol. Macromol.*, vol. 148, pp. 11–19, Apr. 2020, doi: 10.1016/j.ijbiomac.2019.12.240.

- [222] S. T. Koshy, T. C. Ferrante, S. A. Lewin, and D. J. Mooney, "Injectable, porous, and cell-responsive gelatin cryogels," *Biomaterials*, vol. 35, no. 8, pp. 2477–2487, Mar. 2014, doi: 10.1016/j.biomaterials.2013.11.044.
- [223] S. S. Suner *et al.*, "Cryogel composites based on hyaluronic acid and halloysite nanotubes as scaffold for tissue engineering," *Int. J. Biol. Macromol.*, vol. 130, pp. 627–635, 2019, doi: 10.1016/j.ijbiomac.2019.03.025.
- [224] C. Y. Kuo, C. H. Chen, C. Y. Hsiao, and J. P. Chen, "Incorporation of chitosan in biomimetic gelatin/chondroitin-6-sulfate/hyaluronan cryogel for cartilage tissue engineering," *Carbohydr. Polym.*, vol. 117, pp. 722–730, 2015, doi: 10.1016/j.carbpol.2014.10.056.
- [225] U. Hersel, C. Dahmen, and H. Kessler, "RGD modified polymers: biomaterials for stimulated cell adhesion and beyond," *Biomaterials*, vol. 24, no. 24, pp. 4385–4415, Nov. 2003, doi: 10.1016/S0142-9612(03)00343-0.
- [226] C. Kelly, N. H. McClenaghan, and P. R. Flatt, "Role of islet structure and cellular interactions in the control of insulin secretion," *Islets*, vol. 3, no. 2, pp. 41–47, 2011, doi: 10.4161/isl.3.2.14805.
- [227] K. I. Aamodt and A. C. Powers, "Signals in the pancreatic islet microenvironment influence β -cell proliferation," *Diabetes, Obes. Metab.*, vol. 19, pp. 124–136, Sep. 2017, doi: 10.1111/dom.13031.
- [228] K. Socha, M. Socha, and P. Fiedor, "Proliferation of transplanted allogeneic pancreatic islets," *Transplant. Proc.*, vol. 35, no. 6, pp. 2341–2342, Sep. 2003, doi: 10.1016/S0041-1345(03)00787-5.
- [229] F. Ciregia *et al.*, "Palmitate-induced lipotoxicity alters acetylation of multiple proteins in clonal β cells and human pancreatic islets," *Sci. Rep.*, vol. 7, no. 1, p. 13445, Dec. 2017, doi: 10.1038/s41598-017-13908-w.
- [230] H. Zhang and A. I. Cooper, "Aligned porous structures by directional freezing," *Adv. Mater.*, vol. 19, no. 11, pp. 1529–1533, 2007, doi: 10.1002/adma.200700154.
- [231] J. Yang, Y. S. Zhang, K. Yue, and A. Khademhosseini, "Cell-laden hydrogels for osteochondral and cartilage tissue engineering," *Acta Biomater.*, vol. 57, pp. 1–25, Jul. 2017, doi: 10.1016/j.actbio.2017.01.036.
- [232] T. T. Demirtaş, G. Irmak, and M. Gümüşderelioğlu, "A bioprintable form of chitosan hydrogel for bone tissue engineering," *Biofabrication*, vol. 9, no. 3, p. 035003, Jul. 2017, doi: 10.1088/1758-5090/aa7b1d.
- [233] S. Ashe, S. Behera, P. Dash, D. Nayak, and B. Nayak, "Gelatin carrageenan sericin hydrogel composites improves cell viability of cryopreserved SaOS-

- 2 cells,” *Int. J. Biol. Macromol.*, vol. 154, pp. 606–620, Jul. 2020, doi: 10.1016/j.ijbiomac.2020.03.039.
- [234] Y. Hong *et al.*, “A strongly adhesive hemostatic hydrogel for the repair of arterial and heart bleeds,” *Nat. Commun.*, vol. 10, no. 1, p. 2060, Dec. 2019, doi: 10.1038/s41467-019-10004-7.
- [235] P. Rastogi and B. Kandasubramanian, “Review of alginate-based hydrogel bioprinting for application in tissue engineering,” *Biofabrication*, vol. 11, no. 4, p. 042001, Sep. 2019, doi: 10.1088/1758-5090/ab331e.
- [236] I. Rajzer, E. Menaszek, R. Kwiatkowski, J. A. Planell, and O. Castano, “Electrospun gelatin/poly(ϵ -caprolactone) fibrous scaffold modified with calcium phosphate for bone tissue engineering,” *Mater. Sci. Eng. C*, vol. 44, pp. 183–190, Nov. 2014, doi: 10.1016/j.msec.2014.08.017.
- [237] S. Ribeiro, A. C. Gomes, I. Etxebarria, S. Lanceros-Méndez, and C. Ribeiro, “Electroactive biomaterial surface engineering effects on muscle cells differentiation,” *Mater. Sci. Eng. C*, vol. 92, pp. 868–874, 2018, doi: 10.1016/j.msec.2018.07.044.
- [238] H. Y. Gong, J. Park, W. Kim, J. Kim, J. Y. Lee, and W. G. Koh, “A Novel Conductive and Micropatterned PEG-Based Hydrogel Enabling the Topographical and Electrical Stimulation of Myoblasts,” *ACS Appl. Mater. Interfaces*, vol. 11, no. 51, pp. 47695–47706, 2019, doi: 10.1021/acsami.9b16005.
- [239] J. Park, J. H. Choi, S. Kim, I. Jang, S. Jeong, and J. Y. Lee, “Micropatterned conductive hydrogels as multifunctional muscle-mimicking biomaterials: Graphene-incorporated hydrogels directly patterned with femtosecond laser ablation,” *Acta Biomater.*, vol. 97, pp. 141–153, 2019, doi: 10.1016/j.actbio.2019.07.044.
- [240] A. García-Lizarribar, X. Fernández-Garibay, F. Velasco-Mallorquí, A. G. Castaño, J. Samitier, and J. Ramon-Azcon, “Composite Biomaterials as Long-Lasting Scaffolds for 3D Bioprinting of Highly Aligned Muscle Tissue,” *Macromol. Biosci.*, vol. 18, no. 10, p. 1800167, Oct. 2018, doi: 10.1002/mabi.201800167.
- [241] V. Hosseini *et al.*, “Engineered Contractile Skeletal Muscle Tissue on a Microgrooved Methacrylated Gelatin Substrate,” *Tissue Eng. Part A*, vol. 18, no. 23–24, pp. 2453–2465, Dec. 2012, doi: 10.1089/ten.tea.2012.0181.
- [242] C. Snyman, K. P. Goetsch, K. H. Myburgh, and C. U. Niesler, “Simple silicone chamber system for in vitro three-dimensional skeletal muscle tissue formation,” *Front. Physiol.*, vol. 4, p. 349, 2013, doi: 10.3389/fphys.2013.00349.
- [243] C. Monge, K. Ren, K. Berton, R. Guillot, D. Peyrade, and C. Picart,

- “Engineering muscle tissues on microstructured polyelectrolyte multilayer films,” *Tissue Eng. - Part A*, vol. 18, no. 15–16, pp. 1664–1676, Aug. 2012, doi: 10.1089/ten.tea.2012.0079.
- [244] N. F. Huang, R. J. Lee, and S. Li, “Engineering of aligned skeletal muscle by micropatterning,” *Am. J. Transl. Res.*, vol. 2, no. 1, pp. 43–55, Jan. 2010, Accessed: Mar. 05, 2020. [Online]. Available: <http://www.ncbi.nlm.nih.gov/pubmed/20182581>.
- [245] N. Jiwlawat *et al.*, “Micropatterned substrates with physiological stiffness promote cell maturation and Pompe disease phenotype in human induced pluripotent stem cell-derived skeletal myocytes,” *Biotechnol. Bioeng.*, vol. 116, no. 9, pp. 2377–2392, Sep. 2019, doi: 10.1002/bit.27075.
- [246] L. E. Bertassoni *et al.*, “Hydrogel bioprinted microchannel networks for vascularization of tissue engineering constructs,” *Lab Chip*, vol. 14, no. 13, pp. 2202–11, 2014, doi: 10.1039/c4lc00030g.
- [247] A. J. Engler, S. Sen, H. L. Sweeney, and D. E. Discher, “Matrix Elasticity Directs Stem Cell Lineage Specification,” *Cell*, vol. 126, no. 4, pp. 677–689, 2006, doi: 10.1016/j.cell.2006.06.044.
- [248] J. H. Kim *et al.*, “Neural cell integration into 3D bioprinted skeletal muscle constructs accelerates restoration of muscle function,” *Nat. Commun.*, vol. 11, no. 1, pp. 1–12, 2020, doi: 10.1038/s41467-020-14930-9.
- [249] Y. Zhao, H. Zeng, J. Nam, and S. Agarwal, “Fabrication of skeletal muscle constructs by topographic activation of cell alignment,” *Biotechnol. Bioeng.*, vol. 102, no. 2, pp. 624–631, Feb. 2009, doi: 10.1002/bit.22080.
- [250] K. Yue, G. Trujillo-de Santiago, M. M. Alvarez, A. Tamayol, N. Annabi, and A. Khademhosseini, “Synthesis, properties, and biomedical applications of gelatin methacryloyl (GelMA) hydrogels,” *Biomaterials*, vol. 73, pp. 254–271, Dec. 2015, doi: 10.1016/j.biomaterials.2015.08.045.
- [251] B. J. Klotz, D. Gawlitta, A. J. W. P. Rosenberg, J. Malda, and F. P. W. Melchels, “Gelatin-Methacryloyl Hydrogels: Towards Biofabrication-Based Tissue Repair,” *Trends Biotechnol.*, vol. 34, no. 5, pp. 394–407, May 2016, doi: 10.1016/j.tibtech.2016.01.002.
- [252] H.-H. Kao, C.-Y. Kuo, K.-S. Chen, and J.-P. Chen, “Preparation of Gelatin and Gelatin/Hyaluronic Acid Cryogel Scaffolds for the 3D Culture of Mesothelial Cells and Mesothelium Tissue Regeneration,” *Int. J. Mol. Sci.*, vol. 20, no. 18, p. 4527, Sep. 2019, doi: 10.3390/ijms20184527.
- [253] M. Mehrli *et al.*, “Pectin Methacrylate (PEMA) and Gelatin-Based Hydrogels for Cell Delivery: Converting Waste Materials into Biomaterials,” *ACS Appl. Mater. Interfaces*, vol. 11, no. 13, pp. 12283–12297, Apr. 2019, doi: 10.1021/acsami.9b00154.

- [254] D. M. Varma, G. T. Gold, P. J. Taub, and S. B. Nicoll, "Injectable carboxymethylcellulose hydrogels for soft tissue filler applications," *Acta Biomater.*, vol. 10, no. 12, pp. 4996–5004, Dec. 2014, doi: 10.1016/j.actbio.2014.08.013.
- [255] J. R. Docherty and P. A. McCormick, "A carboxymethylcellulose–heparin combination for the prevention of surgical adhesions," *J. Surg. Res.*, vol. 213, pp. 228–233, Jun. 2017, doi: 10.1016/j.jss.2017.02.066.
- [256] Y. Ogushi, S. Sakai, and K. Kawakami, "Adipose tissue engineering using adipose-derived stem cells enclosed within an injectable carboxymethylcellulose-based hydrogel," *J. Tissue Eng. Regen. Med.*, vol. 7, no. 11, pp. 884–892, Nov. 2013, doi: 10.1002/term.1480.
- [257] J. Ramón-Azcón *et al.*, "Dielectrophoretically Aligned Carbon Nanotubes to Control Electrical and Mechanical Properties of Hydrogels to Fabricate Contractile Muscle Myofibers," *Adv. Mater.*, vol. 25, no. 29, pp. 4028–4034, 2013, doi: 10.1002/adma.201301300.
- [258] A. L. Glieberman *et al.*, "Synchronized stimulation and continuous insulin sensing in a microfluidic human Islet on a Chip designed for scalable manufacturing," *Lab Chip*, vol. 19, no. 18, pp. 2993–3010, 2019, doi: 10.1039/c9lc00253g.
- [259] R. K. Christensen, C. Von Halling Laier, A. Kiziltay, S. Wilson, and N. B. Larsen, "3D Printed Hydrogel Multiassay Platforms for Robust Generation of Engineered Contractile Tissues," *Biomacromolecules*, vol. 21, no. 2, pp. 356–365, 2020, doi: 10.1021/acs.biomac.9b01274.
- [260] S. M. Maffioletti *et al.*, "Three-Dimensional Human iPSC-Derived Artificial Skeletal Muscles Model Muscular Dystrophies and Enable Multilineage Tissue Engineering," *Cell Rep.*, vol. 23, no. 3, pp. 899–908, 2018, doi: 10.1016/j.celrep.2018.03.091.
- [261] Thermo Fisher, *Chemical Reactivity of Crosslinkers and Modification Reagents*. 2012.

8. RESUM EN CATALÀ

La incidència de la diabetis ha augmentat considerablement en els últims anys. Segons l'IDF (International Diabetes Federation), al 2019 hi havia 463 milions de persones que patien diabetis i les estimacions estimen un augment considerable de casos, arribant als 700 milions de persones diabètiques cap al 2045 [1]. Entre els diferents tipus de diabetis, la diabetis tipus 2, és la que té major incidència en la població, corresponent al 90% dels casos de pacients amb diabetis. Aquest tipus de diabetis, succeeix quan el cos es torna resistent a la insulina.

Aquesta resistència a la insulina per part dels teixits perifèrics ens prova que la diabetis no és només una malaltia del pàncreas, sinó que hi ha altres teixits relacionats, com el fetge, el teixit adipós o el múscul esquelètic. Aquest últim té un factor molt rellevant en la homeòstasi de la insulina i la glucosa, ja que és un dels principals teixits consumidors de glucosa. La interacció, però, entre aquest dos teixits encara presenta molts interrogants.

Actualment, per estudiar com dos teixits interactuen entre ells, el testeig animal és el mètode més fiable. No obstant, presenta certes limitacions, com la poca similitud en quan a l'activitat dels illots, la variabilitat fisiològica entre diferents animals, dilemes ètics o la necessitat d'encarar la recerca cap a una medicina més personalitzada. Aquesta finalitat és el que ha portat als científics a buscar alternatives a l'experimentació animal. Entre moltes, una de les més prometedores són els anomenats Òrgans-en-un-xip, plataformes 3D de cultiu cel·lular combinades amb microfluídica i biomaterials que permeten simular les funcions específiques d'un òrgan.

Per tal de generar el teixit dins d'aquesta plataforma, l'encapsulació de cèl·lules dins de hidrogels és la tècnica més utilitzada, degut al seu alt contingut d'aigua, la seva adaptabilitat mecànica o la possibilitat de generar una certa estructura geomètrica [2]. No obstant, la seva petita porositat, limita la difusió homogènia d'oxigen i de nutrients dins seu [3].

Aquest problema creix quan es volen encapsular illots pancreàtics en bastides d'hidrogel, degut a la seva mida ($\sim 100 \mu\text{m}$ de diàmetre). Els illots pancreàtics són agregacions de varis tipus diferent de cèl·lules, on destaquen les cèl·lules secretores de insulina (cèl·lules beta) i les secretores de glucagó (cèl·lules alfa). Per altre costat, el teixit muscular s'encapsula en petits constructes per tal d'imitar l'estructura d'aquest. El múscul esquelètic és un teixit altament alineat, amb cèl·lules multi nucleades, anomenades miotubs, que s'obtenen a partir de la fusió de cèl·lules soles, anomenades mioblasts.

Per tal de solucionar aquests problemes, els criogels han aparegut com a alternativa. Els criogels, estan fabricats a temperatures sota zero, així mentres el polímer crosslinca es formen cristalls de gel. Un cop formada la matriu, la

bastida es descongela i aquests cristalls es desfaran, deixant pas a espais buits, anomenats pors. Aquests, seran els que posteriorment li donaran la l'estructura porosa, altament interconnectada, amb alta permeabilitat i amb una arquitectura de pors determinada a la nostra bestida.

En aquesta tesi s'han desenvolupat dos bastides de cel·lulosa carboxymetilada diferents seguint la tècnica de la criogelificació. Cada bastida ha estat dissenyada per tenir una distribució i una arquitectura de pors diferent d'acord amb la necessitat i propietat del teixit que es vulgui generar. A més, les propietats físiques i mecàniques de les dos bastides tenen alta semblança amb les propietats físiques i mecàniques de la matriu extracel·lular de cada teixit.

Per el teixit pancreàtic, s'ha generat una bastida amb un diàmetre de pors similar als illots pancreàtics, per tal que, semblant cèl·lules beta, aquestes formin pseudoillots similars als illots fisiològics. A més, s'ha demostrat que aquests illots tenen el diàmetre i la arquitectura desitjada, són viables i capaços de respondre a diferents nivells de glucosa. A més, s'ha demostrat que aquestes cèl·lules agregades en forma de pseudoillots responen millor a la glucosa que les cèl·lules configurades en distribució dispersa.

En el cas del múscul esquelètic, s'ha desenvolupat una bastida amb una arquitectura de pors altament alineada per promoure l'alineament cel·lular i la fusió cel·lular. A més, s'han pogut incorporar nanotubs de carboni per millorar les propietats elèctriques de la bastida. D'aquesta manera, aplicant pulsos elèctrics per estimular el teixit, s'han pogut millorar les etapes primerenques de la maduració miogènica.

9. JOURNAL ARTICLES

PAPER

View Article Online
View Journal | View Issue

Cite this: *Nanoscale Adv.*, 2020, 2, 2885

New volumetric CNT-doped gelatin–cellulose scaffolds for skeletal muscle tissue engineering†

Ferran Velasco-Mallorquí,^a Juan M. Fernández-Costa,^{id a} Luisa Neves^b and Javier Ramón-Azcón^{id *a}

Currently, the fabrication of scaffolds for engineered skeletal muscle tissues is unable to reach the millimeter size. The main drawbacks are the poor nutrient diffusion, lack of an internal structure to align the precursor cells, and poor mechanical and electric properties. Herein, we present a combination of gelatin-carboxymethyl cellulose materials polymerised by a cryogelation process that allowed us to reach scaffold fabrication up to millimeter size and solve the main problems related to the large size muscle tissue constructs. (1) By incorporating carbon nanotubes (CNT), we can improve the electrical properties of the scaffold, thereby enhancing tissue maturation when applying an electric pulse stimulus (EPS). (2) We have fabricated an anisotropic internal three-dimensional microarchitecture with good pore distribution and highly aligned morphology to enhance the cell alignment, cell fusion and myotube formation. With this set up, we were able to generate a fully functional skeletal muscle tissue using a combination of EPS and our doped-biocomposite scaffold and obtain a mature tissue on the millimeter scale. We also characterized the pore distribution, swelling, stiffness and conductivity of the scaffold. Moreover, we proved that the cells were viable and could fuse in three-dimensional (3D) functional myotubes throughout the scaffold. In conclusion, we fabricated a biocompatible and customizable scaffold for 3D cell culture suitable for a wide range of applications such as organ-on-a-chip, drug screening, transplantation and disease modelling.

Received 4th April 2020
Accepted 28th May 2020

DOI: 10.1039/d0na00268b

rsc.li/nanoscale-advances

Introduction

Nanomaterials have recently gained significant attention as tools to improve the electrical and mechanical properties of biomaterials.¹ For instance, alginate hydrogels impregnated with gold nanostructures improved the electrical conductivity and cellular excitability of both cardiomyocytes and neural cells.^{2,3} Nanomaterials encapsulated in scaffold materials could also enhance the sensitivity of engineered tissues mimicking the native nervous system,⁴ which can be used in fundamental cell biology and diagnostics. For example, carbon nanotubes (CNTs)⁵ and nanowires⁶ have been used to sense the extra- and intra-cellular activities of cells or to tailor the delivery of therapeutic molecules to cells.

The aim of tissue engineering is to fabricate, repair, and/or replace tissues and organs using cell technology, medicine, advanced materials, and engineering approaches.^{7,8} Nanotechnology and microtechnology have made significant contributions to the field of tissue engineering in recent years. In

particular, nanotechnology provides novel tissue engineering fabrication techniques and nano-composed biomaterials.

Scaffolds are the key part in the development of engineered tissues. They support the growth and differentiation of progenitor cells in 3D environments. Hydrogels are often used as scaffolds due to their high water content, biocompatibility, and biodegradability.^{9,10} However, they generally have poor mechanical properties and low conductivity, which limit their application in regulating the behaviour of electroactive cells, such as skeletal, cardiac, and neural cells.² Therefore, controlling the mechanical and electrical properties of hydrogels is desirable in regulating cell behaviours. Electrically conductive and mechanically strong hydrogels have other important applications, such as the real-time monitoring of cellular activities^{11,12} and developing hybrid three-dimensional (3D) electronics-tissue materials¹³ and as bioactuators.¹⁴

To date, scaffolds for skeletal muscle tissue engineering have been generated mostly by the encapsulation of cells inside hydrogels,¹⁵ both by bioprinting^{16–18} or stamping^{19,20} techniques. However, it is difficult to obtain a single hydrogel that meets all desirable properties. As mentioned above, these hydrogels are not conductive, and they lack optimal mechanical properties. *In vivo*, skeletal muscle cells are constantly triggered to contract by nerve signals that are transmitted to the muscle tissue through the neuromuscular junctions.^{21,22} Without these nerve signals,

^aInstitute for Bioengineering of Catalonia (IBEC), The Barcelona Institute of Science and Technology (BIST), Baldiri I Reixac, 10-12, Barcelona, Spain. E-mail: jramon@ibecbarcelona.eu

^bMultiwave Imaging, Hotel Technoptic, 2 Rue Marc Donadille, 13013 Marseille, France

† Electronic supplementary information (ESI) available. See DOI: 10.1039/d0na00268b



muscle development is impaired. Therefore, controlling the mechanical and electrical properties of hydrogels is desirable to facilitate the regulation of muscle cell behaviours (Fig. 1a). The positioning of cells, delivery of molecules, and design of scaffolds from the nanoscopic scale to the macroscopic scale can be achieved using novel nanotechnologies.^{7,23–27} In order to enhance the electrical properties of the scaffolds, some approaches have integrated nanoparticles as graphene,²⁸ gold,²⁹ silver,³⁰ iron oxide³¹ or CNTs.^{32,33} However, these fabrication approaches cannot be scaled up to engineer scaffolds in the centimeter or millimeter range, because the porosity is small and the low nutrient diffusion makes them inadequate for long-term cell culture. Another issue is the pre-alignment of cells to obtain long and functional differentiated tissues. To overcome these limitations and in order to generate a bigger 3D functional aligned muscle tissue, the cryogel approach technology has been proposed in this work. This technique allows the generation of a millimeter range scaffold, with high pore interconnectivity and a better mechanical stability than the hydrogel-based scaffolds for generating skeletal muscle tissue by mimicking its 3D environment.

Cryogels are microporous scaffolds^{34–36} with a pore range from a few micrometers up to hundreds of micrometers. The pores are a consequence of water ice crystallization after freezing the polymer solution (Fig. 1b). Once the cryogel is thawed, the ice crystals leave behind empty pores. We were able to modulate the pore morphology by applying different freezing directionalities.^{37,38} As the skeletal muscle needs a highly aligned morphology to enhance its alignment and fusion, we generated an anisotropic morphology by forcing the

directionality of the freezing from one single axis. In that way, the ice crystallization allowed us to fabricate a mechanically stable scaffold for skeletal muscle tissue engineering.

Here, we present a new gelatin–microcellulose biomaterial composite (Fig. 2) doped with CNTs with mechanical stability, anisotropic pore morphology and electrical properties applied in skeletal muscle tissue engineering. We have fabricated a scaffold based on the combination of a natural degradable biomaterial with a non-biodegradable material by mammalian cells using gelatin and carboxymethyl cellulose. Gelatin has good properties for tissue regeneration, such as pore structure, permeability, and hydrophilicity, with natural cell binding motifs, such as the tripeptide Arg-Gly-Asp (RGD) and it is stable *in vivo*.^{37,39} However, to improve its mechanical stability, the incorporation of carboxymethyl cellulose (CMC) has been proposed. CMC is a linear, long-chain, water-soluble, anionic polysaccharide that is taken from the cellulose and can be degraded by non-mammalian cells.⁴⁰ This new doped bio-composite has an anisotropic pore distribution, high fiber alignment and good pore diameter that allow for highly efficient nutrient diffusion. The formation of nanofiber web-like structures of CNTs within hydrogels resulted in hybrid hydrogels with enhanced mechanical properties compared with the unmodified hydrogels. An anisotropic conductive scaffold is highly beneficial for the fabrication of functional skeletal muscle tissue constructs with the aid of electrical stimulation. All of these features combined with the technique of cryogelation allow us to generate millimeter-range scaffolds. In this work, we demonstrated that myoblasts could be aligned following this pore structure, colonizing the whole 3D structure,

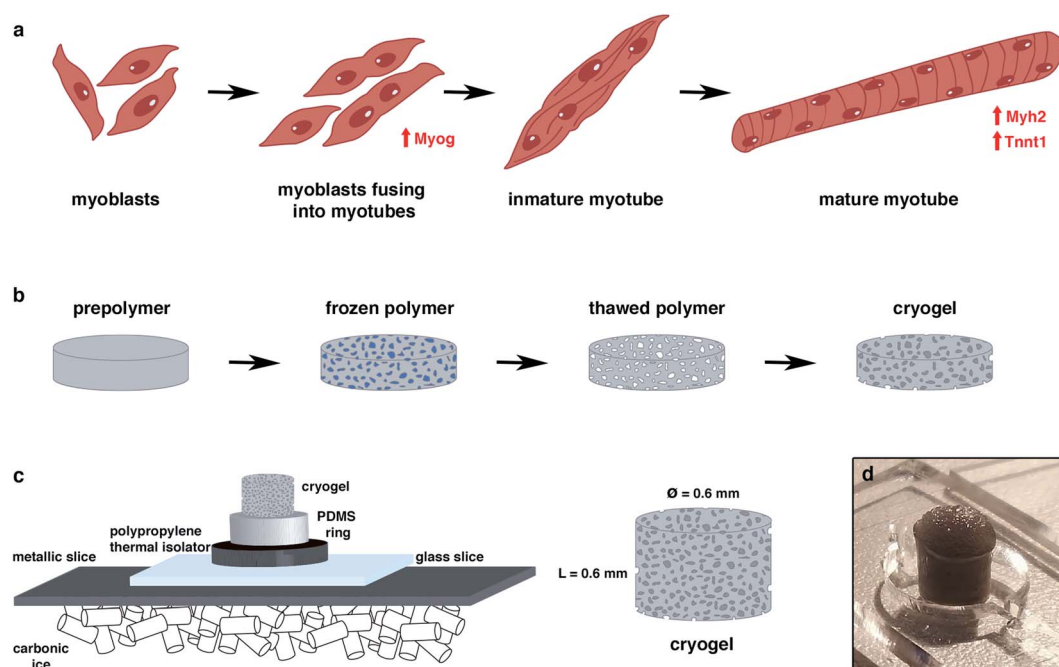
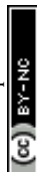


Fig. 1 General overview of the study. (a) Myogenic differentiation process. Muscle precursor cells and myoblasts were fused to form immature myotubes, while the myogenin (Myog) expression increased. Myotube maturation implied an upregulation of Myosin Heavy Chain 2 (Myh2) and tropomyosin (Tnni1) genes. (b) Principle of the cryogelation technique. (c) Protocol to generate a highly anisotropic cryogel.



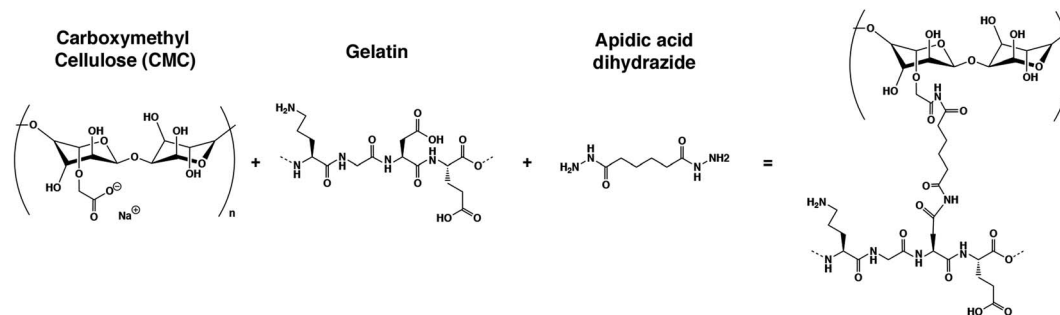


Fig. 2 Chemical structure of the reagents and final structure after crosslinking.

and fusing into myotubes. We also proved that the electrical stimulation, in combination with this scaffold, enhances the maturation of these cells. All of these features make this new CNT-doped gelatin-CMC biomaterial composite a promising scaffold to engineer millimeter-range skeletal muscle tissue for many applications.

Experimental procedures

Cryogel fabrication

To fabricate carboxymethyl cellulose (Sigma Aldrich) at 1% (w/v), gelatin from porcine skin (Sigma Aldrich) and 2% (w/v) cryogels were dissolved into Milli-Q water under stirring conditions. Once the CMC and gelatin were dissolved, the crosslinking reagents were prepared. Adipic acid dihydrazide (AAD, Sigma Aldrich) at 50 mg mL⁻¹, MES buffer from MES hydrate (Sigma Aldrich) at 0.5 M and pH at 5.5 and *N*-(3-dimethylaminopropyl)-*N*'-ethylcarbodiimide hydrochloride (EDC, Sigma Aldrich) at 1 mg μL⁻¹ all dissolved in Milli-Q water and were vortexed to ensure homogeneity throughout the solution. To fabricate the prepolymer solution, 0.5 mL of CMC was mixed with 0.5 mL of gelatin, 100 μL of MES buffer, 100 μL of Milli-Q water, 21 μL of AAD and 4 μL of EDC. The mixture was then vigorously pipetted to avoid early crosslinking before freezing. For the stained cryogels, 12 μL of 1 mM fluoresceinamine (Sigma Aldrich) was added to the prepolymer solution. In the case of the doped cryogels with carbon nanotubes, 100 μL of CNT (Sigma Aldrich) at 2 mg mL⁻¹ dissolved in Milli-Q water was added in substitution of the 100 μL of Milli-Q water. Then, the molds, which consisted of a circular pool of PDMS (5 mm height × 6 mm diameter) surrounded by a polypropylene thermal isolator and a square cover glass (24 × 24 mm²) on the top, were filled with the final prepolymer solution. Once filled, the mold was quickly placed over a metallic sheet above carbonic ice and allowed to freeze for 1 hour (Fig. 1c). Then, the molds were placed into a -20 °C freezer for 24 hours. The next day, the crosslinked cryogels (Fig. 2) were removed carefully from the cover glass and PDMS mold, and subsequently cut. For the 3D approach, the top and bottom parts were cut to avoid the regions with small porosity. After slicing the cryogels, they were submerged in cleaning solution for 5 minute consecutive cleaning steps. The cleaning solution was composed of 1 × Milli-Q water, 1 × 100 mM NaOH (Panreac), 1 × 10 mM EDTA (Sigma

Aldrich), 1 × MilliQ and 3 × PBS (Sigma Aldrich). Once the cleaning protocol was finished, the cryogels were sterilized in an autoclave for further cell seeding experiments.

Mechanical and electrical properties of the GelMA-CMC and GelMA-CMC-CNTs cryogels

Pore analysis. For the pore analysis, we used stained cryogels. Once autoclaved, the z-stack images were examined with a confocal microscope. The different pore diameters were quantified with ImageJ software. We analyzed 20 different images per cryogel, with 20 μm of distance in the z-axis between the images, and 3 cryogels. For the diameter quantification, the minFerret approximation was used in order to calculate the small diameter of each pore. The small diameter was used as the minimal distance of the pore, so it was a good indication to see if the cells could infiltrate the cryogel.

The cryogels were fabricated for the SEM images. After sterilizing, ethanol dehydration was done to substitute the water for ethanol. Starting at 50% ethanol, consecutive washings were done by increasing the percentage of ethanol up to 70%, 80%, 90%, 96% (×2) and 99.5% ethanol. Once all of the water was substituted with ethanol, a critical point dry was done in order to remove all the ethanol and replace it with CO₂. Then, carbon sputtering was performed, and the SEM images were taken using a JEOL JSM-7001F at 10 kV.

Conductivity. To measure the dielectric properties of the samples, a tapered transmission line method was used. The conical feature of the cell allows the insertion of a watertight sample-holder (SH), providing a significant increase of the net sample volume. This modification permitted the evolution of the coaxial line in terms of the types of materials measured,^{41,42} in addition to the speed and flow of acquisition.⁴³

In this study, the cell was connected to a calibrated Anritsu MS46122B VNA, which enabled the extraction of the *S*-parameters *S*₁₁, *S*₁₂, *S*₂₁, and *S*₂₂ of the cell and sample. Knowing the intrinsic electric distances between the connectors and sample, and considering the attenuation of the cell, it is possible to carry out a de-embedding process, where the *S*-parameters of the sample are extracted through the *S*-parameters of the cell and sample.

The acquisition method of the complex permittivity is based on the Nicolson-Ross⁴⁴ & Weir⁴⁵ algorithm. Through the sample



S-parameters, it is possible to determine the reflection (Γ) and transmission (T) coefficient, as seen in eqn (1)–(6),

$$\Gamma = \frac{1 + S_{11}^2 - S_{21}^2}{2S_{11}} \pm \sqrt{\left(\frac{1 + S_{11}^2 - S_{21}^2}{2S_{11}}\right)^2 - 1} \quad (1)$$

$$T = \frac{S_{11} + S_{21} - \Gamma}{1 - (S_{11} + S_{21})\Gamma} \quad (2)$$

$$z_r = \left(\frac{1 + \Gamma}{1 - \Gamma}\right) \quad (3)$$

where z_r is the reduced impedance of the system. A condition that must be respected at this point is that the magnitude of $|\Gamma|$ must be equal or inferior to the unit. Thus, it is possible to determine the complex permittivity (ϵ^*), the complex permeability (μ^*), and the conductivity (σ), expressed in S m^{-1} .

$$\mu_r = j \frac{c}{2\pi f L} \left(\frac{1 + \Gamma}{1 - \Gamma}\right) \ln\left(\frac{1}{\Gamma}\right) \quad (4)$$

$$\epsilon_r = j \frac{c}{2\pi f L} \left(\frac{1 - \Gamma}{1 + \Gamma}\right) \ln\left(\frac{1}{\Gamma}\right) \quad (5)$$

$$\sigma = 2\pi f \epsilon'' \epsilon_0 \quad (6)$$

Here, L represents the sample length, c is the speed of light in a vacuum, and ϵ_0 is the permittivity of the free space, $8.85 \times 10^{-12} \text{ F m}^{-1}$.

An SH of length 6 mm was used to measure the samples from 10 MHz to 8 GHz, at room temperature (RT) conditions (26.8 °C, 31% humidity).

The cylindrical samples have a similar diameter and length as the SH, so the samples were simply introduced into the SH. In this configuration, the CNTs were aligned with the axis of the cell.

Swelling. Swelling is the water uptake capability of a biomaterial. In order to measure this capability, cryogels were fabricated as explained previously, sterilized, dried at RT and weighed. Next, the cryogels were submerged into Milli-Q water for up to 5 days when they reached equilibrium, and weighed again. The swelling ratio was calculated as follows:

$$\text{Swelling ratio} = \frac{W_{\text{eq}} - W_{\text{d}}}{W_{\text{eq}}} \times 100$$

where W_{eq} is the weight in equilibrium and W_{d} is the dry weight. 3 cryogels per condition were measured in this assay.

Stiffness. Compression assays were performed to determine the stiffness of our samples. The compression was applied both in the x - and y -axis in order to check the correct anisotropy of the cryogels. Biaxial compression assays were performed in a Zwick Z0.5 TN instrument (Zwick-Roell) with 5 N load cell. The experiment was performed with samples at room temperature at up to 30% of the final compression range at 0.1 mN of the preloading force, and at 20%/minute of the strain rate. Finally, the Young modulus was calculated from the slope of the range from 10% to 20% of the final compression. In these experiments, we tested 3 measurements per cryogel and axis and 3 cryogels per condition.

Culture of C2C12 myoblasts in the GelMA-CMC and GelMA-CMC-CNTs cryogels

Cell culture. The C2C12 myoblasts (American Type Culture Collection (ATCC)) were cultured in growth medium (DMEM, high glucose with L-glutamine (Gibco, Thermofisher) supplemented with 10% FBS (Thermofisher) and 1% Pen/Strep (Thermofisher)). When 70–80% confluence was reached, the C2C12 myoblasts were trypsinized using 0.25% trypsin/0.1% EDTA and subsequently plated in a 1 : 4 density ratio. The cells were maintained in a cell culture incubator (Sanyo) with a 5% CO_2 atmosphere at 37 °C.

C2C12 seeding into the cryogel. First, the cryogel pores were kept dry for 30 minutes at RT. For cell seeding, a concentration of 9×10^6 cells per mL was used. Upon achieving this concentration, a drop of 20 μL was seeded into the upper part of the cryogel. After 10 minutes, we collected the medium from the bottom that could pass through the cryogel, and we reseeded it at the top of the cryogel again. After cell inoculation, the cryogels were in the growth medium for 10 days, and then the medium was changed to a differentiation medium (DMEM high glucose with L-glutamine (Thermofisher) supplemented with 2% horse serum (Thermofisher) and 1% Pen/Strep (Thermofisher)) for up to 22 days of culture in order to promote myotube formation.

Immunostaining protocol. For confocal analysis, stained cryogels were used. After culturing the cells, the cryogels were washed with PBS and fixed with a 10% formalin solution (Sigma Aldrich) for 30 minutes. Then, the cryogels were washed with Tris Buffered Saline (TBS, Canvax Biotech) and permeabilized with 0.1% v/v Triton X-100 (Sigma Aldrich) solution in TBS for 15 minutes. Following this procedure, the blocking of the cryogels was done with a blocking solution of 0.3% v/v Triton X-100 and 3% v/v Donkey serum (Sigma-Aldrich) in TBS for 2 hours. Then, 100 nM Rhodamine-Phalloidin 480 (Cytoskeleton Inc) and 5 $\mu\text{g mL}^{-1}$ MF20 Alexa Fluor 488 (eBioscience) in blocking solution was incubated overnight at 4 °C. Rhodamine-Phalloidin 480 was used for F-actin and MF20 Alexa Fluor 488 for Myosin Heavy Chain (red and green staining, respectively). The following day, the cryogels were washed with permeabilization solution (3 \times , 10 minutes each). Subsequently, the cryogels were incubated with 1 μM DAPI (Thermofisher) for nuclei counterstain into the blocking solution for 15 minutes. Finally, the cryogels were washed with TBS for 15 minutes and stored at 4 °C until acquired for confocal microscopy. Images were taken using a LSM 800 confocal microscope from Zeiss.

Viability assay. Viability assays were performed using the Live/Dead assay kit (Thermofisher), in accordance with the manufacturer's instructions. The assays were performed at days 1, 5 and 7 of culture after seeding in both types of cryogels with or without CNTs. Briefly, the cryogels were washed for 5 minutes with PBS (Phosphate Buffered Saline, 0.01 M phosphate buffer, 0.0027 M potassium chloride and 0.137 M sodium chloride, pH 7.4, Sigma-Aldrich) five times to replace the culture medium, and subsequently incubated with the final dye solution. This solution consisted of 12 μL of 12 mM EthD-1, 3 μL of 4 mM calcein AM and 6 μL of Hoechst for the dead cells, live cells and



nuclei, respectively, into 6 mL of PBS. Then, the solution was vortexed, and 2 mL of this solution was added to each cryogel and incubated for 25 min at 37 °C. Then, the cryogels were washed 3 times with PBS. Finally, confocal images were taken using a Zeiss LSM 800 confocal microscope. The quantification of the live/dead ratio was calculated using ImageJ software, and was determined as follows:

$$\text{Live ratio} = \frac{\# \text{Nuclei} - \#(\text{Nuclei} - \text{EthD areas})}{\# \text{Nuclei}} \times 100$$

Cell alignment. To calculate the alignment of the fibers, fluorescein-stained cryogels were used. In addition, nuclei and F-actin for the cells were stained following the immunostaining protocol. Confocal images were obtained using a Zeiss LSM 800 confocal microscope. For this quantification, 5 images per cryogel were taken. The ImageJ PlugIn "OrientationJ" software was used to see the distribution of the aligned fibers and the alignment of the cells in a random fiber distribution of the cryogel against the anisotropic cryogels.

Electrical stimulation. An electric pulse stimulation (EPS) was applied at day 11 after induction of the myogenic differentiation. The stimulation was performed by placing the cryogels inside a 6-well plate C-dish from IonOptix connected to a multifunction generator (WF 1948; NF Co.) with a specified regime (1 Hz of frequency, 1 V p-p and 10 ms of width) for 12 consecutive hours.

Fusion index. For differentiation of the myoblast into myotubes, the cells were seeded as previously explained in the cryogel and cultivated for 22 days. For those that were stimulated, EPS was applied to the cryogels at day 21 of culture. Cryogels were immunostained as described above, and sliced vertically to improve the image acquisition. Then, the confocal images were taken at 5 random areas over the cryogel, and 3 cryogels per condition were used. From these images, the fusion index was calculated. The index fusion consisted of the number of cells that were differentiated and fused. To calculate the fusion index, the following equation was used:

$$\text{Fusion index} = \frac{\# \text{Green \& blue areas}}{\text{Total \#nuclei}} \times 100$$

For the index fusion analysis, 5 images per sample and 3 samples per condition were taken and analysed.

RNA isolation, retrotranscription and real-time quantitative polymerase chain reaction (qRT-PCR)

For the total RNA isolation of the single cryogels, a standard organic extraction using TriReagent (Sigma) was performed. Briefly, single cryogels were homogenized with 1 mL of TriReagent at room temperature and mixed with 200 µL of chloroform. Samples were centrifuged at 12 000 rcf for 15 minutes at 4 °C and the aqueous phase was collected. Finally, RNA was precipitated using isopropanol and GlycoBlue (Invitrogen) as the carrier. One microgram of total RNA was digested with DNase I (Invitrogen), and retrotranscribed with SuperScriptII

(Invitrogen) using random hexanucleotides. For each biological replicate, qRT-PCR reactions from 10 ng of cDNA were carried out per triplicate using HOT FIREPol EvaGreen qPCR Mix Plus (SolisBiodyne). The primers used were: 5'-CATTGCTGACAGGATGCAGAAAGG-3'/5'-TGCTGGAAGGTGGACAGTGAGG-3' for ActB, 5'-GCTGGAAGATGAGTGCTCAGAG-3'/5'-TCCAAAC-CAGCCATCTCCTCTG-3' for Myog, 5'-GCGACTTGAAGTTAGCC-CAGGA-3'/5'-CTCGTCCTCAATCTTGCTCTGC-3' for Myh2 and 5'-GAGCAGAGGATGACGCCAAGAA-3'/5'-TTCATCTCCCGAC-CAGTCTGTC-3' for Tnnt1. Expression levels were measured using an Applied Biosystems StepOnePlus Real Time PCR System. The expression level relative to the ActB endogenous genes and the control group was calculated using the $2^{-\Delta\Delta C_t}$ method. Pairs of samples were compared using the two-tailed *t* tests ($\alpha = 0.05$), applying Welch's correction when necessary. The statistical differences were estimated by the Student's *t* tests ($p < 0.05$) on normalized data. At least three cryogels per condition were evaluated.

Statistical analysis. For pore analysis, we analysed 20 different images per cryogel, with 20 µm of distance in the z-axis between images, and 3 cryogels. For swelling, 3 cryogels per condition were assessed. This was performed similarly for the stiffness, where we tested 3 measurements per cryogel and axis, and 3 cryogels per condition. In the case of the alignment image quantification, 3 samples per condition and 5 images per sample were taken and evaluated. For the viability and fusion index analysis, 3 cryogels per condition and 20 images per sample were taken and evaluated. For the qPCR, 2 different experiments were done. In each experiment, 3 cryogels per condition and 2 replicas per sample were performed. For statistical analysis, the two-tailed Student *t*-test ($\alpha = 0.05$) was used to check the statistical significance of all samples.

Results and discussion

Cryogel fabrication and mechanical characterization

The protocol to fabricate cryogels (Fig. 1c) was taken and modified from a previous study.³⁶ The size of the scaffold (6 mm of diameter × 6 mm of height) was chosen as a good area for seeding in the x-axis and a good length in the y-axis. This was enough to form the desired anisotropic structure. 2% gelatin – 1% CMC (w/v) cryogels (Fig. 2) was chosen as the ideal one. This was because it is the lowest possible material concentration with enough stiffness to hold and handle the scaffold without breaking it. In addition, results not shown in this study proved that as the material concentration was decreased, a bigger pore size could be achieved.³⁷ According to the approach used, big tubular pores were expected to facilitate the cell seeding and migration through the cryogel. We have obtained volumetric constructions in the range of millimeters. Previous scaffolds made by encapsulation into hydrogels could not reach these dimensions due to their low mechanical properties or pore distribution, leading to a lack of nutrient diffusion. As we have shown in previous works, when the cells are encapsulated in depths of more than 200 µm, their viability decreases.⁴⁶ The pore sizes of most hydrogels described to date are small. This characteristic feature in the hydrogels leads to difficulties in



nutrient diffusion. This is the main reason why bioprinted hydrogels have dimensions that are smaller than 500 μm .^{21,47,48} However, using our unidirectional cryogelation technique, we obtained cryogels with enough pore size and high-water retention capability to allow for fast nutrient and medium diffusion along the entire scaffold. Specifically, our cryogel has a flow rate of 0.034 mL min^{-1} .

By analyzing the pore distribution, we can observe that small pores are always present (Fig. 3a and b). However, most of the pores are in a specific range between 30 and 75 μm of the diameter. This pore range is appropriate for seeding the cells over the cryogel. Moreover, this pore size range allowed for cell growth and migration, and finally colonization throughout the whole cryogel. Myotube maturation implied the alignment and fusion of myoblast precursors. The mature myotubes had a dimension that was not larger than 30 μm in width,^{49,50} so the pore size of our cryogels would allow for the correct myotube maturation. Supporting the pore distribution analysis, the scanning electron microscope images showed this same distribution, where most of the pores were bigger than 30 μm diameter (Fig. 3a). In addition, we can appreciate the tubular shape of these pores. The vertical cross-section of the fluorescein-stained cryogels taken with a confocal microscope proved that the anisotropy of the fibers was achieved (Fig. 3c). This feature is a highly important feature for engineering the skeletal muscle tissue, as the skeletal muscle tissue needs high alignment and superorganization to differentiate between the

myoblasts and myotubes. With the technique, we achieved a good pore distribution and pore size that allowed for a good infiltration of the cells. Moreover, the cryogel pores had a high alignment that enhanced the fusion and differentiation of the skeletal muscle myotubes. Although there are other techniques to achieve this alignment to enhance cell fusion, such as bio-printing,⁴⁶ stamping^{48,51} or stretching,⁵² our technique allowed us to enhance this alignment using surface directionality, as some 2D approaches used to generate this alignment without encapsulating.^{52–55} Combining 3D directionality plus millimeter size, we were able to obtain volumetric tissue constructions. By combining these features with our technique, we could obtain a good scaffold to engineer highly organized tissue as skeletal muscle. Cryogelation showed a strong and nonharmful technique for generating the scaffolds with a higher pore distribution, synonymous with a higher nutrient diffusion and low confinement of the cells. This implied less difficulties in the proliferation and migration.

Electric stimulation improves *in vitro* myotube maturation.⁵⁶ Unfortunately, most of the scaffolds used for tissue engineering have low conductivity. Therefore, this electrical stimulation to myogenic maturation is not very effective. In order to increase the conductivity of our scaffolds, we incorporated carbon nanotubes (CNTs) to our cryogels. In order to do this, we incorporated the CNTs mixed in the prepolymer solution. By doing so, when all of the process of crosslinking happens, the CNTs stay in the fiber network. Analysis of CNTs distribution by bright field microscopy showed that the incorporation of CNTs was not homogeneous (Fig. 3d). The CNTs formed aligned aggregates through the cryogel. To test if the CNTs improved the electric properties of the cryogels, we performed conductivity assays (Fig. 4a). This conductivity was similar in the low frequency ranges. From 1×10^7 to 2.5×10^8 Hz, the conductivity was around 1 S m^{-1} for cryogels both without and with CNTs. However, the conductivity of the CNT cryogels increased faster with frequency than the ones without CNT. Moreover, CNTs increased the conductivity of the cryogels at higher frequencies up until 2×10^9 Hz, where the cryogels with CNTs reached 5.71 S m^{-1} vs. 4.08 S m^{-1} for the cryogels without CNTs (Fig. 4b). The conductivity achieved with our scaffolds was similar to or higher than other scaffolds used for the maturation of myotubes.^{57,58} In previous electrically stimulated scaffolds for skeletal muscle tissue engineering studies, conductivities from 10 mS m^{-1} to 6.4 S m^{-1} were achieved, and maturation of the tissue was enhanced. In our case, we could enhance the electrical properties of the scaffold. In addition, we were able to modulate the frequency and conductivity of these scaffolds. In this way, we can obtain different conductive values, but always in the range of previous studies. Notably, the conductivity can be modulated by changing the concentration of CNT.⁵⁹ However, there is a big disparity in the literature about the ideal conductivity of a scaffold to engineer and enhance myogenic differentiation. This disparity gives a real advantage for our scaffold, as we are able to modulate the conductivity. The high conductivity of our cryogels makes them suitable for many EPS (Electrical Pulse Stimulation) assays for the maturation or even contraction of the skeletal muscle tissue.

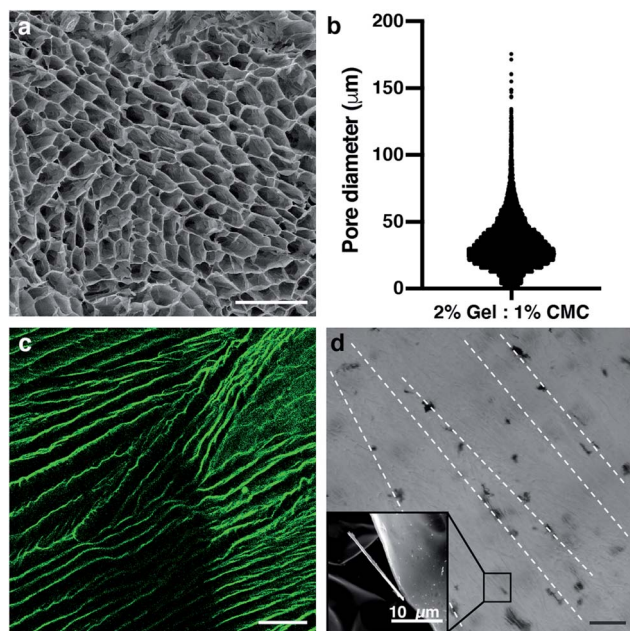


Fig. 3 The pore size distribution and tubular pore morphology among the scaffold fit with the skeletal muscle tissue engineering needs. (a) Scanning electron microscope (SEM) image of the pores of the cryogel. (b) Diameter distribution of the pores among the 2% gelatin – 1% CMC cryogel. (c) Confocal image of the cryogel anisotropic fibers marked with aminofluorescein in green. (d) Bright field image of the CNT distribution inside the cryogel. SEM image of a CNT is shown in the small inset. Scale bars = 100 μm .



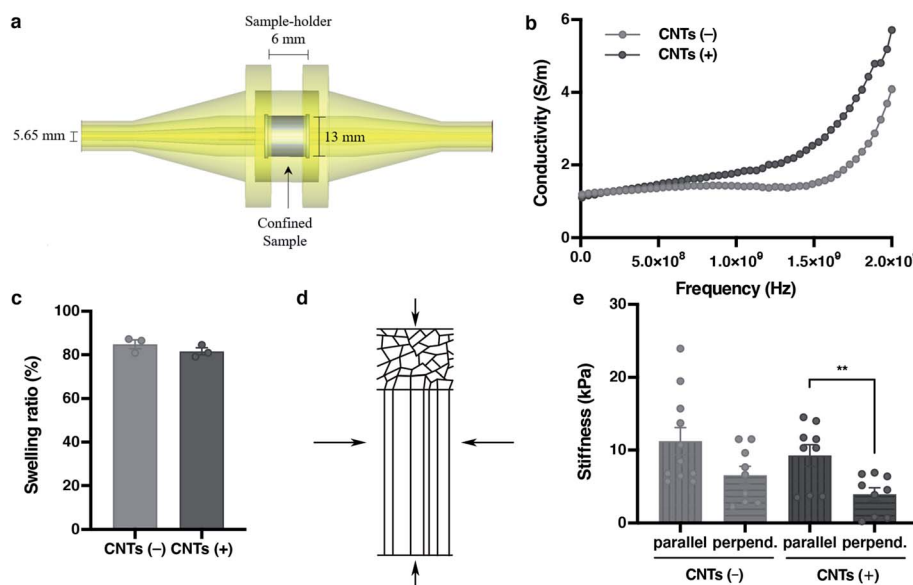


Fig. 4 Mechanical characterization of the scaffold sets. Its features are the ideal ones for generating skeletal muscle tissue. (a) The conical coaxial adjustment of the EpsiMu transmission line. (b) Conductivity (S m^{-1}) of the cryogels. (c) Swelling ratio of each cryogel. (d) Compression axis from the stiffness assay of the cryogel. Vertical arrows are the parallel condition and horizontal arrows are the perpendicular condition. (e) Stiffness results for cryogels in both directions. (b, c and e) CNTs(–) in light grey and CNTs(+) in dark grey. All results are mean \pm SEM. * p -value = 0.05.

Nutrient diffusion is an important feature for scaffolds in tissue engineering, and even more so for big volumetric scaffolds. To estimate the nutrient diffusion in our cryogels, we analysed the swelling ratio. The swelling ratio is the water uptake capability of a scaffold. Several features of the scaffold could affect the swelling ratio. We observed that the main factor is the amount of material. Also, we observed that the pore morphology had an effect in the swelling ratio (data not shown). A lower material concentration implies a higher pore distribution. In addition, a higher pore distribution implies more capability for the cryogel to take up water and more nutrient diffusion. The analyses of the swelling show that our cryogels have a high swelling ratio ($84.81 \pm 3.52\%$), indicating that the cryogels have not only a good porosity, but also a good interconnectivity. This would lead to a high nutrient diffusion. Notably, the addition of CNTs into the cryogels did not affect the swelling characteristic of the cryogel ($84.81 \pm 3.52\%$ for CNTs(–) vs. $81.58 \pm 2.78\%$ for CNTs(+)) (Fig. 4c).

In addition, every tissue has its own characteristic environment. For this reason, the resemblance with the *in vivo* ECM is a highly important feature for the proper tissue formation. To generate a scaffold that mimics the physiological environment, stiffness is another important property to consider in designing good scaffolds for tissue engineering. As cells behave differently when the scaffold stiffness changes,^{51,60} it is fundamental to have a scaffold that most closely resembles the *in vivo* condition for tissue engineering. To analyse the stiffness of the cryogels, a compression assay was performed. The Young's modulus was calculated from the linear part of the stress–strain curves, and measurements from two different axes were made to prove the anisotropy structure of the cryogel. As expected, the stiffness changed due to the fiber anisotropy when the compression was

applied perpendicularly or parallel to the fibers (Fig. 4d). This tendency of the values proved that the stiffness changed, depending on the directionality of the applied compression (11.21 ± 6.11 kPa for parallel/CNTs(–) vs. 6.52 ± 3.75 kPa for perpendicular/CNTs(–)) against the fibers (Fig. 4e). When the compression was applied along the perpendicular axis, there were some empty spaces from the pores that allowed the cryogel to compress. On the other hand, when the compression was applied in the parallel direction, it was harder to compress the fibers due to its alignment. In addition, as with the swelling properties, the addition of the carbon nanotubes did not affect the stiffness along any of the axes (9.24 ± 4.46 kPa for parallel/CNTs(+) vs. 11.21 ± 6.22 kPa for parallel/CNTs(–), and 3.90 ± 2.7 kPa for perpendicular/CNTs(+) vs. 6.52 ± 3.75 kPa for perpendicular/CNTs(–)). Remarkably, the stiffness of the cryogel showed *in vivo* similarity mechanical properties^{51,61} at around 12 kPa stiffness, while the traditional hydrogels with the same amount of material had less *in vivo* resemblance.^{46,62} Of importance, our results suggest that the addition of CNTs did not change the mechanical features of the scaffolds. So, we can improve the conductivity without losing any important feature of the scaffold. The combination of all of these features is a good point for engineering electrically stimulated tissues, such as skeletal muscle.

CNT-doped cryogels allow cell alignment and viability for long term cultures

C2C12 cells (mouse skeletal muscle immortalized myoblasts) were seeded inside the cryogel by gravity, as they cannot be encapsulated like hydrogels. To be able to form tissue without cell encapsulation is another important point to consider. Normally, encapsulation of the cells inside hydrogels implies



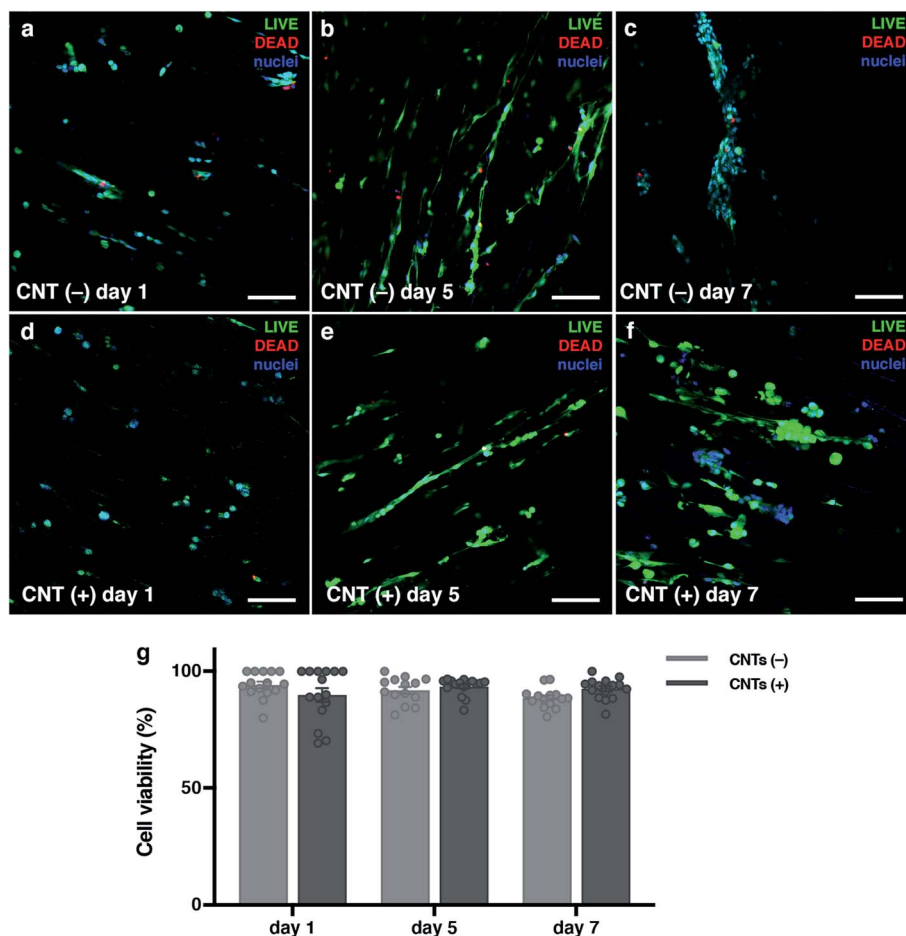


Fig. 5 Cells are viable when seeded inside the cryogel. (a–f) Confocal merged images of Live/Dead assay on different days. Live cells are marked in green with calcein AM, dead cells are marked in red with EthD-1, and cell nuclei are counterstained in blue with DAPI. (g) Graphs of the viability results. CNTs(–) in light grey and CNTs(+) in dark grey. Results are mean \pm SEM. * p -value = 0.05.

the polymerization of the matrix using external crosslinkers like UV light, chemical reagents or temperature changes. This exposition to different crosslinkers could damage these cells. The cryogelation technique can solve this main drawback, as the scaffold polymerization occurs before seeding. An important point for engineering skeletal muscle is the cell density for seeding into the scaffold, as myoblasts need to be confluent in order to fuse into myotubes. We optimized the cells density at 9×10^6 cells per mL to allow for proliferation and colonization throughout the biomaterial. Other models for engineering the skeletal muscle tissue use similar or higher densities.^{19,63} Nevertheless, at higher concentration, the cells did not properly colonize our cryogel because they formed a layer on the top (data not shown). After seeding, cells were cultured for 10 days in growth medium to promote cell proliferation and scaffold colonization. Then, the medium was replaced to differentiation media to promote myotube formation for 12 additional days. By immunostaining and confocal microscopy analysis, we could prove that the cells were found throughout the scaffold and they were distributed homogeneously through the cryogel, demonstrating that the cells could colonize the entire depth of the cryogel (Fig S11†).

To determine if the CNT-doped cryogel could be toxic for the cells, we decided to analyse the viability of the cells and if they could proliferate in the first few days. A Live/Dead assay was performed, and we determined that the viability of the C2C12 cells was always higher than 88%. In addition, there was no statistical significance between any day and condition (Fig. 5). However, an increase of the dead cells could be seen throughout the entire experiment. As the cells also proliferated, this ratio did not increase statistically. These high viability results are due to the crosslinking technique that allow us to seed the cells without suffering any damage due to the crosslinking process. The pore size and high pore distribution, which led to a high nutrient diffusion, also positively affected the high cell viability. More importantly, as reported previously, the CNT had no toxic effect.^{64,65} The results compared on the same day with and without CNT were non-statistically significant, meaning there was also a good viability in the CNT scaffolds.

As mentioned, another important feature for engineering skeletal muscle is the cell alignment to enhance myogenic maturation. For this reason, one of the properties we wanted for our scaffold is the high anisotropy of the pores to promote cell alignment and fusion. Comparing the random pore



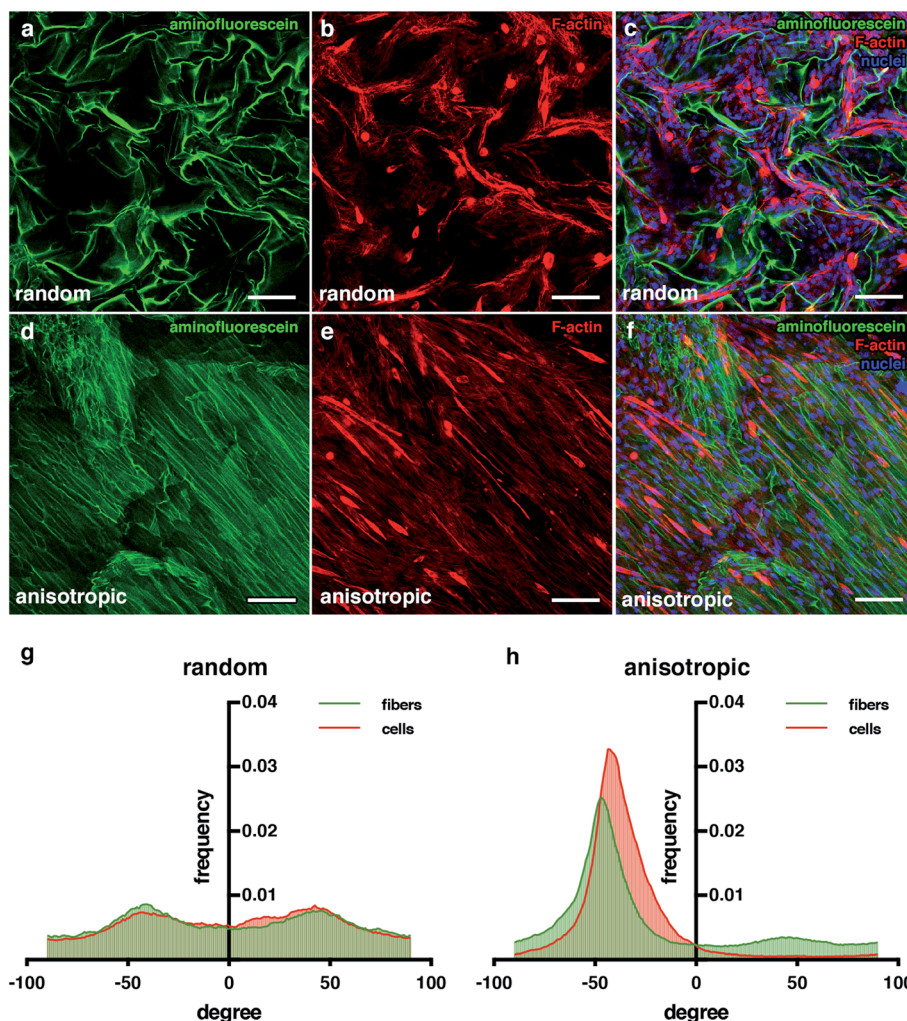


Fig. 6 Anisotropic cryogels improve cell alignment. (a–f) Confocal microscopy images showing an aminofluorescein-marked cryogel in green (a and d), cells marked with phalloidin in red (b and e) and cell nuclei counterstained in blue with DAPI. (c and f) Images showing merged channels. Scale bars = 100 μ m. (g and h) Quantification of fibers and cell orientation. Graphs show frequency of fibers in each orientation degree.

morphology *versus* the anisotropic pore morphology (Fig. 6), we can appreciate that the cells in the anisotropic aligned much more clearly than the random one. Analysis with the ImageJ software demonstrated that the distribution obtained for the random pore distribution had more variability among all angles compared with the anisotropic structure one. In addition, it can be appreciated that in both pore morphologies, the alignment distributions for the cryogel fibers and cells were very similar (Fig. 6b). These results indicate that the cells sensed the pore morphology, and they could distribute and align following the morphology of the pores. The alignment of the cells was proved by the enhancement of their fusion;^{50,66} thus, these results indicate that our cryogels could improve the myogenic maturation.

Electric stimulation of C2C12 cultured in CNT-doped cryogels enhances myoblasts fusion and myogenic maturation

Electrical Pulse Stimulation (EPS) was applied to prove that this new electrically improved composite enhanced the myogenic

maturation of the C2C12 myoblasts. To check the myotube formation, we analysed the expression of the muscle maturation marker Myosin Heavy Chain (Mhc) by immunostaining (Fig. 7a and b and ESI Fig. 2†). Cryogels with EPS applied had a higher fusion index ($51.84 \pm 5.30\%$) in comparison with non-EPS stimulation ($25.54 \pm 5.06\%$) (Fig. 7c), indicating that the electrically stimulated cryogel enhanced the fusion of the cells into myotubes.^{56,67,68} We performed a complementary study on the gene expression of some myogenic markers by qPCR to further analyze the effect of EPS in myogenic maturation. We selected three genes whose dynamic expressions would change during the muscle maturation: myogenin (Myog), myosin heavy chain 2 (Myh2) and troponin T1 (Tnnt1) (Fig. 7d–f). Myog is a marker that is expressed in the early maturation steps, when the myotubes are fusing. By gene amplification, we could observe that myogenin was still expressed in the EPS(+) cryogels. These results are in correlation with the obtained fusion index results. We observed that the cells started the myogenic differentiation as the myotubes were formed. However, this



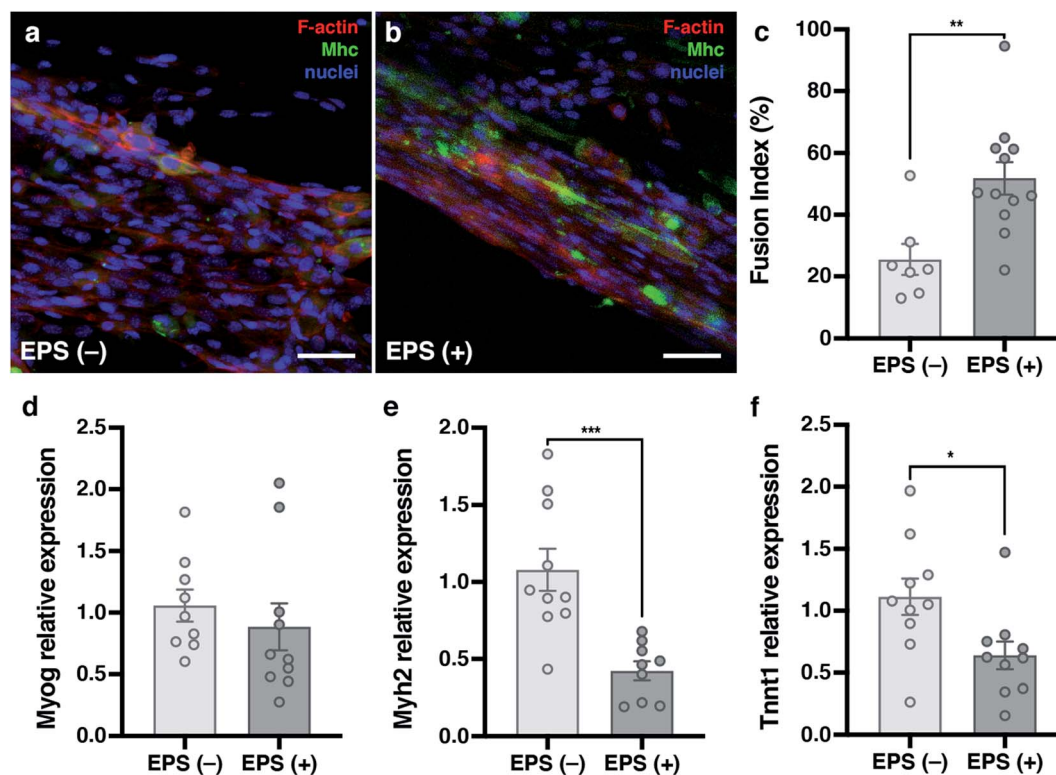


Fig. 7 Electrical Pulse Stimulation (EPS) enhances myogenic maturation. (a and b) Confocal merged images showing cells marked with phalloidin in red, cell nuclei counterstained in blue with DAPI and Mhc marked with Alexa-488 in green. Scale bars = 100 μ m. (c) Graphs showing fusion index of CNTs(-) cryogels in light grey and CNTs(+) cryogels in dark grey. (d-f) Graphs of myogenic maturation marker expression. EPS(-) in light grey and EPS(+) in dark grey. (d) Myogenin. (e) Myosin heavy chain 2. (f) Troponin T1. Results are mean \pm SEM. * p -value = 0.05.

might indicate that they were still in an early phase of the maturation. To confirm our hypothesis, we also analyzed both Myh2 and Tnnt1, which are late maturation markers. These markers are expressed when the tissue is fully mature. However, in our assay, these markers from a later myotube differentiation were downregulated, confirming that most myotubes in EPS(+) were in the first steps of the maturation process. Although we did not detect an increase of the late maturation markers by qPCR, we showed that the myotubes were formed and expressed Mhc (Fig. 7a and b). Moreover, the fusion index was higher in the EPS(+) cryogels and Myog was still expressed, meaning that the maturation process of the tissue already started. Taking this point as a mature step, we can conclude that our scaffold enhanced the cell maturation when EPS was applied. However, more research would be necessary to further enhance the myotube maturation.

Conclusion

Here, we present a new methodology to fabricate volumetric scaffolds to generate skeletal muscle *in vitro*. The technique used allows us to control not only the external morphology of the scaffold, but also the internal pore morphology and size in a highly controlled way. Our protocol shows a micro-porosity range scaffold with highly aligned fibers. In addition, its mechanical properties match well with the needs to engineer

skeletal muscle. Moreover, the addition of CNT to our scaffold has enhanced its electrical properties. All of this is possible without the loss of any other important properties of the scaffold to generate volumetrically larger skeletal muscle tissue. Herein, we proved that these composite scaffolds with integrated CNT are non-toxic, as the cells were viable, and enhanced the fusion of the cells due to its high alignment. Once the cells fused, taking advantages of the improved electrical properties of our doped-biomaterial scaffold, we could stimulate the cells. We proved that they could mature faster and better. In conclusion, our protocol shows a new doped-biomaterial composite scaffold that enhances the fusion and maturation of the cells by applying EPS, leading to a complete skeletal muscle generated *in vitro* with strong possibilities in tissue engineering, organ-on-a-chip technology or drug screening.

Conflicts of interest

There are no conflicts to declare.

Acknowledgements

The authors acknowledge financial support from the European Research Council program under grants ERC-StG-DAMOC (714317), Fundació; the CERCA program and the Spanish Ministry of Economy and Competitiveness through the "Severo



Ochoa" Program for Centres of Excellence in R&D (SEV-2016-2019) and "Retos de investigación: proyectos I+D+i" (TEC2017-83716-C2-2-R), the CERCA Programme/Generalitat de Catalunya (2014-SGR-1460) and Fundació Bancaria "la Caixa"-Obra Social "la Caixa" (project IBEC-La Caixa Healthy Ageing).

References

- 1 S. Ahadian, J. Ramón-Azcón, S. Ostrovidov, G. Camci-Unal, V. Hosseini, H. Kaji, K. Ino, H. Shiku, A. Khademhosseini and T. Matsue, *Lab Chip*, 2012, **12**, 3491–3503.
- 2 M. Estili, A. Kawasaki and Y. Sakka, *Adv. Mater.*, 2012, **24**, 4322–4326.
- 3 S. Ahadian, J. Ramón-Azcón, S. Ostrovidov, G. Camci-Unal, H. Kaji, K. Ino, H. Shiku, A. Khademhosseini and T. Matsue, *Biomed. Microdevices*, 2013, **15**, 109–115.
- 4 T. D. Schmittgen and K. J. Livak, *Nat. Protoc.*, 2008, **3**, 1101–1108.
- 5 Y. A. Kim, T. Hayashi, M. Endo, Y. Kaburagi, T. Tsukada, J. Shan, K. Osato and S. Tsuruoka, *Carbon*, 2005, **43**, 2243–2250.
- 6 M. L. P. Langelaan, K. J. M. Boonen, K. Y. Rosaria-Chak, D. W. J. van der Schaft, M. J. Post and F. P. T. Baaijens, *J. Tissue Eng. Regener. Med.*, 2011, **5**, 529–539.
- 7 P. Zorlutuna, N. Annabi, G. Camci-Unal, M. Nikkhah, J. M. Cha, J. W. Nichol, A. Manbachi, H. Bae, S. Chen and A. Khademhosseini, *Adv. Mater.*, 2012, **24**, 1782–1804.
- 8 R. Gauvin and A. Khademhosseini, *ACS Nano*, 2011, **5**, 4258–4264.
- 9 M. Estili and A. Kawasaki, *Adv. Mater.*, 2010, **22**, 607–610.
- 10 M. Estili, A. Kawasaki, H. Sakamoto, Y. Mekuchi, M. Kuno and T. Tsukada, *Acta Mater.*, 2008, **56**, 4070–4079.
- 11 H. Aubin, J. W. Nichol, C. B. Hutson, H. Bae, A. L. Sieminski, D. M. Cropek, P. Akhyari and A. Khademhosseini, *Biomaterials*, 2010, **31**, 6941–6951.
- 12 D. Wang, S. Fujinami, H. Liu, K. Nakajima and T. Nishi, *Macromolecules*, 2010, **43**, 9049–9055.
- 13 H. Liu, N. Chen, S. Fujinami, D. Louzguine-Luzgin, K. Nakajima and T. Nishi, *Macromolecules*, 2012, **45**, 8770–8779.
- 14 B. Derjaguin, V. Muller and Y. Toporov, *J. Colloid Interface Sci.*, 1975, **53**, 314–326.
- 15 J. Ramon-Azcon, S. Ahadian, R. Obregon, G. Camci-Unal, S. Ostrovidov, V. Hosseini, H. Kaji, K. Ino, H. Shiku, A. Khademhosseini and T. Matsue, *Lab Chip*, 2012, **12**, 2959–2969.
- 16 H.-W. Kang, S. J. Lee, I. K. Ko, C. Kengla, J. J. Yoo and A. Atala, *Nat. Biotechnol.*, 2016, **34**, 312–319.
- 17 S. Ostrovidov, S. Salehi, M. Costantini, K. Suthiwanich, M. Ebrahimi, R. B. Sadeghian, T. Fujie, X. Shi, S. Cannata, C. Gargioli, A. Tamayol, M. R. Dokmeci, G. Orive, W. Swieszkowski and A. Khademhosseini, *Small*, 2019, **15**, 1805530.
- 18 A. García-Lizarriar, X. Fernández-Garibay, F. Velasco-Mallorquí, A. G. Castaño, J. Samitier and J. Ramon-Azcon, *Macromol. Biosci.*, 2018, **18**, 1–13.
- 19 M. A. Ortega, X. Fernández-Garibay, A. G. Castaño, F. De Chiara, A. Hernández-Albors, J. Balaguer-Trias and J. Ramón-Azcón, *Lab Chip*, 2019, **19**, 2568–2580.
- 20 W. Bian and N. Bursac, *Biomaterials*, 2009, **30**, 1401–1412.
- 21 Y. Morimoto, M. Kato-Negishi, H. Onoe and S. Takeuchi, *Biomaterials*, 2013, **34**, 9413–9419.
- 22 K. H. Nakayama, M. Shayan and N. F. Huang, *Adv. Healthcare Mater.*, 2019, 1801168.
- 23 L. Y. Jiang and Y. Luo, *Soft Matter*, 2013, **9**, 1113–1121.
- 24 M. Nikkhah, F. Edalat, S. Manoucheri and A. Khademhosseini, *Biomaterials*, 2012, **33**, 5230–5246.
- 25 R. Obregón, J. Ramón-Azcón, S. Ahadian, H. Shikul, H. Bae, M. Ramalingam and T. Matsue, *J. Nanosci. Nanotechnol.*, 2014, **14**, 487–500.
- 26 E. Engel, A. Michiardi, M. Navarro, D. Lacroix and J. A. Planell, *Trends Biotechnol.*, 2008, **26**, 39–47.
- 27 W. H. Ryu, R. J. Fasching, M. Vyakarnam, R. S. Greco and F. B. Prinz, *J. Microelectromech. Syst.*, 2006, **15**, 1457–1465.
- 28 A. E. Jakus, E. B. Secor, A. L. Rutz, S. W. Jordan, M. C. Hersam and R. N. Shah, *ACS Nano*, 2015, **9**, 4636–4648.
- 29 J.-O. You, M. Rafat, G. J. C. Ye and D. T. Auguste, *Nano Lett.*, 2011, **11**, 3643–3648.
- 30 H.-L. Tan, S.-Y. Teow and J. Pushpamalar, *Bioengineering*, 2019, **6**, 17.
- 31 V. Bonfrate, D. Manno, A. Serra, L. Salvatore, A. Sannino, A. Buccolieri, T. Serra and G. Giancane, *J. Colloid Interface Sci.*, 2017, **501**, 185–191.
- 32 S. Ahadian, J. Ramón-Azcón, M. Estili, X. Liang, S. Ostrovidov, H. Shiku, M. Ramalingam, K. Nakajima, Y. Sakka, H. Bae, T. Matsue and A. Khademhosseini, *Sci. Rep.*, 2015, **4**, 4271.
- 33 S. R. Shin, H. Bae, J. M. Cha, J. Y. Mun, Y.-C. Chen, H. Tekin, H. Shin, S. Farshchi, M. R. Dokmeci, S. Tang and A. Khademhosseini, *ACS Nano*, 2012, **6**, 362–372.
- 34 X. Su, Q. Zhang, Q. Zhong, L. Liu, H. Gao, R. Meng and J. Yao, *Fibers Polym.*, 2016, **17**, 712–720.
- 35 P. B. Welzel, M. Grimmer, C. Renneberg, L. Naujox, S. Zschoche, U. Freudenberg and C. Werner, *Biomacromolecules*, 2012, **13**, 2349–2358.
- 36 A. Bédier, T. Braschler, O. Peric, G. E. Fantner, S. Mosser, P. C. Fraering, S. Benchérif, D. J. Mooney and P. Renaud, *Adv. Healthcare Mater.*, 2015, **4**, 301–312.
- 37 X. Wu, Y. Liu, X. Li, P. Wen, Y. Zhang, Y. Long, X. Wang, Y. Guo, F. Xing and J. Gao, *Acta Biomater.*, 2010, **6**, 1167–1177.
- 38 J. Wu, Q. Zhao, J. Sun and Q. Zhou, *Soft Matter*, 2012, **8**, 3620.
- 39 C. B. Hutson, J. W. Nichol, H. Aubin, H. Bae, S. Yamanlar, S. Al-Haque, S. T. Koshy and A. Khademhosseini, *Tissue Eng., Part A*, 2011, **17**, 1713–1723.
- 40 R. Reeves, A. Ribeiro, L. Lombardo, R. Boyer and J. B. Leach, *Polym.*, 2012, **2**, 252–264.
- 41 É. Georget, R. Abdeddaim and P. Sabouroux, *C. R. Phys.*, 2014, **15**, 448–457.
- 42 D. Ba and P. Sabouroux, *Microw. Opt. Technol. Lett.*, 2010, **52**, 2643–2648.
- 43 A. L. Neves, E. Georget, N. Cochinaire and P. Sabouroux, *Rev. Sci. Instrum.*, 2017, **88**, 084706.



- 44 A. M. Nicolson and G. F. Ross, *IEEE Trans. Instrum. Meas.*, 1970, **19**, 377–382.
- 45 W. B. Weir, *Proc. IEEE*, 1974, **62**, 33–36.
- 46 A. García-Lizarribar, X. Fernández-Garibay, F. Velasco-Mallorquí, A. G. Castaño, J. Samitier and J. Ramon-Azcon, *Macromol. Biosci.*, 2018, **18**, 1800167.
- 47 R. Seyedmahmoud, B. Çelebi-Saltik, N. Barros, R. Nasiri, E. Banton, A. Shamloo, N. Ashammakhi, M. R. Dokmeci and S. Ahadian, *Micromachines*, 2019, **10**, 679.
- 48 V. Hosseini, S. Ahadian, S. Ostrovidov, G. Camci-Unal, S. Chen, H. Kaji, M. Ramalingam and A. Khademhosseini, *Tissue Eng., Part A*, 2012, **18**, 2453–2465.
- 49 P. Molnar, W. Wang, A. Natarajan, J. W. Rumsey and J. J. Hickman, in *Biotechnology Progress*, 2007, vol. 23, pp. 265–268.
- 50 A. Bettadapur, G. C. Suh, N. A. Geisse, E. R. Wang, C. Hua, H. A. Huber, A. A. Viscio, J. Y. Kim, J. B. Strickland and M. L. McCain, *Sci. Rep.*, 2016, **6**, 1–14.
- 51 A. J. Engler, M. A. Griffin, S. Sen, C. G. Bönnemann, H. L. Sweeney and D. E. Discher, *J. Cell Biol.*, 2004, **166**, 877–887.
- 52 C. Snyman, K. P. Goetsch, K. H. Myburgh and C. U. Niesler, *Front. Physiol.*, 2013, **4**, 349.
- 53 C. Monge, K. Ren, K. Berton, R. Guillot, D. Peyrade and C. Picart, *Tissue Eng., Part A*, 2012, **18**, 1664–1676.
- 54 N. F. Huang, R. J. Lee and S. Li, *Am. J. Transl. Res.*, 2010, **2**, 43–55.
- 55 N. Jiwwat, E. M. Lynch, B. N. Napiwocki, A. Stempien, R. S. Ashton, T. J. Kamp, W. C. Crone and M. Suzuki, *Biotechnol. Bioeng.*, 2019, **116**, 2377–2392.
- 56 H. Park, R. Bhalla, R. Saigal, M. Radisic, N. Watson, R. Langer and G. Vunjak-Novakovic, *J. Tissue Eng. Regener. Med.*, 2008, **2**, 279–287.
- 57 S. Sirivisoot and B. S. Harrison, *Int. J. Nanomed.*, 2011, **6**, 2483–2497.
- 58 M. C. Chen, Y. C. Sun and Y. H. Chen, *Acta Biomater.*, 2013, **9**, 5562–5572.
- 59 M. Kharaziha, S. R. Shin, M. Nikkhah, S. N. Topkaya, N. Masoumi, N. Annabi, M. R. Dokmeci and A. Khademhosseini, *Biomaterials*, 2014, **35**, 7346–7354.
- 60 S. Romanazzo, G. Forte, M. Ebara, K. Uto, S. Pagliari, T. Aoyagi, E. Traversa and A. Taniguchi, *Sci. Technol. Adv. Mater.*, 2012, **13**, 064211.
- 61 N. Sachot, E. Engel and O. Castano, *Curr. Org. Chem.*, 2014, **18**, 2299–2314.
- 62 L. E. Bertassoni, M. Cecconi, V. Manoharan, M. Nikkhah, J. Hjortnaes, A. L. Cristino, G. Barabaschi, D. Demarchi, M. R. Dokmeci, Y. Yang and A. Khademhosseini, *Lab Chip*, 2014, **14**, 2202–2211.
- 63 A. S. Salimath and A. J. García, *J. Tissue Eng. Regener. Med.*, 2016, **10**, 967–976.
- 64 J. Ramón-Azcón, S. Ahadian, M. Estili, X. Liang, S. Ostrovidov, H. Kaji, H. Shiku, M. Ramalingam, K. Nakajima, Y. Sakka, A. Khademhosseini and T. Matsue, *Adv. Mater.*, 2013, **25**, 4028–4034.
- 65 J. Ren, Q. Xu, X. Chen, W. Li, K. Guo, Y. Zhao, Q. Wang, Z. Zhang, H. Peng and Y. G. Li, *Adv. Mater.*, 2017, **29**, 1–8.
- 66 H. Takahashi, T. Shimizu, M. Nakayama, M. Yamato and T. Okano, *Biomaterials*, 2013, **34**, 7372–7380.
- 67 A. Ito, Y. Yamamoto, M. Sato, K. Ikeda, M. Yamamoto, H. Fujita, E. Nagamori, Y. Kawabe and M. Kamihira, *Sci. Rep.*, 2015, **4**, 4781.
- 68 R. Banan Sadeghian, M. Ebrahimi and S. Salehi, *J. Tissue Eng. Regener. Med.*, 2018, **12**, 912–922.



Cellulose-based scaffolds enhance pseudoislets formation and functionality

Ferran Velasco-Mallorquí^{1*}, Júlia Rodríguez-Comas^{1*}, Javier Ramón-Azcón^{1,2}

¹ Institute for Bioengineering of Catalonia (IBEC), The Barcelona Institute of Science and Technology (BIST), Baldri I Reixac, 10-12, Barcelona, Spain.

² ICREA-Institució Catalana de Recerca i Estudis Avançats, 08010 Barcelona, Spain.

*Authors contributed equally to this work

E-mail: jramon@ibecbarcelona.eu

Abstract

The limitations of obtaining pancreatic islets from different sources as animal models or human donors complicate the study of type 2 diabetes (T2D) *in vitro*. Immortalized cell lines as the insulin-producing INS1E β -cells appeared as a valid alternative to model insulin-related diseases. The formation of 3D structures to promote cell aggregations from single cells is a handy tool to generate resemblance islet-like pseudoislets. Traditionally used hydrogel encapsulation methods induce a lack of nutrient and oxygen diffusion for pancreatic tissue engineering. Here, we use cryogelation technology to develop a more resemblance scaffold with the mechanical and physical properties needed to engineer pancreatic tissue. This study shows that carboxymethyl cellulose (CMC) cryogels prompted cells to generate β -cell clusters. The high porosity achieved with this approach allowed us to create specific range pseudoislets. However, gelatin-based scaffolds did not induce this cell organization. Pseudoislets formed within CMC-scaffolds showed cell viability for up to 7 days and responded better to the glucose over conventional monolayer cultures. Overall, our results demonstrate that CMC-scaffolds can be used to control the organization and function of insulin-producing β -cells, representing a suitable technique to generate β -cell clusters to study pancreatic islet function.

Keywords: tissue engineering, biomaterial, scaffold, cryogel, β -cell, pancreatic islets

1. Introduction

The worldwide prevalence of type 2 diabetes (T2D) has been increasing over the last decades, attaining the status of a global pandemic. T2D is a chronic metabolic disorder characterized by hyperglycemia. It occurs either when the pancreas does not produce enough insulin, when the peripheral tissues cannot effectively use the insulin it produces, or both [1].

In vitro research for the study of T2D is frequently limited by the availability of a functional model for islets of Langerhans. Pancreatic islets are responsible for maintaining glucose homeostasis by secreting the glucose-lowering hormone insulin and its antagonist, glucagon. Cell lines are a suitable alternative to model T2D *in vitro* and avoid human donor material or primary mouse pancreatic islets. Both mouse insulinoma MIN6 and rat insulinoma INS1E cell lines are commonly used for *in vitro* research. Nevertheless, INS1E cells have been reported to present better

responsiveness to glucose within the physiological range and relatively high insulin content [2,3].

Monolayer cell cultures have been shown to function differently than cells *in vivo*, and results of *in vitro* tests may not accurately reflect cell response occurring *in vivo* [2]. Pancreatic islets are round-shaped cell aggregations of around 100 μm in diameter. Their size and shape determine their functionality, crucial to orchestrate the metabolic adjustments [4]. Indeed, β -cell aggregations into pseudoislets have been proven to represent a more suitable model to study β -cell function, demonstrating a better biological response than cultured monolayered cells [5,6]. However, most of these studies use pseudoislets in suspension, therefore not representing an accurate image of the *in vivo* environment to study its behavior [7,8].

To solve this problem, biomaterials and tissue engineering appeared as a valid alternative to generate 3D microenvironments. The use of scaffolds has allowed the generation of a wide variety of 3D environments that have enabled better to mimic the *in vivo* situation of each tissue (e.g., skeletal muscle [9,10], intestine [11], or liver [12]).

With this purpose, hydrogel encapsulation has appeared as the gold standard. This technique allows modulating the external morphology (i.e., lines [10], pillars [11], or meshes [13]), the stiffness, the pore size, or the biochemical cues to promote cell attachment [14,15] to better fit with the needs of every engineered tissue. However, this approach entails several drawbacks that can end up in cell death. Exposure to the UV light or other toxic crosslinking reagents [16] or the small pore sizes (usually in the nanometer range) can lead to insufficient nutrient diffusion, clumping problems, hypoxia, and difficulties inducing vascularization [17,18]. These limitations make this approximation non-suitable for all kinds of tissues. These problems become more detrimental when cell aggregations are encapsulated [19,20] and explicitly challenging with β -cells, specialized cell types adapted to sense rapid changes in glucose [21]. Therefore, a perturbation of the glucose-sensing machinery in these cells can entail a suboptimal insulin release.

Extensive efforts have been made to develop the ideal scaffold to support these cells. Such scaffold must be fabricated with biocompatible polymers, suitable for mammalian cell growth. It must be highly porous to allow adequate oxygen and nutrient diffusion, and it also needs to be mechanically stable, with the appropriate structure to avoid shear-stress-induced cell damage [22]. With the intention to aggregate β -cells in a 3D microenvironment, we engineered gelatin and carboxymethyl cellulose (CMC)-based cryogels, which enabled us to design a supportive material for the growth and proliferation of β -cells. Cryogels, are sponge-like scaffolds with micrometer pore range formed at sub-zero temperatures [23]. This technique entails several advantages compared to other approaches. It allows high pore diameters [24], fundamental to precisely controlling the cell aggregates diameter. Moreover, it provides mechanical support suitable to manipulate the structure easily [26]. And finally, it enables cell seeding after polymerization of the scaffold, therefore avoiding exposure to harmful crosslinking reagents or UV light. Additionally, both materials have been reported to present excellent biocompatible properties [25,26]. Gelatin is a derivate of collagen which displays weak mechanical properties and presents the tripeptide Arg-Gly-Asp (RGD), a cell-binding motif [27]. On the other hand, CMC is a derivate compound from cellulose, which has better mechanical stability and good biocompatibility but without the presence of cell-binding motifs [28].

In this study, INS1E cells were seeded onto 3D gelatin and CMC scaffolds to investigate the substrate architecture's effect on the cell's organization and function. We examined cell viability and formation of cell-clusters after 1, 4, and 7 days of culture, and we compared them with cells seeded in a plate. CMC-based scaffolds promoted the formation of INS1E aggregations into pseudoislets, whereas dispersed organization was observed in gelatin-based cryogels. We also show that INS1E pseudoislets ameliorated their response to glucose stimuli and presented a more closely related mature β -cell phenotype than non-organized cells seeded in gelatin-based cryogels or a traditional well-plate.

Our results demonstrate that scaffold biomaterials can be used to control the organization and enhance the function of insulin-producing β -cells. These advantageous properties make this approach an ideal model for the study of pancreatic islet function, representing a valuable tool for 3D diabetes drug testing and development.

2. Materials and methods

2.1 Cryogel fabrication

Carboxymethyl cellulose (Sigma Aldrich, Germany), or gelatin from porcine skin (Sigma Aldrich, Germany) were diluted into MilliQ water with stirring conditions at 45°C. Once the prepolymer solution is homogeneous, the crosslinking reagents were prepared; MES buffer from MES hydrate (Sigma Aldrich, Germany) at 0.5 M and pH at 5.5, adipic acid dihydrazide (AAD, Sigma Aldrich, Germany) at 50 mg/mL, and N-(3-Dimethylaminopropyl)-N'-ethylcarbodiimide hydrochloride (EDC, Sigma Aldrich, Germany) at 1 μ g/ μ l all dissolved in MilliQ water and vortexed to ensure the homogeneity in all the solution. Prepolymer solution, 1 ml of the prepolymer, 50 mM of MES buffer, 1.83 mM of AAD, and 18.9 μ M of EDC were added into a tube vigorously pipetted, avoiding early crosslinking before freezing. For stained cryogels, 10.9 μ M fluoresceinamine (Sigma Aldrich, Germany) was added to the final prepolymer solution. Then Polydimethylsiloxane (PDMS) molds were filled with the final prepolymer solution. These molds consist of a PDMS pool with 1 mm high and 10 mm of diameter over a squared 24x24 mm cover glass. After filling, they were placed into a -20°C freezer for 24 hours. The next day, the crosslinked cryogels were removed carefully from the mold and then submerged into consecutive 5 minutes cleaning steps; 1x MilliQ water, 1x 100 mM NaOH (Panreac, Germany), 1x 10 mM Ethylenediaminetetraacetic acid (EDTA, Sigma Aldrich, Germany), 1x MilliQ and 3x Phosphate Buffered Saline (PBS, 0.01 M phosphate buffer, 0.0027 M potassium chloride and 0.137 M sodium chloride, pH 7.4, Sigma-Aldrich, Germany). Once finished the cleaning protocol, the cryogels were sterilized for further cell seeding experiments in an autoclave.

2.2 Biomaterial characterization

2.2.1 Pore analysis

For the pore analysis, the fibers of the cryogel were stained, adding 10.9 μ M of fluoresceinamine. Once stained, z-stack images were taken in a confocal microscope, and the different pore diameters were quantified with ImageJ version 1.52b software (National Institutes of Health).

Scanning electron microscopy (SEM) observations were performed with a NOVA NanoSEM 230 microscope at 10 kV. Before imaging, cryogel scaffolds were subjected to

consecutive ethanol dehydration steps, washing the cryogels with ethanol 50%, 70%, 80%, 90%, 96% (x2), and 99.5%. Once all the water was substituted for ethanol, ethanol was replaced by CO₂, performing a critical point dry step. A final stage of carbon sputtering was done before SEM images were taken.

2.2.2 Swelling

Swelling experiments were performed to calculate the water uptake ratio by a cryogel. Cryogels were fabricated as explained previously, and after sterilizing, cryogels were dried at room temperature and weighted. Next, cryogels were submerged into MilliQ water for 24 hours, when they reached equilibrium and weighted again. The swelling ratio was calculated as follows:

$$\text{Swelling ratio} = \frac{W_{eq} - W_d}{W_{eq}} \times 100$$

Where W_{eq} is the weight in equilibrium and W_d is the dry weight. Three cryogels per condition were measured in this assay.

2.2.3 Stiffness

Compression assays were performed to determine the stiffness of our samples. The compression assays were performed in a Zwick Z0.5 TN instrument (Zwick-Roell) with a 5N load cell. The experiment was performed with samples at room temperature up to 30% final compression range at 0.1 mN of preloading force and 20%/minute of strain rate. Finally, the Young modulus was calculated from 10% to 20% of compression from the line's slope. In these experiments, three measurements per cryogel and three cryogels per condition were tested.

2.2.4 Permeability assay

Cryogels were placed over a transwell inside a 12 well-plate. 500 ml of 1.5 mM fluorescein (Sigma Aldrich) were added at the transwell's upper compartment, and 1.5 ml of PBS were added in the lower chamber. 100 µl of PBS from the well were taken out in consecutive times. The same amount of fresh PBS was added to the lower compartment to readjust the volume. This procedure was repeated during different times up to an overnight when equilibrium was reached. Finally, the concentration of fluorescein was obtained by absorbance measurements at 494 nm with a Power wave X microplate spectrophotometer.

Permeability was calculated in the linear part of the diffusion curve by the following equation:

$$\text{Permeability} = \frac{\Delta Q}{\Delta t} \frac{1}{AC_0}$$

Where Q is the milligrams of fluorescein that pass through the cryogel at a specific time, T is the time, A is the area of the cryogel, and C_0 is the initial concentration of fluorescein. Finally, the permeability of the cryogel was the difference between the total permeability and the permeability of the transwell.

2.3 Cell culture

Rat pancreatic β -cell line INS1E cells were cultured in RPMI-1640 with 11.1 mM glucose, supplemented with 10 mM HEPES (Gibco), 2 mM L-glutamine (Gibco), 1 mM sodium-pyruvate (Gibco), 0.05 mM de 2-mercaptoethanol (ThermoFisher), 10% fetal bovine serum (FBS) (v/v) (ThermoFisher) and 1% penicillin/streptomycin (v/v) (ThermoFisher) (complete media). When cells reached confluency, cells were trypsinized with 0.25 Trypsin/0.1% EDTA and plated in a new flask at 1:4 density. Cells were maintained in an incubator at 37°C and 5% CO₂.

2.4 Cell seeding

Cryogels were dried for 30 minutes. After trypsinization of the cells, 200,000 cells mixed with a drop of 20 µl of medium were seeded in each cryogel. After seeding the cells, cryogels were left at RT for 20 minutes, and a complete RPMI-1640 medium was added and left at the incubator until needed for experimental assay.

2.5 Viability

2.5.1 Live/dead

Viability assays were performed with the Live/dead assay kit (ThermoFischer) according to manufacturer instructions. The assays were performed at days 1, 4, and 7 of culture after seeding in traditional well plates and gelatin and CMC cryogels. Briefly, the cryogels were washed 5 minutes with PBS three times to replace culture medium and incubated with the working solution (4 µM EthD-1, 2 µM Calcein AM, and 16.2 µM Hoechst) for 25 min at 37 °C. Then cryogels were washed three times with PBS. Finally, confocal images were taken using a Zeiss LSM 800 confocal microscope. The quantification of Live/Dead ratio was calculated as follows:

$$\text{Live ratio} = \frac{\# \text{Live cells}}{\#(\text{Live cells} + \text{Dead cells})} \times 100$$

2.5.2. AlamarBlue

AlamarBlue test was performed according to manufacturer specifications. Briefly, the medium was removed from the well plate and substituted for new RPMI-1640 with 11.1 mM of glucose medium with 1:10 dilution of AlamarBlue. After 2-hour incubation, 100 µl of each condition was placed in a well of 96 well-plate and read in a

Power wave X microplate spectrophotometer at 570 nm wavelength.

2.6 Immunostaining

For confocal analysis, stained cryogels were used. After culturing the cells, cryogels were washed with PBS and fixed with 10% formalin solution (Sigma – Aldrich) for 30 minutes. Then, cryogels were washed with Tris Buffered Saline (TBS, Canvax Biotech) and permeabilized with 0.1% Triton X-100 (v/v) (Sigma Aldrich) solution in TBS for 15 minutes. Cryogels were blocked with 0.5% Triton X-100 (v/v) and 3% Donkey serum (v/v) (Sigma-Aldrich) into TBS for 2 hours. Cryogels were incubated overnight with primary antibodies against Rabbit-anti Ki-67 (1:250, Invitrogen) and mouse anti-insulin (1:500, Origene) in a blocking solution. The following day, cryogels were washed with permeabilization solution and incubated with secondary antibodies for 2 hours at room temperature (Alexa-Fluor 647 conjugate anti-mouse 1:200 and Alexa-Fluor 568 conjugate anti-rabbit 1:200, Invitrogen). DAPI (1:1000 Thermofisher) was used to stain nuclei. Finally, cryogels were washed with TBS for 15 minutes and stored at 4 °C until confocal microscopy acquisition. Images were taken using an LSM 800 from Zeiss.

2.7 Confocal microscopy

Different z-stacks were acquired for pore quantification, and pores were analyzed from images with 20 µm of z-gap between them. For quantification of live/dead and proliferation assays, 20 images per cryogel were taken and then analyzed. All images were acquired using an LSM 800 from Zeiss.

2.8 Gene expression analysis

Total RNA was isolated from the sample cells using the RNeasy MinElute Cleanup kit (Qiagen) following the manufacturer's instructions. Of total RNA, 200 ng were used for reverse transcription using high capacity cDNA reverse transcription kit (Applied Biosystems). Quantitative PCR reactions were run using SyberGreen (Invitrogen) in a 7900HT fast real-time PCR system (Applied Biosystems) as described elsewhere [29]. Primer sequences used for gene expression analysis are listed in Supplementary Table 1. Tbp1 was used to normalize the mRNA expression of genes of interest.

2.9 Glucose-stimulated insulin secretion (GSIS)

Cells seeded within the cryogels or in a well plate were preincubated with Krebs-Ringer bicarbonate HEPES buffer solution (115 mM NaCl, 24 mM NaHCO₃, 5 mM KCL, 1 mM MgCa₂-6H₂O, 1 mM CaCl₂-2H₂O and 20 mM HEPES, pH 7.4) containing 2.8 mM glucose for 30 min. Then, cells were incubated at low glucose (2.8 mM) for 1h, followed by incubation at high glucose (16.7 mM) and an additional step

at 2.8 mM. After each incubation step, supernatants were collected, and cellular insulin contents were recovered in acid-acetic lysis buffer (Glacial Acetic Acid 5.75%). Insulin concentration was determined by ELISA experiments.

2.10 ELISA

Briefly, mouse mAB insulin 26.6 nM of capture antibody (Novus) was diluted into coating buffer (0.05 M of Sodium Carbonate and Sodium Bicarbonate, pH 9.6) and placed into 96-well plate at 4°C O/N. Next, samples were placed into the plate, and a calibration curve, previously optimized, was performed. After protein attachment into the primary antibody, the biotinylated secondary anti-insulin antibody was placed at 0.2 nM. Next, streptavidin was added at 4.73 nM (Thermo Scientific). Then, citrate buffer (0.04 M Sodium Citrate, pH 5.4, 96 µg/mL of Tetramethylbenzidine and 0.004 % of Oxygen Peroxide) was added to start the reaction. Finally, 4 M Sulfuric acid was added to stop the reaction. The colorimetric quantification was made with a Power wave X microplate spectrophotometer at 490 nm of wavelength.

2.11 Statistical analysis

Data are expressed as the mean ± SEM of at least 3 independent experiments with 3 replicates each. Statistical significance was determined by a two-tailed Student t-test and one-way ANOVA with post hoc Tukey test as appropriate. Results were considered significant at $p < 0.05$.

3. Results and discussion

3.1 Cryogel scaffold characterization

The difficulty of obtaining pancreatic islets from human patients or rodents conceives a big deal to study T2D *in vitro*. The limited availability of primary pancreatic islets has prompted investigators to use cell lines to study β-cell function to model this disease. However, two-dimensional monolayer cell cultures fail to recapitulate the main key characteristics of primary β-cells. The lack of a 3D structure has been proven to be one of the main problems associated with decreased functionality [30]. Despite this limitation, many *in vitro* approaches focused on generating 3D functional pancreatic tissue using hanging-drop methods [31] or cell encapsulation into hydrogels [32,33]. The origin of the pancreatic cells is from animals, cadaveric donors, or immortalized cell lines. However, having cell aggregations of 100 µm (the average size of a pancreatic islet) drives encapsulation problems, such as lack of oxygen and nutrient diffusion [20,21].

Thereby, it is complicated to engineer a fully functional pancreatic tissue. To solve the problems exposed in β-cell obtention and cell encapsulation, we combined clustering cell ability with cryogelation to generate the scaffold. We developed a proper scaffold for *in vivo* mimicking of β-cells

while improving its diffusion with this approximation. These scaffolds were generated at sub-zero temperatures. Thus, while the material fibers crosslink between them, water-ice crystals are formed. When thawed, these ice crystals lead to empty pores (Fig. 1a). This scaffold has a sponge-like, highly interconnected structure with a controllable pore size. This feature makes this scaffold good material to handle due to its elastic properties (Supp. Video 1). Moreover, the good mechanical stability and elasticity allowed manipulating and moving the scaffold from one place to another without breaking it or suffering any damage (Fig. 1b).

One of the remarkable properties of cryogelation is the possibility to modulate the pore size. For this, we studied different material (gelatin and carboxymethyl cellulose) concentrations and quantified the diameter of each pore. Regardless of the material type, in the case of 5% (w/v), porosity ranged from 10 μm up to 100 μm of diameter while in 1% pores ranged from 10 to 150 μm and at 0.5% pores ranged up to 200 μm (Fig. 1c). By observing the fiber mesh, we can note this ascendant porosity range (Fig. 1d). Our goal was to generate β -cell aggregations that match in size with primary pancreatic islets, which are very heterogeneous in size. Therefore, the pore distribution of our scaffold should also present a wide range distribution. Additionally, *in vivo* small pancreatic islets are more common than big ones [34,35]. Knowing all this, we concluded that with 1%

cryogels, we achieved the porosity that suited all the needs exposed.

3.2 CMC cryogel has good physical properties, similar to the native pancreas

We tested two different materials to develop this new approximation, each with various beneficial properties to aggregate β -cells. Carboxymethyl cellulose (CMC) is a biocompatible biomaterial with good mechanical stability and non-mammalian-cell degradable [36]. Importantly, *in vitro* and *in vivo* evaluations of those cellulose-based materials have demonstrated excellent biocompatibility [25,26]. The other material studied is gelatin, a biocompatible biomaterial, mammalian cell degradable, and with RGD cell adhesive points, but with low mechanical stability [27]. In this case, gelatin was selected as it was previously studied that it can enhance pseudoislet formation [30,37].

To prove that the pore distribution fits our needs and does not vary between materials, we studied the pore distribution of the 1% CMC cryogels and 1% gelatin cryogels (Fig. 1a). We could observe that by changing the material, the pore distribution did not change. The pores, as expected, range from 10 μm up to 170 μm . Despite a high amount of small pores found in the cryogel, big pores are also observed. As previously reported, this pore distribution fits with the range that we want to generate cell aggregations.

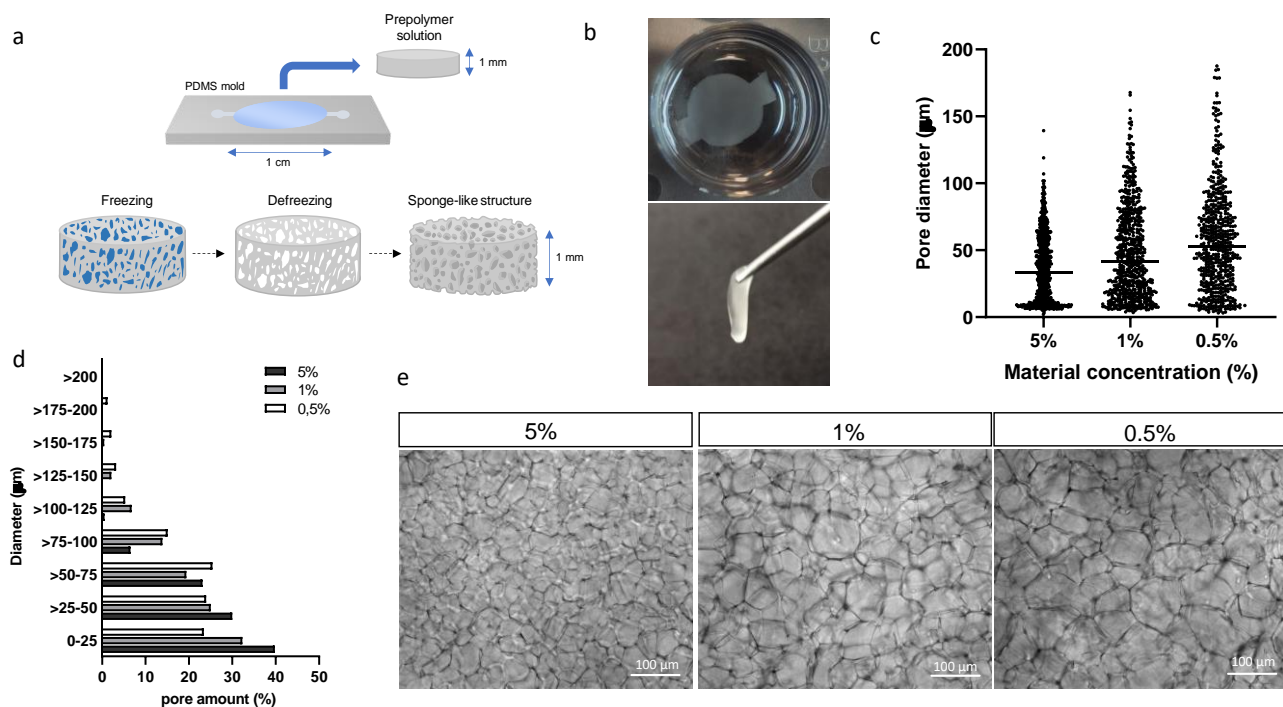


Figure 1: General overview of the study. a) Cryogel fabrication process scheme. Cylinder-like scaffolds were generated, placing the prepolymer solution in a PDMS mold. After, the prepolymer solution within the mold is placed at -20°C . Thus, when material crosslinks, water ice crystals are formed. When thawed, this ice leads to the porosity of the scaffold. b) Images of the cryogel scaffold when deep in water (left) and when tweezered (right), proving the mechanical resistance of the scaffold. c) Pore distribution using different concentrations of the material. d) Percentage of pores in different diameter ranges according to the concentration of the material. Of note, the higher the concentration, the higher the percentage of pores between 0-25 μm of length. e) General magnifying glass images of the scaffold structure among different material concentrations. Scale bar = 100 μm

Additionally, the porosity was analyzed through scanning electron microscopy (SEM) images (Fig. 2b) and confocal images (Fig. 2c). In SEM images acquired after dehydration and critical point dry, it can be observed that pore distribution is heterogeneous, and pores from many different sizes were formed. Following the same tendency, in confocal images, where fibers are stained in green, many different pore sizes can be observed, both in CMC and gelatin cryogels (Fig. 2c). Also, in confocal images, it can be appreciated that there are no significant visual differences in pore size between CMC and gelatin cryogels.

Knowing that the porosity is in the desired range to form pseudoislets with a similar size to the *in vivo*, the next step was to check our scaffold mechanical properties. As we wanted to mimic the extracellular matrix and the pancreatic islet environment, the stiffness is an essential property. The ECM mainly has the objective to support cells and plays an important role in the cells viability and functionality by dotting the cells of specific biochemical and physical signals [38]. Moreover, knowing that cells modulate their behavior in different substrate stiffness [39–41], maintaining a similar stiffness as the pancreas should help the cells to function and differentiate better. Compression assays were performed to study bulk stiffness. CMC cryogel are stiffer than gelatin ($0.67 \text{ kPa} \pm 0.08$ vs $0.30 \text{ kPa} \pm 0.1$) (Fig. 2d). This stiffness achieved correlates well with the proper stiffness defined for pancreatic tissue. As the pancreas is a soft tissue, its stiffness ranges from 0.1 kPa to 10 kPa [42]. The pancreas seems to respond properly to this interval's lower stiffness, as cells can increase insulin mRNA expression and glucose sensitivity [43]. In other approaches, the stiffness of native healthy pancreas was set as approximately 1 kPa when measured by magnetic resonance elastography (MRE) [44,45], a value that fits with the scaffold stiffness achieved. Also, soft scaffolds favor cell coalescence and preserve the cluster-like organization, while in stiff substrates, the extracellular-cell interactions cause cell scattering and loss of islet-like structure [46].

Another feature that we wanted to improve is the diffusion of nutrients through the scaffold. Swelling is the water uptake capability of a hydrogel, an indirect measurement of pore interconnectivity [47]. The high pore diameter distribution and the high pore interconnectivity, typical from cryogels, enhances this swelling property [48]. Also, as better are these properties, faster diffusion among all the scaffold. After only 24 hours, our cryogel reached equilibrium, and with a swelling ratio of $98.14 \% \pm 0.32$ for CMC and $96.30 \% \pm 0.38$ for gelatin cryogel (Fig. 2e). Although this property is higher in CMC cryogels than in gelatin, as expected, both ratios are higher than 95%. This high percentage indicates that the scaffold's structure is highly interconnected, as water could colonize all the scaffold structure after drying.

Moreover, one of the strong points of this approach is the high diffusion of oxygen and nutrients through the scaffold. A fluorescein diffusion experiment was performed to test scaffold features. We could observe that the control sample, where the transwell was placed without cryogel, reaches

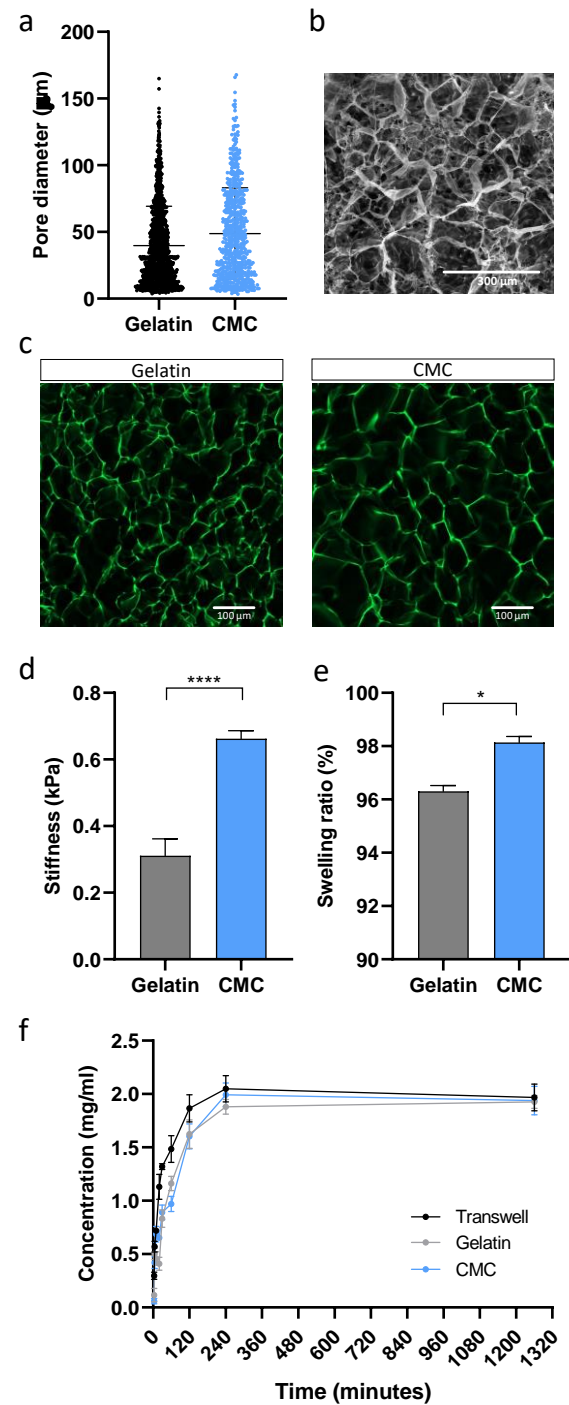


Figure 2: Mechanical characterization of the scaffold. a) Comparison of the pore distribution between gelatin and CMC cryogels with the same material concentration (1% (w/v)). b) Scanning electron microscope (SEM) images of the cryogel porosity. Scale bar = 300 μm. c) Aminofluorescein stained fibers of gelatin (left) and CMC (right) obtained with confocal microscopy. Scale bar = 100 μm. d) Stiffness results from different cryogels. e) Swelling ratio. f) Diffusion profile of fluorescein through the scaffold. Results are expressed as the mean \pm SEM. * $p < 0.05$, **** $p < 0.0001$.

equilibrium faster than the cryogels. However, these conditions reached equilibrium equally after 240 minutes (Fig. 2f). Calculating the scaffold's permeability, we obtained values of 5.72 mm/s in CMC cryogels and 0.61 mm/s in gelatin cryogels. This difference in diffusion indicates that CMC cryogels are more permeable than gelatin cryogels [48]. This rapid equilibrium reached shows that the cryogel has barely any interaction as a diffusion barrier. After 3 minutes, fluorescein can be found in the lower part of the transwell. This high permeability ensures us to generate a microporous cryogel able to sustain cells in all the scaffold's depths with no hypoxia or lack of nutrient problems.

We can conclude that our scaffold satisfies all the mechanical and physical needs of the β -cells. Overall, these results show a well-defined and reproducible method to afford non-degradable and microporous cell supportive scaffold.

3.3 CMC-based scaffold enhances INS1E pseudoislet formation

To generate a functional 3D structure able to support β -cells, we seeded INS1E cells onto the scaffolds. After cell seeding, INS1E morphology was evaluated in gelatin and CMC-based scaffolds at days 1, 4, and 7. Interestingly, at day 1, after seeding, instead of the typical monolayer architecture, cells cultured in 3D CMC cryogel scaffolds formed round-shaped clusters (Fig. 3b), morphologically resembling pancreatic islets (Fig. 3a). In contrast, a dispersed organization was observed in gelatin-based cryogels (Fig. 3b). The difference in cell organization observed in CMC and gelatin scaffolds can be explained by the presence or absence of the cell adhesion motifs in these structures. Gelatin is known to contain RGD (arginine-glycine-aspartic acid) motifs, cell adhesion sites found in several ECM proteins [49]. Hence, gelatin has a profound effect on the ability of cells to adhere to this material. On the other hand, CMC cryogels do not present cell-binding motifs, so it displays shallow adhesion properties for anchorage-dependent growth of INS1E cells, promoting cells to interact between them and to cluster together, forming islet-like structures.

Confocal image analysis of INS1E clusters revealed that at day 1, pseudoislets were about 60.6 μm in diameter, and they increased in size during the first 7 days, reaching an average diameter of 75.5 μm after 1 week of culture. At this point, we obtained a heterogeneous pseudoislet population in size, ranging from 16.8 μm to 216.7 μm (Fig. 3c). Primary rodent pancreatic islets present a considerable heterogeneity in size and shape, varying from small cell clusters to larger islets [50,51]. Several studies have revealed that islet heterogeneity influences the insulin secretory response of β -cells, so heterogeneity should be an essential consideration when understanding T2D pathogenesis, both at a single-cell and islet level [52–54]. On day 1, up to 12% of the clusters ranged from 0–25 μm , whereas on days 4 and 7, aggregations smaller than 25 μm represented less than 3% (Fig. 3d). Pseudoislets bigger than 200 μm were only observed on day

7. Of note, percentages of clusters higher than 25 μm diameter correlate with those of the scaffold porous sizes (Fig. 1d), indicating that cells keep proliferating until they reach the porous diameter.

Indeed, cells within the gelatin-based cryogel presented high proliferation rates at day 1 after seeding ($67.0\% \pm 3.9$), determined by immunostaining of Ki67, but this ratio decreased to $46.8\% \pm 2.9$ at day 4 and $10.8\% \pm 1.6$ at day 7 (Fig. 3e). This trend was also observed in cells cultured within the CMC-based scaffold, presenting $51.3\% \pm 1.6$ at day 1, $17.1\% \pm 1.5$ at day 4, and $8.0\% \pm 1.0$ at day 7 (Fig. 3f). In rodent islets, the proliferative capacity of β -cells is confined to the early stages of life, linked to an immature functional phenotype [55,56]. Thus, reduced proliferative capacity is one of the characteristics of mature β -cells, and maturation of β -cells defines their functional identity. Therefore, a strategy to obtain a heterogeneous population of islet cell clusters with low proliferation capacity offers excellent potential to engineer a model for the study of β -cell function and viability.

3.4 CMC-based scaffold maintains cell viability and promotes β -cell identity

Since 3D pseudoislets may have less access to nutrients, it was of interest to establish cells viability along one week of culture. Cell viability was assessed at culture days 1, 4, and 7 by a live/dead assay (Fig. 4a). We found that after 7 days of culture, encapsulated cells retained their viability compared to non-encapsulated cells, and both gelatin and CMC scaffolds presented a similar percentage of viability (Fig. 4a, b). Changes in viability or cell proliferation can be easily detected with the AlamarBlue test. Encapsulated cells at day 7 showed decreased metabolic activity (Fig. 4c). As no differences were observed in cell viability (Fig. 4a), this decreased metabolic activity correlates with a reduced proliferation ratio, confirming our previous results (Fig. 3). Overall, these results demonstrated that the highly porous cryogels were suited for engineering cell-supportive tissue scaffolds, facilitating the diffusion of oxygen and nutrients, and enabling cell viability for up to 7 days.

The ability of CMC scaffolds to efficiently aggregate single cells into engineered pseudoislets, with round-shaped structures similar to native islets, prompted us to examine the gene expression profile of these pseudoislets over time compared to gelatin-based monolayer INS1E cells and INS1E cells cultured without a 3D scaffold. We first focused on the genes encoding MafA, Pdx1, and NeuroD1, three β -cell specific transcription factors involved in β -cell functionality. Although many transcription factors (TF) have been involved in the maintenance of the β -cell identity, these specific transcriptional regulators have been demonstrated to play a crucial role in maintaining the function of the insulin-producing cells. Indeed, it has been demonstrated that this TF activates the insulin gene expression in a coordinated and synergistic manner in response to increased glucose levels. Furthermore, the fine-tune regulation of these TF ensures β -cell identity [57–59].

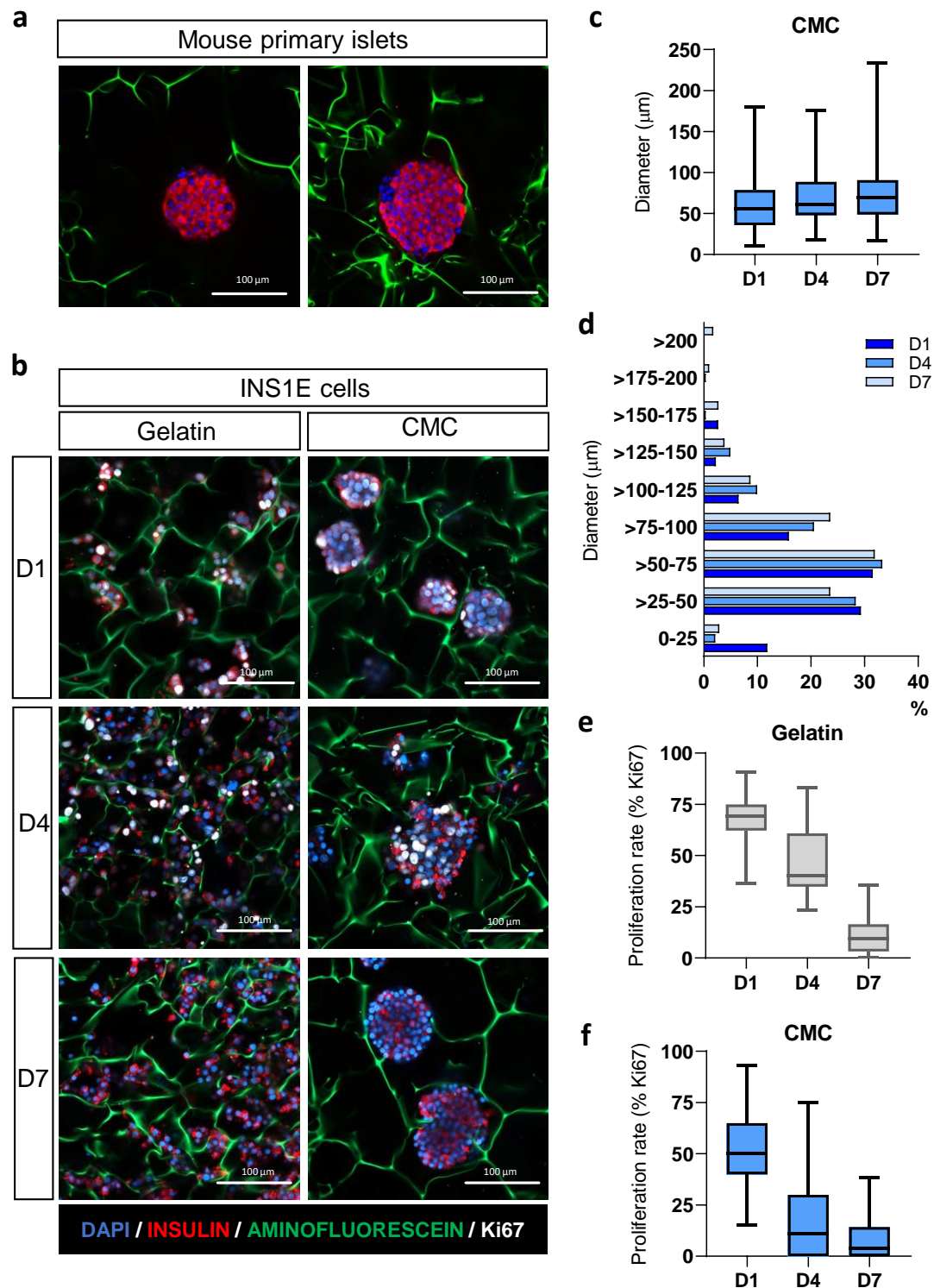


Figure 3: Pseudoislets generated in the scaffold have a high resemblance with primary pancreatic islets. a) Immunostaining of mouse primary pancreatic islets within a 1% CMC-scaffold stained for insulin (red), Ki67 (white) and nuclei (DAPI). Aminofluorescein was used to stain the fibers of the cryogel (green). Scale bar = 100 μ m. b) Representative images of INS1E cells inside the scaffold at days 1, 4, and 7 stained as in a. Note that INS1E cells within CMC scaffolds aggregate forming pseudoislets already 1 day after seeding. In contrast, cells within the gelatin are spread out. Scale bar = 100 μ m. c) Diameter of the pseudoislets on day 1, day 4, and day 7. d) Diameter distribution of the pseudoislets formed inside the CMC cryogel along the week. e-f) Proliferation rate (calculated as the percentage of Ki67-positive β -cells concerning the total number of β -cells) of INS1E cells inside the (e) gelatin cryogel and (f) CMC cryogel. Results are expressed as box plots indicating the first quartile, the median, the third quartile, and the minimum and maximum values.

Interestingly, cells supported within the cellulose-based scaffold presented a gradually increased expression level of the β -cell specific marker *Pdx1* concerning cells cultured in a well plate (Fig. 4d), even though results are not statistically significant. The results obtained are consistent with previous works demonstrating how reaggregating cells to form 3D spheroids significantly enhances the gene expression profile of β -cells [60]. Similarly, recapitulating endocrine cell clustering in culture has been demonstrated to foster the maturation of human stem-cell-derived β -cells [61].

This better-differentiated phenotype of β -cells when cultured within a 3D extracellular matrix, is consistent with the decreased proliferation markers, *Ki67* and *Pbk* (Fig. 4d), corroborating the balance between an increased β -cell identity and a reduced ability to proliferate of these cells [55].

3.5 Cell aggregation improves glucose-stimulated insulin secretion and can be used as a suitable cellular model for the study of the β -cell function

Several findings indicate that islet architecture has a pivotal role in determining β -cell functionality as cell-cell interactions are fundamental for the correct cellular function [62,63]. Indeed, it has been described that the secretory response of structurally coupled β -cells is higher than that of insulin-producing β -cells not arranged within the islet architecture [53,64]. INS1E cells traditionally seeded in a monolayer do not present reproducible responses to dynamic

glucose stimulations [6].

To determine whether pseudoislet formation within the cryogel correlates with increased β -cell function, we tested the dynamic response of pseudoislets to glucose. To check islet functionality, a glucose-stimulated insulin secretion (GSIS) assay, which defines the ability of β -cells to secrete the suitable amount of insulin in response to proportional extracellular glucose stimuli, was performed in all conditions. As shown in Fig. 5a, cell clustering improved the insulin secreted stimulation index under high glucose stimulation concerning the basal insulin secreted in low glucose conditions. This result demonstrates the benefit of cell aggregation in islet functionality. For primary islets of Langerhans, a threshold stimulation index of at least five defines a functional response, and often β -cell lines do not reach this threshold level or display a reproducible behavior. Indeed, at day 1, INS1E cells seeded in 48 well-plate presented a 2.51 ± 0.6 -fold increase of insulin secretion when cells were challenged with 16.7 mM compared to cells incubated with 2.8 mM glucose. Cells seeded in gelatin cryogels showed a 6.47 ± 1.8 -fold increase. Interestingly, we reached a fold increase of 7.52 ± 1.6 of insulin secretion when CMC-based pseudoislets were challenged with 16.7 mM glucose. This trend was repeated along the week, indicating that the stimulation index for insulin response to glucose is significantly higher in pseudoislets than dispersed and non-organized cells (Fig. 5b).

Like other tissues, β -cell functionality is greatly influenced by cell-cell and cell-matrix interactions,

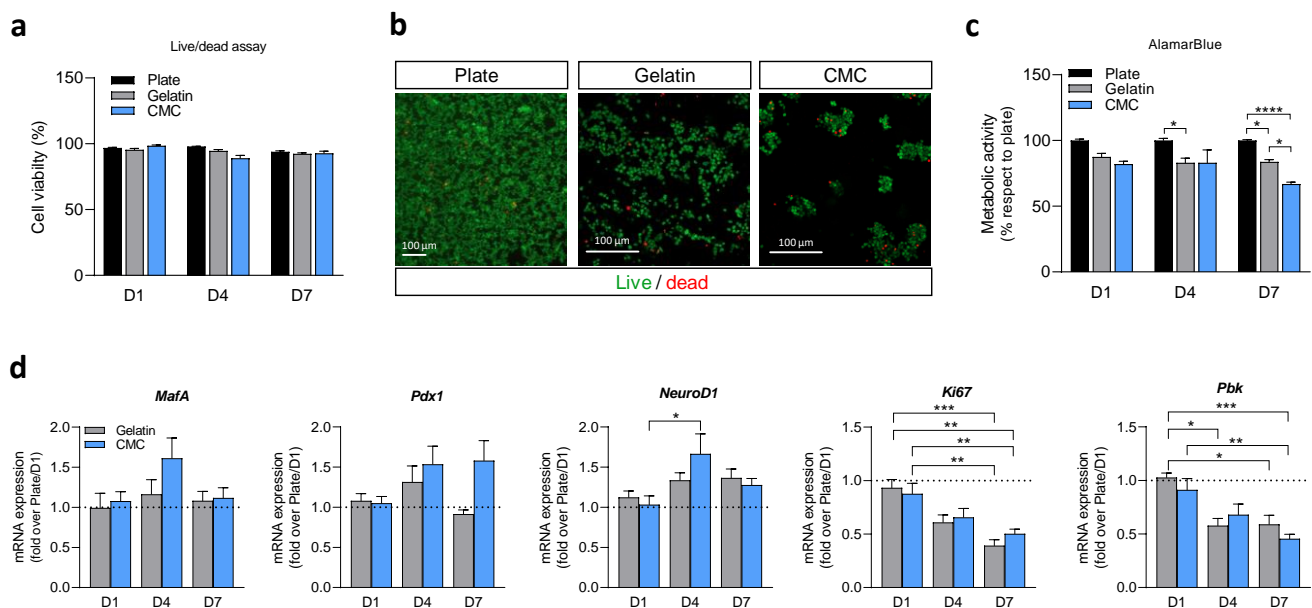


Figure 4: Cell viability and β -cell identity are preserved when pseudoislets are generated inside the scaffold. a) Analysis of Live/Dead INS1E cells at day 1, 4, and 7 seeded in a traditional plate and within the scaffolds. b) Representative fluorescent images were taken by confocal microscopy of cells seeded in a monolayer and gelatin and CMC-based scaffolds. Live cells are marked with Calcein AM in green, and dead cells are marked with EthD-1 in red. Note that cells within the CMC cryogel appear as clusters. Scale bar = 100 μ m. c) Alamar blue test of the cells in monolayer at the plate, monolayer on the gelatin cryogel and in the form of pseudoislets in the CMC cryogels, at days 1, 4, and 7. Data are shown relative to cells seeded in a plate. d) Gene expression analysis of the β -cell identity markers, *MafA*, *Pdx1*, and *NeuroD1*, and proliferation markers *Ki67* and *Pbk*. Gene expression was normalized against *Thp1*. Results are expressed as mean \pm SEM from three independent experiments. * $p < 0.05$, ** $p < 0.01$, *** $p < 0.001$, **** $p < 0.0001$.

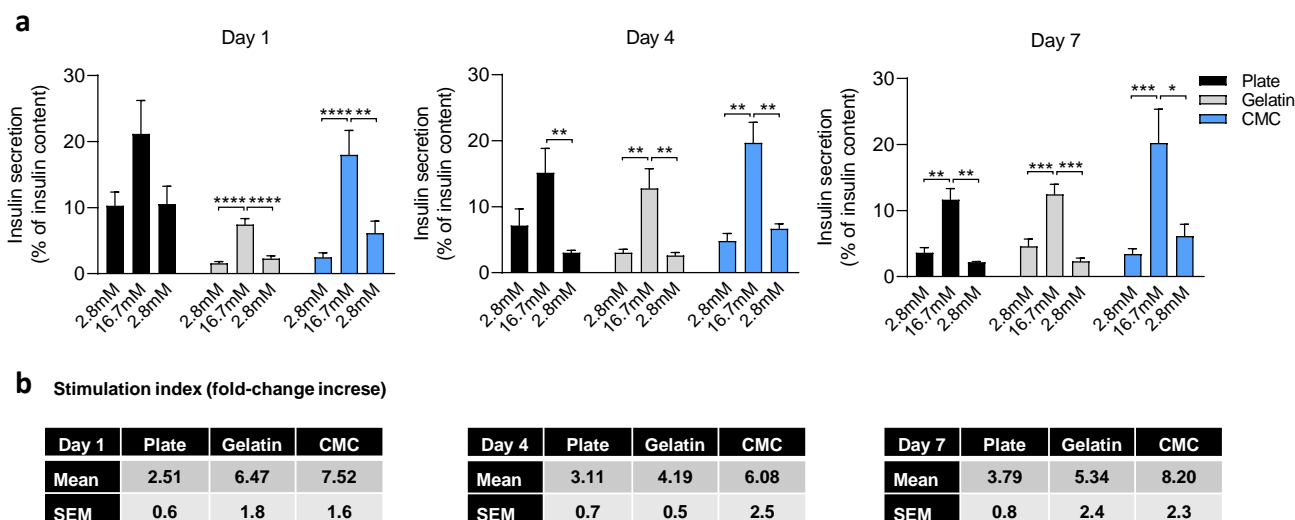


Figure 5: Pseudoislet formation enhances β -cell responsiveness to glucose. a) Glucose stimulation insulin secretion (GSIS) assay at day 1, 4, and 7 in plate monolayers, gelatin cryogels, and CMC cryogels. For the GSIS assays, cells were incubated for one hour at 2.8 mM glucose, followed by 16.7 mM glucose, and returning to basal condition (2.8 mM glucose). Results are expressed as the percentage of insulin secreted related to the corresponding sample \pm SEM's total insulin content from three independent experiments, each one including at least 3 different replicates per condition. * $p<0.05$, ** $p<0.01$, *** $p<0.001$, **** $p<0.0001$. b) Stimulation index, calculated as the fold-change increased between the insulin secreted at basal levels (first incubation with 2.8 mM glucose) and after challenging the cells with 16.7 mM glucose. Results are expressed as the mean \pm SEM.

controlling basal and stimulated insulin secretion [65,66]. Remarkably, GSIS defects in monolayer INS1E cell cultures arise from an increased insulin release under basal conditions (2.8 mM glucose) in addition to a decreased insulin secretory response under stimulatory glucose conditions. These results are consistent with other studies showing that aggregating β -cells enhances the secretory responsiveness to nutrients compared with cells configured as monolayers [69,70]. And it also suggests that β -cells interactions might be sufficient to sustain a normal glucose response.

Therefore, our study validates that a correct structural arrangement is essential for appropriate insulin response, demonstrating a robust glucose-stimulated insulin secretion by pseudoislets formed within a cryogel.

4. Conclusions

An increasing need to engineer advanced 3D scaffolds for tissue engineering has emerged to provide cellular structural support and mimic the complicated physical and biochemical properties of the native extracellular matrix. With this improvement, more resemblance tissues can be engineered for many applications as drug screening or disease modeling. Until now, many tissues have been generated in the laboratory. Particular attention must be paid when engineering islet-like structures as an adequate round-shaped islet architecture to maintain and improve β -cell functionality. Moreover, the formation of islet-like structures or pseudoislets, with the consequent β -cell communications, is required for an appropriate insulin secretory response [67,68].

This study reports a new CMC cryogel scaffold that favors pseudoislet generation and functionality. Here, we proved the cryogelation allows to generate a sponge-like scaffold with controllable structural properties. We demonstrated that we could create and modulate a wide range of porosity that fits with primary pancreatic 'islets' size and shape. Our scaffold's diffusion and permeability overcome some of the most problematic conditions, such as the lack of nutrient and oxygen diffusion through all the scaffold. Moreover, the mechanical properties of the cryogels match with the previously reported stiffness of the native pancreas ranges around 1 kPa.

All these properties of cryogels favor the viability of the β -cells and promote their β -cell identity. In their natural environment, β -cells interact with each other behavior is strongly influenced by cell-cell and cell-matrix interactions, allowing better control of basal and stimulated insulin secretion. However, clustering formation varies depending on the material. As proved, in gelatin cryogels, dispersed cell distribution was obtained. On the other hand, in CMC cryogels, pseudoislets were formed. Finally, we demonstrated that pseudoislets generated in CMC cryogels respond better to glucose stimulation.

In summary, in this study, we have generated a new approximation to engineer pancreatic tissue, combining the cryogelation technique with cell aggregation in microporous scaffolds. Because cell clustering improves β -cell identity and functionality, our results demonstrated the feasibility of using these microporous gel materials as 3D scaffolds culturing islet-like cell aggregates as an *in vitro* model to study T2D and other related diseases.

5. Authors contribution

F.V.-M. and J.R.-C. contributed to the study design, performance of experiments, data analysis, and writing and review of the manuscript. J.R.-A. contributed to the study design, data analysis, and report and review of the manuscript. J.R.-A. is the guarantor of this work. It had full access to all the data in the study and takes responsibility for the data integrity and data analysis accuracy.

6. Acknowledgements

The authors thank Dr. Rosa Gasa (IDIBAPS) for providing INS1E cells and Dr. Joan Marc Servitja for providing mouse pancreatic islets to perform immunostaining assays.

This project received financial support from the European Research Council program under grants ERC-StG-DAMOC (714317), the Spanish Ministry of Economy and Competitiveness, through the “Severo Ochoa” Program for Centres of Excellence in R&D (SEV-2016-2019) and “Retos de investigación: Proyectos I+D+i” (TEC2017-83716-C2-2-R), the CERCA Programme/Generalitat de Catalunya (2014-SGR-1460) and Fundación Bancaria “la Caixa”- Obra Social “la Caixa” (project IBEC-La Caixa Healthy Ageing).

7. References








- [1] N.H. Cho, J.E. Shaw, S. Karuranga, Y. Huang, J.D. da Rocha Fernandes, A.W. Ohlrogge, B. Malanda, IDF Diabetes Atlas: Global estimates of diabetes prevalence for 2017 and projections for 2045, *Diabetes Res. Clin. Pract.* 138 (2018) 271–281. <https://doi.org/10.1016/j.diabres.2018.02.023>.
- [2] M. Skelin, M. Rupnik, A. Cencic, Pancreatic beta cell lines and their applications in diabetes mellitus research., *ALTEX*. 27 (2010) 105–113. <https://doi.org/10.14573/altex.2010.2.105>.
- [3] M. Asfari, D. Janjic, P. Meda, G. Li, P.A. Halban, C.B. Wollheim, Establishment of 2-mercaptoethanol-dependent differentiated insulin-secreting cell lines., *Endocrinology*. 130 (1992) 167–178. <https://doi.org/10.1210/endo.130.1.1370150>.
- [4] P.M. Pour, J. Standop, S.K. Batra, Are islet cells the gatekeepers of the pancreas?, *Pancreatol.* 2 (2002) 440–448. <https://doi.org/10.1159/000064718>.
- [5] H. Guo-Parke, J.T. McCluskey, C. Kelly, M. Hamid, N.H. McClenaghan, P.R. Flatt, Configuration of electrofusion-derived human insulin-secreting cell line as pseudoislets enhances functionality and therapeutic utility, *J. Endocrinol.* 214 (2012) 257–265. <https://doi.org/10.1530/JOE-12-0188>.
- [6] A.C. Hauge-Evans, P.E. Squires, S.J. Persaud, P.M. Jones, Pancreatic β -cell-to- β -cell interactions are required for integrated responses to nutrient stimuli: Enhanced Ca^{2+} and insulin secretory responses of MIN6 pseudoislets, *Diabetes*. 48 (1999) 1402–1408. <https://doi.org/10.2337/diabetes.48.7.1402>.
- [7] J.C. Stendahl, D.B. Kaufman, S.I. Stupp, Extracellular matrix in pancreatic islets: Relevance to scaffold design and transplantation, *Cell Transplant.* 18 (2009) 1–12. <https://doi.org/10.3727/096368909788237195>.
- [8] J. Daoud, M. Petropavlovskaya, L. Rosenberg, M. Tabrizian, The effect of extracellular matrix components on the preservation of human islet function in vitro, *Biomaterials*. 31 (2010) 1676–1682. <https://doi.org/10.1016/j.biomaterials.2009.11.057>.
- [9] J.M. Fernández-Costa, X. Fernández-Garibay, F. Velasco-Mallorquí, J. Ramón-Azcón, Bioengineered in vitro skeletal muscles as new tools for muscular dystrophies preclinical studies, *J. Tissue Eng.* in press (2020) in press.
- [10] A. García-Lizarribar, X. Fernández-Garibay, F. Velasco-Mallorquí, A.G. Castaño, J. Samitier, J. Ramon-Azcon, Composite Biomaterials as Long-Lasting Scaffolds for 3D Bioprinting of Highly Aligned Muscle Tissue, *Macromol. Biosci.* 18 (2018) 1800167. <https://doi.org/10.1002/mabi.201800167>.
- [11] A.G. Castaño, M. García-Díaz, N. Torras, G. Altay, J. Comelles, E. Martínez, Dynamic photopolymerization produces complex microstructures on hydrogels in a moldless approach to generate a 3D intestinal tissue model, *Biofabrication*. 11 (2019). <https://doi.org/10.1088/1758-5090/ab0478>.
- [12] S. Ye, J.W.B. Boeter, L.C. Penning, B. Spee, K. Schneeberger, Hydrogels for liver tissue engineering, *Bioengineering*. 6 (2019). <https://doi.org/10.3390/bioengineering6030059>.
- [13] G. Marchioli, L. van Gurp, P.P. van Krieken, D. Stamatialis, M. Engelse, C.A. van Blitterswijk, M.B.J. Karperien, E. de Koning, J. Alblas, L. Moroni, A.A. van Apeldoorn, Fabrication of three-dimensional bioprinted hydrogel scaffolds for islets of Langerhans transplantation., *Biofabrication*. 7 (2015) 25009. <https://doi.org/10.1088/1758-5090/7/2/025009>.
- [14] S. Mantha, S. Pillai, P. Khayambashi, A. Upadhyay, Y. Zhang, O. Tao, H.M. Pham, S.D. Tran, Smart hydrogels in tissue engineering and regenerative medicine, *Materials (Basel)*. 12 (2019). <https://doi.org/10.3390/ma12203323>.
- [15] C.D. Spicer, Hydrogel scaffolds for tissue engineering: The importance of polymer choice, *Polym. Chem.* 11 (2020) 184–219. <https://doi.org/10.1039/c9py01021a>.
- [16] T.R. Hoare, D.S. Kohane, Hydrogels in drug delivery: Progress and challenges, *Polymer (Guildf)*. 49 (2008) 1993–2007. <https://doi.org/10.1016/j.polymer.2008.01.027>.
- [17] A.L. Farris, A.N. Rindone, W.L. Grayson, Oxygen delivering biomaterials for tissue engineering, *J. Mater. Chem. B*. 4 (2016) 3422–3432. <https://doi.org/10.1039/C5TB02635K>.
- [18] M. Gholipourmalekabadi, S. Zhao, B.S. Harrison, M. Mozafari, A.M. Seifalian, Oxygen-Generating Biomaterials: A New, Viable Paradigm for Tissue Engineering?, *Trends Biotechnol.* 34 (2016) 1010–1021. <https://doi.org/10.1016/j.tibtech.2016.05.012>.
- [19] Y. Evron, C.K. Colton, B. Ludwig, G.C. Weir, B. Zimmermann, S. Maimon, T. Neufeld, N. Shalev, T. Goldman, A. Leon, K. Yavriyants, N. Shabtay, T. Rozenshtein, D. Azarov, A.R. DiIenno, A. Steffen, P. de Vos, S.R. Bornstein, U. Barkai, A. Rotem, Long-term viability and function of transplanted islets macroencapsulated at high density are achieved by enhanced oxygen supply, *Sci. Rep.* 8 (2018) 1–13. <https://doi.org/10.1038/s41598-018-23862-w>.
- [20] K.K. Papas, H. De Leon, T.M. Suszynski, R.C. Johnson, Oxygenation strategies for encapsulated islet and beta cell transplants, *Adv. Drug Deliv. Rev.* 139 (2019) 139–156. <https://doi.org/10.1016/j.addr.2019.05.002>.
- [21] R. Cao, E. Avgoustiniatos, K. Papas, P. de Vos, J.R.T. Lakey, Mathematical predictions of oxygen availability in micro- and macro-encapsulated human and porcine pancreatic islets, *J. Biomed. Mater. Res. - Part B Appl. Biomater.* 108 (2020) 343–352. <https://doi.org/10.1002/jbm.b.34393>.
- [22] K.R. Hixon, T. Lu, S.A. Sell, A comprehensive review of cryogels and their roles in tissue engineering applications, *Acta Biomater.* 62 (2017) 29–41. <https://doi.org/10.1016/j.actbio.2017.08.033>.
- [23] F. Velasco-Mallorquí, J.M. Fernández-Costa, L. Neves, J. Ramón-Azcón, New volumetric CNT-doped gelatin–cellulose scaffolds for skeletal muscle tissue engineering, *Nanoscale Adv.* 2 (2020) 2885–2896. <https://doi.org/10.1039/D0NA00268B>.
- [24] D.J. Borg, P.B. Welzel, M. Grimmer, J. Friedrichs, M. Weigelt, C. Wilhelm, M. Prewitz, A. Stübel, A. Hommel, T. Kurth, U. Freudenberg, E. Bonifacio, C. Werner, Macroporous biohybrid cryogels for co-housing pancreatic islets with mesenchymal stromal cells, *Acta Biomater.* 44 (2016) 178–187. <https://doi.org/10.1016/j.actbio.2016.08.007>.
- [25] M. Oprea, S.I. Voicu, Recent advances in composites based on cellulose derivatives for biomedical applications, *Carbohydr. Polym.* 247 (2020) 116683. <https://doi.org/10.1016/j.carbpol.2020.116683>.
- [26] T. Miyamoto, S. Takahashi, H. Ito, H. Inagaki, Y. Noishiki, Tissue biocompatibility of cellulose and its derivatives., *J. Biomed. Mater. Res.* 23 (1989) 125–133.

- <https://doi.org/10.1002/jbm.820230110>.
- [27] A.I. Van Den Bulcke, B. Bogdanov, N. De Rooze, E.H. Schacht, M. Cornelissen, H. Berghmans, Structural and rheological properties of methacrylamide modified gelatin hydrogels, *Biomacromolecules*. 1 (2000) 31–38. <https://doi.org/10.1021/bm990017d>.
- [28] B. Gaihe, A.C. Jayasuriya, Fabrication and characterization of carboxymethyl cellulose novel microparticles for bone tissue engineering, *Mater. Sci. Eng. C*. 69 (2016) 733–743. <https://doi.org/10.1016/j.msec.2016.07.060>.
- [29] J. Rodríguez-Comas, J. Moreno-Vedia, M. Obach, C. Castano, S. de Pablo, G. Alcarraz-Vizan, D. Diaz-Catalan, A. Mestre, R. Horriño, M. Costa, A. Novials, J.-M. Servitja, Alpha1-antitrypsin ameliorates islet amyloid-induced glucose intolerance and beta-cell dysfunction., *Mol. Metab.* (2020) 100984. <https://doi.org/10.1016/j.molmet.2020.100984>.
- [30] B.N. Blackstone, A.F. Palmer, H.R. Rilo, H.M. Powell, Scaffold architecture controls insulinoma clustering, viability, and insulin production, *Tissue Eng. - Part A*. 20 (2014) 1784–1793. <https://doi.org/10.1089/ten.tea.2013.0107>.
- [31] B. Gao, C. Jing, K. Ng, B. Pingguan-Murphy, Q. Yang, Fabrication of three-dimensional islet models by the geometry-controlled hanging-drop method, *Acta Mech. Sin.* 35 (2019) 329–337. <https://doi.org/10.1007/s10409-019-00856-z>.
- [32] G. Marchioli, L. Van Gurp, P.P. Van Krieken, D. Stamatis, M. Engelse, C.A. Van Blitterswijk, M.B.J. Karperien, E. De Koning, J. Alblas, L. Moroni, A.A. Van Apeldoorn, Fabrication of three-dimensional bioplotter hydrogel scaffolds for islets of Langerhans transplantation, *Biofabrication*. 7 (2015). <https://doi.org/10.1088/1758-5090/7/2/025009>.
- [33] S. Duin, K. Schütz, T. Ahlfeld, S. Lehmann, A. Lode, B. Ludwig, M. Gelinsky, 3D Bioprinting of Functional Islets of Langerhans in an Alginate/Methylcellulose Hydrogel Blend, *Adv. Healthc. Mater.* 8 (2019) 1–14. <https://doi.org/10.1002/adhm.201801631>.
- [34] G. Kilimnik, J. Jo, V. Periwai, M.C. Zielinski, M. Hara, Quantification of islet size and architecture, *Islets*. 4 (2012) 167–172. <https://doi.org/10.4161/isl.19256>.
- [35] J. Jo, M. Hara, U. Ahlgren, R. Sorenson, V. Periwai, Mathematical models of pancreatic islet size distributions, *Islets*. 4 (2012) 10–19. <https://doi.org/10.4161/isl.18660>.
- [36] A. Bédier, T. Braschler, O. Peric, G.E. Fantner, S. Mosser, P.C. Fraering, S. Bencherif, D.J. Mooney, P. Renaud, A compressible scaffold for minimally invasive delivery of large intact neuronal networks, *Adv. Healthc. Mater.* 4 (2015) 301–312. <https://doi.org/10.1002/adhm.201400250>.
- [37] A.C. Hauge-Evans, P.E. Squires, V.D. Belin, H. Roderigo-Milne, R.D. Ramracheya, S.J. Persaud, P.M. Jones, Role of adenine nucleotides in insulin secretion from MIN6 pseudoislets, *Mol. Cell. Endocrinol.* 191 (2002) 167–176. [https://doi.org/10.1016/S0303-7207\(02\)00051-5](https://doi.org/10.1016/S0303-7207(02)00051-5).
- [38] J. Liu, S. Liu, Y. Chen, X. Zhao, Y. Lu, J. Cheng, Functionalized self-assembling peptide improves INS-1 β -cell function and proliferation via the integrin/FAK/ERK/cyclin pathway, *Int. J. Nanomedicine*. 10 (2015) 3519–3531. <https://doi.org/10.2147/IJN.S80502>.
- [39] S. Nemir, J.L. West, Synthetic materials in the study of cell response to substrate rigidity, *Ann. Biomed. Eng.* 38 (2010) 2–20. <https://doi.org/10.1007/s10439-009-9811-1>.
- [40] P. Fomby, A.J. Cherlin, A. Hadjizadeh, C.J. Doillon, V. Sueblinvong, D.J. Weiss, J.H.T. Bates, T. Gilbert, W.C. Liles, C. Lutzko, J. Rajagopal, D.J. Prockop, D. Chambers, A. Giangreco, A. Keating, D. Kotton, P.I. Lekes, D.E. Wagner, D.J. Prockop, Stem cells and cell therapies in lung biology and diseases: Conference report, *Ann. Am. Thorac. Soc.* 12 (2010) 181–204. <https://doi.org/10.1002/term>.
- [41] D.E. Discher, P. Janmey, Y.L. Wang, Tissue cells feel and respond to the stiffness of their substrate, *Science* (80-.). 310 (2005) 1139–1143. <https://doi.org/10.1126/science.1116995>.
- [42] G. Alessandra, M. Algerta, M. Paola, S. Carsten, L. Cristina, M. Paolo, M. Elisa, T. Gabriella, P. Carla, Shaping Pancreatic β -Cell Differentiation and Functioning: The Influence of Mechanotransduction, *Cells*. 9 (2020) 413. <https://doi.org/10.3390/cells9020413>.
- [43] C.E. Nyitray, M.G. Chavez, T.A. Desai, Compliant 3D microenvironment improves β -cell cluster insulin expression through mechanosensing and β -catenin signaling, *Tissue Eng. - Part A*. 20 (2014) 1888–1895. <https://doi.org/10.1089/ten.tea.2013.0692>.
- [44] F. Dittmann, H. Tzschätzsch, S. Hirsch, E. Barnhill, J. Braun, I. Sack, J. Guo, Tomoelastography of the abdomen: Tissue mechanical properties of the liver, spleen, kidney, and pancreas from single MR elastography scans at different hydration states, *Magn. Reson. Med.* 78 (2017) 976–983. <https://doi.org/10.1002/mrm.26484>.
- [45] Y. Shi, Y. Liu, F. Gao, Y. Liu, S. Tao, Y. Li, K.J. Glaser, R.L. Ehman, Q. Guo, Pancreatic Stiffness Quantified with MR Elastography: Relationship to Postoperative Pancreatic Fistula after Pancreaticoduodenal Anastomosis, *Radiology*. 288 (2018) 476–484. <https://doi.org/10.1148/radiol.2018170450>.
- [46] A. Galli, E. Maffioli, E. Sogne, S. Moretti, E.S. Di Cairano, A. Negri, S. Nonnis, G.D. Norata, F. Bonacina, F. Borghi, A. Podestà, F. Bertuzzi, P. Milani, C. Lenardi, G. Tedeschi, C. Perego, Cluster-assembled zirconia substrates promote long-term differentiation and functioning of human islets of Langerhans, *Sci. Rep.* 8 (2018) 1–17. <https://doi.org/10.1038/s41598-018-28019-3>.
- [47] S.A. Bencherif, R.W. Sands, D. Bhatta, P. Arany, C.S. Verbeke, D.A. Edwards, Injectable preformed scaffolds with shape-memory properties, *PNAS*. (2012). <https://doi.org/10.1073/pnas.1211516109>.
- [48] A. Memic, T. Colombani, L.J. Eggermont, M. Rezaeeyazdi, J. Steingold, Z.J. Rogers, K.J. Navare, H.S. Mohammed, S.A. Bencherif, Latest Advances in Cryogel Technology for Biomedical Applications, *Adv. Ther.* 2 (2019) 1800114. <https://doi.org/10.1002/adtp.201800114>.
- [49] H. Shin, S. Jo, A.G. Mikos, Biomimetic materials for tissue engineering, *Biomaterials*. 24 (2003) 4353–4364. [https://doi.org/10.1016/S0142-9612\(03\)00339-9](https://doi.org/10.1016/S0142-9612(03)00339-9).
- [50] O. Cabrera, D.M. Berman, N.S. Kenyon, C. Ricordi, P.-O. Berggren, A. Caicedo, The unique cytoarchitecture of human pancreatic islets has implications for islet cell function, *Proc. Natl. Acad. Sci.* 103 (2006) 2334–2339. <https://doi.org/10.1073/pnas.0510790103>.
- [51] F. Folli, S. La Rosa, G. Finzi, A.M. Davalli, A. Galli, E.J. Dick, C. Perego, R.G. Mendoza, Pancreatic islet of Langerhans' cytoarchitecture and ultrastructure in normal glucose tolerance and in type 2 diabetes mellitus, *Diabetes, Obes. Metab.* 20 (2018) 137–144. <https://doi.org/10.1111/dom.13380>.
- [52] R.K.P. Benninger, D.J. Hodson, New understanding of β -cell heterogeneity and in situ islet function, *Diabetes*. 67 (2018) 537–547. <https://doi.org/10.2337/dbi17-0040>.
- [53] S.S. Roscioni, A. Migliorini, M. Gegg, H. Lickert, Impact of islet architecture on β -cell heterogeneity, plasticity and function, *Nat. Rev. Endocrinol.* 12 (2016) 695–709. <https://doi.org/10.1038/nrendo.2016.147>.
- [54] A. Wojtuszczyk, M. Armanet, P. Morel, T. Berney, D. Bosco, Insulin secretion from human beta cells is heterogeneous and dependent on cell-to-cell contacts, *Diabetologia*. 51 (2008) 1843–1852. <https://doi.org/10.1007/s00125-008-1103-z>.
- [55] S. Puri, N. Roy, H.A. Russ, L. Leonhardt, E.K. French, R. Roy, H. Bengtsson, D.K. Scott, A.F. Stewart, M. Hebrok, Replication confers β cell immaturity, *Nat. Commun.* 9 (2018) 1–12. <https://doi.org/10.1038/s41467-018-02939-0>.
- [56] R.N. Kulkarni, E.B. Mizrahi, A.G. Ocana, A.F. Stewart, Human β -cell proliferation and intracellular signaling: Driving in the dark without a road map, *Diabetes*. 61 (2012) 2205–2213. <https://doi.org/10.2337/db12-0018>.
- [57] T. Matsuka, H. Kaneto, R. Stein, T. Miyatsuka, D. Kawamori, E. Henderson, I. Kojima, M. Matsuhisa, M. Hori, Y. Yamasaki, MafA regulates expression of genes important to islet β -cell function, *Mol. Endocrinol.* 21 (2007) 2764–2774. <https://doi.org/10.1210/me.2007-0028>.
- [58] S.S. Andrali, M.L. Sampley, N.L. Vanderford, S. Özcan, Glucose regulation of insulin gene expression in pancreatic β -cells, *Biochem. J.* 415 (2008) 1–10. <https://doi.org/10.1042/bj20081029>.

- [59] K. Fujimoto, K.S. Polonsky, Pdx1 and other factors that regulate pancreatic β -cell survival, *Diabetes, Obes. Metab.* 11 (2009) 30–37. <https://doi.org/10.1111/j.1463-1326.2009.01121.x>.
- [60] A.D. Green, S. Vasu, N.H. McClenaghan, P.R. Flatt, Pseudoislet formation enhances gene expression, insulin secretion and cytoprotective mechanisms of clonal human insulin-secreting 1.1B4 cells, *Eur. J. Physiol.* 467 (2015) 2219–2228. <https://doi.org/10.1007/s00424-014-1681-1>.
- [61] G.G. Nair, J.S. Liu, H.A. Russ, S. Tran, M.S. Saxton, R. Chen, C. Juang, M. Ian Li, V.Q. Nguyen, S. Giacometti, S. Puri, Y. Xing, Y. Wang, G.L. Szot, J. Oberholzer, A. Bhushan, M. Hebrok, Recapitulating endocrine cell clustering in culture promotes maturation of human stem-cell-derived β cells, *Nat. Cell Biol.* 21 (2019) 263–274. <https://doi.org/10.1038/s41556-018-0271-4>.
- [62] A. Chowdhury, O. Dyachok, A. Tengholm, S. Sandler, P. Bergsten, Functional differences between aggregated and dispersed insulin-producing cells, *Diabetologia.* 56 (2013) 1557–1568. <https://doi.org/10.1007/s00125-013-2903-3>.
- [63] D. Pipeleers, P. In't Veld, E. Maes, M. Van De Winkel, Glucose-induced insulin release depends on functional cooperation between islet cells, *Proc. Natl. Acad. Sci. U. S. A.* 79 (1982) 7322–7325. <https://doi.org/10.1073/pnas.79.23.7322>.
- [64] T. Schulze, M. Morsi, D. Brünig, K. Schumacher, I. Rustenbeck, Different responses of mouse islets and MIN6 pseudo-islets to metabolic stimulation: a note of caution, *Endocrine.* 51 (2016) 440–447. <https://doi.org/10.1007/s12020-015-0701-z>.
- [65] G. Parnaud, V. Lavallard, B. Bedat, D. Matthey-Doret, P. Morel, T. Berney, D. Bosco, Cadherin engagement improves insulin secretion of single human β -cells, *Diabetes.* 64 (2015) 887–896. <https://doi.org/10.2337/db14-0257>.
- [66] A. Charollais, A. Gjinovci, J. Huarte, J. Bauquis, A. Nadal, F. Martín, E. Andreu, J. V. Sánchez-Andrés, A. Calabrese, D. Bosco, B. Soria, C.B. Wollheim, P.L. Herrera, P. Meda, Junctional communication of pancreatic β cell contributes to the control of insulin secretion and glucose tolerance, *J. Clin. Invest.* 106 (2000) 235–243. <https://doi.org/10.1172/JCI9398>.
- [67] C. Kelly, N.H. McClenaghan, P.R. Flatt, Role of islet structure and cellular interactions in the control of insulin secretion, *Islets.* 3 (2011) 41–47. <https://doi.org/10.4161/isl.3.2.14805>.
- [68] M.J. Luther, A. Hauge-Evans, K.L.A. Souza, A. Jöms, S. Lenzen, S.J. Persaud, P.M. Jones, MIN6 β -cell- β -cell interactions influence insulin secretory responses to nutrients and non-nutrients, *Biochem. Biophys. Res. Commun.* 343 (2006) 99–104. <https://doi.org/10.1016/j.bbrc.2006.02.003>.

Article

In Situ LSPR Sensing of Secreted Insulin in Organ-on-Chip

María A. Ortega ^{1,†}, Júlia Rodríguez-Comas ^{1,†} , Ozlem Yavas ² , Ferran Velasco-Mallorquí ¹, Jordina Balaguer-Trias ¹, Victor Parra ¹ , Anna Novials ^{3,4} , Joan M. Servitja ^{3,4} , Romain Quidant ^{2,5,6}  and Javier Ramón-Azcón ^{1,6,*} 

- ¹ Biosensors for Bioengineering Group, Institute for Bioengineering of Catalonia (IBEC), The Barcelona Institute of Science and Technology (BIST), Baldiri I Reixac, 10-12, 08028 Barcelona, Spain; mortega@ibecbarcelona.eu (M.A.O.); jrodriguez@ibecbarcelona.eu (J.R.-C.); fvelasco@ibecbarcelona.eu (F.V.-M.); jbalaguer@ibecbarcelona.eu (J.B.-T.); victor.a.parramonreal@gmail.com (V.P.)
- ² Plasmon Nano-Optics Group, ICFO-Institute for Photonics Sciences, The Barcelona Institute of Science and Technology, 08860 Barcelona, Spain; oezlem.yavas@gmail.com (O.Y.); rquidant@ethz.ch (R.Q.)
- ³ Diabetes and Obesity Research Laboratory, Institut d'Investigacions Biomèdiques August Pi i Sunyer (IDIBAPS), 08036 Barcelona, Spain; anovials@clinic.cat (A.N.); servitja@clinic.cat (J.M.S.)
- ⁴ Centro de Investigación Biomédica en Red de Diabetes y Enfermedades Metabólicas (CIBERDEM), 28029 Madrid, Spain
- ⁵ Nanophotonic Systems Laboratory, Department of Mechanical and Process Engineering, ETH Zurich, 8092 Zurich, Switzerland
- ⁶ ICREA-Institució Catalana de Recerca i Estudis Avançats, 08010 Barcelona, Spain
- * Correspondence: jramon@ibecbarcelona.eu
- † These authors contributed equally to this work.



Citation: Ortega, M.A.; Rodríguez-Comas, J.; Yavas, O.; Velasco-Mallorquí, F.; Balaguer-Trias, J.; Parra, V.; Novials, A.; Servitja, J.M.; Quidant, R.; Ramón-Azcón, J. In Situ LSPR Sensing of Secreted Insulin in Organ-on-Chip. *Biosensors* **2021**, *11*, 138. <https://doi.org/10.3390/bios11050138>

Received: 19 March 2021

Accepted: 25 April 2021

Published: 28 April 2021

Publisher's Note: MDPI stays neutral with regard to jurisdictional claims in published maps and institutional affiliations.



Copyright: © 2021 by the authors. Licensee MDPI, Basel, Switzerland. This article is an open access article distributed under the terms and conditions of the Creative Commons Attribution (CC BY) license (<https://creativecommons.org/licenses/by/4.0/>).

Abstract: Organ-on-a-chip (OOC) devices offer new approaches for metabolic disease modeling and drug discovery by providing biologically relevant models of tissues and organs in vitro with a high degree of control over experimental variables for high-content screening applications. Yet, to fully exploit the potential of these platforms, there is a need to interface them with integrated non-labeled sensing modules, capable of monitoring, in situ, their biochemical response to external stimuli, such as stress or drugs. In order to meet this need, we aim here to develop an integrated technology based on coupling a localized surface plasmon resonance (LSPR) sensing module to an OOC device to monitor the insulin in situ secretion in pancreatic islets, a key physiological event that is usually perturbed in metabolic diseases such as type 2 diabetes (T2D). As a proof of concept, we developed a biomimetic islet-on-a-chip (IOC) device composed of mouse pancreatic islets hosted in a cellulose-based scaffold as a novel approach. The IOC was interfaced with a state-of-the-art on-chip LSPR sensing platform to monitor the in situ insulin secretion. The developed platform offers a powerful tool to enable the in situ response study of microtissues to external stimuli for applications such as a drug-screening platform for human models, bypassing animal testing.

Keywords: LSPR sensors; organ-on-a-chip; in situ insulin monitoring

1. Introduction

Type 2 diabetes (T2D) is one of the most common metabolic diseases, affecting millions of people worldwide [1]. Patients with T2D present a progressive decline in pancreatic β -cell function, mainly characterized by impaired insulin secretion. For this reason, the study of insulin secretion aimed at addressing islet functionality requires the ability to monitor insulin in situ over time, and measurements of insulin secretion dynamics are of significant clinical relevance. Traditionally, pancreatic β -cell function is assessed by measuring the insulin released by glucose-stimulated insulin secretion (GSIS) assays. These experiments involve manual liquid handling, static incubation of the islets, and enzyme-linked immunosorbent assays (ELISA) that require a long processing time.

Several approaches have emerged for engineering biomimetic, easy-to-use, and compatible organ-on-a-chip (OOC) microfluidic devices capable of reproducing physiological cell responses *in vitro*. Indeed, numerous micro-scale engineering OOC have been fabricated, modeling different tissues (e.g., muscle [2], blood vessels [3], liver [4], gut [5], or pancreatic islets [6]). Recent advances in miniaturizing microfluidic systems and advanced tissue fabrication procedures have enabled researchers to create multiple tissues-on-a-chip with a high degree of control over experimental variables for high-content screening applications [7–11].

Currently, there is a gap in the integration of these potential platforms to sensing modules, capable of monitoring *in situ* fast metabolic behaviors subjected to external stimuli, such as stress or drugs. Extensive efforts have been made to integrate three-dimensional (3D) tissue platforms with a sensing system for *in situ* continuous measurements of relevant targets [2,12–14]. However, the integration and application of sensing strategies are still far from providing a high throughput and reliable data to reveal the status and dynamics of the OOC.

Regarding pancreatic islets, there are only few examples where microfluidic systems have been integrated with free-labeled sensing platforms to study the dynamic of the insulin secretion profile. These works are focused on the monitoring of electrophysiology phenomena using complex microelectronic arrays with fluidic systems [15,16]. However, in those studies, neither do the biological models represent the islets in a 3D environment (biomimicking native pancreas configuration), nor can the electrochemical sensors efficiently monitor in a label-free way the secretion of insulin, as they only provide a recording of the cell activity. To fully exploit the potential of these platforms, there is a need to interface them with an integrated sensing module capable of directly monitoring the islet insulin response.

Among the different existing transduction methods, optical biosensors have the advantage of being highly sensitive, enabling label-free, cost-effective, and real-time sensing. As a well-studied optical sensing scheme, localized surface plasmon resonance (LSPR)-based sensors, which exploit the unique properties of noble metal nanostructures, have shown a great ability to detect all kinds of molecular biomarkers (proteins [17], peptides [18], mRNA [19], DNA [20,21], and miRNA [22]) in biological samples. The ease of optical transduction and the compact nature of LSPR sensors means their integration into fully automated microfluidic devices to perform multiplexed quantitative detection can be achieved [23].

In this work, we present an integrated on-chip insulin secretion study platform, combining novel islet-on-a-chip (IOC) technology interfaced with an on-chip LSPR biosensing platform (Figure 1). Unlike other IOC devices that are based on multiple tiny wells to trap the islets [24–27], which can promote shear stress-induced cell damage, we have developed an IOC that houses primary mouse pancreatic islets embedded in a non-biodegradable cellulose-based scaffold that intends to biomimic the native pancreas host. The integration of both platforms allows, for the first time, a highly sensitive and label-free monitoring of *in situ* insulin secretion by pancreatic islets subjected to different glucose concentrations, under physiological conditions, offering a powerful tool for future biomedicine and pharmaceutical research related to diabetes.

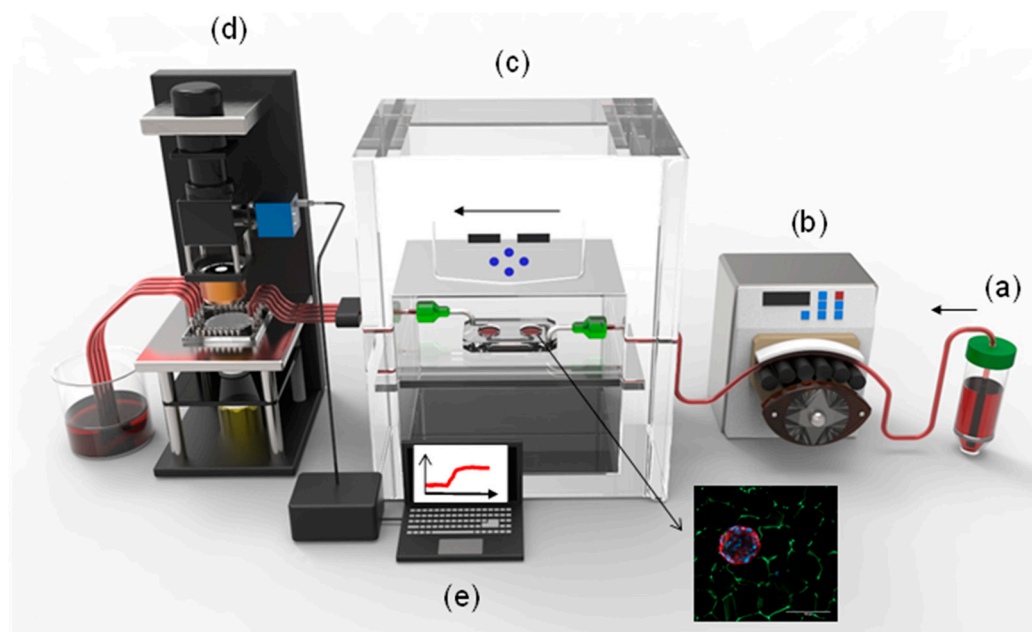


Figure 1. Schematic overview of the integration of the islet-on-a-chip (IOC) device with the on-chip LSPR sensing platform. (a) KRBH buffer with a chosen glucose content; (b) a peristaltic pump to drive the buffer into the IOC device; (c) IOC device containing mouse islets embedded in a cellulose-based scaffold; (d) the LSPR sensing platform to interrogate the buffer from the IOC device; and (e) monitoring of the insulin detection as a consequence of glucose stimulation.

2. Materials and Methods

2.1. Carboxymethyl Cellulose (CMC)-Cryogel Fabrication

Carboxymethyl cellulose (CMC, 419273, Merck Life, Darmstadt, Germany) is dissolved in MilliQ water (DI) to the desired concentration of 0.5% and crosslinking initiated by adding 50 mg mL^{−1} of adipic acid dihydrazide (AAD, ref A0638, Merck Life, Darmstadt, Germany), 1 µg µL^{−1} of N-(3-Dimethylaminopropyl)-N'-ethylcarbodiimide hydrochloride (EDC, E7750, Merck Life, Darmstadt, Germany), and MES buffer 0.5 M, pH 5.5. To stain the CMC cryogels, aminofluorescein (Merck Life, Darmstadt, Germany) was added to the prepolymeric solution in case the fibers need to be stained. The reaction mixture is rapidly dispensed inside a mold and placed overnight at −20 °C resulting in ice crystal nucleation. Finally, the cryogels are thawed and washed consecutively by submerging them in DI, 100 mM NaOH (Panreac, Darmstadt, Germany), 10 mM ethylenediaminetetraacetic acid (EDTA, 03690, Merck Life, Darmstadt, Germany), and 3 times in PBS. Once finished, the cryogels were autoclaved for further experiments.

2.2. Characterization of CMC Cryogels

The swelling ratio indicates, quantitatively, the water uptake capability of the scaffold. After the cryogel fabrication, scaffolds were dried at room temperature for 2 days and weighted. Subsequently, the cryogel was submerged into MilliQ water for 4 days until it reached equilibrium state and was weighted for a second time. For the swelling measurements, Equation (1) was used:

$$\text{Swelling ratio} = (W_{eq} - W_d) / W_d \times 100 \quad (1)$$

where W_{eq} represent the scaffold equilibrium weight and W_d is the scaffold dry weight. A total of 3 cryogels per condition were measured in this assay. On the other side, stiffness measurements were obtained from compression assays using a Zwick Z0.5 TN instrument (Zwick-Roell, Ull, Germany) with 5 N load cell. Compression assays were performed with samples at room temperature up to 30% final compression range at 0.1 mN of preloading

force and at 20%/min of strain rate. Finally, the Young's modulus was calculated from the slope of the curve in a range from 10% to 20% of compression.

Scanning electron microscopy (SEM) characterization was performed using a NOVA NanoSEM 230 at 10 kV. Different washing steps were performed using ethanol as a solvent, gradually incrementing its concentration from 50% to 99.5%. Samples were treated with critical point drying and carbon sputtering before the SEM acquisition.

2.3. Mouse Pancreatic Islet Isolation

Mouse pancreatic islets were isolated from 8- to 10-week-old C57BL/6J male mice by collagenase (Roche, Basel, Switzerland) digestion of the pancreas followed by Histopaque gradient (Sigma-Aldrich, St. Louis, MO, USA), as described previously [28]. Islets were cultured for 24 h at 37 °C and 5% CO₂ in RPMI 1640 medium (11.1 mM glucose) supplemented with 10% FBS (*v/v*), 2 mM glutamine, 100 units/mL penicillin, and 100 µg mL⁻¹ streptomycin before performing the experiments. Experimental procedures were approved by the Animal Ethics Committee of the University of Barcelona according to the Principles of Laboratory Animal Care.

2.4. Gene Expression Analysis

The miRNeasy kit (ref 74204, Qiagen, Hilden, Germany) was used to extract total RNA, and the high-capacity cDNA reverse transcription kit (ref 4368813, ThermoFisher Scientific, Carlsbad, CA, USA) was used to reverse transcribe it. Gene expression was examined by quantitative Polymerase Chain Reaction (PCR) using SYBR Green (ref 1178401K, Invitrogen, Carlsbad, CA, USA) in a 7900HT Fast Real-Time PCR System (ref 4329001, Applied Biosystems, Foster City, CA, USA). The primer sequences used are listed in Table 1. The expression levels of genes of interest were normalized to the expression of *Tbp1*.

Table 1. Primer sequences used for gene expression analysis for qPCR.

Gene	Species	Fw	Rv
<i>MafA</i>	Mouse	CAAGGAGGAGGTCATCCGAC	TCTCCAGAATGTGCCGCTG
<i>Pdx1</i>	Mouse	CCCCAGTTTACAAGCTCGCT	CTCGGTTCCATTCTGGGAAAGG
<i>NeuroD1</i>	Mouse	GGATCAATCTTCTCTTCCGGTG	TGCGAATGGCTATCGAAAGAC
<i>Ddit3/Chop</i>	Mouse	TCATCCCCAGGAAACGAAGAG	GCTTTGGGATGTGCGTGTG
<i>Trib3</i>	Mouse	CGTGGCACACTGCCACAAG	TCCAGGTTCTCCAGCACCAG
<i>Atf3</i>	Mouse	GTCCGGGCTCAGAATGGAC	CGTGCCACCTCTGCTTAGCT
<i>Tbp1</i>	Mouse	ACCCTTCACCAATGACTCCTATG	ATGATGACTGCAAATCGC

2.5. Glucose-Stimulated Insulin Secretion (GSIS)

Islets housed within CMC cryogels were transferred into the microfluidic chip and were allowed to settle to the bottom of the chamber for 24 h. Subsequently, they were preincubated with Krebs–Ringer bicarbonate HEPES (KRBH) buffer solution (115 mM NaCl, 24 mM NaHCO₃, 5 mM KCl, 1 mM MgCl₂·6H₂O, 1 mM CaCl₂·2H₂O, and 20 mM HEPES, pH 7.4) containing 11.1 mM glucose for 30 min at 37 °C (basal condition). The cryogels were then incubated at 2.8 mM glucose, followed by perfusion with KRBH solution with 16.7 mM glucose. First, supernatants were collected, and the cellular insulin contents were recovered in an acid-ethanol solution. Insulin concentration was determined by Insulin Mouse ELISA. For in situ and label-free detection of insulin levels, we integrated the microfluidic chip with the on-chip LSPR platform.

2.6. Immunofluorescence

Cryogels stained with aminofluorescein (green) were fixed with 10% formalin solution (Merck Life, Darmstadt, Germany) for 30 min and were then permeabilized with 0.5% Triton X-100 (Merck Life, Dorset, UK) and blocked by adding 3% donkey serum (Merck Life, Darmstadt, Germany). The cryogels were incubated overnight at 4 °C with the primary antibody anti-insulin (mouse anti-insulin (+proinsulin) monoclonal antibody 1:500; ref BM508,

OriGene EU, Herford, Germany) to stain the insulin from the pancreatic β -cells. Subsequently, secondary antibody was added for 2 h at room temperature (ref A32, AlexaFluor 555 conjugate anti-mouse 1:250; Life Technologies, Carlsbad, CA, USA). 4',6-diamidino-2-phenylindole (DAPI) (1:1000; ThermoFisher Scientific, Carlsbad, CA, USA) was used to counterstain the nuclei. Fluorescent images were obtained using confocal microscopy (LSM 800 microscope model, Zeiss, Oberkochen, Germany).

2.7. Immunoreagents and ELISA Immunoassay Protocol

The 96-well plate (Polystyrene Maxisorp 96 well microplates, Nunc, Roskilde, Denmark) was coated with 50 μ L per well of the capture antibody (also used as the capture antibody in the LSPR measurements) mouse anti-insulin monoclonal antibody (ref NB100-73008, clone 3A6, Novus biologicals, Littleton, CO, USA) at 4 μ g mL⁻¹ prepared in a coating buffer (0.05 M of Na₂CO₃/NaHCO₃, pH 9.6). The plate was washed and 8 solutions of recombinant human insulin (ref 91077C, Merck Life, Darmstadt, Germany) from 580 to 0 ng mL⁻¹ prepared in PBST (PBS = 0.01 M phosphate buffer, 0.14 M NaCl, and 0.003 M KCl, with 0.05% (*v/v*) Tween 20 at pH 7.5) was added as an internal calibration curve together with the samples to interrogate (50 μ L/well). The plate was incubated at room temperature for 1 h. A second wash step was performed, and detection antibody (Biotinylated Insulin Antibody (ref NB100-64697B, clone D3E7 (5B6/6), Novus Biologicals, Littleton, CO, USA) prepared in PBST at 0.031 μ g mL⁻¹ was added (50 μ L per well) and incubated at RT for 30 min. Finally, 50 μ L/well of streptavidin-horseradish peroxidase (SAv-HRP) solution at 0.25 μ g mL⁻¹ prepared in PBST was added and incubated for 30 min at RT. Following that step, 50 μ L/well of the substrate solution was added and incubated for 3–5 min, protected from light. Finally, 50 μ L/well of H₂SO₄ 4 N was added to stop the enzymatic reaction. The absorbances were read at 450 nm. Calibration curves were fitted using a sigmoidal fit function.

2.8. Fabrication of IOC Microfluidic Platform

The microfluidic chip was firstly designed using CleWin software and fabricated using a standard soft lithography replica molding technique. Briefly, a silicon wafer mold was created through a one-layer process using negative photoresist SU8-2100 (MicroChem, Westborough, MA, USA). The microfluidic chip design was printed on a high-quality acetate film to be used as a mask, and finally a microfeatured master mold was then obtained by contact photolithography. To obtain a polydimethylsiloxane (PDMS) fluidic chip, a mixture of prepolymer with curing agent (Sylgard 184, Dow corning, Midland, TX, USA) was prepared at a 10:1 ratio, degassed in a vacuum chamber for 1 h, and poured on the SU8 master mold. The polymer mix quantity was calculated to obtain a 3 mm layer (Layer 2, see Figure 4(ai)). After 4 h at 80 °C in an oven, the PDMS replica was cured and carefully peeled off from the mold. Holes were punched both for the entry and exit of liquids. In parallel, a 2 mm layer of PDMS (Layer 1, see Figure 4(aii)) was prepared (using a non-patterned silicon mold), cured, and cut out. The two layers were finally bonded irreversibly by oxygen plasma activation (Expanded Plasma Cleaner, PCD-002-CE Model, Harrick Scientific Corporation, Ossining, NY, USA), and chambers for the CMC-islet scaffolds were punched. The final microfluidic chip was bound to a standard cover slide, allowing handling and visualization under the microscope if needed (Figure 4(aiii)). Finally, a customized glass cover (37 mm \times 20 mm) was activated using oxygen plasma and bound to the PDMS chip irreversibly in order to seal the chip (Figure 4(aiv)).

2.9. Statistics

Statistical analysis was performed using Graph Prism software (GraphPad Software, San Diego, CA, USA). Data are expressed as the mean \pm SEM, and statistical significance was determined by two-tailed Student's *t*-test. Results were considered significant at *p* < 0.05.

3. Results and Discussions

3.1. Fabrication of a 3D Effective Cellulose Matrix to House Pancreatic Islets

We developed a functional islet-on-a-chip (IOC) microfluidic device to monitor insulin secretion under flow conditions. It is known that platforms of islet perfusion mimic in vivo physiology better than static culture systems, therefore improving the islet health [29]. Islets of Langerhans are clusters of cells within the pancreas that are responsible for the production and secretion of different hormones that regulate circulating glucose levels. β -cells are the predominant cell type within the pancreatic islets in mammals and the unique source of circulating insulin, being fundamental for the maintenance of glucose homeostasis [30–32]. Unlike the other IOC devices that are based on multiple tiny wells to trap the islets [24–27,33–36], we have precisely engineered a heterogeneous porous cryogel scaffold which offers a robust approach for spatially organizing the islets, and which can limit shear-induced cell damage. It was recently demonstrated that 3D polymeric-based scaffolds offer mechanical and chemical properties that make them valuable in tissue engineering applications [37].

The most extensively utilized technique to achieve in vitro tissue engineering is to use the encapsulated hydrogels which present a high-water content and highly resembling in vivo physical properties [38–42]. However, conventional hydrogels present several limitations due to the small pore size. They present an inadequate diffusion of oxygen and nutrients/waste products, as well as limited cellular mobility and cell spreading. To address these challenges, we used the cryogelation technique, a procedure that allows the formation of cryogels at sub-zero temperatures. Typically, the liquid prepolymer solution is cooled at $-20\text{ }^{\circ}\text{C}$. At this temperature, a large percentage of the material crystallizes due to its water content. When thawed, the ice crystals leave behind empty spaces, allowing us to obtain different pore diameters, as shown in Figure 2a. Following this principle, we can generate a 3D extracellular matrix mimicking scaffolds with a specific range of porosity (Figure 2b,c), in which the islets can be seeded, allowing the transfer of oxygen, nutrient and waste removal, and avoiding possible apoptosis or cell death. The scaffold properties can be modulated simply by altering the concentrations of the polymer and varying the freezing temperature [43]. As the cryogel technique allows us to achieve a micro-range porosity with a wide distribution range, and mouse pancreatic islets are diverse in size ($\sim 50\text{--}150\text{ }\mu\text{m}$ in diameter) with an average size of $100\text{ }\mu\text{m}$, we determined 0.5% of CMC cryogel as a potential suitable niche for the islets (Figure 2b,c). The designed carboxymethyl cellulose (CMC) cryogel presents several advantages—besides its high porosity, it also offers the mechanical strength required for housing pancreatic islets, with a stiffness of $0.67 \pm 0.1\text{ KPa}$ and a swelling ratio of $98.1\% \pm 0.3\%$ [44] (Figure 2d), as well as being elastic. It is a non-degradable material from mammalian cells and it also allows surgical sterility by means of autoclaving [45]. Indeed, we have recently demonstrated that CMC scaffolds can be used to generate functional pseudoislets from insulin-producing INS1E-cells, representing a suitable technique to generate β -cell clusters and to study pancreatic islets in vitro [46].

Pancreatic islets were obtained from C57BL6 wild-type mice as described elsewhere [47]. A total of 30 islets were seeded in a 0.5% CMC cryogel as shown in Figure 3a and were allowed to recover overnight prior to performing the microfluidic experiments. Figure 3b shows the bright field image of the pancreatic islets housed in a CMC scaffold and immunofluorescent confocal images of the islets integrated within the cellulose fibers. The gene expression analysis of the three β -cell-specific transcriptional regulators and positive indicators of β -cell health and functionality, *Pdx1* (pancreas/duodenum homeobox protein 1), *MafA* (V-maf musculoaponeurotic fibrosarcoma oncogene homolog A), and *NeuroD1* (Neuronal Differentiation 1), revealed no significant differences when comparing the islets housed within CMC-based scaffolds and isolated pancreatic islets in suspension (Figure 3c). Additionally, the stress markers *Chop* (C/EBP homologous protein), *Trib3* (Tribbles pseudokinase 3), and *Atf3* (activating transcription factor 3) did not present significant differences either (Figure 3c), indicating that our cellulose-based cryogel provides a physio-

logically relevant environment and facilitates the diffusion of oxygen and nutrients, as well as demonstrating that islets do not suffer stress when integrated inside the CMC scaffold.

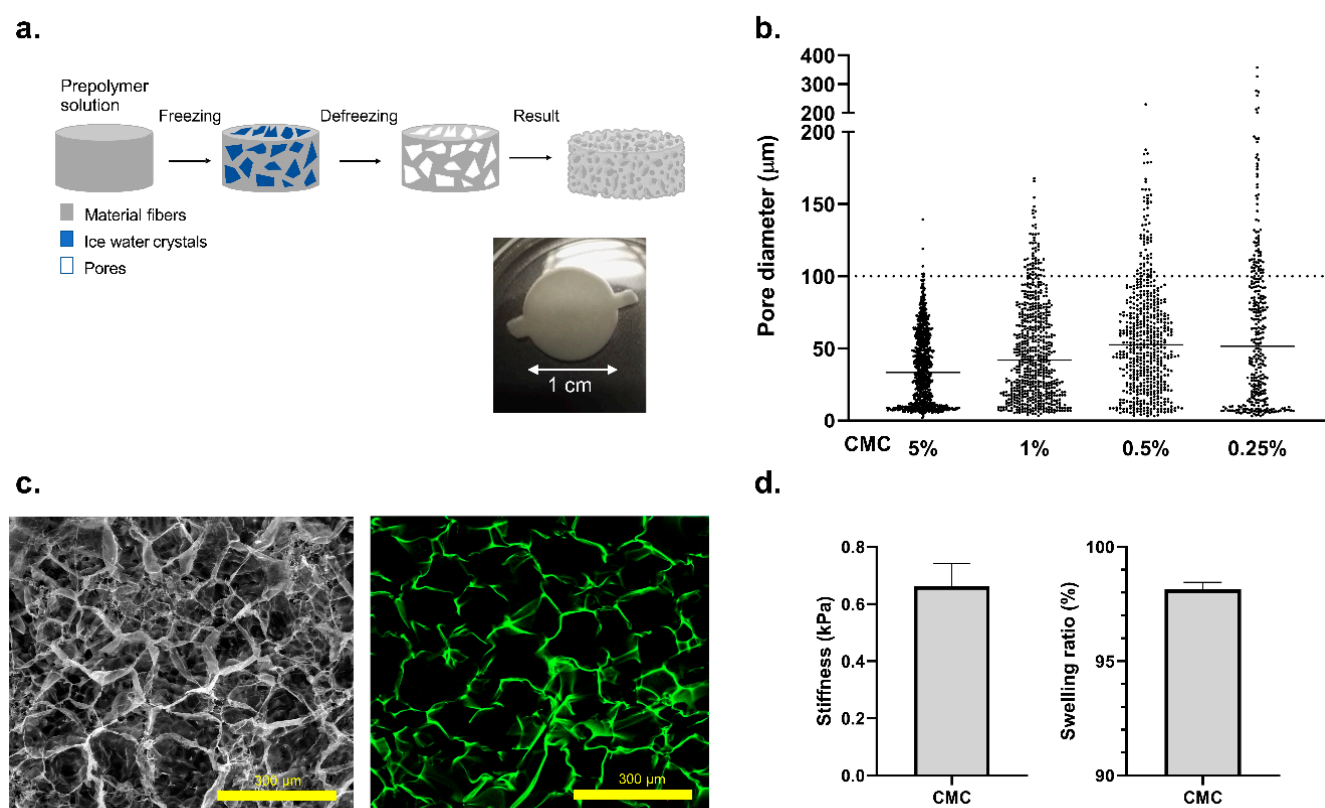


Figure 2. Cellulose-based cryogel fabrication and characterization. (a) General overview of the CMC cryogel fabrication protocol. Real images of CMC cryogel 0.5% (*w/v*) before islet seeding. Dimensions are 0.5 cm in height and 1 cm in diameter. (b) Pore diameter distribution of the cryogel at different CMC concentrations: 5%, 1%, 0.5%, and 0.25% (*w/v*), respectively. A total of 3 replicates and 20 images from 5 different depths were analyzed. (c) SEM image of the 0.5% (*w/v*) CMC cryogel condition after critical point drying. A confocal image of the same sample stained using 1 mM aminofluorescein (green) is on the right. (d) Characterization of the mechanical properties of the 0.5% (*w/v*) CMC cryogel. Young's modulus of 0.67 ± 0.1 kPa was obtained by compression assays with 5 N load cell. Data corresponds with 3 compressions per cryogel and $n = 3$. The swelling ratio was determined obtaining values of $98.1\% \pm 0.3\%$ for replicates $n = 3$ and 3 measures per cryogel. Values are expressed as mean \pm SD; $p < 0.05$.

3.2. Islet-on-a-Chip Microfluidic Platform

A microfluidic device was designed and fabricated to host the *in vitro* model integrated by the CMC cryogel and mouse pancreatic islets. The dimensions of the device are shown in Figure 4a. Two circular chambers with a diameter of 10 mm were designed, where the CMC islets 3D *in vitro* model is located. Microfluidic channels of 1 mm width and 0.20 mm height were designed to connect those chambers and enable the circulation of the liquids inside the device (Figure S1a).

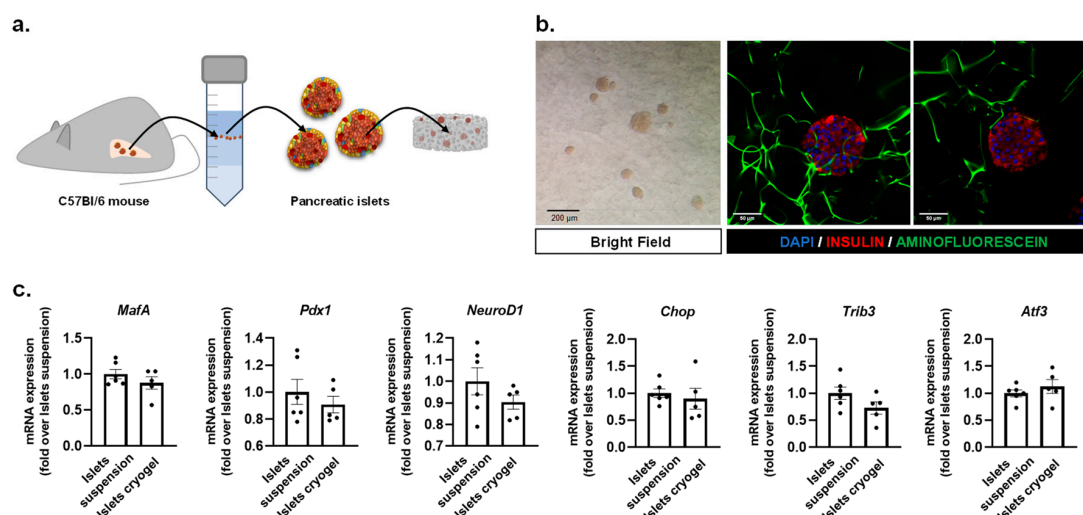


Figure 3. Development and characterization of the CMC islet construct. Gene expression analysis and immunostaining assays of islets were performed 24 h after being seeded within the cryogel. (a) Schematic diagram of mouse islet isolation. Islets inside the cryogel are also represented. (b) Left: pancreatic islets embedded within a carboxymethyl cellulose (CMC) cryogel under bright field (scale bar: 200 μm); middle and right: images of islets stained with insulin (red) and DAPI (blue). Cellulose fibers are stained with fluorescein (green). Images show islets at different depths through the cryogel (along the z-axis) (scale bar: 50 μm). (c) Gene expression analysis of *MafA*, *Pdx1*, *NeuroD1*, *Chop*, *Trib3*, and *Atf3* from islets in suspension and islets housed within the cryogel. Gene expression data were normalized against *Tbp1* and are shown relative to islets in suspension. Results are expressed as the mean \pm SEM from three independent experiments. A *t*-test was applied to compare the data set, evidencing no statistical differences between islets in suspension and islets in the cryogel.

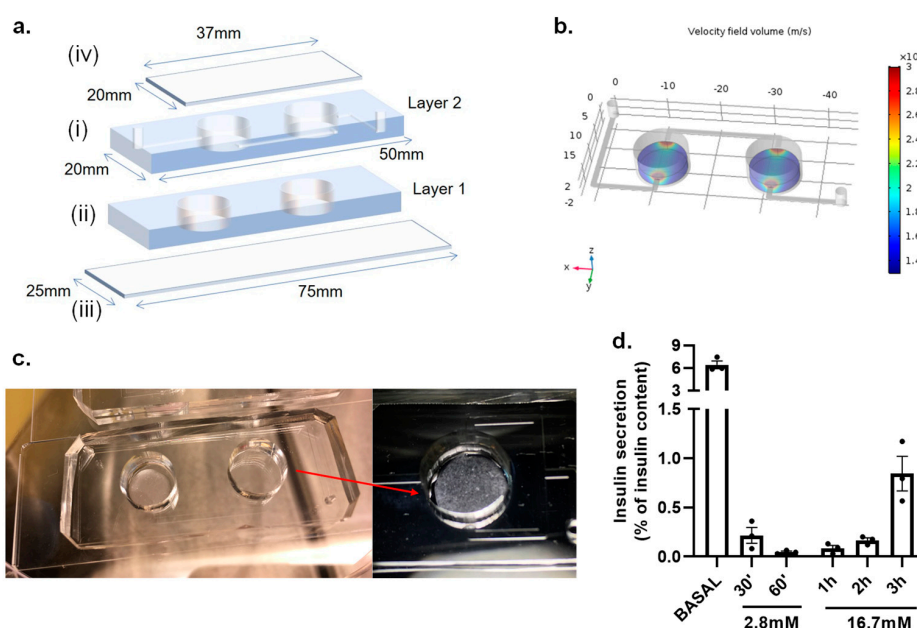


Figure 4. Design and fabrication of the IOC device. (a) Schematic image showing the assembling of the IOC: (i) a 3 mm layer of PDMS containing channels, inlet and outlet (Layer 2); (ii) a 2 mm layer of PDMS with the chambers for CMC islets (Layer 1); (iii) two-layers of microfluidic chip is bound on a (25 mm \times 75 mm) standard cover slide; and, finally, (iv) a customized (37 mm \times 20 mm) cover slide is used to sealed tissue chambers. (b) COMSOL Multiphysics[®] simulation of the flow velocity and dynamics through the IOC device showing a maximum velocity of 0.03 mm s^{−1} (red zones) at the boundaries of the scaffold. (c) Real picture of the IOC device with a close-up view of the CMC islets fabricated inside the chamber. (d) A glucose-stimulated insulin secretion (GSIS) assay was performed in static conditions to evaluate the secretory capacity of pancreatic islets housed within the CMC-based cryogel inside the device. Results are expressed as mean \pm SEM from three independent experiments.

The microfluidic IOC device was fabricated using a standard soft lithography replica molding technique as previously described in the methods section. The IOC microfluidic chip is integrated by two layers of PDMS with the purpose of elevating the microfluidic channels and creating a pool where the scaffold with the islets can be located, decreasing possible shear stress produced by a direct flow (Figure 4(ai,aii)). The device provides biomimicking of the physiological environment of the organ, supplying nutrient and oxygen exchange to the 3D in vitro construct. The flow profile inside the microfluidic device was simulated by COMSOL Multiphysics Software. The fluid velocity field for each intersection was solved using the laminar flow physics module with a customized mesh (3327 tetrahedral elements). The boundary conditions of the inlets were defined by the channel geometry, resistance of $4.8 \times 10^{10} \text{ Pa s m}^{-3}$, operational flow rate of $50 \mu\text{L min}^{-1}$, and an inlet pressure of 39.84 Pa. The remaining boundaries were specified as walls (no-slip boundary condition) and the material filling the channels was chosen as water under an incompressible flow. A stationary solver was used for the calculations. In order to create a realistic approximation, a solid cylinder with the dimensions and mechanical and chemical properties of the CMC scaffold was incorporated in the simulations. Supplementary Videos V1 and V2 show the velocity profile inside the whole device. The red zones indicate a higher flow velocity ($7 \times 10^{-4} \text{ m s}^{-1}$ at the well mouth and $3.69 \times 10^{-2} \text{ m s}^{-1}$, as a maximum velocity, in the center of the chamber) appearing in the boundaries of the scaffold. The study shows that the flow rates and geometry used during the experiments do not affect the stability of the 3D construct and, additionally, do not exert shear stress to the cell system as a consequence of flow, showing a maximum velocity of 0.03 mm s^{-1} (red zones in Figure 4b). Figure 4c shows a real picture of the microfluidic device with the CMC islets fabricated inside the chamber. The fluidic system also helps the delivery of the secreted insulin from the IOC to the on-chip LSPR sensing platform.

We examined the functionality of the islets housed within the CMC cryogel before running microfluidic measurements by performing a glucose-stimulated insulin secretion (GSIS) assay without flow inside the IOC device. Initially, the islets were incubated with 2.8 mM glucose, a condition that dampens the secretory capacity of the β -cells, followed by incubation with 16.7 mM glucose. Our results show that the islets remain as functional units in the cryogel scaffolds, validated by the release of insulin from the pancreatic β -cells in response to glucose and quantified by a conventional ELISA (enzyme-linked immunosorbent assay). Figure 4d shows how a high glucose concentration (16.7 mM) causes a time-dependent insulin secretion from the β -cells, normalized by the total insulin content of the islets. The basal condition represents the accumulated insulin released by the islets 30 min after an overnight culture in media containing 11.1 mM glucose. Having demonstrated that islets housed within the cryogel respond to glucose, we set up the integration of the LSPR system into the microfluidic system in order to detect the insulin levels in situ.

3.3. On-Chip LSPR Measurements

The on-chip LSPR platform was incorporated to quantify the insulin levels from the IOC device. The platform is a state-of-the-art integrated opto-fluidic module that had been previously used for the detection of several protein biomarkers [17,23]. It enables parallel and controlled measurements on a single chip ($2.5 \times 2.5 \text{ cm}^2$), reducing the reagent volumes, and providing in situ and label-free detection of insulin concentrations in the samples. The LSPR sensing regions consist of arrays of gold nanorods, fabricated by electron beam lithography on a glass substrate, using the optimized parameters of references [17,23,48]. The LSPR peak was set to be around 800 nm as measured by a custom-built transmission microscopy set-up integrated with a spectrometer. The optical set-up uses a galvanometric mirror to interrogate up to 32 different sensing regions in parallel. Our data analysis software delivers both peak and centroid positions of the sensed regions in situ [23]. To complete the assembly of the LSPR sensing platform, the gold sensors on glass were integrated into a microfluidic environment (Figure 5a). The latter, built by multilayer soft lithography [49], consists of two layers of PDMS networks,

namely, flow and control layers. The flow network, hosting the LSPR sensors, is where the insulin detection measurements are performed. In the upper layer, the control network includes pneumatic “Quake valves” that are used to control the reagent flow through the underneath channels. Each valve is individually managed by an external controller that enables full automation of the successive steps of the detection bioassay. The microfluidic architecture includes parallel channels that are individually addressable to perform, on the same chip, eight parallel measurements with up to four replicas, which can be easily used for multiplexed experiments.

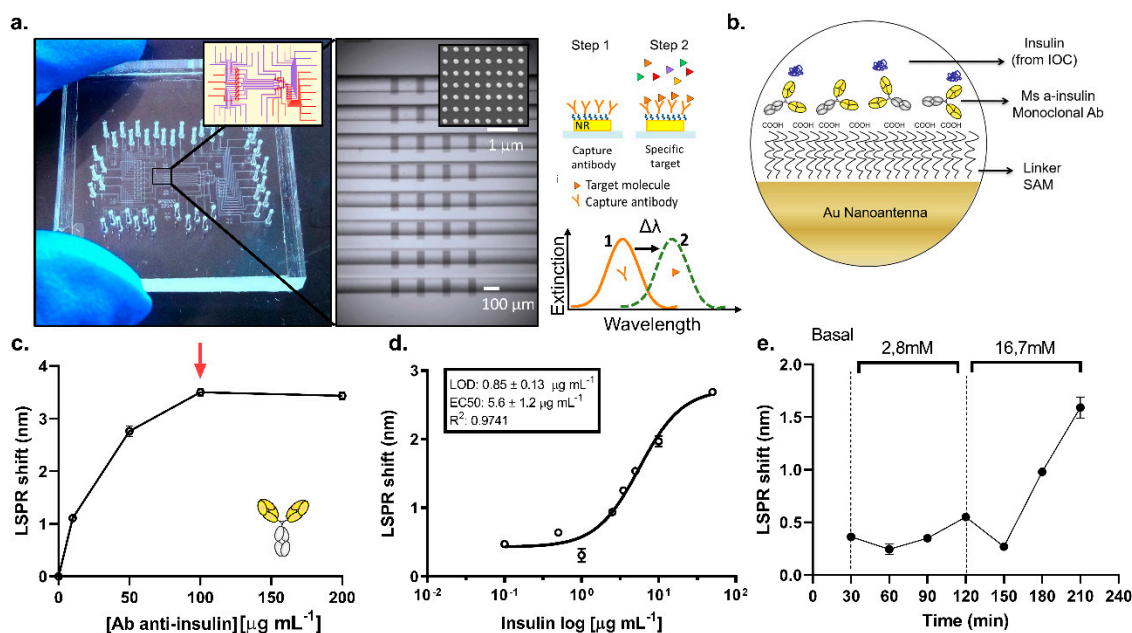


Figure 5. On-chip LSPR sensing platform description and detection. (a) Overview of LSPR sensing platform integrated by functionalized gold nanoantennas couple with a complex microfluidic network. (b) Functionalization strategy applied on gold nanoantenna sensors. (c) Optimization of capture monoclonal anti-insulin antibody. A saturation plateau is observed at 100 µg mL^{−1} antibody concentration (red arrow). (d) Calibration curve performed in KRBH basal glucose content (11.1 mM). Curve shows a limit of detection of (0.85 ± 0.13) µg mL^{−1} (n = 3). (e) Real-time insulin detection by the LSPR sensing platform every 30 min from the connected IOC device stimulated with KRBH buffer at low (2.8 mM) and high glucose (16.7 mM) concentrations, respectively.

The Au sensors were biofunctionalized by immobilizing the insulin antibody to capture the insulin from the sample. To this end, a self-assembled monolayer of MUA (mercaptopundecanoic acid) was formed on the nanorods prior to chip assembly. The assembled chip with a stable MUA layer was then used to immobilize a monoclonal antibody against insulin through EDC/NHS chemistry. A scheme with the functionalization strategy is shown in Figure 5b. Once the antibody is immobilized on the sensors from all eight parallel channels, the separate channels are then used to detect, consecutively, the secreted insulin from the IOC device at eight different times. The eight channels chip design allowed us to divide the whole sensor array in individual sensing areas, monitoring the secreted insulin from the IOC device in situ and in a continuous way. Prior to running the sample measurements, we optimized the antibody concentration (Figure 5c) obtaining a saturation plateau at 100 µg mL^{−1}. Sensograms are shown in Figure S2a,b corresponding to 2 h of functionalization of 0, 10, 50, and 100 µg mL^{−1}, and a functionalization of 200 µg mL^{−1} (which reached the saturation in a shorter time ~45 min), respectively. Furthermore, a direct detection of a recombinant insulin solution of 5 µg mL^{−1} prepared in basal (11.1 mM), low (2.8 mM), and high (16.7 mM) glucose conditions were compared to study the bulk refractive index effect on LSPR measurements. Figure S3a reveals that there is no significant bulk refractive index effect observed for the glucose concentrations considered here, greatly simplifying the integration of the on-chip LSPR

platform with the IOC device. All experiments presented here were performed under direct detection mode (without the need for a secondary antibody to amplify the signal), which allows the continuous monitorization of secreted insulin from a connected IOC device.

For the reference of insulin detection of the IOC samples, the eight-point calibration curve of insulin in KRBH buffer with 16.7 mM glucose in eight parallel channels was obtained. The calibration curve (Figure 5d) shows a limit of detection (LOD) of $0.85 \pm 0.13 \mu\text{g mL}^{-1}$ and EC_{50} of $5.6 \pm 1.2 \mu\text{g mL}^{-1}$. Every data point represents the mean value of three on-chip replicas, and error bars stand for the standard deviations. The IOC device with CMC islets was connected to the LSPR sensing platform to interrogate the secreted insulin. Basal, low (2.8 mM), and high (16.7 mM) glucose levels in KRBH buffer were used to stimulate the CMC islets in the IOC device for different durations in fluidic conditions. Every 30 min was defined as a cycle, and every cycle was flown into separate channels of the LSPR chip for the detection of the accumulative secreted insulin concentration from the IOC device during that cycle (Figure 5e). The raw data obtained for the LSPR measurements during these measurements are shown in Figure S3b. The insulin secretion profile obtained by LSPR measurements shown in Figure 5e reveals that our integrated platform was able to detect an incremental insulin secretion by the pancreatic islets in response to high glucose stimulation over time. The basal level corresponds to insulin accumulated for a time interval of 30 min inside the chamber. With the aim to validate these results, a second IOC device under the same experimental conditions was implemented and the samples were interrogated by ELISA technique. Even though the results cannot be directly compared between both techniques, the insulin secretion profile shown in Figure S3c reveals the same trend in insulin secretion: a remarkable increment of the insulin levels in response to a high glucose content, which supports the results obtained by the on-chip LSPR platform. These results are the preliminary steps to monitor, in a continuous way, the dynamics of insulin secretion by native pancreatic islets under physiological conditions. They demonstrate the potential of the integrated platform to perform OOC experiments with real-time insulin detection, providing a strong tool for drug testing, toxicity studies, and the elucidation of secretion dynamics in relevant tissues linked to metabolic diseases, such as T2D.

4. Conclusions

In this work, we present an OOC platform integrated with an on-chip biosensing platform, enabling in situ monitoring of the insulin secretion from an OOC device. Previously described microfluidic perfusion systems aimed at studying islet functionality are based on the off-line quantification of insulin by ELISA or on-line insulin detection by means of immunofluorescence, therefore labeling this hormone with antibodies. To our knowledge, this is the first time that an IOC device has been coupled with an LSPR sensing module to monitor, in situ and label-free, the insulin released by pancreatic islets. This integrated platform carries the potential to investigate the different secretion dynamics of cells, tissues, and spheroids in OOC platforms, and can be used in new applications, especially in drug screening and personalized medicine technologies. First, we presented here the development of a cellulose-based scaffold to embed pancreatic islets, which provide adequate mechanical properties to biomimic its native architecture. This approach could be extrapolated to other biological systems which require a soft, biocompatible, and non-biodegradable environment to biomimic physiological conditions. The scaffold is integrated into a versatile transparent microfluidic bioreactor to provide the medium exchange, simulate the physiological conditions, and optical monitoring of the islet morphologies. Finally, we developed an automated modular platform that used a microfluidics-controlling breadboard for the timed routing of fluids to interface with an LSPR biosensor chip for measuring soluble biomarkers, such as insulin in situ. All sensing was performed in situ in an uninterrupted and automated manner, allowing for the long-term monitoring of insulin secretion under external glucose stimuli for up to 3 h. We believe that our integrated modular on-line fluid routing and biosensing platform will be compatible with existing

tissue organoid models and will promote their performance in drug screening by providing the capability for the real-time in situ monitoring of their microenvironment.

Even though the experimental set-ups we presented here are not optimally miniaturized, at the initial prototyping stage, such a platform has allowed us to validate our approach to biosensor integration. Combining, for the first time, these two unique technologies will open up new avenues of research into metabolic pathologies in a bid to meet the strong need for the combination of organ-on-a-chip system with microfluidics-integrated, non-invasive biosensing modules to achieve continual bioanalysis of microtissue behaviors. These themes are in line with current efforts to find new techniques to reduce the amount of animal testing, to provide personalized medicine, and to understand the onset and progression of diabetes.

Supplementary Materials: The following are available online at <https://www.mdpi.com/article/10.3390/bios11050138/s1>. Figure S1: Schematic representation of dimensions of IOC device: (a) dimensions of channels and chambers where CMC islets are located; (b) 3D overview of the two layers of PDMS microfluidic IOC device. Figure S2: raw data of the sensograms obtained during optimization of capture monoclonal anti-insulin antibody attached on LSPR gold antennas for (a) 0, 10, 50 and 100 $\mu\text{g mL}^{-1}$ antibody concentrations and (b) 200 $\mu\text{g mL}^{-1}$ antibody concentration respectively. 200 $\mu\text{g mL}^{-1}$ concentration raw data curve showed a faster binding kinetics reaching saturation after ~40 min after injection. Figure S3: (a) sensograms showing the matrix effect observed for the relevant glucose concentrations used in IOC experiments; (b) sensograms (raw data) obtained for insulin detection every 30 min of secretion using low (2.8 mM) and high (16.7 mM) glucose-stimulation regimes. Signals were acquired from different channels of the microfluidics LSPR chip; (c) insulin detection profile from a second IOC device analyzed by ELISA technique every 30 min stimulated with KRBH buffer at low and high glucose concentration, respectively. Video S1, Video S2.

Author Contributions: M.A.O. and J.R.-C. designed the experiments. M.A.O. and O.Y. performed and analyzed LSPR experiments, M.A.O., J.R.-C., and F.V.-M. performed and analyzed IOC experiments. J.B.-T. performed immunoassays experiments. A.N. and J.M.S. provided all the mouse islets during all the work. M.A.O. and V.P. designed and analyzed theoretical simulations. R.Q. and J.R.-A. provided overall guidance of the project. All authors have read and agreed to the published version of the manuscript.

Funding: This research was funded by the European Research Council program under grants ERC-CoG Qnano-334 MECA (64790) and ERC-StG-DAMOC (714317), Fundació Privada Cellex, the CERCA program and the Spanish Ministry of Economy and Competitiveness, through the “Severo Ochoa” Program for Centres of Excellence in R&D (SEV-2015-0522), R&D (SEV-2016-2019) and “Retos de investigación: proyectos I+D+i” (ENE2017-339 87671-C3-2-R and TEC2017-83716-C2-2-R), the CERCA Programme/Generalitat de Catalunya (2014-SGR-1442 and 2014-SGR-1460), Fundació Bancaria “la Caixa”-Obra Social “la Caixa” (project IBEC-La Caixa Healthy Ageing) and the Swedish Research Council (637-2014-340 6894).

Institutional Review Board Statement: The study was approved by the Ethics Committee of Universitat de Barcelona (OB23/19, 7 February 2019) and the Principles of Laboratory Animal Care were followed.

Informed Consent Statement: Not applicable.

Data Availability Statement: The data presented in this study are available on request from the corresponding author. The raw/processed data required to reproduce these findings cannot be shared at this time as the data also forms part of an ongoing study.

Conflicts of Interest: The authors declare no conflict of interest.

References

1. International Diabetes Federation (IDF). *IDF Diabetes Atlas*, 9th ed.; International Diabetes Federation: Brussels, Belgium, 2019; ISBN 9782930229874.
2. Ortega, M.A.; Fernández-Garibay, X.; Castaño, A.G.; De Chiara, F.; Hernández-Albors, A.; Balaguer-Trias, J.; Ramón-Azcón, J. Muscle-on-a-chip with an on-site multiplexed biosensing system for: In situ monitoring of secreted IL-6 and TNF- α . *Lab Chip* **2019**, *19*, 2568–2580. [[CrossRef](#)]

3. Günther, A.; Yasotharan, S.; Vagaon, A.; Lochovsky, C.; Pinto, S.; Yang, J.; Lau, C.; Voigtlaender-Bolz, J.; Bolz, S.S. A microfluidic platform for probing small artery structure and function. *Lab Chip* **2010**, *10*, 2341–2349. [[CrossRef](#)] [[PubMed](#)]
4. Van Midwoud, P.M.; Verpoorte, E.; Groothuis, G.M.M. Microfluidic devices for in vitro studies on liver drug metabolism and toxicity. *Integr. Biol.* **2011**, *3*, 509–521. [[CrossRef](#)] [[PubMed](#)]
5. Beaurivage, C.; Naumovska, E.; Chang, Y.X.; Elstak, E.D.; Nicolas, A.; Wouters, H.; van Moolenbroek, G.; Lanz, H.L.; Trietsch, S.J.; Joore, J.; et al. Development of a gut-on-a-chip model for high throughput disease modeling and drug discovery. *Int. J. Mol. Sci.* **2019**, *20*, 5661. [[CrossRef](#)]
6. Castiello, F.R.; Heileman, K.; Tabrizian, M. Microfluidic perfusion systems for secretion fingerprint analysis of pancreatic islets: Applications, challenges and opportunities. *Lab Chip* **2016**, *16*, 409–431. [[CrossRef](#)]
7. Huh, D.; Matthews, B.D.; Mammoto, A.; Montoya-Zavala, M.; Yuan Hsin, H.; Ingber, D.E. Reconstituting organ-level lung functions on a chip. *Science* **2010**, *328*, 1662–1668. [[CrossRef](#)] [[PubMed](#)]
8. Materne, E.M.; Maschmeyer, I.; Lorenz, A.K.; Horland, R.; Schimek, K.M.S.; Busek, M.; Sonntag, F.; Lauster, R.; Marx, U. The multi-organ chip—A microfluidic platform for long-term multi-tissue coculture. *J. Vis. Exp.* **2015**, *2015*, 52526. [[CrossRef](#)]
9. Bauer, S.; Wennberg Huld, C.; Kanebratt, K.P.; Durieux, I.; Gunne, D.; Andersson, S.; Ewart, L.; Haynes, W.G.; Maschmeyer, I.; Winter, A.; et al. Functional coupling of human pancreatic islets and liver spheroids on-a-chip: Towards a novel human ex vivo type 2 diabetes model. *Sci. Rep.* **2017**, *7*, 14620. [[CrossRef](#)]
10. Novak, R.; Ingram, M.; Marquez, S.; Das, D.; Delahanty, A.; Herland, A.; Maoz, B.M.; Jeanty, S.S.F.; Somayaji, M.R.; Burt, M.; et al. Robotic fluidic coupling and interrogation of multiple vascularized organ chips. *Nat. Biomed. Eng.* **2020**. [[CrossRef](#)]
11. Yu, F.; Iliescu, F.S.; Iliescu, C. A comprehensive review on perfusion cell culture systems. *Inf. MIDEEM* **2016**, *46*, 163–175.
12. Adam Kratz, S.R.; Höll, G.; Schuller, P.; Ertl, P.; Rothbauer, M. Latest trends in biosensing for microphysiological organs-on-a-chip and body-on-a-chip systems. *Biosensors* **2019**, *9*, 110. [[CrossRef](#)]
13. Zhang, Y.S.; Aleman, J.; Shin, S.R.; Kilic, T.; Kim, D.; Mousavi Shaegh, S.A.; Massa, S.; Riahi, R.; Chae, S.; Hu, N.; et al. Multisensor-integrated organs-on-chips platform for automated and continual in situ monitoring of organoid behaviors. *Proc. Natl. Acad. Sci. USA* **2017**, *114*, E2293–E2302. [[CrossRef](#)]
14. Gliberman, A.L.; Pope, B.D.; Zimmerman, J.F.; Liu, Q.; Ferrier, J.P.; Kenty, J.H.R.; Schrell, A.M.; Mukhitov, N.; Shores, K.L.; Tepole, A.B.; et al. Synchronized stimulation and continuous insulin sensing in a microfluidic human Islet on a Chip designed for scalable manufacturing. *Lab Chip* **2019**, *19*, 2993–3010. [[CrossRef](#)]
15. Pedraza, E.; Karajić, A.; Raoux, M.; Perrier, R.; Pirog, A.; Lebreton, F.; Arbault, S.; Gaitan, J.; Renaud, S.; Kuhn, A.; et al. Guiding pancreatic beta cells to target electrodes in a whole-cell biosensor for diabetes. *Lab Chip* **2015**, *15*, 3880–3890. [[CrossRef](#)] [[PubMed](#)]
16. Perrier, R.; Pirog, A.; Ja, M.; Gaitan, J.; Catargi, B.; Renaud, S.; Raoux, M.; Lang, J. Bioelectronic organ-based sensor for microfluidic real-time analysis of the demand in insulin. *Biosens. Bioelectron.* **2018**, *117*, 253–259. [[CrossRef](#)] [[PubMed](#)]
17. Acimović, S.S.; Ortega, M.A.; Sanz, V.; Berthelot, J.; Garcia-Cordero, J.L.; Renger, J.; Maerkl, S.J.; Kreuzer, M.P.; Quidant, R. LSPR chip for parallel, rapid, and sensitive detection of cancer markers in serum. *Nano Lett.* **2014**, *14*, 2636–2641. [[CrossRef](#)] [[PubMed](#)]
18. Heo, N.S.; Oh, S.Y.; Ryu, M.Y.; Baek, S.H.; Park, T.J.; Choi, C.; Huh, Y.S.; Park, J.P. Affinity peptide-guided plasmonic biosensor for detection of noroviral protein and human norovirus. *Biotechnol. Bioprocess Eng.* **2019**, *24*, 318–325. [[CrossRef](#)]
19. Kyriazi, M.-E.; Muskens, O.L.; Kanaras, A.G. DNA: Gold nanoparticles designed for mRNA sensing in cells: Imaging of the gold nanoparticles using two photon photoluminescence spectroscopy. In Proceedings of the Colloidal Nanoparticles for Biomedical Applications XIV 2019, San Francisco, CA, USA, 2–4 February 2019; Volume 10892.
20. Kaye, S.; Zeng, Z.; Sanders, M.; Chittur, K.; Koelle, P.M.; Lindquist, R.; Manne, U.; Lin, Y.; Wei, J. Label-free detection of DNA hybridization with a compact LSPR-based fiber-optic sensor. *Analyst* **2017**, *142*, 1974–1981. [[CrossRef](#)] [[PubMed](#)]
21. Soares, L.; Csáki, A.; Jatschka, J.; Fritzsche, W.; Flores, O.; Franco, R.; Pereira, E. Localized surface plasmon resonance (LSPR) biosensing using gold nanotriangles: Detection of DNA hybridization events at room temperature. *Analyst* **2014**, *139*, 4964–4973. [[CrossRef](#)] [[PubMed](#)]
22. Joshi, G.K.; Deitz-McElyea, S.; Johnson, M.; Mali, S.; Korc, M.; Sardar, R. Highly specific plasmonic biosensors for ultrasensitive microRNA detection in plasma from pancreatic cancer patients. *Nano Lett.* **2014**, *14*, 6955–6963. [[CrossRef](#)]
23. Yavas, O.; Acimovic, S.S.; Garcia-Guirado, J.; Berthelot, J.; Dobosz, P.; Sanz, V.; Quidant, R. Self-Calibrating On-Chip Localized Surface Plasmon Resonance Sensing for Quantitative and Multiplexed Detection of Cancer Markers in Human Serum. *ACS Sens.* **2018**, *3*, 1376–1384. [[CrossRef](#)]
24. Hori, T.; Yamane, K.; Anazawa, T.; Kurosawa, O.; Iwata, H. Compact fluidic system for functional assessment of pancreatic islets. *Biomed. Microdevices* **2019**, *21*, 91. [[CrossRef](#)] [[PubMed](#)]
25. Mohammed, J.S.; Wang, Y.; Harvat, T.A.; Oberholzer, J.; Eddington, D.T. Microfluidic device for multimodal characterization of pancreatic islets. *Lab Chip* **2009**, *9*, 97–106. [[CrossRef](#)] [[PubMed](#)]
26. Lee, D.; Wang, Y.; Mendoza-Elias, J.E.; Adewola, A.F.; Harvat, T.A.; Kinzer, K.; Gutierrez, D.; Qi, M.; Eddington, D.T.; Oberholzer, J. Dual microfluidic perfusion networks for concurrent islet perfusion and optical imaging. *Biomed. Microdevices* **2012**, *14*, 7–16. [[CrossRef](#)] [[PubMed](#)]
27. Silva, P.N.; Green, B.J.; Altamentova, S.M.; Rocheleau, J.V. A microfluidic device designed to induce media flow throughout pancreatic islets while limiting shear-induced damage. *Lab Chip* **2013**, *13*, 4374–4384. [[CrossRef](#)]

28. Rodríguez-Comas, J.; Moreno-Vedia, J.; Obach, M.; Castano, C.; de Pablo, S.; Alcarraz-Vizan, G.; Diaz-Catalan, D.; Mestre, A.; Horrillo, R.; Costa, M.; et al. Alpha1-antitrypsin ameliorates islet amyloid-induced glucose intolerance and beta-cell dysfunction. *Mol. Metab.* **2020**, 100984. [\[CrossRef\]](#)
29. Jun, Y.; Lee, J.; Choi, S.; Yang, J.H.; Sander, M.; Chung, S.; Lee, S.-H. In vivo-mimicking microfluidic perfusion culture of pancreatic islet spheroids. *Sci. Adv.* **2019**, 5, eaax4520. [\[CrossRef\]](#)
30. Folli, F.; La Rosa, S.; Finzi, G.; Davalli, A.M.; Galli, A.; Dick, E.J.; Perego, C.; Mendoza, R.G. Pancreatic islet of Langerhans' cytoarchitecture and ultrastructure in normal glucose tolerance and in type 2 diabetes mellitus. *Diabetes Obes. Metab.* **2018**, 20, 137–144. [\[CrossRef\]](#)
31. Röder, P.V.; Wu, B.; Liu, Y.; Han, W. Pancreatic regulation of glucose homeostasis. *Exp. Mol. Med.* **2016**, 48, e219. [\[CrossRef\]](#)
32. Cabrera, O.; Berman, D.M.; Kenyon, N.S.; Ricordi, C.; Berggren, P.-O.; Caicedo, A. The unique cytoarchitecture of human pancreatic islets has implications for islet cell function. *Proc. Natl. Acad. Sci. USA* **2006**, 103, 2334–2339. [\[CrossRef\]](#)
33. Dishinger, J.F.; Reid, K.R.; Kennedy, R.T. Quantitative monitoring of insulin secretion from microfluidic chip. *Anal. Chem.* **2009**, 81, 3119–3127. [\[CrossRef\]](#)
34. Schulze, T.; Mattern, K.; Früh, E.; Hecht, L.; Rustenbeck, I.; Dietzel, A. A 3D microfluidic perfusion system made from glass for multiparametric analysis of stimulus-secretion coupling in pancreatic islets. *Biomed. Microdevices* **2017**, 19, 47. [\[CrossRef\]](#)
35. Schrell, A.M.; Mukhitov, N.; Yi, L.; Adablah, J.E.; Menezes, J.; Roper, M.G. Online fluorescence anisotropy immunoassays for monitoring insulin secretion from isolated human islets of Langerhans. *Anal. Methods* **2017**, 9, 38–45. [\[CrossRef\]](#)
36. Misun, P.M.; Yesildag, B.; Forschler, F.; Neelakandhan, A.; Rousset, N.; Biernath, A.; Hierlemann, A.; Frey, O. In vitro platform for studying human insulin release dynamics of single pancreatic islet microtissues at high resolution. *Adv. Biosyst.* **2020**, 4, 1900291. [\[CrossRef\]](#) [\[PubMed\]](#)
37. Eggermont, L.J.; Rogers, Z.J.; Colombani, T.; Memic, A.; Bencherif, S.A. Injectable Cryogels for Biomedical Applications. *Trends Biotechnol.* **2020**, 418–431. [\[CrossRef\]](#)
38. García-Lizarribar, A.; Fernández-Garibay, X.; Velasco-Mallorquí, F.; Castaño, A.G.; Samitier, J.; Ramon-Azcon, J. Composite Biomaterials as Long-Lasting Scaffolds for 3D Bioprinting of Highly Aligned Muscle Tissue. *Macromol. Biosci.* **2018**, 18, 1800167. [\[CrossRef\]](#)
39. Chen, Y.; Lin, R. Functional Human Vascular Network Generated in Photocrosslinkable Gelatin Methacrylate Hydrogels. *Adv. Funct. Mater.* **2012**, 22, 2027–2039. [\[CrossRef\]](#)
40. Nichol, J.W.; Koshy, S.; Bae, H.; Hwang, C.M.; Khademhosseini, A. Cell-laden microengineered gelatin methacrylate hydrogels. *Biomaterials* **2011**, 31, 5536–5544. [\[CrossRef\]](#) [\[PubMed\]](#)
41. Huber, B.; Borchers, K.; Tovar, G.E.M.; Kluger, P.J. Methacrylated gelatin and mature adipocytes are promising components for adipose tissue engineering. *J. Biomater. Appl.* **2016**, 30, 699–710. [\[CrossRef\]](#) [\[PubMed\]](#)
42. Marchioli, G.; van Gurp, L.; van Krieken, P.P.; Stamatialis, D.; Engelse, M.; van Blitterswijk, C.A.; Karperien, M.B.J.; de Koning, E.; Alblas, J.; Moroni, L.; et al. Fabrication of three-dimensional bioplotting hydrogel scaffolds for islets of Langerhans transplantation. *Biofabrication* **2015**, 7, 025009. [\[CrossRef\]](#) [\[PubMed\]](#)
43. Henderson, T.M.A.; Ladewig, K.; Haylock, D.N.; McLean, K.M.; O'Connor, A.J. Cryogels for biomedical applications. *J. Mater. Chem. B* **2013**, 1, 2682. [\[CrossRef\]](#) [\[PubMed\]](#)
44. Goh, S.; Bertera, S.; Olsen, P.; Candiello, J.; Halfter, W.; Uechi, G.; Balasubramani, M.; Johnson, S.; Sicari, B.; Kollar, E.; et al. Perfusion-decellularized pancreas as a natural 3D scaffold for pancreatic tissue and whole organ engineering. *Biomaterials* **2013**, 34, 6760–6772. [\[CrossRef\]](#) [\[PubMed\]](#)
45. Bédier, A.; Braschler, T.; Peric, O.; Fantner, G.E.; Mosser, S.; Fraering, P.C.; Benchérif, S.; Mooney, D.J.; Renaud, P. A compressible scaffold for minimally invasive delivery of large intact neuronal networks. *Adv. Healthc. Mater.* **2015**, 4, 301–312. [\[CrossRef\]](#) [\[PubMed\]](#)
46. Velasco-Mallorquí, F.; Rodríguez-Comas, J.; Ramón-Azcón, J. Cellulose-based scaffolds enhance pseudoislets formation and functionality. *Biofabrication* **2021**, in press.
47. Rodríguez-Comas, J.; Moreno-Asso, A.; Moreno-Vedia, J.; Martín, M.; Castaño, C.; Marzà-Florensa, A.; Bofill-De Ros, X.; Mir-Coll, J.; Montané, J.; Fillat, C.; et al. Stress-induced microRNA-708 impairs β -cell function and growth. *Diabetes* **2017**, 66, 3029–3040. [\[CrossRef\]](#) [\[PubMed\]](#)
48. Chen, S.; Svedendahl, M.; Käll, M.; Gunnarsson, L. Dmitriev, a Ultrahigh sensitivity made simple: Nanoplasmonic label-free biosensing with an extremely low limit-of-detection for bacterial and cancer diagnostics. *Nanotechnology* **2009**, 20, 434015. [\[CrossRef\]](#)
49. Unger, M.A.; Chou, H.P.; Thorsen, T.; Scherer, A.; Quake, S.R. Monolithic microfabricated valves and pumps by multilayer soft lithography. *Science* **2000**, 288, 113–116. [\[CrossRef\]](#)